Università degli studi di Milano-Bicocca
Dottorato di Ricerca in Astronomia ed Astrofisica
XVII ciclo

DEVELOPMENT OF MULTILAYER-COATED MIRRORS FOR FUTURE X-RAY TELESCOPES

Ph.D. supervisor: **Dr. Giovanni PARESCHI**
INAF - Brera Astronomical Observatory
Ph.D. tutor: **Prof. Silvio BONOMETTO**
Università di Milano-Bicocca
Ph.D. coordinator: **Prof. Guido CHINCARINI**
Università di Milano-Bicocca

Ph.D. Thesis by **Daniele SPIGA**

Anno accademico 2004-2005

Dedicato a Laura, mia moglie

Contents

List of acronyms

AFM	Atomic Force Microscope
AGN	Active Galactic Nuclei
ASCA	Advanced Satellite for Cosmology and Astrophysics
ASI	Agenzia Spaziale Italiana (*Italian Space Agency*)
BAT	Burst Alert Telescope
BH	Black Hole
CCC	Channel Cut Crystal
Ce. Te. V	Centro Tecnologie del Vuoto (*Vacuum Technology Center* Carsoli, Italy)
CfA	Center for Astrophysics
CGRO	Compton Gamma Ray Observatory
CNES	Centre National d'Etudes Spatiaux (the French Space Agency)
COST	European COoperation in the field of Scientific and Technical research
CTE	Coefficient of Thermal Expansion
CVD	Chemical Vapour Deposition
CXB	Cosmic X-ray Background
DSC	Detector SpaceCraft
EE	Encircled Energy
e.g.	exaempli gratia (*for example*)
EGRET	Energetic Gamma Ray Experiment Telescope
ESA	European Space Agency
ESF	European Science Foundation
ESRF	European Synchrotron Radiation Facility
(E)UV	(Extreme) UltraViolet
EXIST	Energetic X-ray Imaging Survey Telescope
FOM	Figure Of Merit
FOV	Field Of View
FWHM	Full Width Half Maximum

GC	Galaxy Cluster
GRB	Gamma-Ray Burst
HEW	Half-Energy Width
HEXIT	High-Energy X-ray Imaging Telescope
HEAO	High-Energy Astrophysics Observatory
HERO	High-Energy Replicated Optics
HMXB	High-Mass X-ray Binary
HOPG	Highly Oriented Pyrolithic Graphite
HPD	Half-Power Diameter
IBAD	Ion Beam Assisted Deposition
ISAS	Japan's Institute for Space and Astronautical Science
IBS	Ion Beam Sputtering
i.e.	id est (*that is*)
INAF	Istituto Nazionale di AstroFisica (*National Institute for Astrophysics*)
INTEGRAL	INTErnational Gamma-Ray Astrophysics Laboratory
ISM	InterStellar Medium
JET-X	Joint European Telescope X
LMXB	Low-Mass X-ray Binary
LSF	Line Spread Function
LTP	Long Trace Profilometer
MBE	Molecular Beam Epitaxy
MPE	Max Planck Institut fur Extraterresrische Physik
MSC	Mirror SpaceCraft
NASA	National Aeronautics and Space Administration
NEXT	NEw X-ray Telescope mission
NS	Neutron Star
OAB	Osservatorio Astronomico di Brera (*Brera Astronomical Observatory*)
PDS	Phoswitch Detector System
PPM	Pythonic Program for Multilayers
PSD	Power Spectral Density
PSF	Point Spread Function
PSPC	Position Sensitive Proportional Counter
PVD	Physical Vapour Deposition
QPO	Quasi Periodic Oscillations

QSO Quasi Stellar Objects

RF Radio Frequency

rms Root Mean Square

ROSAT ROntgen SATellite

SAX Satellite per Astronomia X (*X-ray Astronomy Satellite*)

SEM Scansion Electronic Microscope

SNR SuperNova Remnant

SPIE Society of Photo-optical Instrumentation Engineers

STSM Short Term Scientific Mission

TBD To Be Determined

TEM Transmission Electronic Microscope

ULX Ultra Luminous X-ray sources

vs. versus (*against*)

WD White Dwarf

XEUS X-ray Evolving Universe Spectroscopic mission

XMM X-ray Multimirror Mission

XRB X-Ray Background

XRR X-Ray Reflectivity

XRS X-Ray Scattering

XRT X-Ray Telescope

Introduction

Since years 60s, our knowledge of the Universe has known a dramatic leap forward by the opening of the X-ray window. The discovery of cosmic X-ray sources and of the X-ray background by Riccardo Giacconi (Nobel Prize 2002) has shown how we can observe the violent processes at work in the sky, has given a chance of observing objects invisible in other energy bands and measuring their physical properties due to the strong penetration power of X-rays and their spectral features.

As X-rays cannot penetrate Earth's atmosphere, our knowledge of the X-ray sky had to wait the advent of space era. To observe X-rays it is necessary to remove the 99% of the atmosphere, and the softer the X-rays are even more difficult they are to be detected. Balloon-borne missions in the Earth's stratosphere at 30 Km altitudes can observe X-rays only over 20 keV, but a rocket above 80 Km is needed to observe 3 keV X-rays. Finally, only an instrument on-board a satellite spacecraft above 200 Km can observe X-rays below 1 keV, hence the telescope has to outstand the rigours of launch and to resist to the extreme environmental orbital conditions. Thus, X-ray astronomy is expensive and has to take into account a number of logistical difficulties.

After the discovery of cosmic X-ray sources many missions were conceived improving the performances of the X-rays telescopes at every step. In particular, the introduction of X-rays focusing optics in X-ray telescopes have allowed a great improvement in sensitivity, in resolving single X-ray sources, in X-ray imaging. Soft X-ray focusing exploits a single or double reflection in grazing incidence on a until today, through EXOSAT, ROSAT, ASCA, BeppoSAX, and allowed to obtain images of the soft X-ray sky like optical telescopes. Operating X-ray satellites (Newton-XMM, CHANDRA) are noticeable for their unprecedented experienced effective area and angular resolution, respectively.

However, all of these focusing optics have an exploitable effective area only in the soft X-ray band (1-10 keV) but a negligible area in the band of hard X-rays (10-100 keV), because the incidence angles necessary to get an high reflectivity in this energy range would be too shallow to offer a useful collecting area. Since now, the most sensitive telescope ever made is the simply collimated SAX-PDS, whose sensitivity is very far from the reached ones in soft X-rays. Moreover, the source resolution in hard X-rays is still unsatisfactory in many astrophysical targets: for instance the X-ray background (which peaks at about 30 keV as result of a probable superposition of X-ray spectrum of obscured and unobscured AGN) has not yet been resolved in single sources.

A further leap forward in X-ray astronomy could then be done by the realization of hard X-ray optics: this aim can be reached by coating the shells of the X-ray optics with a film which is able to reflect even hard X-rays with larger grazing incidence angles than the reachable ones with a traditional (Au, Ir) single layer. Such films can be multilayer coatings, successions of alternated layers of two materials like Pt/C or Ni/C or W/Si. Such films are able to extend the reflectivity band of grazing incidence optics to hard X-rays from about 10 to 80 keV. Over 80 keV up to 130 keV other techniques (Laue mosaic crystals) are suitable.

Multilayer films require a carefully study in order to guarantee the performance of the focusing optics. The reflectivity requires a very low interlayer roughness and the film has to be very steady in the extreme orbital environment: the reflecting layer must be easily reproducible and the shape of the mirror has not to be affected by stresses which arise in the layered film during and after its deposition. The mirror substrate, however, has to be thin enough so that the resulting mass of the optics will meet the operative requirements of the mission.

This Ph.D. thesis, resulting from my work at the Astronomical Observatory of Brera-Merate (INAF-OAB in Merate (LC), Italy), is devoted to the development of focusing optics for the next X-ray missions, especially the balloon-borne telescope HEXIT (funded by ASI, launch foreseen in 2005) and its follow-up on-board satellite HEXIT-SAT (2010), the CNES mission SIMBOL-X (2008) the NASA mission Constellation-X (2013) and the ESA mission XEUS (2020). All of these missions will carry a focusing optics for hard X-rays in order to bring the sensitivity over 10 keV to levels never reached before: this goal will be reached mainly by implementing multilayer coatings on the mirrors. The first chapter will shortly introduce the main X-ray sources paying a special attention to the actual knowledge of the hard X-ray sky and what we can expect from an improvement of sensitivity in this field.

The second chapter will provide the basics of the X-ray focusing and the manufacturing technique used to make the traditional soft X-ray optics. Basic theory of multilayer coatings is the subject of the third chapter, in particular I have derived practical formulas to evaluate the peak reflectivity of a multilayer coating and the electric fields in a multilayer stack. In the fourth chapter we will describe the techniques used to produce multilayer optics, and in the fifth chapter a description of substrates and multilayer coatings characterization methods, with thickness and roughness measurements. In this chapter I have also given an interpretation of the classical link scattering/surface PSD, using a formalism that can be easily extended to characterize multilayer coatings.

The chapter 6 describes the characterization I performed on flat prototypes of new possible mandrel coatings to extend the replication technique to hard X-rays using multilayer coatings: the chapter 7 describes my experimental work in multilayer coatings development during my Ph.D.: I have performed both deposition (at Media-Lario s.r.l.) and characterization (at INAF-OAB), using the same facilities and the experience this collaboration recently acquired in conceiving and manufacturing the XMM mirrors. This work has led to the production of a prototype of multilayer-coated, hard X-ray mirror shell by Nickel electroforming. The characterization performed at the PANTER X-ray facility (MPE-Germany) on this mirror shell and on two mirror shell prototypes for the hard X-ray telescope Constellation-X will be exposed in the chapter 8, including my interpretation of the reflectivity data.

The chapter 9, finally, will present the use of the numerical code PPM (by A. Mirone, ESRF) in the multiparametric fitting of X-ray multilayer structures, a very powerful tool to interpret X-ray multilayer reflectivity scans.

Chapter 1

The hard X-ray Universe: an overview

Forty years later the discovery of the Diffuse Cosmic X-ray Background (CXB) (discovered by Giacconi et al. in 1962 during one of the first rocket-borne experiments) and of compact X-ray sources we are able to understand the basics of the physical nature of various classes of the galactic X-ray binaries, and a similar situation is confronted to the origin of the CXB. There is now little doubts that the CXB is due to the integrated contribution by discrete sources rather than to a truly diffuse emission, and below 10 keV a large fraction of it has been resolved into sources by Chandra and XMM. A model for these sources are also available: they are mainly *Active Galactic Nuclei* (AGN) with a minority of Galaxy Clusters (GC) and the CXB is regarded as the superposition of the X-ray emission produced by mass accretion onto supermassive black holes in galactic nuclei along the cosmic history. We can thus calculate the black hole mass density in the Universe from the measure of the CXB energy density.

However, the energy range where most of accretion power is radiated (20-60 keV, peaking at 30 keV) is still essentially unexplored, and almost all results on black hole mass density are based on extrapolations of measurements dealt under 10 keV. This situation is *mainly due to the lack of focusing/imaging optics in hard X-rays*. If we were able to produce a focusing telescope to explore the hard X-ray sky we would answer to one of the most standing issue in X-ray astronomy, that is, the explanation of the X-ray background. Moreover, such a telescope would have the capability of observing a wide set of X-ray sources: it would so supply very useful data to clarify their physical nature and the X-ray radiative processes. A focusing hard X-ray telescope would make a leap forward in X-ray comparable to the achieved one in late 70s by the Einstein (HEAO-2) observatory.

It will be shown in the sect. 2.1.2, page 16, how the introduction of hard X-rays focusing optics allows a great improvement not only in angular resolution, but in the sensitivity in this band also (see fig.1.1). The following of this chapter will present the main scientific targets of a hard X-ray focusing telescope and the scientific throughput expected by their observation in next X-ray missions.

1.1 Hard X-rays galactic sources

1.1.1 The Galactic Centre and the Galactic Ridge

The Central region of our own Galaxy hosts a black hole, whose mass can be estimated as around 3×10^6 solar masses. Its accretion rate is likely very low, as well as its radiative conversion efficiency, because its emission in X-rays is very low. Newton-XMM detected (see bibl. [2]) an X-ray emission than could not be explained a simple thermal plasma emission, as its temperature would be more than 10 keV, i.e. completely ionised.

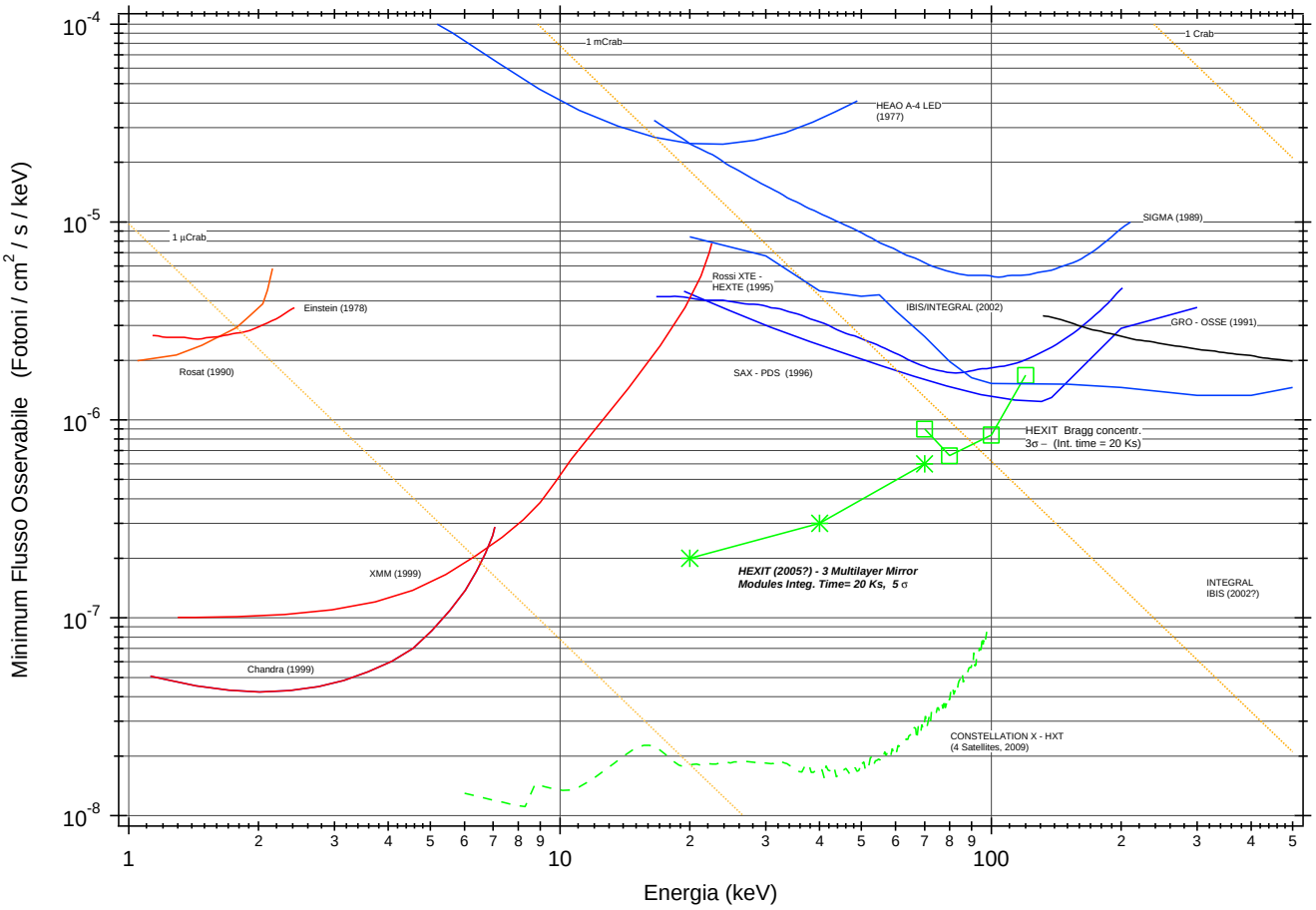

Figure 1.1: Present reached sensitivity (5σ) of past, actual and future X-ray telescopes. The integration time is 10^5 sec (except HEXIT, being a balloon-borne mission), the energy band is the 50% of E. The sensitivity in hard X-rays ($10 \div 100$ keV) is still worse than in soft X-rays ($1 \div 10$ keV) because of lack of focusing optics over 10 keV. A great improvement is expected from the launch of HEXIT and Constellation-X (2013?).

This contrasts with the observation of many emission lines (e.g. the Kα H and He-type of Fe, S, Ar ... lines). Moreover, a so hot gas could not be held in the Galactic Center by its gravity. The emission over 9 keV is probably non-thermal, producing a rather hard spectrum. Moreover, Chandra detected a flaring activity (see bibl. [3]), with a spectrum hardening in the active phases: the spectrum nature is difficult to explain with a thermal model, but the existing data do not permit to discriminate between different scenarios, and to argue some black holes parameters. A hard X-ray spectrum (over 9 keV) and a timing observation would permit to constrain the physical models, but it cannot be obtained with XMM (see fig. 1.2). The necessary sensitivity can be reached only with an extension of the focusing techniques to the hard X-rays.

The Galactic Center hosts also Molecular clouds (like Sgr B2, at the projected distance of 100 pc away from the center) which emit a hard X-ray spectrum with a prominent Fe-K line, probably as result of X-ray photon reprocessing. As this region does not include enough strong primary hard X-ray sources, this fact might suggest the clouds are reverberating the past emission of the supermassive Black Hole, which had to be active in the last centuries. A sensitive mission with a good angular resolution over 10 keV could confirm the Compton reflection nature of the spectrum and provide clues on the radiated power in the active phases.

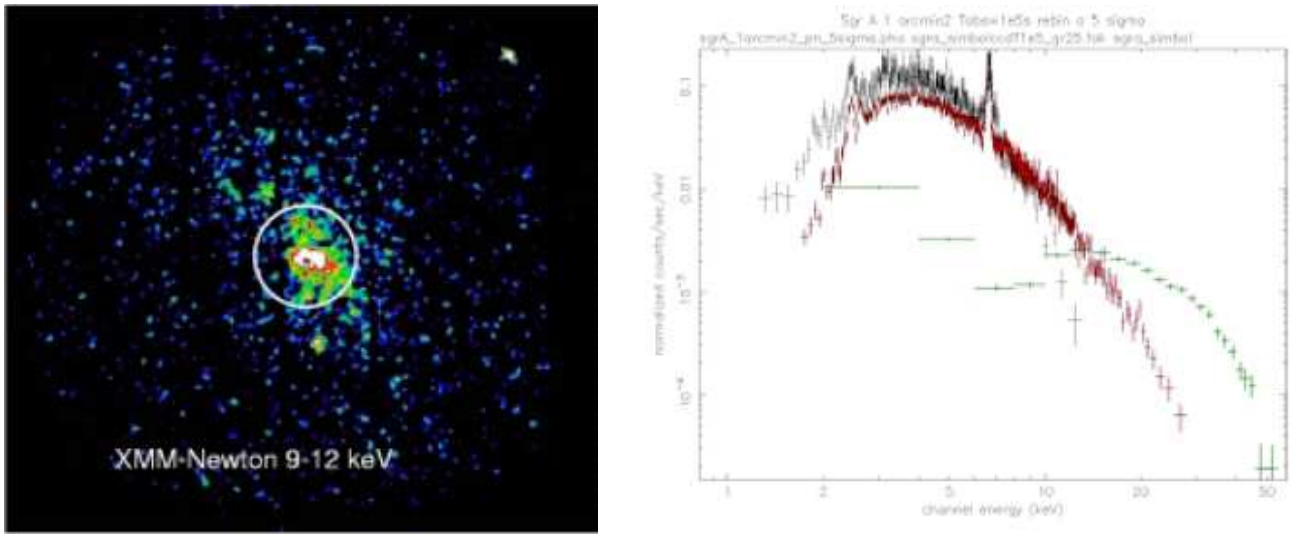

Figure 1.2: (left) The Galactic Center observed in X-rays (9-12 keV) by XMM-EPIC with 20 ksec integration time (credits: ESA). (right) The spectrum around Sgr A* (1^o wide) by XMM-EPIC (black line) and a simulation of the spectrum observed by SIMBOL-X (CCD: red plot, CZT: green plot). The SIMBOL-X spectrum is much more extended in the hard X-rays (credits: CNES).

The Galactic Ridge is also an X-ray source, mainly a soft thermal one ($kT \sim 1keV$). A 6.7 keV (Fe K line) is also present and the data could account for the presence of a non-thermal component. Since now no data are available because of lack of imaging systems over 10 keV. A future mission with a good angular resolution in this band could trace a map of this region, discriminating it from the crowded field of galactic X-ray sources.

1.1.2 Supernova Remnants

Galactic Supernova Remnants (SNR) are very interesting objects to be observed in hard X-rays: they are characterized by a thermal ($10^7 \div 10^8$ K) and a non-thermal component (synchrotron in radio) at the shock front where the ejected matter meets the ISM. The ultrarelativistic electrons are accelerated in the shock front, and they can be ejected to increase the cosmic rays populations. The maximum attainable energy in this acceleration process is a very interesting open question in understanding the origin of cosmic rays: a measurement would be, indeed, possible by detecting the eventual presence of a hard X-ray tail taking over the thermal component (i.e. over 10 keV, see fig. 1.3 emitted by the synchrotron emission of electrons in the energy range 1-10 TeV. A detailed survey of these object would give important constraints about the energy electron spectrum in the SNR acceleration process.

Some SNR show, moreover, the presence of radioactive isotopes produced in the explosion. The young SNR Cas A, e.g., has been found by BeppoSAX to be a emitter in the line at 68 keV of the ^{44}Sc, a decay product of the ^{44}Ti (the detection required 500 ksec to have a 3-5 σ confidence level). Similar detections in other young supernova (even fainter, Tycho or Kepler SNR) remnants with a higher sensitivity level in the hard X-rays could be achieved in few 10 ksec.

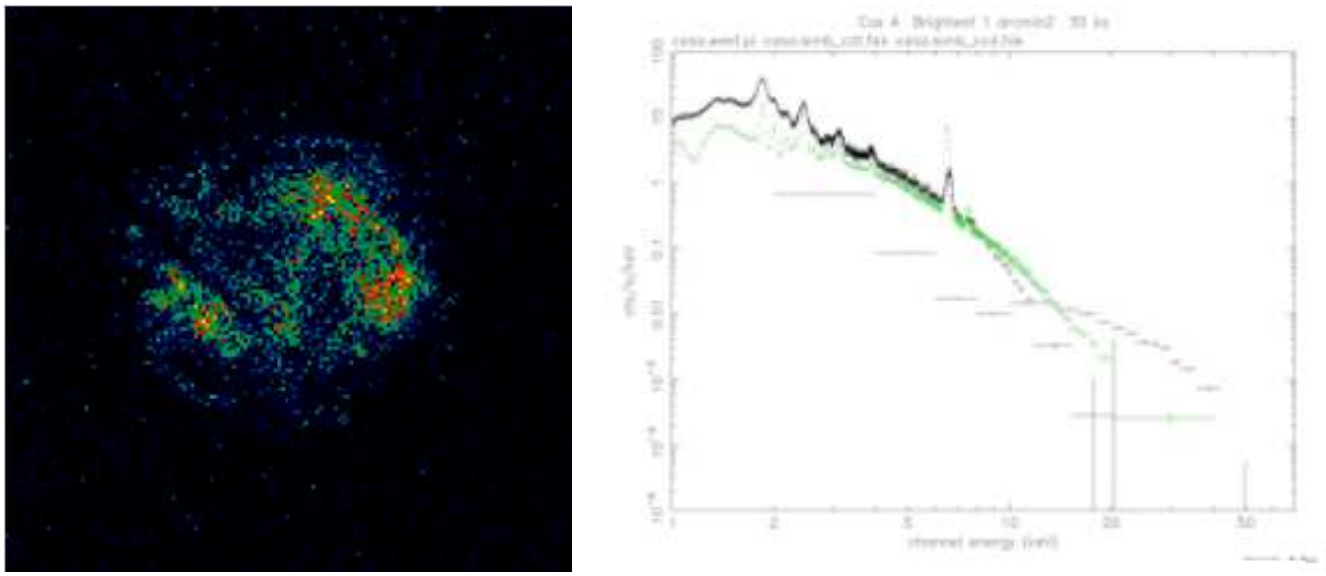

Figure 1.3: (left) Simulation of the emission of Cas A over 20 keV, observed by SIMBOL-X in 100 ksec (credits: CNES). (right) The Cas A spectrum observed by XMM-EPIC (black line) and a simulation of the spectrum observed by SIMBOL-X (CCD: green plot, CZT: red plot). The SIMBOL-X sensitivity allows a better coverage of the hard X-rays (credits: CNES).

1.1.3 Galactic X-ray binaries

Galactic X-ray binaries can host many physical processes producing a hard X-ray spectrum, either in binary systems containing Neutron Stars or those containing Black Holes.

Cyclotron lines in HMXBs The spectra of HMXBs are harder than in LMXBs, usually power law with a photon index ~ 1. Over 15-20 keV the emission has an exponential cut-off. This spectral pattern is commonly believed to be produced by an inverse Compton scattering. It is very interesting that in the harder part of the spectrum of a number of accreting X-ray pulsars broad absorption lines have been detected. They are interpreted as cyclotron resonant scattering: i.e. the lines correspond to the gyro frequency of electrons in a NS strong magnetic field and to its harmonics. As the cyclotron frequency $\omega_B = \frac{e}{mc}B$ depends only on the magnetic field, the detection allows a direct B measurement of the Neutron Star.

The detection of cyclotron lines in binaries started in 1979 (Her X-1, Wheaton et al.). BeppoSAX provided a large number of results in this field (see bibl. [4], bibl. [5]). Since now, 11 sources show cyclotron lines in their spectrum. However, many features are still to be investigated: some sources, for instance, do not present cyclotron lines at all. Some disagreements involve also the strengths of the absorption lines, which do not decrease with their order as the theory requires. Their positions also are not always exactly spaced. More complicated models have been proposed, and only a detection on a wider HMXB sample can help to understand the underlying physical processes. This can be done only by improving the hard X-ray sensitivity flux limit.

INTEGRAL hard sources Since the first months of activity, the (coded-mask equipped) hard X-ray and Gamma telescope ISGRI-INTEGRAL has detected a new class of hard X-ray sources in the band 15-40

keV (flux limit: 10-50 mCrab[1]) with strong interstellar absorption ($N_H > 10^{22} cm^{-2}$) and a hard spectrum. They are located within a degree away from the galactic plane, thus they are galactic objects. Their nature is not yet clear: likely they are NS with high mass companion (Be stars), as suggested by their periodic variability with period of some hours. On the basis of INTEGRAL detections, the PDS data archive is being reanalyzed and many sources are discovered in the PDS serendipitous surveys, corresponding to the INTEGRAL sources (see bibl. [6]). Bright transients were observed in at least one case (the CI Cam star: see e.g. bibl. [8]).

The strong obscuration of this class of sources makes very difficult the detection in soft X-rays: this was possible with relatively near objects (like CI Cam, 1 kpc): this makes us guess that these objects must be quite common in the Galaxy. Hence, a systematic study can be performed only with sensitive hard X-ray telescopes.

Hard X-ray emission from LMXBs and HMXBs Many binary systems show a hard variable component. Its detection started since 1966 in Sco X-1 over 40 keV, with strong variations. Cyg X-1, hosting an accreting black hole, shows two spectral states with a strong hard X-ray emission in the hard state with a break around 100 keV, during the soft state there is instead no evident break up to 200 keV (see bibl. [7]). The presence of such a hard spectrum gives strong constraints to the accretion disks models: the classical model of a geometrically thin, optically thick disk was so modified including the presence of a hot inner corona, where the soft photons are comptonized up to the observed energies.

Currently (BeppoSAX, RXTE) we have evidence of hard X-ray emission in all the classes of X-ray binaries up to 100-200 keV. The hardness of the emission seems to be anti-correlated with the mass accretion rate (as observed first by Van Paradijs and Van der Klis in 1994): this is evident from the fall in luminosity corresponding to the soft/hard state transitions, especially in the atoll sources (low magnetized NS). Moreover, the X-ray flux transients are correlated with the corresponding radio transients (Fender 2001), which is interpreted as the presence of jets. The underlying physics, however, is still uncertain. Great advances are expected from a telescope with a wide band sensitivity in hard X-rays.

Quiescent transient sources Some LMXBs are persistent, i.e. they are stable systems with an accretion disk extended in the depth of the gravitational potential. Most X-ray sources are instead transient. NS in LMXBs have been accelerated by accretion torques to millisecond periods, due to a strong interaction with the accretion disk via the NS magnetic field. This scenario was confirmed by the presence of Quasi-Periodic Oscillations (QPOs) during bursts in a number of LMXRBs (see bibl. [9]).

The magnetic fields of LMXRBs are low (10^8 -10^9 G) and this allows the formation of a magnetosphere which expands during the decreasing phase of the outburst. When the accreting matter pressure decreases, the magnetospheric radius drags the matter at such velocities that the accretion is hampered by the centrifugal forces. In this regime the accretion is very small ("propeller" state) but at the magnetospheric boundary very strong shocks arise, producing hard X-rays. Such peculiar scenario implies that emission mechanisms are dominated by the interaction between the magnetic field and the ionized matter: the resulting spectrum over 10 keV is very sensitive to the mechanism details and so it could be studied with a sensitive hard X-ray mission. For systems containing black holes, the low radiation efficiency in the soft X-ray band in the qui-

[1]The Crab is the Crab nebula X-ray photon flux, often used as X-ray measurement unit. Its spectrum is $S(E) = 10 \times E^{-2.05}$ ph cm^{-2} s^{-1} keV^{-1}. In the band 2-10 keV 1 μCrab corresponds to 2.4×10^{-14} erg cm^{-2}s^{-1}.

escent state is usually explained by models including the advection of energy into the hole (ADAF models, Advection Dominated Accretion Disks). These models are very weakly constrained by the soft X-ray data. Only sharp data over 10 keV will be a probe for these models.

Cataclismic variables They are accreting WD and they are usually strong X-ray emitters: they show a very soft X-ray emission, but a hard component is always present (produced at the base of the accretion column by optically thin plasma) with temperatures of 10-20 keV and sometimes also 40 keV. A sensitive coverage over 10 keV would allow the determination of the accretion column structure and the WD mass determination.

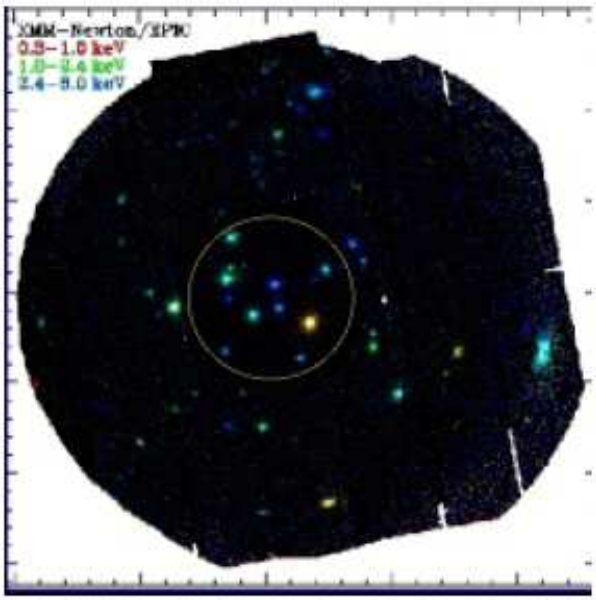

Figure 1.4: XMM image of the densest ρ Ophiuchi region: a number of protostars is crowded in the field. The observation with hard X-ray telescopes will allow avoiding the extinction effects, that overcome completely the soft emission in the youngest protostars (credits: Grosso et al.).

1.1.4 Star-forming regions

Protostars The imaging protostars of class O and I in high energies is a field almost unexplored since now. These objects are very young ($10^4 \div 10^5$ yr) and they are embedded into a massive and cold collapsing envelope, which forms, in the inner regions, a rapidly rotating accretion disk. These protostars, very obscured, have shown since the 80s an X-ray emission (TENMA 1987, GINGA 1992, ASCA 1996) having the spectrum of a very absorbed ($N_H = 3 \times 10^{22}$ cm^{-2}) bremsstrahlung model (kT = 7 keV), showing high temperatures processes at work. In 2001 (Tsuboi et al.) a couple of very obscured sources were discovered with Chandra. The next step in the study of so largely absorbed sources is the exploration in the 20 -100 keV at high angular resolution, with a simultaneous observation in the NIR and the Microwaves.

Hard X-ray emission from flaring stars BeppoSAX-PDS has detected hard X-ray emission flares in Algol-type stars (up to 40 -50 keV). Flares in such stars, highly magnetized (see bibl. [10]), produce a significant hard X-ray emission as interaction of eruption shock with the circumstellar disk. The hard X-ray

flux seems to be a tail of thermal components of hot plasma, but it is known that also in the Sun the coronal X-ray spectrum is non-thermal over some tenth keV, and it is caused by synchrotron emission of MeV-electrons accelerated by the shocks.

Flares stars, with their intense magnetic activity, are expected to be hard X-ray emitters: eventually they could also contribute to the galactic Cosmic Rays population and produce also a γ-ray emission as effect of the nuclear spallation in the coronal gas. The spectroscopy of non-thermal components around 30 keV in the flares would be possible with a higher sensitivity in the hard X-rays, but also a detection with imaging capabilities would be very useful as such flaring stars are often closed in a dense dust envelope and cannot be observed: the high penetrating power of hard X-rays could allow the detection of a much larger population of young stars (see fig. 1.4).

1.2 Hard X-rays extragalactic sources

1.2.1 Active Galactic Nuclei (AGN)

Galaxies with an active nucleus show an intense and variable luminosity ($10^{42} \div 10^{47}$ erg/s) from a very small volume, where the gravitational attraction of a supermassive black hole ($10^6 \div 10^9$ solar masses) on the circumnuclear matter develops a radiative emission with efficiency much higher than in stellar nuclear reactions. This process is very common in Universe from nearby galaxies up to cosmological distances (10-20 % of the age of the Universe): the superposition of the accretion power of AGNs is the main source of the X-ray background. In X-rays, the AGN accretion is observed very near to the black hole horizon (maximum some light days), but also secondary effects are observed up to a distance of 300 light-years, where the primary X-rays interacts with the surrounding environment. The main processes are:

- The *Compton reflection* from optically thick gas, producing a broad spectral component peaking around 30 keV.
- The fluorescence of heavy elements, especially the iron K line blend at 6.4-6.9 keV.
- The photoelectric absorption by circumnuclear gas, that cuts off the spectrum to higher energies as the column density goes from $10^{20}\ cm^{-2}$ to $10^{24}\ cm^{-2}$.

Over column density of $10^{24}\ cm^{-2}$ the gas becomes Compton thick and the primary radiation is completely absorbed, leaving only the reprocessed radiation.

The absorption from the dust has effects on the optical spectrum, traditionally the AGN are classified into two types: the type 1 has a little or no absorption at all, the type 2 shows instead a strong absorption in the visible spectrum.

Type 1 AGN Their X-ray spectrum is a combination of a power-law $F \propto E^{-\alpha}$ with energy spectral index $\alpha = 0.5 \div 1$ and an exponential cut-off at energies of order $100 \div 300\, keV$. A Compton component appears over 10 keV and peaks at 30 keV: metals fluorescence lines are also observed. BeppoSAX was since now the only satellite which was able to analyse the spectral components for a dozen of objects, all brighter than 1 mCrab over 10 keV. This kind of objects belongs to the class of *Seyfert Galaxies* ($L \sim 10^{43} \div 10^{44} erg/s$). However, the sample is limited to few objects and it does not cover a wide range of luminosities: it is then impossible to test how the spectral features (i.e. the physical conditions) vary with the X-rays luminosity, black hole mass and accretion rate. The extension of the study to fainter objects would be possible with

a focusing satellite over 10 keV, up to include the more distant Quasi Stellar Objects (QSO) and the least luminous Seyfert galaxies ($\sim 0.1 mCrab$).

Chandra and XMM have discovered that a number of AGN 1 is associated to a relativistic outflow ($\beta \approx 0.1 \div 0.4$) carrying masses close to the Eddington Limit of the black hole. They are blue-shifted and highly ionized, with Fe-K absorption features (see fig. 1.5). Accurate measurements are difficult because of the decrease of the instrument sensitivity above 6-7 keV, being this due to the loss of the mirror effective area with increasing energy. A telescope with mirrors for energies over 10 keV could have instead a more constant sensitivity in the energy range of the Fe-K line. Moreover, the precise measurement of the high-energy spectrum would allow a best evaluation of the continuum spectrum also in the soft region.

Type 2 AGN These AGN are seen through a screen of neutral gas, thus biased against their identification (both in optical and in X-rays). The bias in X-rays is maximal for sources with column densities around $1.5 \times 10^{24}\, cm^{-2}$. Under this limit the nuclear emission can be partly transmitted, and observed *over* 10 keV, because the photoelectric cross-section of nuclear gas is less for harder photons. The data about column densities are still very uncertain, because what is known is based only on optically selected objects (that were mainly observed by BeppoSAX, at its sensitivity limit over 10 keV). A mission able to increase the X-ray sensitivity up to 60 keV could extend the sample and provide a statistics of column densities, a very important clue to explain the CXB as spectrum synthesis of the AGN outputs.

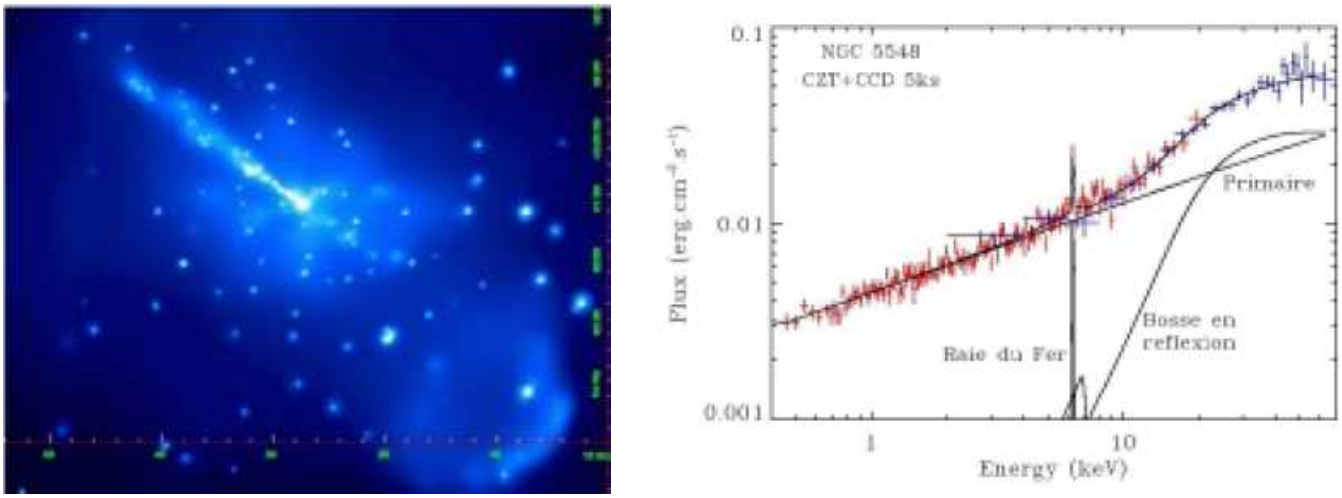

Figure 1.5: (left) Chandra X-ray image in the band 1-3 keV of the Cen A nucleus. The jet is clearly visible, together with the hot spots, probably caused by shocks. The image size is $10' \times 8'$. (right) A spectrum of the NGC 5548 AGN: simulation for SYMBOL-X. The Fe Kα is clearly emerging on the continuum: the reflection spectrum is detected in 5 ksec of observation over 10 keV (credits: CNES).

Blazars Extragalactic Radio Sources can radiate a total energy as large as 10^{60} erg to distances of about 100 Kpc. This emission is produced by relativistic plasma jets accelerated by the nucleus to velocities close to the light speed (see fig. 1.5). If the relativistic jet has an orientation near to the line of sight, the non-thermal emission is strongly amplified by special Relativity effects and constitutes most of the observed flux at almost all frequencies. These sources are called *Blazars*. The spectral energy distribution radio to γ-rays is the combination of two components. The first one is a synchrotron emission and covers the range from radio to X-rays. The second one is due to inverse Compton (from X to γ-rays). Often, the latter component

is the brightest one. In high luminosity Blazars, the first peak is in the infrared band, the second in the MeV range.

According to the most widely accepted model, the emission of Blazars is caused by particles accelerated in shocks produced in collisions of different shells in the jet travelling at different velocities: hence, from the spectral study of the two spectral components, information on the physical properties of the jets could be inferred. BeppoSAX was able, for the first time to observe a few sources in which the peak of synchrotron emission reached 100 keV. In these sources, the Inverse Compton component should peak in the GeV or even TeV range. γ-ray emission in about 50 sources have been detected by the EGRET instrument on-board the Compton Gamma Ray Observatory.

Generally, the hard X-ray band is where the inverse Compton Component takes over the synchrotron component, thus a wider and more sensitive band coverage than BeppoSAX will allow a systematic investigation of the energy spectrum in a much much representative objects sample in distance and luminosity.

A hard X-rays focusing telescope could measure the hard X-ray component in hundreds of sources. In particular, it would be possible to have some guesses about the cosmological evolution of spectrum of the relativistic jets. Moreover, simultaneous multiwavelength observations from radio to γ-rays will be possible: the γ-ray band might be covered by the observatory GLAST, operating from 1 to 100 GeV (and by ground-based Cherenkov telescopes), and a very sensitive X-ray telescope could fill the gap between the soft X-rays and γ instruments. Multiwavelength variability studies will permit to investigate the particle acceleration mechanism and the physical evolution of the relativistic jets.

1.2.2 The Cosmic X-ray Background (CXB)

The missions from UHURU to HEAO-1 with their collimated detectors have allowed to recognize at the end of the years 70s a number of X-ray sources in the 2-10 keV band. Their number increase by a threefold factor in this decade was due to a factor 12 increase in collecting area, a gain quite modest because of the limited angular resolution and the increase in the number density of sources as the flux S decreases ($N(< S) \propto S^{1.5}$).

An important result obtained by HEAO-1 is the discovery of the *CXB peak*: the energy density has a broad maximum around 30 keV, about 5 times more intense than at 1 keV and 1.5 times more intense than at 10 keV (see fig. 1.6). This fact, as suggested by Setti and Woltjer (1973,1979) is a clue of the origin of the CXB; it could be due to the unresolved contribution of many discrete sources at cosmological distances. Resolving the CXB could be possible by increasing the angular resolution and lowering the flux detection limit; the HEAO-1 survey, however, could explain less than 1% of the CXB in term of discrete sources.

The Einstein Observatory (HEAO-2) launched in 1978 allowed for the first time to obtain a direct image of the X-ray sky due to to a system of focusing optics (resolution 40" with the IPC and 2" with the HRI). It could detect sources down to 1.5 μCrab before reaching the confusion limit, operating from 0.2 to 4.5 keV, and could first achieve a deep X-ray imaging (see bibl. [13]). It had a resolving power up to 2" and resolved 20-25% of the CXB into discrete sources in the soft X-ray band. The optical counterparts were mainly AGN with a minority of Clusters of Galaxies. In the following years, ROSAT (1990) operated in the 0.1-2.4 band, with a larger collecting area and a wider field of view than Einstein, and an angular resolution of 0.5" (PSPC). A whole-sky survey and a very deep survey in the Lockman Hole[2] was obtained: about

[2]A region of the sky where the interstellar gas is particularly thin, and where the telescope has a better response at low energies.

75% of the CXB had been resolved into discrete sources down to 0.05 μCrab, optically identified with AGN (see bibl. [16]).

This results are a great success of the idea of Setti and Woltjer (1973) and are the observational basis of the CXB intepretation as the integrated output of the accretion processes during the cosmic history (see bibl. [14], bibl. [19]). This process led to the formation of supermassive black holes, which we observe in *active* phase in AGN (quasars, Seyfert galaxies, ...) and in *quiescent* phase in the nearby galaxies and in ours. Nevertheless, the spectra of the AGN (contributing around 1 keV) are softer than the CXB: even if the CXB were totally made of AGN at 1 keV, of the known AGN population and the 30 keV pe

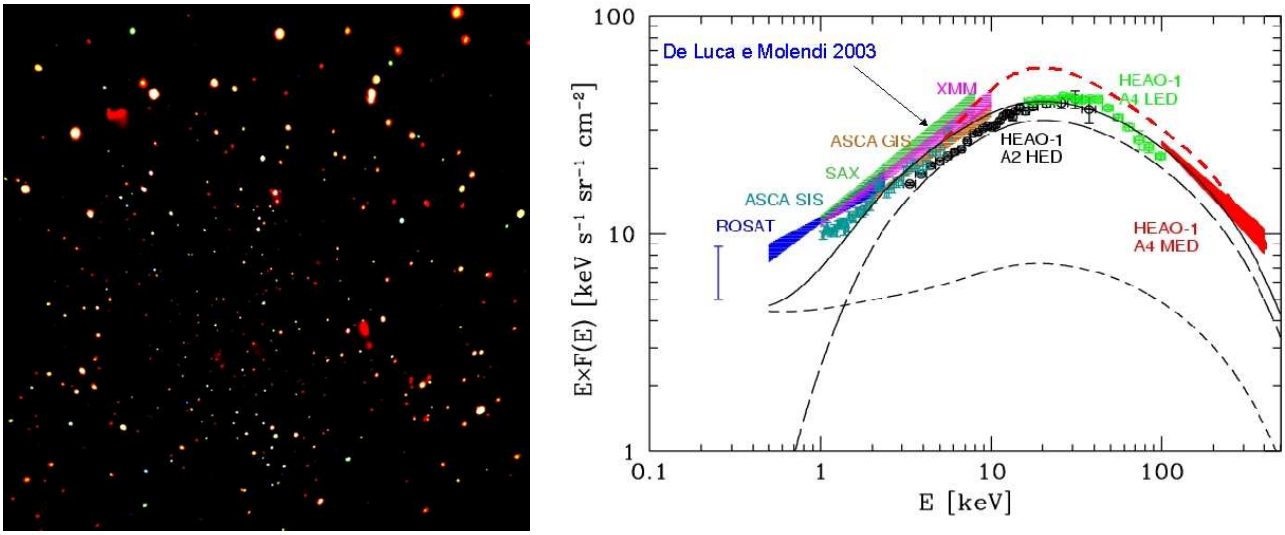

Figure 1.6: (left) The Chandra Deep Field North, obtained after an exposure time of several days, shows that the XRB in the soft band is resolved in discrete object, mostly AGN.
(right) The X-ray background energy density spectrum from different experiments (adapted from Comastri (2000)).

A solution proposed by Setti and Woltjer in 1989, requires that there exist 3 times more AGN type 2, which are strongly *obscured* in the soft X-rays by photoelectric effect in the circumnuclear gas. Such objects are already known in the local universe and they would constitute the majority of the AGN population, whose research and classification is still in progress. The AGN quest is easier in hard X-rays than in optical counterparts, where the circumnuclear dust has an obscuration effect much more intense than in X-rays.

The CXB resolution in the following years was continued by the satellite ASCA (see bibl. [17]) and BeppoSAX (see bibl. [18]). Their grazing incidence telescopes, operative up to 10 keV and with an angular resolution of 2', have resolved the 20% of the CXB in the band 2-10 keV down to 5 μCrab and have found a preliminary confirmations of this solution.

The missions XMM and Chandra, moreover, due to their high sensitivity and angular resolution (0.5" for Chandra), have resolved the almost 100% of the CXB in the band 0.05-8 keV down to 0.05 μCrab[3]. Since now, the observations led in the band below 6-8 keV have confirmed the explanation of the CXB, but the fundamental issue of what is making most of the energy output of the CXB is still open (see bibl. [20]).

The CXB paradigm, if confirmed, would bring us to an evaluation of the black-hole mass density in the

[3]All the optical counterparts sources under 0.5 μCrab (>50%) are over all the spectroscopic capabilities of all the ground-based telescopes

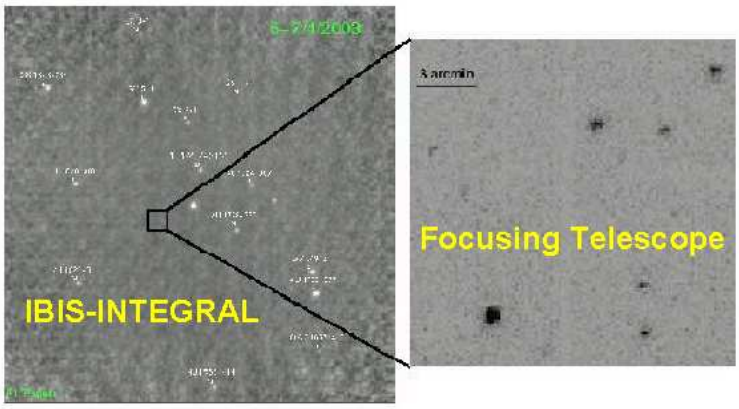

Figure 1.7: (left) A deep observation ($9^o \times 9^o$) of a region near to the Galactic Center by IBIS-ISGRI onboard INTEGRAL between 15 and 40 keV (credits: A. Parmar).
(right) The simulation of the achievable image quality with an hard X-ray focusing telescope in the same field .

Universe based upon the integral of the accretion luminosity, e.g. the CXB energy density (see bibl. [15]) and the mean redshift of the mostly contributing sources. From available data (which assume $\langle z \rangle \sim 2$) the black-hole mass density is near to that inferred from dynamical studies of nearby galaxies (see bibl. [12]), but a factor two higher than that estimated integrating the luminosity function of optically selected AGN. However, most of this accretion luminosity is optically invisible, because it is hidden by gas and dust. Obscured AGNs are common in optical surveys: in Chandra and XMM surveys, however, the number of obscured AGN is smaller than expected. This is probably due to their limited sensitivity band ($0.5 \div 8/10$ keV, and with a collecting area steeply declining over 6 keV), which biases the surveys against highly X-ray obscured sources.

A telescope able to observe the population at the CXB peak at 20-50 keV with a sensitivity able to resolve the 30-50 % of the CXB (i.e. a telescope with focusing optics over $10 \div 20$ keV) could help to understand whether are we missing highly obscured AGN at $z > 1$ observing them only at $E < 8 - 10keV$. This telescope could also detect the spectrum and the obscuration of the sources found by Chandra and XMM, and could resolve the doubts about the fraction of obscured AGN as a function of the luminosity and of the redshift: moreover, it could determine which is the relative contribution of these AGN to the total accretion luminosity density.

1.2.3 Hard X-rays sources in nearby galaxies

Other interesting targets for a hard X-ray mission are the nearby galaxies and starburst galaxies: especially spiral galaxies like M31, M33, M101. These object have already been observed by Einstein, ROSAT, ASCA and BeppoSAX (see bibl. [23]) and more recently, by Chandra and XMM. Their closeness permits detailed observations in the X-ray band and therefore to study the features of X-ray emitting stellar population. There are some reasons for studying the nearby galaxies in hard X-rays:

- their distances are well known, which in turn permits to derive accurately their luminosity:
- the association with the stellar population (bulge or disk) is easier (even easier than in our Galaxy) because it is possible to resolve and locate precisely individual sources in the galaxy:

- the line-of-sight column density is lower than for more distant galaxies, and this reduces the absorption and the spectral distortions.

At present time there is a substantial lack of data in hard X-rays from nearby galaxies: the unique available data come from SAX/PDS (passively collimated), during the observation of M31 (see bibl. [23]) and of giant NGC1553. In NGC1553 the detection is ambiguous because a background AGN could contribute to the measured spectrum: in fact, a Seyfert galaxy at 1^o far away from NGC1553 could be the real emission source. In M31, instead, no background potential sources have been found in the PDS field of view, and the hard X-ray flux is now attributed to the galaxy. However, as no hard X-ray image is still available, the possibility of background sources (maybe strongly absorbed) cannot be discarded. A focusing telescope in hard X-rays could ultimately solve this doubt, due to its angular resolution.

1.2.4 Ultra-luminous X-ray sources (ULX) in nearby galaxies

The ULX nearby galaxies, or super-Eddington sources, are extremely luminous X-ray sources detected in nearby galaxies (see Fabbiano 1989-1995): they emit in appearance more than 10^{39} erg/s, violating the Eddington limit for an accreting neutron star ($\sim 10^{38}$ erg/s). Such an emission requires higher accreting masses than the usual stellar black holes, sometimes more than a hundred solar mass. In 1999 Colbert and Mushotzky called this black-hole class "intermediate mass black holes" (IMBH) to distinguish them from the Galactic binaries black holes and from the supergiants black holes in AGN. According Madau and Rees (2001) these black holes may have played an important role in the very early star formation process which led to the galaxy formation.

A number of ULX has been resolved by Chandra and XMM and allowed to collect their spectra: some of them are believed to be young supernova remnants, others could be background QSOs. However, many of them are believed to be compact systems like accreting binaries (see bibl. [21]): the current debate about their exact nature is open. These sources show almost no counterpart in other bands than X-rays, only in few cases they were (probably) identified as HII regions (maybe X-ray photoionized nebulae) or blue stellar objects (the visible companion of the compact object). A future observation in hard X-rays joined to the capability of resolving sources and of sampling their spectrum, a basic step in understanding their black hole or background QSO nature.

1.2.5 Non-thermal emission from clusters of galaxies and radio galaxies

The gaseous intracluster medium is characterized by temperatures of order $10^7 \div 10^8 K$. The presence of a diffuse relativistic component is detected in some galaxy clusters from a synchrotron diffuse radio emission (radio-halo). These relativistic electrons interact with the Cosmic Microwave Background by inverse Compton Scattering, producing an X-ray emission, whose intensity takes over the usual free-free thermal emission at high energies. The detection of these "hard tail", if confirmed, would give a constraint on the electron density.

The first detection of these hard tail was obtained by BeppoSAX in the PDS range observing the Coma Cluster and Abell 2256 (see bibl. [22]). The result is, indeed, very doubtful because of the limited PDS sensitivity, which did not allow a detection enough separated from the background. Only an increase in sensitivity could give the ability to trace sharply the thermal component and to provide a measurement of the hard tail intensity.

The inverse Compton component could similarly be searched in radio lobes of extended radio galaxies. Since now the measurements below 10 keV have been difficult because of the presence of the X-ray thermal emission from the intracluster medium: at higher energies, the thermal component should drop more steeply than the Compton, and so they could be separated. Its measurement could lead to an estimate of the electron number, and, via the synchrotron emission, to an independent measurement of the magnetic field in radio lobes. This in turn is necessary to formulate theories about their dynamics.

1.2.6 The afterglow of Gamma Ray Bursts

The GRB afterglow is attributed to the interaction of the GRB ejecta with the surrounding medium: to understand the GRB origin it is essential to follow the spectral afterglow evolution along the light curve, especially the evolution of fluorescence lines of heavy elements (like the Ni and Fe Kα line) present in the medium. Since now no measurement of the afterglow spectrum has been possible over 10 keV up to 60-80 keV. A great expectation is given by the SWIFT satellite, that will for the first time locate and study a GRB in the first phases at these energies. Nevertheless, its sensitivity limit (2 mCrab in 16 hours) is insufficient to follow the spectral evolution during its typical decay $t^{-1.3\div1.4}$.

Nevertheless, the use of focusing optics could improve the sensitivity level reducing in the same time the duration of the integration to few hours. The measurement of the Iron and Nickel line strength and time evolution could be a very powerful tool to understand the GRB afterglow process. Moreover, a precise measurement of the afterglow X-ray flux (which has a relevant component in hard X-rays) would be very useful to verify the energetic balance of the GRB.

Chapter 2

Grazing incidence X-ray telescopes

The introduction of X-ray optics has permitted a large leap forward in a set of astrophysical and cosmological problems since the satellite *Einstein* which first was equipped with an X-ray imaging system, exploiting the physical principle of the *grazing incidence reflection*. In this configuration, the X-rays are reflected in the focal plane at very shallow incidence angles by mirrors coated with dense materials: the optical performances of the X-ray optics have now evolved up to the excellence of the imaging X-ray telescopes Chandra and XMM, substantially exploiting the same principle, but improving the manufacturing technique in order to increase the angular resolution and the effective area. However, these imaging systems are severely limited to the soft X-ray band (0.1-10 keV) and the hard band (10-100 keV) has been since now explored only with simply collimated detectors.

In the last chapter we have highlightened that a number of possible hard X-ray measurements are waiting for an increase of sensitivity and angular resolution: in this chapter we will see how the focusing systems can lead to satisfy both requirements, and which are the principles of X-ray focusing.

2.1 X-ray focusing vs X-ray collimation: general advantages

2.1.1 X-ray telescopes angular resolution

A *collimated telescope* is essentially a channel (or a system of channels) in front of the X-ray detector (CCD for X-ray imaging, gratings, crystals, photoelectric or calorimetric detectors for spectroscopy) which limits the solid angle of observation.

The angular resolution of an X-ray collimated telescope almost coincides to its Field of View (FOV) unless we use coded masks (or microchannels plates) and position-sensitive detectors. Anyway, the angular resolution will be poor, unless we reduce the aperture dimensions at cost of the effective area. Also when using coded mask devices, in practical cases the angular resolution will be limited to some arcminutes.

On the other side, a *X-ray focusing system* allows a real, direct chance of doing *X-ray imaging*, resolving the extended source details, avoiding the source confusion in the same FOV, without loss of collection area. At present time the resolution limit is not dictated by the diffraction of light (unlike optical telescopes), but it depends mainly on the optics shape accuracy and design, and on their stability in orbit environmental conditions.

The photon distribution on the focal plane may be defined in different ways. The bidimensional distribution of photons from an object located at infinity on the focal plane is called PSF (Point Spread Function),

its 1-D integral is the LSF (Line Spread Function) The EE (Encircled Energy) is the fraction of focused photons as function of the angular distance from the optical axis.

In practice, the angular resolution is obtained from the above definitions as the HEW (Half-Energy Width) or HPD (Half Power Diameter), which are the angular diameter in the focal plane which include the 50% of the focused photons. The LSF FWHM is also used, even if this parameter is not very useful in X-ray optics, because the X-ray focal spot often deviates from the gaussian profile and shows relevant "wings": hence, the FWHM usually underestimates the photon spread. The HEW allows instead to estimate the fraction of photons which are effectively focused on the detector, which in turn determines the sensitivity of the telescope (see sect. 2.1.2, page 16).

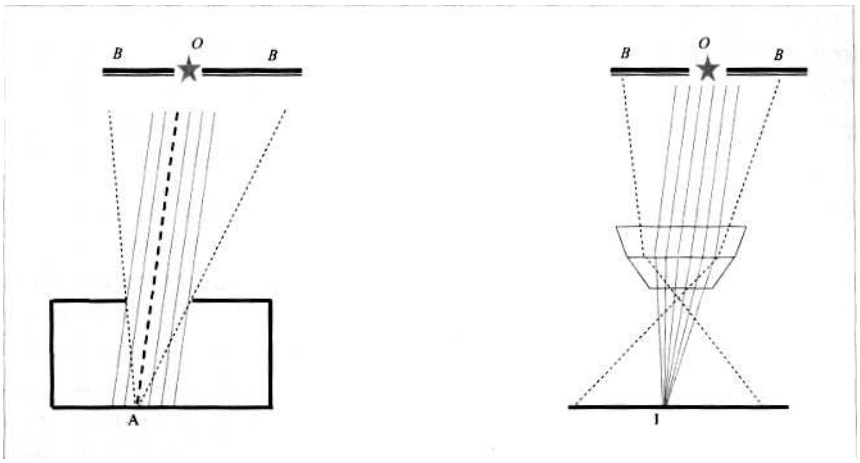

Figure 2.1: The principle of X-rays focusing (credits: ESA).
(left) In a simply collimated telescope the source (the star O) is projected on the detector together with all the background B, and using a very large fraction of the detector surface.
(right) In a focused telescope the image of the star is concentrated on a little surface and most of background is rejected.

2.1.2 X-ray telescopes sensitivity

The use of focusing optics also greatly improves the telescopes sensitivity. The minimum detectable flux (the telescope "sensitivity") is limited by the *background noise* B, defined as the number of background counts per unit time, per energy band and per detector unit area, which is typical of the chosen detector (*intrinsic background*: dark current in the proportional counter, nuclear decays, etc.) and of the operative conditions (*aperture background*: cosmic background, trapped particles in Earth magnetosphere, cosmic rays, solar protons, etc.). A measurement of the average background value is obtained as the recorded flux when the source is out of the field: the source flux is calculated by subtraction. However, as the background flux fluctuates according the Poisson's statistics, the source flux is known with an uncertainty depending on the fluctuation amplitude.

Let us suppose to have a collimated telescope with detector area A_d and a quantum efficiency η_E at the photon energy E, sensitive in the energy band ΔE. In the time Δt the background counts will be $C_B = BA_d\Delta E\Delta t\eta_E$. This count obeys the Poisson's statistics, thus the background uncertainty is $\sigma(C_B) = C_B^{1/2}$. In the same time, the photon count from an X-ray source with flux S_E will be $C_S = S_E\Delta t\Delta E\eta_E A_d$.

During an observation, the background is superposed to the signal C and then subtracted, then the measured count C_{meas} is obtained as $C_{meas} = (C_S + C_B) - C_B$. Since the background fluctuation is much

larger than that of the signal, propagating the error on C_{meas} we obtain

$$\sigma^2(C_{meas}) = 2\sigma^2(C_B) \tag{2.1}$$

The condition to see this source over $N\sigma$ will be $C_{meas} > N\sigma(C_{meas})$, yielding for the minimum detectable flux S:

$$S = \frac{N}{\eta_E}\sqrt{\frac{2B}{A_d \Delta t \Delta E}} \tag{2.2}$$

this is the sensitivity of a collimated X-ray telescope (of course function of the energy).

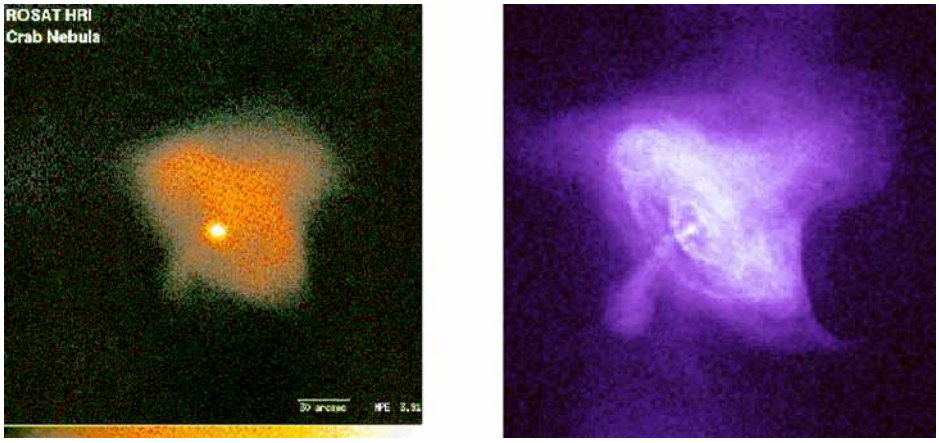

Figure 2.2: A comparison between the observation of the Crab Nebula by Rosat (left, HPD = 5": credits: MPE) and Chandra (right, HPD = 0.5": credits: NASA). The improvement in angular resolution is a 10-fold factor .

Let us suppose instead to have a *focusing optics* with effective area A_e[1] which focuses the flux S on a fraction ϵ of the detector area A_d: in this case the detected signal is $C_S = S\Delta t \Delta E \eta_E A_e$, and the noise will be $\sigma(C_{meas}) = (2BA_d \Delta E \Delta t \epsilon)^{1/2}$. The sensitivity will thus be

$$S = \frac{N}{A_e \eta_E}\sqrt{\frac{2BA_d\epsilon}{\Delta t \Delta E}} \tag{2.3}$$

The comparison between the eq. 2.2 and the eq. 2.3 show the different dependence of the sensitivity on the telescope size. In a collimated telescope the sensitivity depends on $A_d^{1/2}$ i.e. on the *root of the detector area*: considering the size of practically obtainable detectors, it is very difficult to reach a good sensitivity with collimated telescopes. Moreover, very large detectors (including those used with coded masks) are very difficult to be monitored and controlled in response efficiency. On the other side, a focused telescope improves the sensitivity in proportion to A_e, the *effective optics area*: moreover, in this case we should prefer to use *small* detectors, because in this case the photon collection is completely demanded to the optics and smaller detectors will result in a lower background noise.

[1]The effective area is the collecting area times the photon reflectivity: it corresponds to the geometric collecting area that would reflect the 100 % of the incident photons on it.

2.2 Traditional soft X-ray optics

The behaviour of the X-rays when they strike down a reflecting surface is different from that of the usual visible light. A quick outline of the X-ray reflection will be provided: more detailed calculations are performed in app. A.1

2.2.1 Optical constants

Since the discovery of X-rays (1897) W. Roentgen highlighted that X-rays are apparently hard to refract or reflect. The explanation is that the refractive index of all materials in X-rays is very close to 1 and only slightly less than 1: the situation is here completely different from the usual optics in visible light, where the refractive index is larger than 1: in fact, the X-ray energies are above the characteristic energies of the bonded electrons in the atoms, and the materials appear like an almost-free electron gas, with a plasma frequency which is, in general, lower than the incident radiation. A detailed calculation of refractive index in X-rays is exposed in the app. A.1.

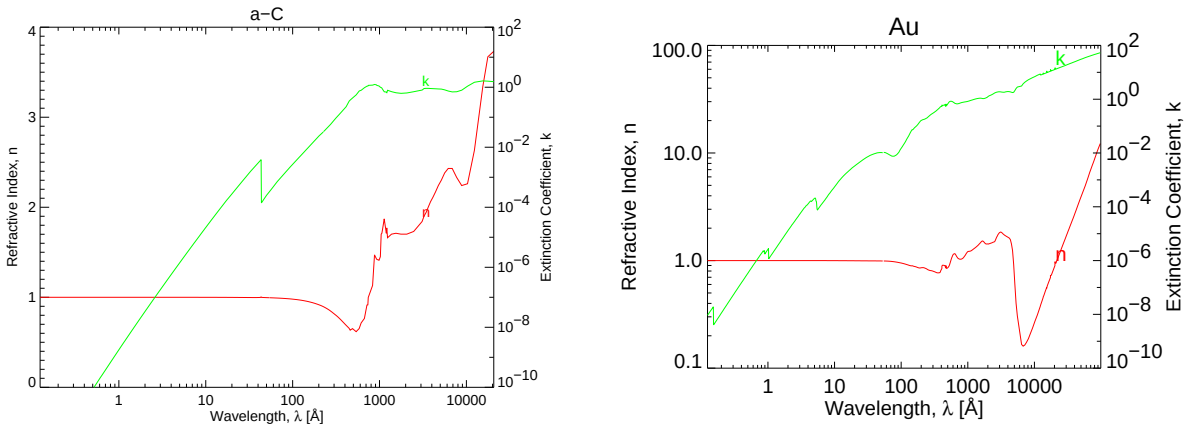

Figure 2.3: Optical constants of Carbon (left) and Gold (right), from X-rays to infrared (credits: *D. Windt*). The absorption edges are visible in the extinction coefficient. The Carbon (due to its very low K-edge energy) is twenty times less absorber than Gold at almost all X-ray energies: for $\lambda \to 0$ n approaches 1 in both cases, but it is less than 1.

The X-ray refractive index may be written in the form (see eq. A.2)

$$n = 1 - \delta + i\beta \tag{2.4}$$

where the real part $\delta \sim 10^{-4} \div 10^{-5}$ accounts for the refraction effect and the imaginary part $\delta \sim 10^{-5} \div 10^{-6}$ causes the X-ray beam photoelectric absorption. The δ and β parameters are the *optical constants* of the material. In app. A.1 is shown that the X-ray refractive index depends on the atomic properties through the equation:

$$n = 1 - \frac{N_a r_e}{2\pi A}\lambda^2 \rho (f_1 + i f_2) \tag{2.5}$$

where N_a is the Avogadro number, r_e the classical electron radius, A the atomic mass number and f_1 (first atomic scattering coefficient) is the number of scattering electrons per atom. At very high energy (say, much larger than the K-shell binding energy), $f_1 \approx Z$. The second scattering coefficient f_2 is included to take into account the photoabsorption, and it is related to the atomic photoelectric cross section by the formula

$$f_2 = \frac{\sigma_{ph}}{2 r_e \lambda} \tag{2.6}$$

The most prominent variations of the optical constants are in correspondence of the K,L,M... atomic shells, where the f_2 coefficient has the typical edge (see fig. 2.3) and the material can show anomalous dispersion.

The main contribution to β is given by the photoelectric effect: it becomes important especially in correspondence of the electronic energy levels, especially for the most tightly bound electrons (K-shell) whose energies are given by the well-known Moseley law: over E_K the photoelectric cross-section decays as Z^5E^{-1}, so low-Z materials (like Carbon) have lower K-edge energies, and for a fixed energy they are less sensitive to the photoelectric effect. At very high energies ($\lambda < \frac{h}{m_e c}$) in light elements the Compton effect may, however, take over the photoelectric absorption, even if the photons are not absorbed. Heavier elements (see fig. 2.4) are instead good absorbers (and they are used as X-ray screens) but they are also better reflectors.

For a compound material the absorption coefficient is obtained as a simple average of the scattering factors of the components, weighted upon the atomic abundances: this approximation neglects completely the interaction between the atomic electrons of different atoms, and is well suitable over 30 eV.

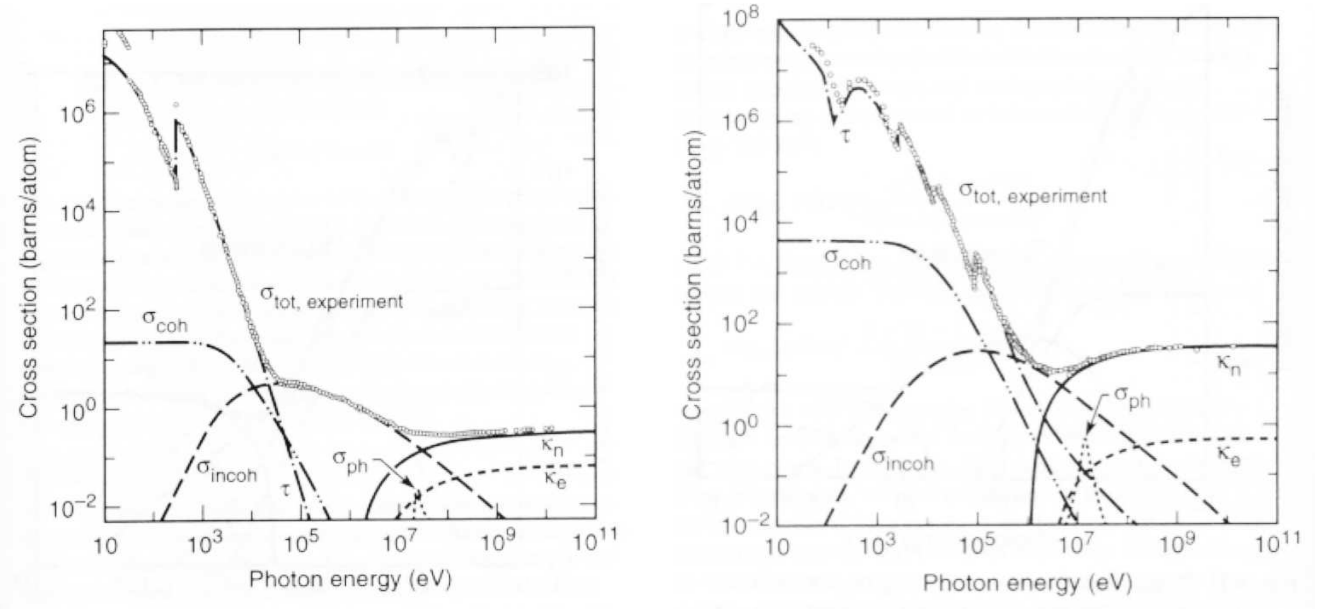

Figure 2.4: Photon cross sections of C (left) and Pb(right).The different processes are shown: the photoelectric absorption dominates in Carbon up to some tenth keV, where the Compton effect starts to be important. In Lead the photoelectric effect is dominant up to the pair production threshold (credits: bibl. [31]).

2.2.2 X-rays reflection

The extremely small deviation of the real part of n from 1 shows that a refractive optics would imply a focal length too long to be implemented on a single spacecraft[2]. Thick lenses are ruled out by the absorption coefficient, so in practice X-ray optics have to be *reflective*. Because of the extreme smallness of δ the reflectivity of single coating layer is, indeed, always small, as it is evident from the Fresnel equations (see app. A.1), except in *grazing incidence*: in fact, as $Re(n) < 1$, the Snell law cannot be satisfied for incidence angles smaller than the critical angle $\cos\theta_c = n$.

[2]There exist now projects that foresee the implementation of refractive X-ray lenses, with a focal length of some 10^4 Km

Remembering that δ is very small, it is easy to derive an approximate expression for θ_c:

$$\theta_c \simeq \sqrt{2\delta} \tag{2.7}$$

for $\theta_i < \theta_c$ the incident ray is *totally reflected*: the reflection angle is always very shallow ($< 1^o$), as A.H. Compton experimentally discovered in 1923.

In soft X-ray optics the total reflection is used to make *grazing incidence optics*, and large effective areas and sensitivities can be reached: however, the critical angle increases for larger reflecting layer density but decreases in proportion to the photon energy (see app. A):

$$\theta_c \propto \frac{\sqrt{\rho}}{E} \tag{2.8}$$

this implies that, at a fixed incidence angle, *only X-ray energies below a cut-off value E_c can be totally reflected*[3] (see fig. 2.5), and this is the main reason why single-layer X-ray optics cannot be used in hard X-rays: over 10 keV, even the critical angles of the densest coatings become too small and the mirror cross section offered to the incident flux becomes too low to return a sufficient effective area.

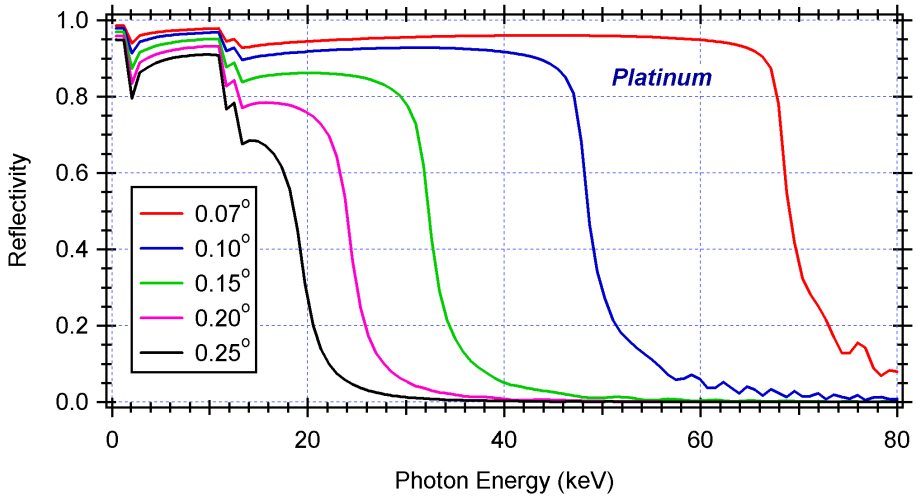

Figure 2.5: X-ray reflectivity curves in Platinum as function of energy for fixed incidence angles. The reflectivity is very good in grazing incidence up to the critical angle (function of the photon energy), where the reflectivity suddenly drops. For increasing incidence angle the cut-off grazing angle decreases (and vice versa).

As an example, the X-ray reflectivity of Platinum (ideally smooth surface) as a function of energy for different grazing incidence angles is shown in figure 2.5. It is evident that the reflectivity is close to 1 (total reflection regime) either for very small incidence angles or for very low X-ray energies: in total reflection regime the reflection takes place in a very thin depth, thus the photoelectric absorption is very limited. When increasing the incidence angle, however, the interested thickness is increased also (see eq. A.24, page 199):

$$d_p(\theta) \approx \frac{\lambda}{2\pi} \frac{1}{\sqrt{\theta_c^2 - \theta_0^2}} \tag{2.9}$$

[3]By the way, the measurement of the critical angle allows the determination of the f_1 optical constant (f_2 is estimated instead from the extinction length): the optical constants can be also derived from the multilayer reflectivity data fit, especially in proximity to the absorption edges.

and the beam is absorbed in a larger extent. If the attenuation is low, the penetration of the beam decays exponentially in the reflective coating: for increasing incidence angles the reflected beam is slowly reduced with respect to 1, as it can be easily computed:

$$R(\theta) \approx 1 - \frac{4\pi\beta d_p(\theta)}{\lambda \sin\theta} \tag{2.10}$$

the reflectivity decreases slowly up to the critical angle, where the penetration becomes infinite (and the refracted ray appears). Beyond the critical angle the reflectivity decays as $\sin^4\theta$ (see eq. A.20).

In principle, materials with low-Z (like Carbon) would be excellent X-ray reflectors as their absorption is very low: unfortunately, at grazing incidence angles which are large enough to allow a convenient mirror effective area only the softer X-rays would be reflected. This fact may, indeed, be exploited in order to overcoat X-ray mirrors in order to enhance the soft X-rays reflectivity (see bibl. [95]).

High-Z materials (Au, Pt, Ir...) have instead reflectivity at $\theta < \theta_c$ which are slightly less than the achievable one with low-Z coatings, but (provided that they have no photoabsorption edges in the vicinity of the X-ray band to be reflected) they have also much larger cut-off angles and they keep a high reflectivity up to 10 keV, at viable grazing incidence angles ($\sim 500 \div 1000''$): finally, the transition from the total reflection regime to the ordinary, low reflectivity regime is more gradual (see bibl. [32]). Gold may be used to coat mirrors in the full range 1-10 keV as at these energies the photoabsorption is less severe than in the very soft band (< 1 keV).

2.2.3 X-rays optics shape: Wolter optics

The idea of using the grazing incidence reflection to produce X-ray optics was born in 1960, when R. Giacconi and B. Rossi evaluated the possibility of making a grazing X-ray reflector with a truncated paraboloid shape (see bibl. [26]): the parabolic shape was of course suggested by its property of concentrating a paraxial beam in the focus without spherical aberration.

The parabolic shape, nevertheless, cannot be used to make grazing incidence telescopes because they would be affected by a strong *coma* aberration, that is, the dependence of the focal length on the reflection position when an off-axis beam strikes on it. As a result, the useful field of view of the optics would be to small to produce any image in the focal plane.

A coma-free optic may be obtained, indeed, if the *Abbe sine condition* is satisfied in all points of the reflecting surface:

$$\frac{h}{\sin\alpha_i} = \frac{i}{\sin\alpha_0} = const \tag{2.11}$$

where h and i denote the distance of the object and of the image point from the optical axis and α_0, α_i, the angle between the optical axis and the ray before and after the reflection. For astronomical objects all rays may be considered parallel, and so the Abbe condition is satisfied if the incident rays intersect the reflected ray directions in a spherical surface centred in the focus. The Abbe condition, thus, rules out a paraboloidal shape as the Abbe surface is simply the same paraboloid, that approximates a sphere only near the vertex, in almost-normal incidence: this configuration is very common in the optical telescopes but in X-rays it would return an almost-zero reflectivity.

The solution to this problem came in 1951, when Hans Wolter showed that the Abbe condition could be approximately satisfied by using a double reflection on two conical mirrors in succession (see bibl. [27]): in particular, in the *Wolter I geometry* the photons are reflected in succession by a *paraboloidal* mirror and by a confocal and coaxial *hyperboloidal* mirror (see fig. 2.6, fig. 2.7). The double reflection takes also the

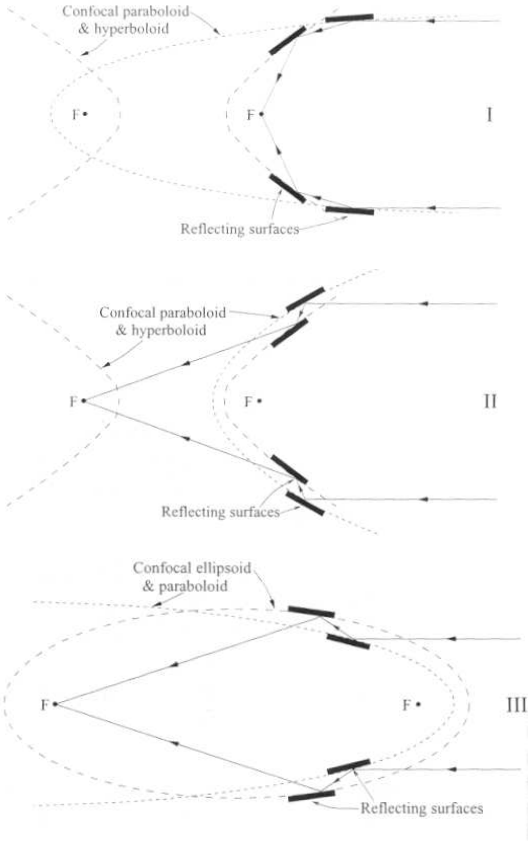

Figure 2.6: Optical schematic of the Wolter optics I, II, III. The double reflection on conical surfaces allows to reduce greatly the coma aberration (credits: bibl. [32])).

advantage of reducing of a twofold factor the focal length, an important requirement for optics that have to operate in space. Two other configurations satisfy the Abbe conditions (Wolter II and III) but they are not used for space application as their focal length is larger than a Wolter I, having the same aperture.

It is possible to show (see bibl. [28]) that for a Wolter I mirror the effective area A_e depends on the energy and it is expressed by the formula:

$$A_e(E) = 8\pi f L \theta^2 R^2(E) \tag{2.12}$$

here f is the focal length, L the mirror length, θ the incidence angle of radiation on the reflective coating, R(E) the reflectivity of the mirror. In particular, the area depends on the squared reflectivity because the rays are reflected two times. The radius R of the mirror is determinated by the focal length and the incidence angle:

$$R = 4f \tan\theta \tag{2.13}$$

as it can be seen with simple geometry considerations. If the angular resolution is not a strict requirement, the Wolter I optic may be substituted by a double-cone approximation, a configuration that simplifies the production process (see bibl. [29]). The angular resolution for a double-cone optic

$$HPD \propto \frac{LR}{f^2} \tag{2.14}$$

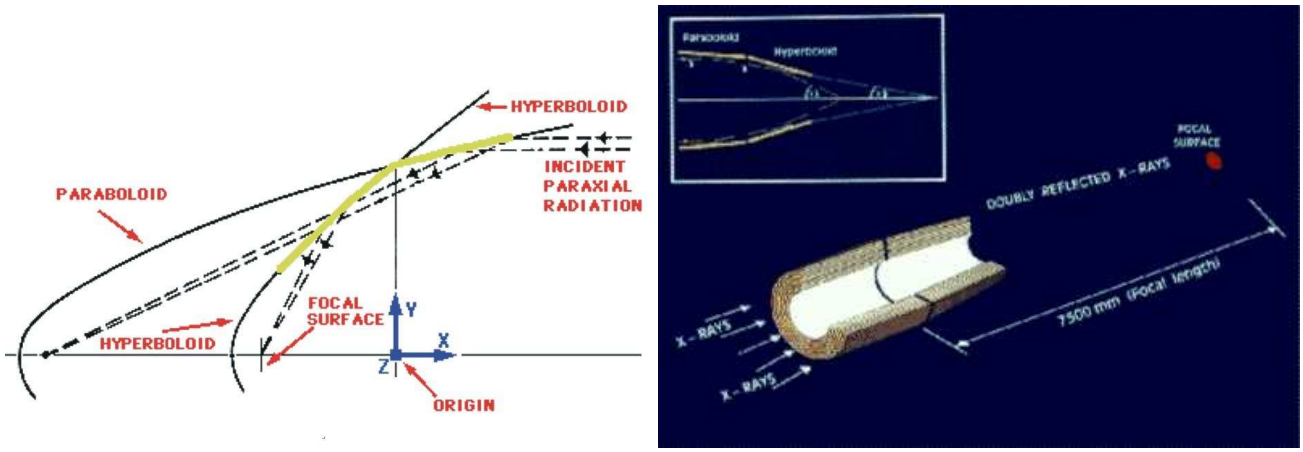

Figure 2.7: (left) A detailed scheme of the Wolter I profile (from bibl. [28]).
(right) Nesting of confocal and coaxial Wolter I shells in order to fully exploit the mirror geometric area.

is worse than for a Wolter I optic. It is worth noting that the optics of the soft X-ray telescope on-board Beppo-SAX were of the double-cone type.

As θ has to be less than $\theta_c(E)$ in order to keep R(E) at a convenient value, the incidence angles have to be very shallow, and the effective area of a single mirror is very modest. In order to increase the effective area of a telescope a number of coaxial and confocal mirrors with decreasing radii ("mirror shells") are assembled (see fig. 2.7): the incidence angle decreases going from the outer to the inner shells according the eq. 2.13.

Even in this case, the effective areas beyond 10 keV with the current geometric apertures are very modest. From the investigation of the eq. 2.12, possible solutions are the adoption of:

- aperture diameter-to-focal-length ratios very small: $0.02 \div 0.01$ vs. $0.09 \div 0.12$ (respective values for XMM e Chandra);
- large number of modules operating in parallel: this is the approach of the mission Constellation-X (see sect. 3.7.3), with 12 identical modules on 4 different independent spacecrafts;
- use of very large diameter optics: this is the way for the ESA project XEUS (see sect. 3.7.4), with $5 \div 10$ m diameter optics and 50 m focal length;
- use of interferential coatings (multilayer coatings) in order to increase the reflectivity at larger incidence angles. This is the solution we will consider in the next chapter (see chapt. 3);
- use of denser single-layer reflecting coatings (Ir or Pt), in conjunction with large focal lengths ($6 \div 100$ m). This is the concept for the mission SIMBOL-X (see sect. 3.7.2), that will have a 30 m focal length with optics and detector on two different spacecrafts in formation flight: indeed, since the use of Ir or Pt would produce a modest area increase with respect to Au coatings, the use of multilayer coatings for the SIMBOL-X optics is also considered.

The Wolter I profile is not the only adoptable solution: in fact, the residual off-axis coma, field curvature and astigmatism aberrations causes a serious limitation to the field of view (more stringent than the obvious limit FOV $< \theta_c$). A possible solution comes from a more general design in which the mirror profile is

described by *polynomial* equations (see e.g. bibl. [65]). The polynomial coefficient are optimized in order to achieve high imaging performances at large incidence angle, despite a little degradation of the on-axis response. The coefficients optimization is a complex numerical task: the polynomial profiles are considered in wide-field X-ray missions like Aster-X (see bibl. [99]) and could be a viable alternative for the XEUS mirrors (see sect. 3.7.4, page 87).

2.2.4 Surface microroughness

The high reflectivity required to an X-ray reflecting surface (and especially to the Wolter I shaped optics, which exploit a *double* reflection) may be seriously hampered by the *microroughness* of the reflecting surface. The mirror surface has to be very smooth in order to return an X-ray reflectivity near to the value predicted by the Fresnel laws. Superpolishing methods have been developed, some of them at the INAF-OAB (see e.g. bibl. [101]), in order to reduce the surface roughness to few angstroms, but the roughness is still the main threat to the reflectivity of an X-ray mirror.

As explained with more detail in app. B, a reflecting, flat surface may be described by a function $z(x, y)$, which gives the height of the surface at each point (x, y): an ideal surface would simply have $z(x, y) = z_0$, but real surfaces are never ideally smooth. We can start to characterize the smoothness of the surface by its rms value σ,

$$\sigma^2 = \frac{1}{L}\int_0^L [z(x,y) - z_0]^2 dx \tag{2.15}$$

which is the most important parameter (but not the one, see app. B) for the characterization of the reflecting surface. In the sect. 5 we shall see the methods we used to measure a surface microroughness.

To understand how the surface reflectivity varies with its roughness, let us suppose to have a flat surface with a Fresnel amplitude reflectivity r and transmissivity t. The surface is isotropic and (for simplicity) let a representative section profile be $z(x)$, with $z_0 = 0$. Let L be the illuminated surface length. A ray with wavelength λ incides with a grazing incidence angle θ_i from an ambient with refractive index n_1 and it is reflected (in the incidence plane) at the angle $\theta_s = \theta_i$. The (eventual) transmitted beam is refracted at the angle θ_r in the reflective layer with refractive index n_2. Moreover, let us suppose that the *smooth-surface condition* $2\pi\sigma \sin\theta_i \ll \lambda$ is met, as usually in practical cases.

If the surface were perfectly smooth, two adjacent parts of the wavefront would be reflected and would arrive to the analyser with the same phase shift they had in incidence: the secondary waves would produce a wavefront only in the θ_i direction and the reflectivity would be r, as predicted by the electromagnetic theory. As the profile shows instead a distribution of heights, it is possible to have a non-zero constructive interference in other directions than θ_i: the consequence is the *scattering* of the beam (see sect. 5.3.1, page 120) and the reduction of reflectivity in the θ_i direction.

As we are observing only the specular direction, the phase shift of a ray reflected in the direction θ_i by an element of surface Δx at a point x with height z will be (see fig. 2.8)

$$\Delta\phi = \frac{2\pi}{\lambda} 2 z(x) n_1 \sin\theta_i \tag{2.16}$$

The reflected electric field will be the superposition of the contribution of all of the elements of the profile with amplitude rE_0 (E_0 is the incident electric field amplitude at the surface), each with its own phase shift, weighted upon the likelihood $p(x)dx = \frac{1}{L}dx$ of striking the surface element dx;

$$E_r = r\frac{E_0}{L}\int_0^L exp\left(i\frac{4\pi}{\lambda} z(x) n_1 \sin\theta_i\right) dx \tag{2.17}$$

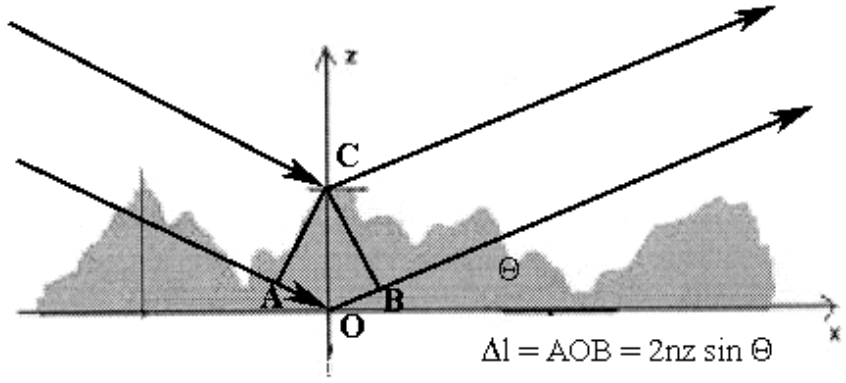

Figure 2.8: Reflection from a rough surface. The reflectivity reduction is caused by the loss of spatial coherence in the incident wavefront.

This sum was possible due to the smooth-surface approximation, which guarantees the reflection of the beam in the θ_i direction. It is impossible, however, to resolve the integral in the eq. 2.17 without more information about the profile $z(x)$. In the following, we shall suppose that the distribution $p(z)$ of heights in $z(x)$ is a *Gaussian*:

$$p(z)dz = \frac{1}{\sigma\sqrt{2\pi}} e^{-\frac{z^2}{2\sigma^2}} dz \tag{2.18}$$

where σ is the rms of the surface. Summing on z instead of x, the eq. 2.17 becomes:

$$E_r = r\frac{E_0}{\sigma\sqrt{2\pi}} \int_{-\infty}^{+\infty} e^{-\frac{z^2}{2\sigma^2} + 1\frac{4\pi}{\lambda} z n_1 \sin\theta_i} dz \tag{2.19}$$

by completing the square in the exponent, this integral may be written:

$$E_r = r\frac{E_0}{\sigma\sqrt{2\pi}} exp\left(-\frac{8\pi^2}{\lambda^2} n_1^2 \sigma^2 \sin^2\theta_i\right) \int_{-\infty}^{+\infty} e^{-\left(\frac{z}{\sqrt{2}\sigma} - i\frac{2\sqrt{2}\pi}{\lambda}\sigma n_1 \sin\theta_i\right)^2} dz \tag{2.20}$$

now the integral may be easily evaluated as $\sigma\sqrt{2\pi}$, and so the reflectivity of the rough surface $R_\sigma = |r_\sigma|^2 = (E_r/E_0)^2$ is

$$R_\sigma = r^2 exp\left[-\left(\frac{4\pi}{\lambda}\sigma n_1 \sin\theta_i\right)^2\right] \tag{2.21}$$

This basic formula (known as *Debye-Waller formula*) shows that:

- *the reflectivity decreases as the exponential of the square of the roughness rms* σ;
- the reflected amplitude E_r is *real and positive:* this means that the reflected wavefront has no phase shift caused by the superposition of scattered waves in the specular direction;
- the reflection at larger angles is more sensitive to the roughness effect, as the phase dispersion depends only on the projected roughness in the direction of incidence.

In a similar fashion we can derive the Debye-Waller formula for the refracted ray:

$$T_\sigma = t^2 exp\left[-\left(\frac{2\pi}{\lambda}\sigma(n_1 \sin\theta_i - n_2 \sin\theta_r)\right)^2\right] \tag{2.22}$$

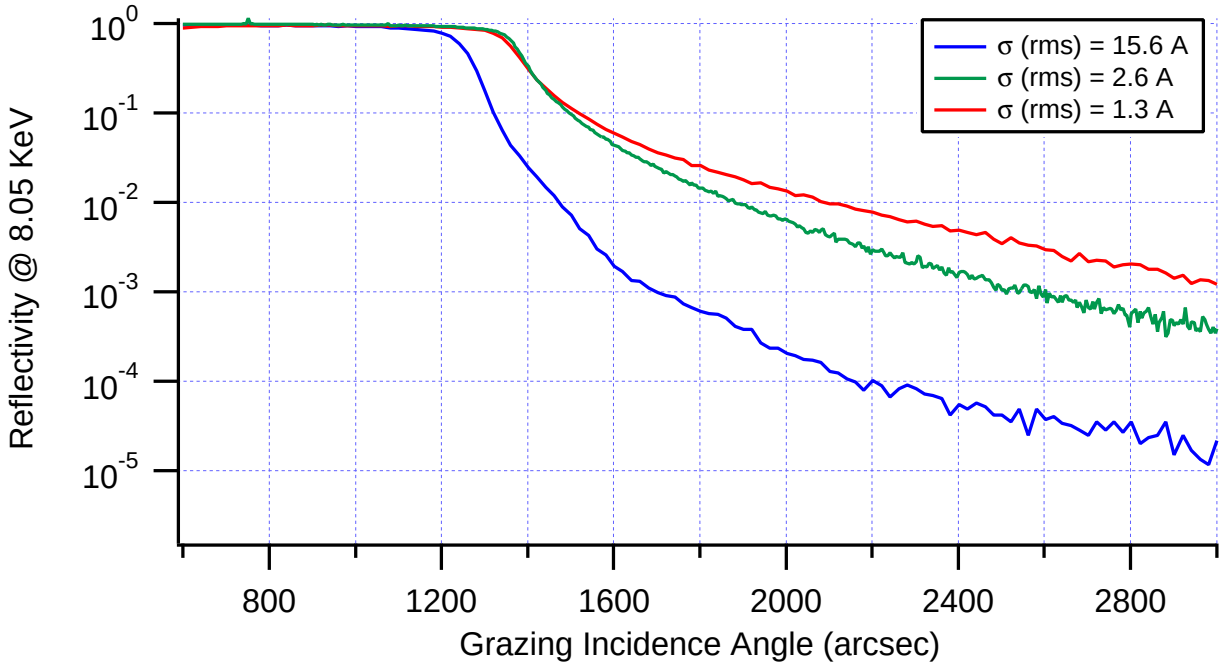

Figure 2.9: Reflectivity scans of three Ni samples, polished at different levels: the reflectivity decreases as the sample is superpolished with a lower accuracy (higher σ), in agreement with the eq. 2.21.

due to the smallness of the difference in refractive index in X-rays, we can guess that $T_\sigma \simeq t^2$ whereas $R_\sigma < r^2$: that is, attenuation in refraction is usually negligible with respect to the roughness attenuation in reflection. The roughness problem will be even more severe with the multilayer coatings (see sect. 3.5.2, page 66).

2.3 Wolter I mirrors manufacturing techniques

The practical manufacturing of Wolter I type X-ray optics is a meeting point of opposite, exacting requirements: space applications expose the mirrors to a number of solicitation that could compromise the entire telescope performances, but on the other side they require also the compliance to the mission logistics, that put strong constraints to the mirror mass: a large mirror mass is indeed unavoidable when one wants a large collecting area, an excellent angular resolution and a good mirror thermo/mechanical stability. Some mission like XEUS are under this viewpoint especially critical, and the choice and study of the optimal manufacturing technique is obviously crucial. An overview of the achieved / to be achieved goals for X-rays telescopes in term of the angular resolution/mass per m^2 geometric area is exposed in fig. 2.10, showing how the low optical weight usually goes at the expenses of the optical performances, and vice-versa.

In this section we will describe some techniques used to manufacture soft X-ray optics. In particular, more details will be provided about the replication technique (adopted for the missions Beppo-SAX, JET-X/SWIFT, Newton-XMM) that returned very good results in the soft X-ray band and that can be extended to the hard X-ray band with the adoption of multilayer coatings. In the next chapter we will shortly consider also a completely different approach (see bibl. [57]) for the future mission XEUS: the *micropore optics*.

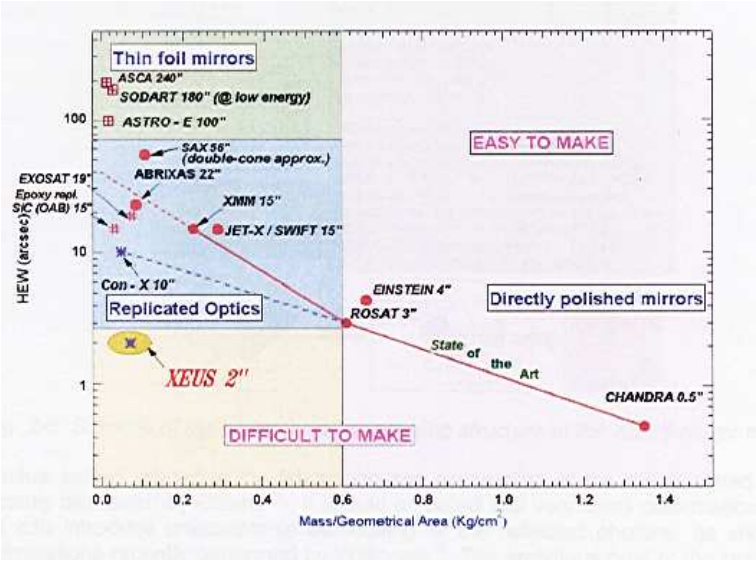

Figure 2.10: The Half Energy Width for a number of past and present X-ray missions as a function of the mirror mass/geometric area ratio. The goal for the XEUS mission is also indicated.

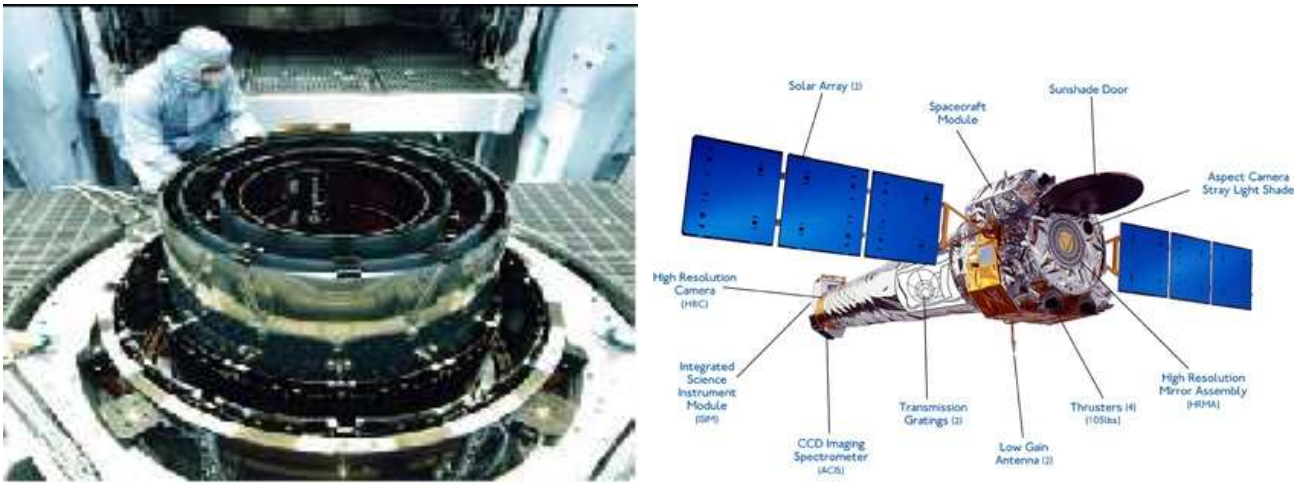

Figure 2.11: (left) The Chandra monolithic mirrors of the Chandra satellite during the assembly (credits: NASA). (right) The overall scheme of the Chandra telescope: the optics are visible in the front of the satellite (credits: NASA).

2.3.1 Traditional mirror manufacturing

By means of this technique the mirrors are manufactured giving first the right shape to the mirror substrate (Quartz for *Einstein* or Zerodur for *Rosat, Chandra*). The choice of these materials is due to their extremely low CTEs (Coefficients of Thermal Expansion) and their relatively low mass. The hyperboloid and the paraboloid are separately grinded and figured by high precision machines: the mirror inner surfaces are superpolished by lapping with ultrathin alumina powders, a process that allow to reach some angstrom of microroughness rms. On the superpolished surface a thin (1000 Å) reflecting layer is then deposited (Au, Ni, Ir, Pt...). This technique allows very high angular resolutions e.g. the HPD of Chandra (whose mirrors have an Ir coating on a thin Cr layer, used as adhesion promoter) is only 0.5", as the geometric profile is very

sharp (bibl. [64]): however, the thickness of the mirror shell substrates are large ($\sim$ cm) and the number of mirrors that can be nested is very limited: this implies that the effective area will be quite low.

Nevertheless, this kind of optics is suitable for detailed observation of extended objects (Supernova Remnants, Galaxy Clusters, nearby galaxies, XRB), where the angular resolution is a primary requirement. In tab. 2.1 some parameters of the mirrors of some telescopes produced using this technique are reported.

	Einstein	ROSAT	Chandra
mirror profile	Wolter / Schwartzschild	Wolter I	Wolter I
modules number	1	1	1
number of shells per mod.	4	4	4
effective area	412 cm^2	1150 cm^2	1150 cm^2
incidence angle	40' $\div$ 70 '	65' $\div$ 145'	27' $\div$ 51'
focal length	3.4 m	2.4 m	10.0 m
surface roughness	25 $\mathring{A}$	3 $\mathring{A}$	7 Å
HPD	4"	3"	0.5"

Table 2.1: Some characteristics of optics produced with the traditional manufacturing technique. The achieved angular resolution is excellent, but the number of nested shells per module is very limited.

2.3.2 Optics based on "thin foils"

This technique is used to produce X-ray optics with high filling factors[4] and with a low mass/geometric area ratio: however, the reachable angular resolution with this technique is quite poor (some arcmin) and these optics may be used for telescopes devoted to spectroscopic applications (that have a large collecting area as primary requirement).

This method approximates the Wolter I profile with a double-cone shape: the two cones are composed by a number *mirror segments*, formed by thin foils (0.1 $\div$ 0.3 mm thick) in glass or Aluminium coated by the reflecting film (Pt, Au). The segments are then assembled to form the double cone structure. The right shape of each foil may be obtained in different ways: in the case of the Aluminium foils a plane foil having the correct size is bent using a mechanical process; when adopting thin glass foils, the segments are curved after heating. The reflecting film may be directly deposited upon the glass/Al bent substrate or replicated on the substrate after deposition on a glass cylinder.

The achievable angular resolution with this manufacturing technique is very limited because the composite structure of a segmented mirror is very sensitive to mechanical deformations that may take place during the satellite launch or the thermal variations. Moreover, during the complex mirror assembly operations alignment unavoidable mistakes can compromise the mirror symmetry that determines the X-ray focusing. Moreover, the double-cone approximation cannot achieve the optical performances of the Wolter I profile. In tab. 2.2 some examples of the missions that adopted this production technique are reported.

[4]the ratio between the collecting area and the geometric aperture area: it is increased by nesting a large number of mirror shells.

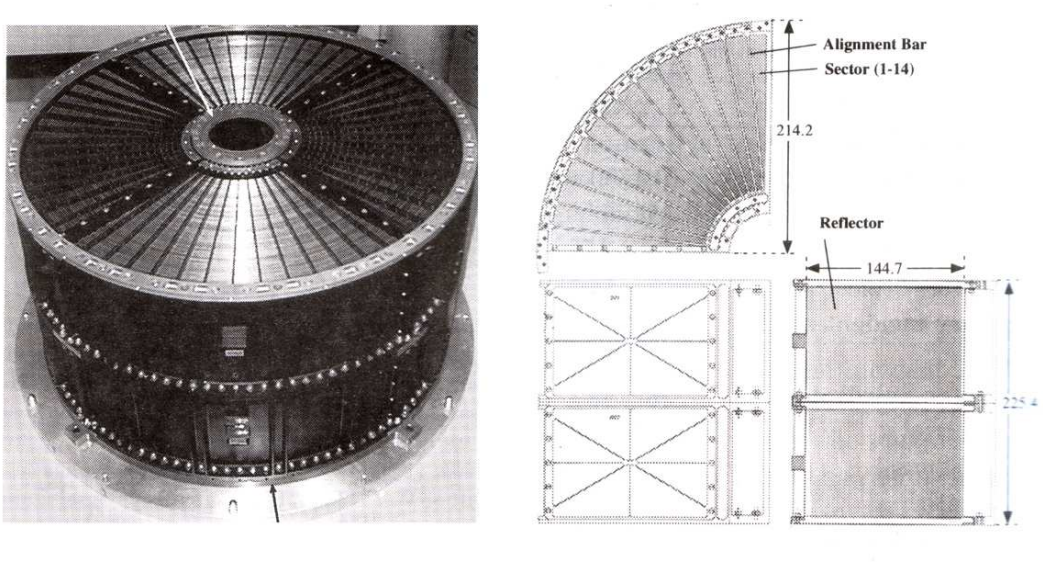

Figure 2.12: (left) A complete optics module of the telescope Astro-E (credits: ISAS).
(right) A scheme of the assembly of the segmented Astro-E mirrors. The segmented structure is apparent (credits: ISAS).

	ASCA	Astro-E	SODART
mirror profile	double cone	double cone	double cone
modules number	4	2	2
number of shells per mod.	120	175	154
shell thickness	0.125 mm	0.155 mm	0.3 mm
effective area (7 keV)	600 cm^2	250 cm^2	1200 cm^2
focal length	3.5 m	4.8 m	8 m
energy range	0.5 ÷ 15 keV	0.5 ÷15 keV	0.5 ÷15 keV
HPD	3.5’	1.5’	4’

Table 2.2: Some characteristics of optics produced with the technique of thin segmented foils. Note the limited angular resolution, caused by the intrinsic mechanical instability of segmented optics with a large diameter.

2.3.3 Optics based on mirror replication

This technique is based on the replication of the reflecting surface grown around a superpolished mandrel, which has the negative mirror profile (called also *master*) and acts as a mirror shell template. Mirrors obtained with this method have several advantages:

1. they can have any cylindrical profile;

2. they are monolithic, so the assembly process is greatly simplified;

3. the cylindrical and monolithic profile makes them very rigid and resistant to mechanical deformations;

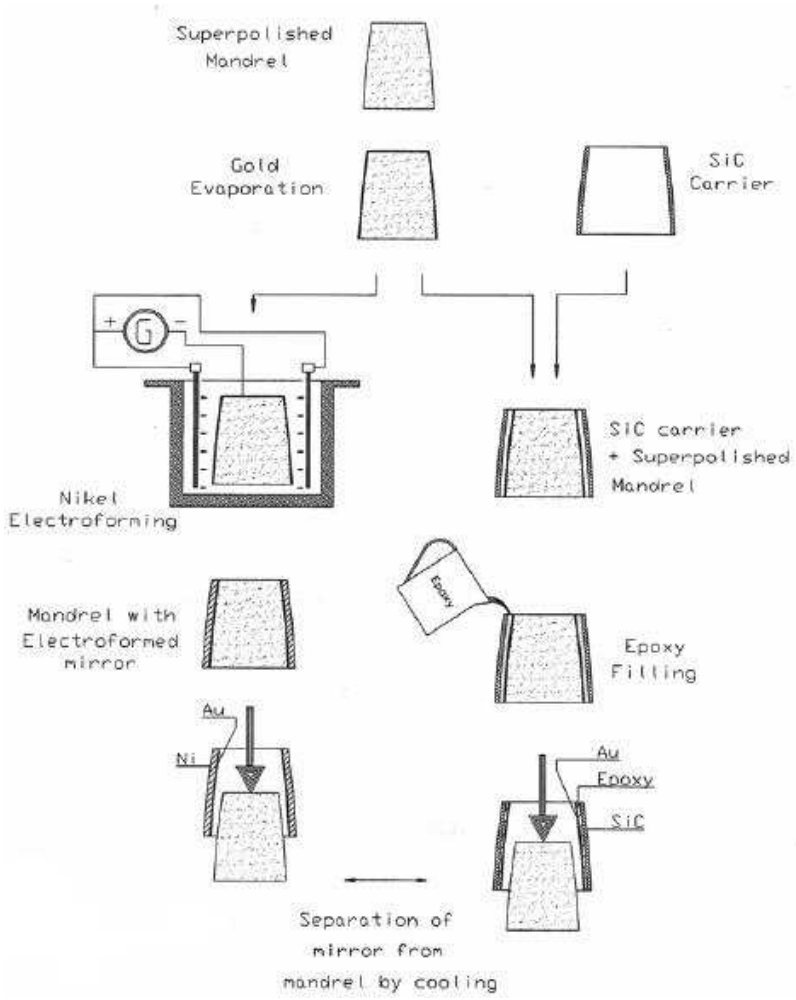

Figure 2.13: The Ni/epoxy electroforming technique: all the process starts from a superpolished mandrel (*master*) which act as a template for the mirror shell to be produced. The X-ray reflecting layer is deposited on the master following one of the methods described in the chapter 4. The construction of the mirror walls may then follow two different ways: by *Nickel electroforming* (left branch) or by *epoxy filling* (right branch). The separation of the mirror shell from the master is done by cooling, due to the difference in the master/mirror wall CTEs.

4. the optical shape reproduces very well the mandrel shape, so the optical performance is very good (HPD ~ 10");

5. the mirror shells that can be obtained may be very thin, so a large number of shells may be nested and large effective area can be achieved

6. finally, the master mandrel may be reused after the replication to produce another identical mirror shell.

The replication method has been the key technique to achieve the performances of the X-ray telescope XMM, whose optics have been produced with this method by INAF-OAB and Media-Lario: the adoption of this method has allowed a strong reduction of production costs, manufacturing and assembly time, and (as we will see) may be upgraded to the production of mirror shells for hard X-rays with multilayer coatings. The replication technique may be implemented following two possible ways: the *Nickel electroforming* and

	SAX	JET-X	XMM
mirror profile	double cone	Wolter I	Wolter I
modules number	4	2	3
number of shells per mod.	30	12	58
max diameter	16.2 cm	30 cm	70 cm
min diameter	6.8 cm	19.1 cm	30 cm
mirror length	30 cm	60 cm	70 cm
shell thickness	0.2-0.4 mm	0.65 -1.1 mm	0.47 -1.1 mm
eff. area per module (7 keV)	40 cm^2	70 cm^2	600 cm^2
eff. area per module (1.5 keV)	80 cm^2	160 cm^2	1400 cm^2
focal length	1.85 m	3.5 m	7.5 m
energy range	0.1 ÷ 10 keV	0.3 ÷10 keV	0.1 ÷15 keV
HPD	2'	20"	15"
incidence angles	$0.23^o \div 0.62^o$	$0.39^o \div 0.60^o$	$0.28^o \div 0.67^o$

Table 2.3: Some characteristics of optics produced with the Ni electroforming and replication technique: this method conjugates a large effective area in a limited module diameter, with a good angular resolution and a focal length not so huge to be implemented on a single spacecraft. Note, in particular, the large number of nested mirror shells.

the use of *ceramic materials* (see fig. 2.13). These two possible approaches differ essentially in the growth process of the material that constitutes the mirror walls: they will be shortly discussed in the following paragraphs.

Nickel electroforming: the XMM mirrors This technique has already given very good results with the mirrors of the soft X-rays telescopes on-board the satellites *Beppo-SAX* and *Newton-XMM* (see tab. 2.3), and also with the soft X-ray optics on-board the satellite SWIFT (JET-X). The steps to produce a mirror shell with this method are:

1. a *master mandrel* in Aluminium having the negative mirror profile is produced: the mandrel is coated with a thin layer (≈ 100 μm) of electrochemical Nickel (*Kanigen*), a Nickel alloy suitable to be superpolished at an excellent level;

2. the mandrel surface is superpolished down to few angstroms rms, using a superpolishing procedure conceived at the INAF-OAB (see sect. 6, tab. 6.1;

3. a thin (1000 Å) layer of X-ray reflecting material (Au, Ir, Pt) is deposited in vacuum on the mandrel surface: this thin layer will constitute the reflective coating for the soft X-ray mirror shell of the optic;

4. the coated mandrel is put in a Nickel electroforming bath, where the walls of the mirror shell are grown around the reflecting layer. The thickness of the walls may vary ($100 \div 1100$ μm) according to the mechanical rigidity requirements and the overall optic mass limits;

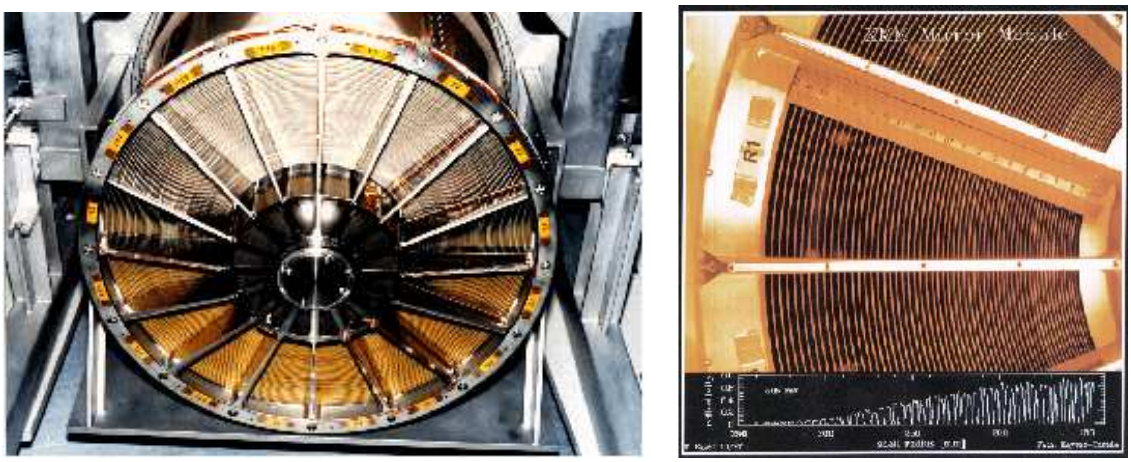

Figure 2.14: (left) A front view of a XMM module: the set of mirror shell is assembled in an integration stand that keeps them in a rigid structure. (right) A detail of the mirror structure that shows the dense filling of the mirror collecting area (credits: ESA).

5. finally, the mirror shell is separated from the mandrel: this is obtained by *cooling* the mandrel, as the Aluminium mandrel body has a larger CTE (about a twofold factor) than the Nickel mirror shell. Moreover, the Gold coating has a low adhesion on the superpolished mandrel surface, ant it favours the separation of the mirror from the mandrel: it acts exactly as a *release agent*; the cylindrical mirror structure permits to reduce the stress that arise in the mirror during the mirror separation.

Using a set of mandrels of different diameters, the mirror shells to be nested can be produced in a relatively short time: in case of multimodular telescopes, moreover, the mandrels can be reused to produce another identical optic, with evident time and cost gains. Another advantage of this technique is that the side of the reflective layer which will reflect the X-rays to be focused is the side that was directly in contact to the superpolished mandrel: this side has usually a lower roughness and a better reflectivity than the outer surface of the layer deposited on the master, because the film growth causes the increase of the surface microroughness. Using the replication technique, the rougher side of the film is not involved in the reflection process and the surface smoothness of the Au layer that will reflect the X-rays reproduces the excellent polishing level of the master mandrel.

In figures 2.14 some details of the XMM mirrors are presented: the XMM mirrors represent (at present time) the highest performance X-ray optics produced by Nickel electroforming, in terms of effective area in the soft X-ray band. Another X-ray telescope (JET-X) was produced to be a part of the *Spectrum-X/Gamma Observatory*: this project was, indeed, aborted and now the JET-X mirrors are implemented in the XRT telescope on-board SWIFT (see sect. 2.5.1, page 36) and will be a fundamental imaging tool to observe the GRB afterglow in the soft X-rays. Some JET-X mandrels, with some replicated shells, are shown in figure 2.15.

The thicknesses of the mirror shells walls are important parameters: the thickness is a merit factor in order to preserve the mirror optical performance since it makes it less sensitive to thermal, gravitational, vibrational deformations. The shell thickness is, hence, one of the most important parameters to determine the mirror angular resolution: on the other side, thin shell walls are necessary to reduce the mirror mass and to permit the tight nesting of a large shell number (whose typical distance is about 1 mm) to increase the effective area.

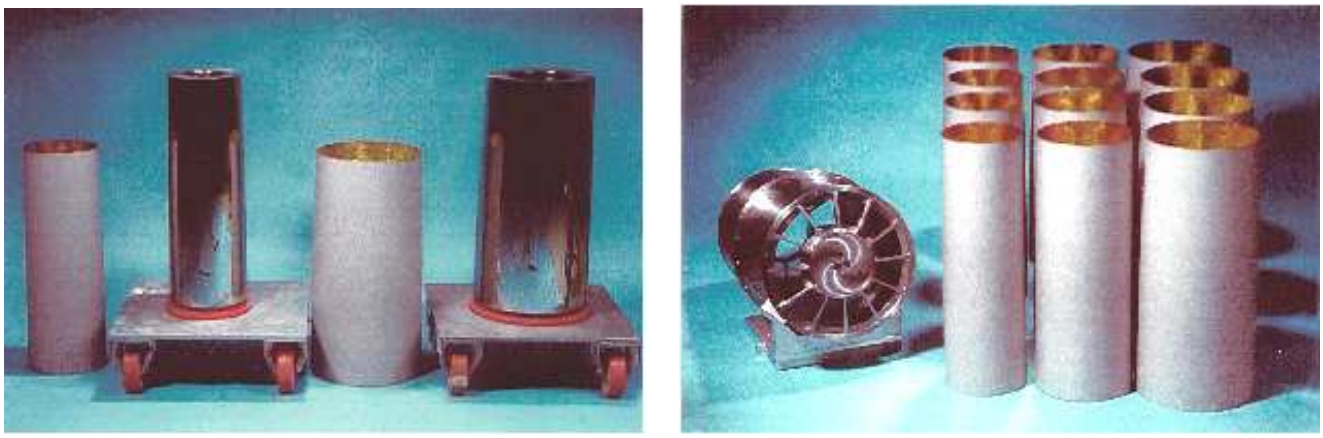

Figure 2.15: The JET-X mirrors: (left) two shells and the mandrels used for the replication.
(right) The set of mirror shells, shown near to the spider used for the integration of the mirror shells.

An X-ray optic has to fullfill a right balance of both requirements: this is one of the most challenging aspect of the research oriented to the development of X-ray mirrors for the next missions.

An important step that determines the mirror optical performances is represented by the *mirror integration*. The integration of the set of mirror shell modules is obtained with a typical mechanical support, visible in fig. 2.14. The rear of the mirror is constituted by a typical radial structure called *spider*, that guarantees a large module stability.

In the adopted assembly procedure, the mirror shells are nested and glued to the rear spider in precise predeterminated locations, starting from the innermost to the outermost shell. All the alignment is done in an optical bench where the optic is fully-illuminated by an UV source and the optic HEW is monitored. When all the shells are glued to the spider, the front-end of the case can be "closed" by another spider (in the case of XMM, indeed, the front spider is not present). The presence of the spiders obviously "shadows" a part of the incident X-rays and reduces the shell effective area (*vignetting*). Another cause of vignetting can be also the mirror collimator which is used to reduce the aperture background flux on the detector.

Replication with ceramic materials An alternative technique for the mandrel replication is represented by the ceramic materials (see fig. 2.13) instead of Nickel. In fact, the future telescopes (like XEUS) will implement optics with a very large diameter (> 5 m): Ni optics with a thickness large enough to guarantee the mirror stability would easily exceed the strict mass requirements, so the current research activity is considering the possibility of manufacturing X-ray optics with a lower specific weight, like the *Silicon Carbide* (SiC) and the *Alumina* (Al_2O_3).

The process used to transfer the reflecting layer to the mirror shell is:

1. the reflective layer is deposited on the master as in the previous case: an external carrier in SiC or Al_2O_3 with a size slightly larger then that of the master is produced;

2. the carrier and the coated master are nested and the small gap (100 -150 μm) remaining between them is filled with a special epoxy resin;

3. the shell separation is done by cooling, as in the previous case.

Optics produced with the replication with ceramic materials have several advantages:

1. they have a reduced density (3.2- 3.4 g/cm^3) with respect to Nickel (8.9 g/cm^3), so the overall optic weight can be low, while the mirror thickness may be large enough to guarantee the optics mechanical rigidity;

2. due to the elasticity of the ceramic materials, the stresses that arise during the mandrel separation do not leave permanent deformations;

3. the ceramic optics typical oscillation frequencies are higher than the corresponding Nickel optics: this is very useful to preserve the optics from deformations caused by the vibrations at the satellite launch.

The sector of production of SiC optics, in particular, looks very promising and some prototypes have already been produced by *Chemical Vapour Deposition* process (see fig. 2.16). SiC is also an interesting alternative to the Nickel overcoating for the master mandrel used for the replication, since it can be super-polished at comparable levels as the Nickel Kanigen but it has excellent hardness properties (see bibl. [92]), a very desirable aspect for mandrels to be reused in order to make identical optics modules.

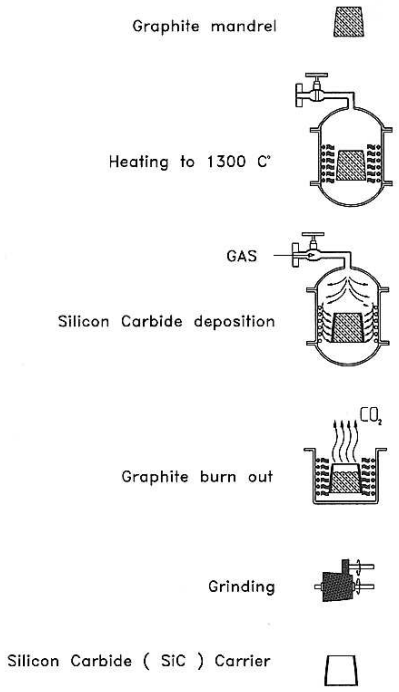

Figure 2.16: The technique used to produce SiC carriers: the shape is determined by a graphite mandrel, which is heated up to 1300 degrees. The SiC is deposited by use of a reactive gas that covers the mandrel surface with a SiC layer. The Graphite is then eliminated and the resulting carrier is grinded to finish the details.

A recent development in the field of replicated optics with lightweight materials has been accomplished with the production of plastic mirror shells with good mechanical stiffness. Some prototypes have already been produced and tested (see bibl. [30]).

2.4 The present state of instruments over 10 keV

The traditional, single-coating optics described in this chapter can operate only up to 10 keV. This is the reason why there are since now no focusing optics for the hard X-rays. The effects of the absence of imaging telescopes observing the hard X-ray sky are evident: in particular (see the fig. 1.1), the achieved sensitivity in hard X-rays is far away from the soft X-rays telescopes performance; actually, the minimum detectable flux in the soft band has fallen down by several order of magnitude after the introduction of increasing effective area optics, and the operating missions (like Newton-XMM) have sensitivity below 10 keV which allow to detect fluxes less than 1 μCrab. Over 10 keV, instead, the most sensitive results in the band 15-150 keV are those obtained down to 1 mCrab by BeppoSAX with the collimated instrument PDS: this good result was due not only to the low particle background ensured by the chosen orbit at 600 Km of altitude, very effectively shielded by the geomagnetic field; but it was also a result of the accurate materials choice and of the CsI anticoincidence design.

As previously mentioned, the poor angular resolution is a severe limit of collimated detectors: a progress (see e.g. bibl. [48]) is expected from the wide FOV, coded mask instrument BAT on-board the satellite SWIFT (US-IT-UK), launched on Nov 20, 2004 and devoted to the Gamma Ray Bursts, that will provide a sky survey in the 15-150 keV down to 1 mCrab with angular resolution $\sim 2'$, corresponding to the capability of resolving the 1-2% of the CXB.

A further step will be accomplished with the US mission EXIST (launch foreseen after 2010), completely devoted to the whole sky survey with coded masks. Its design goal is to reach a flux sensitivity of 0.05 mCrab in the 20-100 keV band with a 2' resolution, corresponding to the 7% of the CXB.

However, a real substantial progress in X-ray astronomy may be accomplished only by using optics for hard X-rays. The extension of the performance (see e.g. bibl. [101]) beyond 10 keV is a progress to which the Italian group led by O. Citterio of the Brera-Merate Observatory is giving a widely recognized contribution, building on the experience made first with BeppoSAX, then with XMM and JET-X. In particular, the multilayer coatings allows a slowly decreasing effective area up to 60-80 keV, and their implementation in the balloon-borne mission HEXIT (angular resolution 30") will strike the mCrab limit in the band 20-70 keV. Its satellite follow-up (HEXIT-SAT) will reach a 3σ sensitivity of 1.6 μCrab in 3×10^5 sec exposure time in the band 0.1-70 keV, corresponding to the resolution of the 40% of the CXB. This progress will be possible due to the use of multilayer reflecting coatings. They will be the subject of the next chapter. In the following pages, instead, we will see some alternative techniques to the multilayer coatings in order to extend the imaging capabilities to the hard X-rays.

Parameter	Con-X/SXT	XEUS	Generation-X
aperture diameter	140 cm	9900 cm	4500 cm
number of modules	4	1	6
shells per module	70	562	TBD
geom. area per module	7500 cm^2	300000 cm^2	125000 cm^2
focal length	10 m	50 m	100 m
resolution (HEW)	10"	2"	0.1"

Table 2.4: Performances of some future missions equipped with *hard* X-rays focusing telescopes (adapted from bibl. [90]).

2.5 Indirect imaging techniques

The X-ray focusing techniques allow the X-ray *direct* imaging: the image is directly produced by the focusing optics on a position-sensitive detector like a CCD array, and the image can be directly seen without further elaborations, except the image handling (background subtraction, ...).

However, the direct imaging is not suitable over 10 keV since now: the multilayer technologies is in development, but alternative technologies are already available to image the hard X-ray sky. These technique allow an *indirect* imaging, with optical performances far away from the focusing telescopes, but they represent a sure improvement with respect to the passively collimated detectors.

In the next pages some basics of the *coded mask imaging* will be provided: the coded mask are since now the only viable alternative to focusing systems in the range 10 keV $\div$ 1 MeV. Over 100 keV the γ-ray sky may be observed with other indirect imaging techniques, like the *Compton Scattering* and the *Earth Occultation* techniques; an exposition of these techniques would be out of our purposes.

2.5.1 Coded masks

The coded mask technique have been semi-seriously defined as *"the worst possible way of making a telescope, except when you can't do anything better" (G. Skinner).* This technique replaces the optic with a pixeled plate with a special distribution of X-ray transparent or opaque pixels (see fig. 2.17). When the coded mask is illuminated by a distant X-ray source, the closed pixels casts an X-ray "shadow" on a position-sensitive detector array that depends on the source position in a non ambiguous way. The mask pattern is properly designed so that its autocorrelation function is a delta function: thus, the response of each detector pixel allows to reconstruct the source direction and intensity.

Figure 2.17: (top) Working principle for coded masks for hard X- and γ-rays. (bottom) An image of a real coded mask: the IBIS mask on-board INTEGRAL. (credits:ESA)

In real cases, the coded mask will be exposed to the whole X-ray sky, and each detector pixel will record the sum of signals projected by the X-ray sky sources through the coded mask (plus the detector background): this signal will be roughly the convolution of X-ray sky with the mask pattern. If the number of detector pixel is large enough, the signal distribution can be deconvolved as the mask pattern is known, and a sky image can be obtained (see fig. 2.18). In figure 2.17 an image of the mask IBIS on-board the satellite INTEGRAL (launched in 2002) is shown.

Coded masks for low energies (E $\sim$ 10-20 keV) are etched metal foils, often gold-plated to increase the absorption, usually self supporting or supported by additional supporting bars, that are integrating part of the mask pattern. At higher energies ($>$ 1 MeV), they are Tungsten blocks some centimeter thick, supported by Carbon fiber honeycomb.

Coded masks take the advantage of a wide FOV, and they are not selective in energy, so the energy response of the detector may be optimized to the targets to be observed: the angular resolution achievable is, indeed, quite poor (some arcmin, see tab. 2.5) if compared to the performances of focusing optics; moreover, the collecting X-ray area (roughly the mask surface area) is not much larger than the detector area: the sensitivity of coded mask equipped telescopes is thus much lower than the achievable one with focusing telescopes (see fig. 1.1).

	JEM-X	IBIS	SPI
Energy range	3 $\div$ 100 keV	15 keV $\div$ 10 MeV	20 keV $\div$ 8 MeV
Mask size	53.5 cm	106.4 cm	77 cm
Thickness	0.5 mm	16 mm	3 cm
Mask pixel size	3.3 mm	11.2 cm	6 cm
Angular resolution	3'	12'	2.5^o
Field of View	4.8^o	9^o	16^o

Table 2.5: Some characteristics of the coded masks on-board INTEGRAL (credits:ESA): the energetic range of sensitivity is extremely large, but the angular resolution cannot compete with the focusing systems. All three masks are in Tungsten.

There are also some limits to the achievable image recovery; one is the aperture background, that can be reduced adopting anticoincidence systems or/and special deconvolution algorithms: moreover, the self-convolution function of the mask pattern is never exactly a delta function because of the finite detector resolution and mask size, leading to the formation of ghosts while deconvolving the image: to help to solve this problem, sophisticate deconvolution methods have been developed.

However, coded masks are at present time the only imaging systems which fill the energetic gap between the soft X-rays imaging and the techniques adopted over 100 keV (e.g. the Compton scattering techniques). The ESA telescope INTEGRAL, the most sensitive γ-ray *imaging* observatory ever launched, is completely based on coded masks (whose properties are shortly described in the tab. 2.5) The limited angular resolution of the coded masks makes them also very useful to study the diffuse X-ray/γ emission (this is the reason why e.g. the mask SPI on-board INTEGRAL has a resolution of only 2.5^o), a field with interesting application in the study of the cosmic radionuclides (e.g. the ^{26}Al emission lines) mapping produced by Supernova explosions in the last millions of years in our Galaxy (see bibl. [41]) or by the nuclear reactions produced by Cosmic Rays in the interstellar medium.

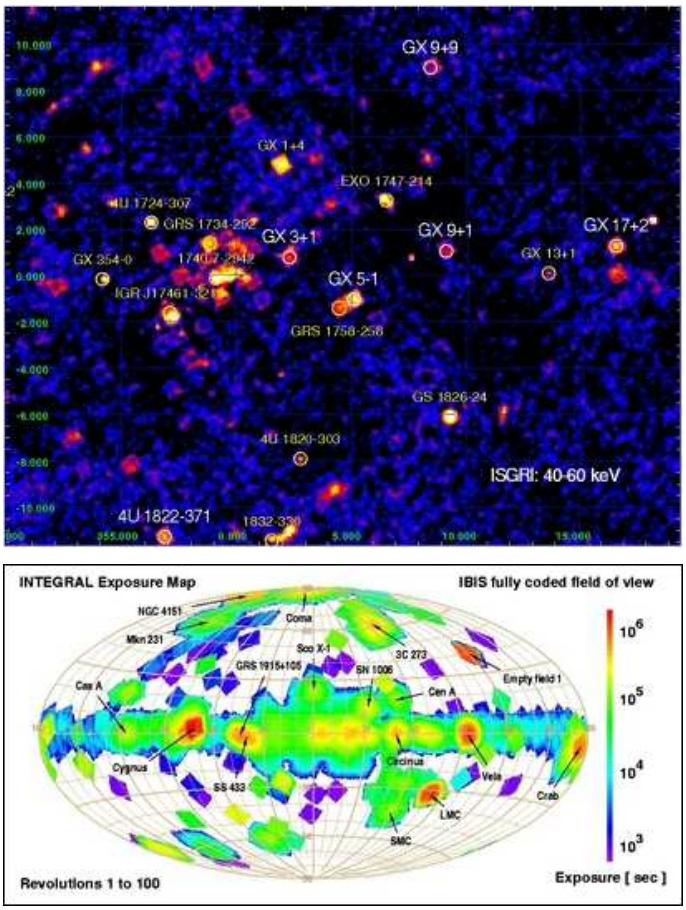

Figure 2.18: (top) The Galactic Center (40-60 keV) seen by INTEGRAL. (bottom) The full sky survey performed with the mask IBIS (credits: ESA)

Coded masks are also a basic tool in the *Burst Alert Telescope* (BAT) on-board the satellite SWIFT (2004), a NASA missions with a large participation of the Italian Space Agency, and many other European institutes as the Brera Astronomical Observatory (see bibl. [37], bibl. [36]). SWIFT will be devoted to the observation of Gamma Ray Bursts, and in particular, will allow it to observe the GRB afterglow in its very first phases in the wavelengths from γ-rays to the optical, and to perform important timing, spectroscopic, imaging measurements in order to understand the GRB origin and the role they play in Astrophysics and Cosmology. SWIFT is expected to detect more than 200 GRBs with a sensitivity almost 3 times better than BATSE on-board the Compton Gamma Ray Observatory (1991-2000). The unprecedented SWIFT observational capability is due mainly to the BAT telescope, that will be able to locate the GRBs with an approximation of $1 \div 4$ arcmin within 15 sec after the first detection, and to re-point the whole spacecraft in $20 \div 75$ sec towards the GRB position.

The BAT telescope (see bibl. [38]) is a very wide field instrument (100^o x 60^o FOV, partially coded) and a high sensitivity from 15 to 150 keV. BAT implements a wide (5200 cm^2) coded mask with a completely random pattern and a large, densely pixeled (4 mm $\times$ 4 mm) solid state detector array (CdZnTe), see fig. 2.19. These characteristics allow BAT to perform all-sky γ-ray surveys, and, when a GRB occur, to locate its position within a few second time: after the very short lag necessary to re-point the instruments, the GRB afterglow will be observed by the narrow-field instruments on-board SWIFT, like the imaging

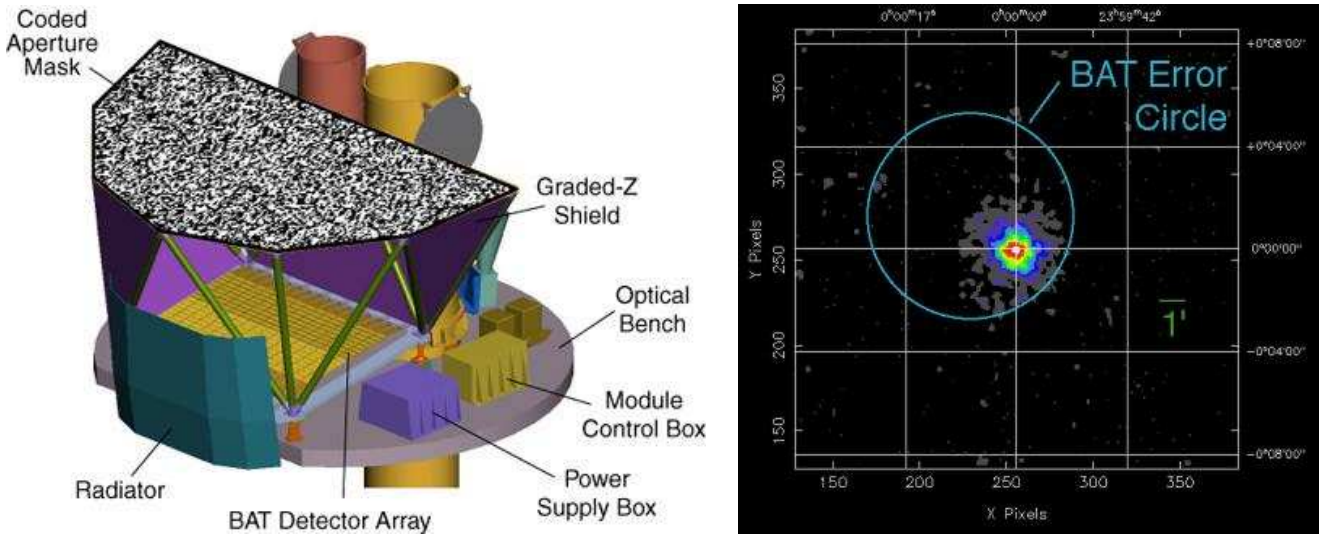

Figure 2.19: (left) The BAT instrument on-board SWIFT (credits:NASA). (right) A simulation of a JET-X XRT field of view, including the BAT error circle. This ensures that the GRB afterglow can be observed with the XRT telescope at the first attempt (credits: NASA).

X-ray telescope (XRT) operating from 0.3 to 10 keV (whose optics have been produced using the replication technique with Nickel electroforming (see bibl. [39]), and the UV/Optical Telescope (UVOT, sensitive in the range 170 $\div$ 650 nm). The FOV of these instruments are included in the BAT FOV, so long duration γ-ray emission from the burst can be studied simultaneously with the X-ray and UV/optical emission (see fig. 2.19), in unprecedently observed earliest afterglow phases.

The XRT telescope on-board SWIFT, in particular, will provide X-ray images of the GRB afterglow soft X-ray emission: the XRT PSF is 18" (at 1.5 keV), a good angular resolution joined to an effective area (110 cm^2 at 1.5 keV) able to return good timing or spectroscopic capabilities. X-ray emission lines detection and measurement will be able to estimate the GRB redshift, and consequently, the GRB distance: the distance measurement will, in turn, allow to estimate the GRB energy emission and put constraints on the GRB origin and cosmological meaning.

Chapter 3

Multilayer coatings

The present lack of focusing optics in hard X-rays comes from the smallness of the reflection angle on a traditional, single-layered coating. A solution would then come from the adoption of a coating which reflects hard X-rays at enough large grazing angles ($\sim 1000''$) in order to guarantee an useful effective area. Such coatings may be *multilayer coatings*. They consist in a repeated, periodic, alternance of two layers with very different densities, hence different refractive index in X-rays. The reflected waves by each interface of the multilayer coating will have a very small amplitude if we are over the critical angles, but at some incidence angles they may have a phase difference of an integer multiple of 2π. The constructive interference of the reflected rays builds up an overall high reflectivity (near to 100%). Multilayer coatings are widely used not only in the X-ray but also to reflect and filter in the UV and optical range (in normal or almost-normal incidence); the multilayer mirrors are not new to astronomy: they were used since 1970s in almost-normal incidence to take images of the Sun in soft X-rays.

Multilayer coatings of the described type, with constant thickness of the bilayers through the multilayer stack, are called *constant period multilayers* and for a fixed incidence angle they are essentially able to reflect only a single wavelength: the reflected wavelength is function of the the incidence angle and of the multilayer period. Constant period multilayer are not very useful in astrophysics (although they have applications in other technological sectors), because it usually necessary observe in a *wide* energy band. A multilayer able to reflect a continuum set of wavelengths at a fixed energy angle is obtained by *changing the multilayer period in its stack*. These *graded multilayers* have a reduced reflectivity in comparison to the constant period-type, but they allow an exploitable reflection from 10 to 40 keV and more.

Multilayer coatings are then a very promising solution to make hard X-rays mirrors up to 80 keV, over this limit the multilayer period would be so little that the microroughness would surely compromise the multilayer reflectivity: in these cases coatings with mosaic crystals in Bragg or Laue geometry must be adopted (see bibl. [134], bibl. [133], bibl. [135], bibl. [136], bibl. [137]). In particular, the adoption of a Laue lens with Copper Mosaic Crystals is foreseen in the balloon-borne mission HEXIT (see sect. 3.7.1, page 78). In the next sections we will see the principles of the X-ray multilayer reflection.

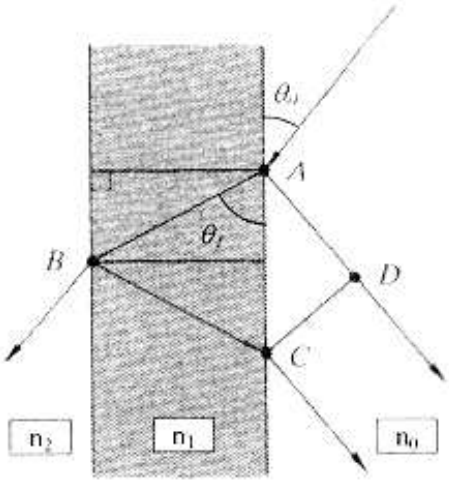

Figure 3.1: Interference in a single, thin layer. At each reflection on the layer upper face a different ray starts with a path delay of $\Delta l = 2n_1\overline{AB} - n_0\overline{AD} = 2n_1 d\cos^{-1}\theta_1 - n_0 d\tan^{-1}\theta_1\cos\theta_0 = 2n_1 d\sin\theta_1$.

3.1 Single layer reflection

The reflection of electromagnetic waves on a thin layer is a common problem of optics. In visible light interference effects are exploited to improve or reduce the transparency of materials. As X-rays are much more penetrating than visible light, a single thin layer has no chance to reflect in a significant amount an X-ray beam whether the incidence angle overcomes the critical angle. Nevertheless, the interference effects in a thin layer in grazing incidence are an useful tool for thickness, density and roughness measurements of a thin layer deposited on a substrate.

Let us have a thin layer of (complex) refractive index $n_1 = n_1(\rho_1)$, thickness d, deposited on a substrate with refractive index $n_2 = n_2(\rho_2)$. An X-ray with wavelength λ and amplitude E_0 incides from the ambient (with refractive index n_0, usually the vacuum and $n_0 = 1$) on the layer with grazing incidence angle θ_0, is refracted in the layer with an angle θ_1 and hence in substrate with angle θ_2. The refraction Snell's law holds:

$$n_0\cos\theta_0 = n_1\cos\theta_1 = n_2\cos\theta_2 \tag{3.1}$$

at each interface, moreover, the beam will be partially reflected according the *Fresnel laws*, which may be approximated in grazing incidence (but provided that $\theta_C < \theta_0 < \theta_{Brewster} \simeq 45^o$):

$$r_{01} = \pm\frac{\delta_1 - \delta_0}{2\sin^2\theta_0} \quad r_{12} = \pm\frac{\delta_2 - \delta_1}{2\sin^2\theta_1} \tag{3.2}$$

the + holds for the s-polarization state. The reflected amplitude on each interface depends essentially on Δn (which is *approximately* proportional to the *density contrast* $\Delta\rho$[1]), but because of the small values of the δs the reflectivity will be extremely low ($r^2 \sim 10^{-4}$).

[1] the difference in the Z/A ratio may be important when densities are very similar.

At each reflection/refraction the phase may be conserved or inverted: from the Fresnel laws the following relationship may be obtained (see also bibl. [24]):

$$r_{01} = -r_{10} \qquad r_{12} = -r_{21} \tag{3.3}$$

$$r_{01}^2 + t_{01}t_{10} = 1 \quad r_{12}^2 + t_{12}t_{21} = 1 \tag{3.4}$$

the second equation is simply the energy conservation at each interface. Both r and t are assumed to be real (neglecting the absorption) The terms t are always positive.

At the first reflection the reflected ray has an amplitude $r_{01}E_0$, and the transmitted one $t_{01}E_0$. This one will be reflected on the substrate and the reflected ray will have an amplitude $r_{12}t_{01}E_0$ (the transmitted ray in substrate is lost by definition). This reflected ray at the layer surface will be furthermore reflected in the layer and partially transmitted. The amplitudes of the reflected (in the layer) and refracted (in vacuum) have respective amplitudes $r_{10}r_{12}t_{01}E_0 = -r_{01}r_{12}t_{01}E_0$ and $t_{10}r_{12}t_{01}E_0 = r_{12}(1-r_{01}^2)E_0$. At this point both rays have a phase shift with respect to the incident one (see fig. 3.1):

$$\Delta\phi = \frac{2\pi}{\lambda} 2nd\sin\theta_1 \tag{3.5}$$

repeating all the steps with the reflected ray in the layer and taking into account the phase shift $\Delta\phi$ at each reflection on the substrate, and by summing all the reflected rays, the resulting reflected amplitude is:

$$E_r = r_{01}E_0 + r_{12}(1-r_{01}^2)E_0e^{-i\Delta\phi} - r_{01}r_{12}^2(1-r_{01}^2)E_0e^{-2i\Delta\phi} + r_{01}^2r_{12}^3(1-r_{01}^2)E_0e^{-3i\Delta\phi} - \cdots \tag{3.6}$$

that is:

$$E_r = r_{01}E_0 + r_{12}(1-r_{01}^2)E_0e^{-i\Delta\phi}\sum_{k=0}^{\infty}(-r_{01}r_{12})^k e^{-ik\Delta\phi} \tag{3.7}$$

by summing the geometric series, we obtain the *complex amplitude reflection by the layer*[2]:

$$\mathcal{R} = \frac{E_r}{E_0} = r_{01} + \frac{r_{12}(1-r_{01}^2)e^{-i\Delta\phi}}{1 + r_{01}r_{12}e^{-i\Delta\phi}} \tag{3.8}$$

all the involved quantities depend both on wavelength and on incidence angle. The first term of the eq. 3.8 is the reflectivity of a single interface (as in the case of thick, single layer reflection) the second term is the interference effect which *modulate* the single interface reflectivity r_{01}. When $r_{01} \approx 1$ (that is, $\theta_0 < \theta_{C1}$) the interference term vanishes because no radiation is transmitted in the layer. The same occurs obviously when $r_{12} \approx 0$, meaning no contrast density layer/substrate.

The measurable quantity is the *reflectivity* $R = |\mathcal{R}|^2$. Supposing that the reflectivities r_{01}, r_{12} are slowly varying with incidence angle, we can find the stationary points of the R at $\Delta\phi = k\pi$ with k integer, that is

$$2n_1 d\sin\theta_1 = k\lambda \tag{3.9}$$

$$2n_1 d\sin\theta_1 = \left(k + \frac{1}{2}\right)\lambda \tag{3.10}$$

if $r_{01}r_{12} > 0$ the angles satisfying the 3.9 are maxima and the 3.10 defines the minima. If $r_{01}r_{12} < 0$ the maxima and the minima are exchanged. In both cases the formula 3.9, known as *Bragg law*, may be used to measure the layer thickness (see sect. 5.2.2, page 115).

[2]This expression has no limit for $d \to \infty$: however, it is reasonable that the interference features disappear as the projected thickness takes over the coherence length of the X-rays.

The reflectivity of a single interface for incidence over the critical angle will always be low, and even in maxima will reach $R \approx (r_{01} + r_{12})^2$. In minima $R \approx (r_{01} - r_{12})^2$: in the case of a layer without a substrate (i.e. in vacuum: more really, on a very light substrate) the layer has a null reflectivity in minima.

The equation 3.8, written as

$$\mathcal{R} = \frac{r_{01} + r_{12}e^{-i\Delta\phi}}{1 + r_{01}r_{12}e^{-i\Delta\phi}} \tag{3.11}$$

is the basis of the recursive theory of the reflectivity of a multilayer (see 3.3).

The reflectivity of a single Au or Ni layer deposited on glass is shown in fig.3.2. Like the reflectivity from a thick layer, it is remarkable the total reflection at grazing incidence less than the Au or Ni critical angle. Over this limit the radiation starts to penetrate the layer and the interference fringes become visible.

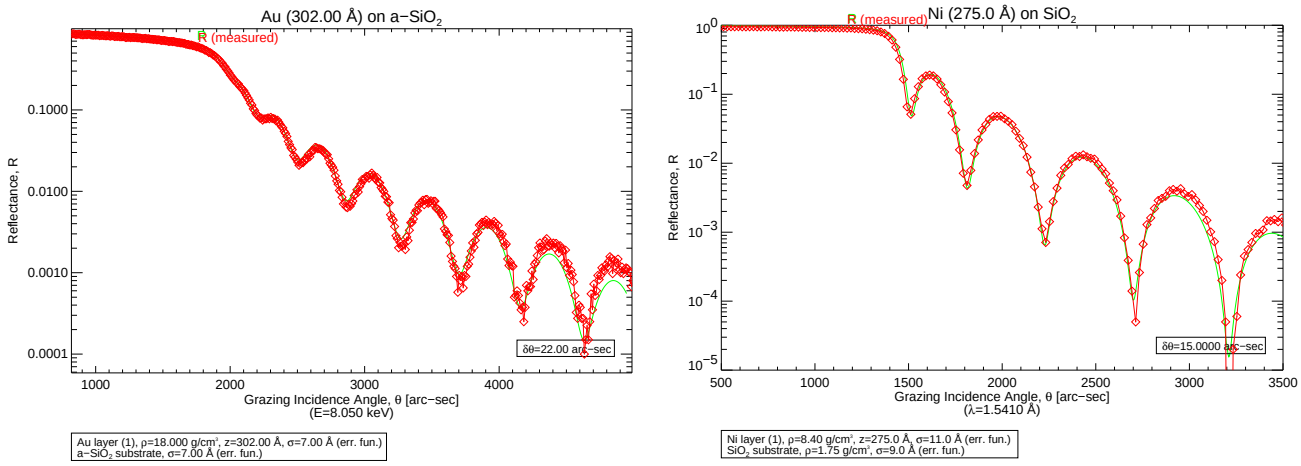

Figure 3.2: X-ray (1.541 Å) reflectivity scan of (left) an Au layer 30 nm thick and (right) Ni layer 27 nm thick. The scans re superposed to a nonzero-roughness fitting model. The curves are to be compared to the thick-layer reflectivity scan in fig. 2.9.

The exposed results supposed ideally smooth interfaces, neglecting completely the *roughness effects*. The roughness reduces strongly the reflectivity (see sect. 2.2.4, page 24) and reduces also the amplitude of the interference fringes. The reflectivity reduction may be calculated by correcting the factors r_{01}, r_{12}, t_{01}, t_{10} with the factors in eq. 2.21, eq. 2.22. Of course, as the roughness subtracts energy to the beam in the specular direction, the second of the eq. 3.4 will be only approximately valid. However, as the reflected amplitude is real, there are no additional phase shifts to take into account and the interference fringes keep their position as in the eq. 3.9.

In the sect. 5.3.1, page 120, we shall see how an X-ray beam is scattered as effect of the surface micro-roughness of a single surface; the photon cross-section of surface is directly related to the power spectrum of the surface profile. In a layered structure, moreover, each interface profile is related to the previous one as a "template" (see sect. 3.5.2, page 68). This fact causes a similarity of the scattering surfaces resulting in interference fringes of the scattered rays. The analysis of the scattering is a powerful tool to check the layer growth process (see bibl. [78]).

3.2 Periodic multilayers: the *Bragg Law*

The most simple kind of multilayer is a succession of N identical *bilayers*, each of them being a superposition of two thin films with a large density contrast (see fig. 3.3). The heavier elements (high Z) is called *absorber*, the lighter one (low Z) is the *spacer*. The absorber provides the partial reflection of the incident waves, the spacer must instead keep the absorbing layers at the right distance in order to build up the constructive interference of reflected wavelets. Typical couples are Ni/C, Pt/C, Mo/Si, W/Si, Co/C. A database of produced multilayers is available in the Internet at the URL http://www-cxro.lbl.gov/multilayer/survey.html.

The absorber and spacer thickness are indicated with the symbols d_h and d_l, respectively, and their refractive indexes are $n_h = 1 - \delta_h + i\beta_h$, $n_l = 1 - \delta_l + i\beta_l$. The constant bilayer thickness is the multilayer *period* $d = d_h + d_l$, and the Γ *factor* is defined as the ratio $\Gamma = d_h/d$ $(0 < \Gamma < 1)$. The multilayer is deposited onto a substrate which is assumed to be thick (i.e. much thicker than the incident wavelength) with a refractive index n_s. As the best refracting materials are also the best absorber (both increase with Z, see the appendix A.1), usually multilayers are designed with $d_h \ll d_l$.

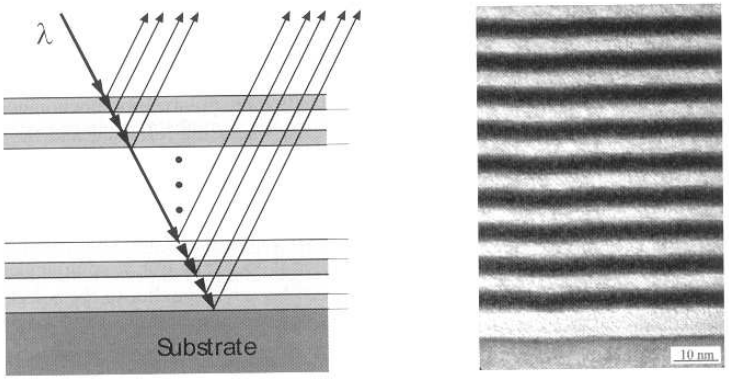

Figure 3.3: (left) Scheme of a multilayer structure (credits: bibl. [44]).
(right) TEM photography of a Mo_2C/Si multilayer with period 7 nm (adapted from bibl. [44]). The low-density (Si) material are the bright bands.

A periodic multilayer coating has the interesting property of reflecting X-rays with a (theoretical) reflectivity near to 100% at larger angles than the critical angles of its materials, where a single interface absorber/spacer would have a reflectivity (see eq. A.20)

$$|r_{hl}|^2 = \frac{(\delta_h - \delta_l)^2}{4\sin^4\theta_i} \propto \left(\frac{\lambda}{\sin\theta_i}\right)^4 \tag{3.12}$$

of the order of magnitude 10^{-2}, too low to make an efficient X-ray mirror, and quickly decaying with increasing energy. However, the phase difference between two rays reflected by consecutive absorber layers, when $d_h \ll d_l$, is (see the fig. 3.1)

$$\Delta\phi = \frac{2\pi}{\lambda} 2d\sin\theta_i \tag{3.13}$$

and because of the high layers number, the resulting interference of the reflected waves will be constructive only when $\Delta\phi = 2k\pi$, with k integer; the film will then show narrow reflectivity peaks at the wavelengths:

$$2d\sin\theta_i = k\lambda \tag{3.14}$$

the eq. 3.14 is the *Bragg law* and it is the most practical approximate formula to evaluate a periodic multilayer reflectivity peaks (*Bragg peaks*) angular positions. This name is taken from the natural crystal X-ray diffraction theory because the multilayer behaviour is similar to that of crystals: we could say that a periodic multilayer is an imitation of the crystalline structures made by the Nature.

The analogy is, however, incomplete, because a crystal is a succession of almost ideal reflecting planes (absorber) in vacuum (spacer) at a distance of few angstroms: they have so an ideal density contrast and the X-rays are not refracted from layer to layer, so crystals obey rigorously the Bragg law.

Typical reflectivity scans of an X-ray Ni/C multilayer are sketched in fig. 3.4. At very small angles (or at low energies) the reflectivity diagram is similar to the usual single-layer model: in this region only the uppermost layer of the multilayer is active and shields the multilayer stack from X-rays. When the typical penetration depth (increasing either angle or energy) becomes larger than the first layer thickness, the total reflection requirements are no more met and the radiation starts to penetrate the multilayer, generating the interferential effects that produce the observed Bragg peaks. Note that the critical angle in a multilayer is located between the critical angles of the absorber and the spacer.

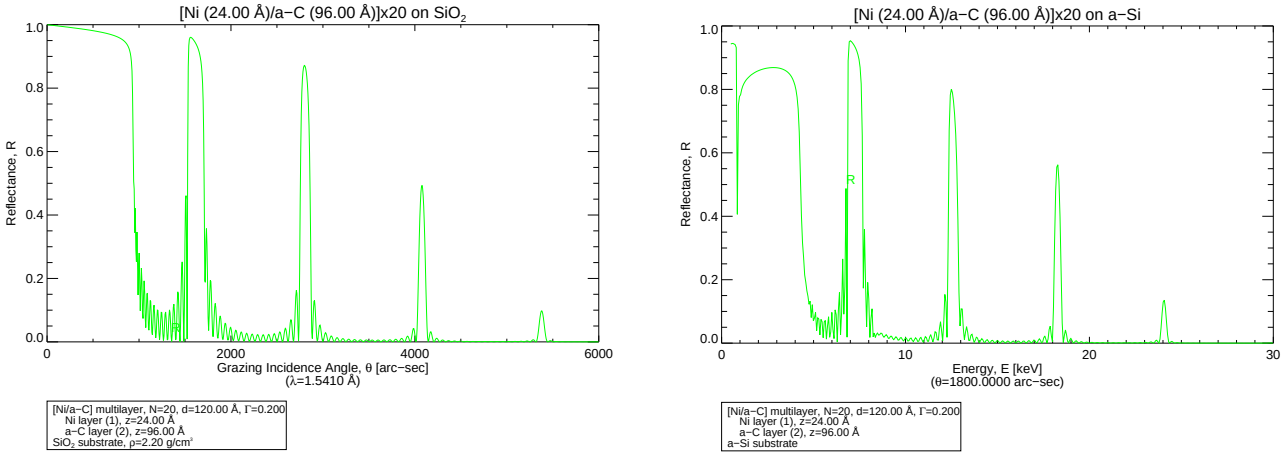

Figure 3.4: IMD reflectivity simulations of a N= 20, periodic multilayer with d = 12 nm, $\Gamma = 0.2$, zero-roughness model.
(left) Incidence angle scan at 8.05 keV: the reflection is concentrated in peaks according to the Bragg law, at larger angles than Ni and C critical angles.
(right) Photon energy scan at 1800" grazing incidence angle: the reflectivity peaks follow again the Bragg law. The minimum at 0.8 keV is an absorption edge of Nickel. Secondary peaks between the primary peaks are also visible.

In an X-ray multilayer, the layers are some nm thick: in the hard X-rays ($\lambda < 1\mathring{A}$) they can be used only in grazing incidence. Moreover, the spacer has a finite density and the refraction absorber/spacer must be taken into account. To do this, we can write the constructive interference condition for each bilayer,

$$\Delta\phi = \frac{2\pi}{\lambda}(2n_h d_h \sin\theta_h + 2n_l d_l \sin\theta_l) = 2k\pi \tag{3.15}$$

and remembering the Snell's law:

$$\cos\theta_i = n_h \cos\theta_h = n_l \cos\theta_l \tag{3.16}$$

we can write

$$n_h \sin\theta_h = (n_h^2 - n_h^2 \cos^2\theta_h)^{1/2} = (n_h^2 - \cos^2\theta_i)^{1/2} \tag{3.17}$$

and the same for $n_l \sin\theta_l$. Approximating $n_h^2 \approx 1 - 2\delta_h$, $n_l^2 \approx 1 - 2\delta_l$, the eq. 3.15 becomes

$$2d_h(\sin^2\theta_i - 2\delta_h)^{1/2} + 2d_l(\sin^2\theta_i - 2\delta_l)^{1/2} = k\lambda \tag{3.18}$$

and using the definition of Γ,

$$2d\sin\theta\left[\Gamma\left(1 - 2\frac{\delta_h}{\sin^2\theta_i}\right)^{1/2} + (1-\Gamma)\left(1 - 2\frac{\delta_l}{\sin^2\theta_i}\right)^{1/2}\right] = k\lambda \tag{3.19}$$

now, $\sqrt{2\delta_h}$ and $\sqrt{2\delta_l}$ are the critical angles of the absorber and of the spacer. The Bragg peaks are observed always at $\sin^2\theta_i \gg 2\delta_h, 2\delta_l$, so we can approximate

$$\Gamma\left(1 - 2\frac{\delta_h}{\sin^2\theta_i}\right)^{1/2} + (1-\Gamma)\left(1 - 2\frac{\delta_l}{\sin^2\theta_i}\right)^{1/2} \approx \left(1 - 2\frac{\Gamma\delta_h + (1-\Gamma)\delta_l}{\sin^2\theta_i}\right)^{1/2} \tag{3.20}$$

and we obtain the *refraction-corrected Bragg law*:

$$2d\sin\theta_i\sqrt{1 - 2\frac{\Gamma\delta_h + (1-\Gamma)\delta_l}{\sin^2\theta_i}} = k\lambda \tag{3.21}$$

which allows to locate exactly the Bragg peaks.

3.3 The recursive theory of multilayers

A rigorous theory (Rouard, 1937) that allows to model the reflectivity of *any* multilayer (with any d-spacing distribution) as a function of the photon energy and of the incidence angle, starts from the single layer reflectivity (eq. 3.11). We number the layers from the bottom to the top of the stack $j = 0, 1, \ldots, N$, ($j = 0$ is the substrate), and the reflectivity of the multilayer composed by the first j interfaces will be indicated by $\mathcal{R}_j$. Obviously the substrate/1^{st} layer interface:

$$\mathcal{R}_1 = r_{10} \tag{3.22}$$

and adding the 2^{st} layer will change the reflectivity to:

$$\mathcal{R}_2 = \frac{r_{21} + \mathcal{R}_1 e^{-i\Delta\phi_1}}{1 + r_{21}\mathcal{R}_1 e^{-i\Delta\phi_1}} \quad \Delta\phi_1 = \frac{2\pi}{\lambda}2d_1 n_1 \sin\theta_1 \tag{3.23}$$

where θ_1 is the incidence angle in the first layer. At the following steps the same formulas may be repeated by recursion, increasing the index j:

$$\mathcal{R}_{j+1} = \frac{r_{j+1\,j} + \mathcal{R}_j e^{-i\Delta\phi_j}}{1 + r_{j+1\,j}\mathcal{R}_j e^{-i\Delta\phi_j}} \qquad \Delta\phi_j = \frac{2\pi}{\lambda}2d_j n_j \sin\theta_j \tag{3.24}$$

after N steps the multilayer ends and its reflectivity is $|\mathcal{R}_N|^2$.

3.3.1 Periodic multilayers: results of the recursive theory

As an application we will approximately derive the reflectivity of a *non-absorbing*, periodic multilayer with N bilayers at the kth Bragg peak. Let us consider at first the s-polarization. If we stop the multilayer at the $(n-1)^{th}$ bilayer and we call its reflectivity $\mathcal{R}^s_{n-1}$, by adding the nth bilayer we add two further layers, with thicknesses d_s and d_a: the reflectivity will change to $\mathcal{R}^s_{n'}$ and $\mathcal{R}^s_n$ respectively. As the multilayer is an alternance absorber-spacer, moreover, we are adding two interfaces absorber/spacer and spacer/absorber, whose reflectivities are r_{hl} and r_{lh}, thus using the eq. 3.24

$$\mathcal{R}^s_n = \frac{r_{lh} + \mathcal{R}^s_{n'} e^{-i\Delta\phi_h}}{1 + r_{lh}\mathcal{R}^s_{n'} e^{-i\Delta\phi_h}} \qquad \mathcal{R}^s_{n'} = \frac{r_{hl} + \mathcal{R}^s_{n-1} e^{-i\Delta\phi_l}}{1 + r_{hl}\mathcal{R}^s_{n-1} e^{-i\Delta\phi_l}} \tag{3.25}$$

and where

$$\Delta\phi_h = \frac{2\pi}{\lambda} 2d\Gamma n_h \sin\theta_h \qquad \Delta\phi_l = \frac{2\pi}{\lambda} 2d(1-\Gamma) n_l \sin\theta_l \tag{3.26}$$

now, assume we are at the kth Bragg peak: if we neglect the refraction[3], we have $2dn_h \sin\theta_h \approx 2dn_l \sin\theta_l \approx k\lambda$, and by substituting[4] $r_{hl} = -r$ and $r_{lh} = r$ $(r > 0)$, after some algebra we find:

$$\mathcal{R}^s_n = \frac{r(1 - e^{-2\pi i k\Gamma}) + \mathcal{R}^s_{n-1}(1 - r^2 e^{2\pi i k\Gamma})}{(1 - r^2 e^{-2\pi i k\Gamma}) + \mathcal{R}^s_{n-1} r(1 - e^{2\pi i k\Gamma})} \tag{3.27}$$

the Bragg peaks are observed over the critical angles, so that the single-boundary reflectivity r is small: we can neglect the terms in r^2 compared to the unity, and so we find

$$\mathcal{R}^s_n e^{\pi i k\Gamma} = \frac{2ir\sin(\pi k\Gamma) + \mathcal{R}^s_{n-1} e^{\pi i k\Gamma}}{1 - 2i\mathcal{R}^s_{n-1} r \sin(\pi k\Gamma) e^{\pi i k\Gamma}} \tag{3.28}$$

now we can have a more suggestive form of the eq. 3.28 by defining:

$$\tan\alpha_n = \mathcal{R}^s_n e^{-\pi i k\Gamma} \qquad \tan\gamma = 2ir\sin(\pi k\Gamma) \tag{3.29}$$

and the eq. 3.28 becomes $\tan\alpha_n = \tan(\alpha_{n-1} + \gamma)$ which is equivalent to[5] $\alpha_n = \alpha_{n-1} + \gamma$: for N bilayers,

$$\alpha_N = \alpha_0 + N\gamma \tag{3.30}$$

and recalling the definitions eq. 3.29 we obtain the complex multilayer reflectivity at the kth Bragg peak:

$$\mathcal{R}^s_N = e^{-i\pi k\Gamma} \tan[\arctan(\mathcal{R}^s_0 e^{-i\pi k\Gamma}) + N \arctan(2ir\sin(\pi k\Gamma))] \tag{3.31}$$

the first term in the [ ] brackets is the reflectivity of the substrate alone and it is usually negligible: the second term is the multilayer contribution and it dominates for large N.

[3] This approximation hypothesis can be weakened replacing the angle θ with the refraction-corrected value in eq. 3.21.

[4] the s-polarized reflected ray has a phase inversion on the interface absorber/spacer: remember that in X-rays denser materials have *lower* refractive indexes (see appendix A.1).

[5] plus $m\pi$ with m integer: we do not consider it because it would be multiplied by N and then cancelled by the following tan operation.

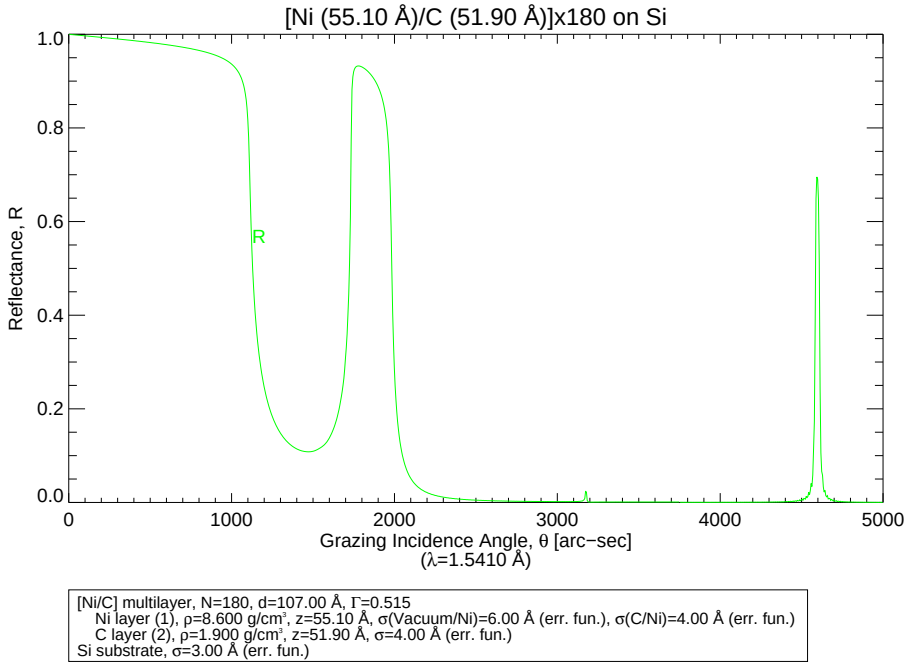

Figure 3.5: IMD reflectivity simulation at 8.05 keV of a Ni/C multilayer with $\Gamma \simeq 0.5$, 180 bilayers and $d \simeq 100$: the second peak has vanished due to the destructive interference between odd and even boundaries.

Moreover, r is often small[6] also and we can approximate the arctan function with its argument,

$$\mathcal{R}_N^s = e^{-i\pi k\Gamma} \tan[2iNr \sin(\pi k\Gamma)] \tag{3.32}$$

and considering that $\tan(ix) = i \tanh x$,

$$\mathcal{R}_N^s = +ie^{-i\pi k\Gamma} \tanh[2Nr \sin(\pi k\Gamma)] \qquad \textit{(s-pol.)} \tag{3.33}$$

the s reflected wave is, hence, phase delayed by $-\frac{\pi}{2} + \pi k\Gamma$ with respect to the incident wave at the multilayer surface.

If the incident ray is p-polarized we can repeat all the calculation, with $r_{hl} = -r$ and $r_{lh} = r$ (see sect. A.1, page 195):

$$\mathcal{R}_N^p = -ie^{-i\pi k\Gamma} \tanh[2Nr \sin(\pi k\Gamma)] \qquad \textit{(p-pol.)} \tag{3.34}$$

thus, the p and s polarized reflected waves are phase opposite. In any case, however, the reflected *intensity* is the same:

$$R_N = |\mathcal{R}_N|^2 = \tanh^2[2Nr \sin(\pi k\Gamma)] \qquad \textit{(any pol.)} \tag{3.35}$$

this equation shows that, for an ideal, non-absorbing multilayer:

1. *The reflectivity increases with the number of bilayers*: this increase is almost linear for small N, but as it approaches the value 1 the increase is slower and slower, tending to 1 asymptotically.

[6] e.g. for the Ni/C pair at 8.05 keV at 2000", $|r|^2 \simeq 10^{-2}$.

This saturation corresponds to the extinction of the incident beam which is mostly (57%) reflected in the first N_{min} stack bilayers:

$$N_{min} \approx \frac{1}{2r \sin(\pi k\Gamma)} \tag{3.36}$$

the achievable reflectivity with $2N_{min}$ bilayers is 92%, and 99 % with $3N_{min}$ bilayers.

2. *The reflectivity depends on the* Γ *ratio: it is maximum for* $k\Gamma$ *semi-integer and zero for* $k\Gamma$ *integer.* This is easy to explain, if we think that the transitions spacer/absorber reflect in phase at the Bragg peak, and the same occurs for the transitions absorber/spacer. The reflected waves which result from this interference have the same amplitude $|E_{as}| = |E_{sa}|$ but a phase difference of

$$\Delta\theta = \pi + \frac{4\pi}{\lambda} d\Gamma \sin\theta = 2\pi\left(k\Gamma + \frac{1}{2}\right) \tag{3.37}$$

the additional π shift comes from the Fresnel equations. The resulting amplitude is of course

$$|E_{as} + E_{sa}|^2 = 2|E_{as}|^2(1 + \cos\Delta\theta) = 2|E_{as}|^2 \sin^2(\pi k\Gamma) \tag{3.38}$$

The reflection pattern is hence *modulated* by the function $\sin^2(\pi k\Gamma)$, i.e. the Γ factor determines the relative peaks reflectivities [7], and in particular it suppresses all the Bragg peak with $k = \Gamma^{-1}$. For $\Gamma = 0.5$, e.g. the even Bragg peaks are cancelled and the odd peaks are enhanced (see fig. 3.5): multilayers with $\Gamma = 0.5$ are called *quarter-wave structures* because each layer covers exactly $\lambda/4$ of the incident wave.

From the previous discussion it is clear that the minimum number of bilayers necessary to achieve a reflectivity of $R \sim 1$ at the Bragg peak is of the order of some (2-3) N_{min}: this number is larger for low-reflectance interfaces, as expected; a further increase of the number of bilayers is useless, because the incident X-rays are gradually reflected and absorbed by the outer bilayers and the deepest bilayers are almost completely screened. Thus, the typical number of bilayers N_{min} which mainly contribute to the reflectivity is usually less than N, and N_{min} can be assumed as the effective number of bilayers at the Bragg peak.

Using the eq. A.20, the eq. 3.35 can take the explicit form:

$$R_N = \tanh^2\left[N\,\Delta\delta\,\frac{\sin(\pi k\Gamma)}{\sin^2\theta_i}\right] \tag{3.39}$$

where $\Delta\delta$ is the absorber/spacer refractive index contrast.

3.3.2 Reflectivity reduction by photoabsorption

Far from the reflectivity saturation, the reflectance obtained with formula 3.35 well approximates the reflectivity obtained with a complete, numerical calculation (see fig. 3.6): the main discrepancy is for large N in the saturation region: in real cases, because of photoabsorption, the reflectivity never reaches 100% for $N \to \infty$; the discrepancy is larger for higher Bragg peaks orders. The absorption can be taken into account by repeating the calculation with the complex part of the refractive indexes β_a and β_s. Remembering that the crossed thickness by the X-rays is $\frac{d\Gamma}{\sin\theta}$ for absorber layers and $\frac{d(1-\Gamma)}{\sin\theta}$ for the spacer, the eq. 3.28 takes the approximate form (provided that $\beta_h < 10^{-5}$, i.e., far from absorption edges) at the kth Bragg peak:

$$\tan\alpha_{n+1} = e^{-\zeta}\tan(\alpha_n + \gamma) \tag{3.40}$$

[7] As well as the peaks widths: the reduction of the Γ is a used method to increase the multilayer resolution, at cost of the larger bilayer number which is to be used

where α_n and γ are defined like in eq. 3.29 and

$$\zeta = \frac{2\pi k}{\sin^2\theta}[\Gamma\beta_h + (1-\Gamma)\beta_l] \tag{3.41}$$

leading to a not so simple recursive equation: only in the non-saturation region, we can approximate the *tan* functions with their argument, yielding $\alpha_{n+1} = e^{-\zeta}(\alpha_n + \gamma)$, i.e.,

$$\alpha_N \simeq \alpha_0 + \gamma\frac{1-e^{-N\zeta}}{1-e^{-\zeta}} \overset{\zeta\to 0}{\approx} \alpha_0 + N\gamma \tag{3.42}$$

and, substituting as before:

$$R_N \simeq \tanh^2\left[2r\sin(\pi k\Gamma)\frac{1-e^{-N\zeta}}{1-e^{-\zeta}}\right] \tag{3.43}$$

this equation estimates the absorption in the non-saturation region (small N).

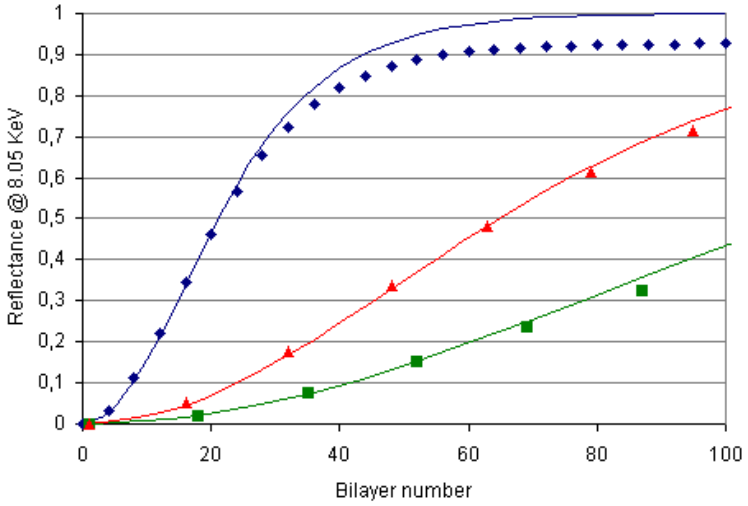

Figure 3.6: Reflectivity at 8.05 keV of a Ni/C multilayer with d = 4 nm (zero-roughness model): comparison of the IMD complete calculation (markers) to the results of the eq. 3.35 (solid lines). The blue line is calculated for the 1^{st} Bragg peak (4112") assuming a value $\Gamma = 0.375$; the green line is the calculated reflectivity at the 2^{nd} peak (8018") for the same value of Γ, the red line represents a calculation assuming a value $\Gamma = 0.1$ at the 1^{st} Bragg peak (4054"). The number of periods necessary to saturate the reflectivity decreases as Γ approaches 0.5 and for lower peak orders.
The agreement of the model to the complete calculation is good far from the saturation region, where the absorption (mainly caused by the Nickel layers) becomes important.

In the saturation region an exact, analytical calculation is not simple: however, the scale length for photoabsorption can be fixed by defining another number of bilayer N_{max} as the number of bilayers necessary to absorb the incident beam when the Bragg law *is not satisfied*: in this case, the incident beam is not reflected but travels across the multilayer stack, the photons are thus gradually absorbed by the multilayers materials; as the absorber thickness crossed per bilayer is roughly $d\Gamma/\sin\theta_i$ and (neglecting the β_l contribution) the intensity attenuation coefficient is $4\pi\beta_h/\lambda$, the beam decays typically after a number N_{max} of bilayers

$$N_{max} \approx \frac{\sin\theta_i\lambda}{4\pi\beta_h\Gamma d} \tag{3.44}$$

hence, the maximum depth reached by the incident X-rays is $N_{max}d$. It is possible, however, that $N < N_{max}$: in this case all bilayers are effective, and the X-rays pass through the whole multilayer (to be eventually absorbed in the substrate). In the last case we can assume $N_{max} \simeq N$.

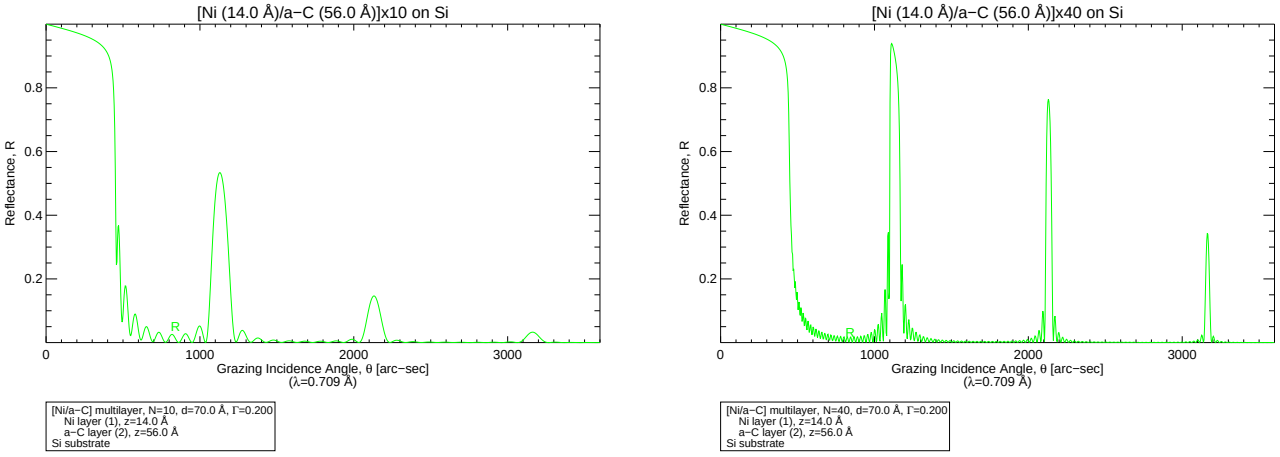

Figure 3.7: IMD simulation of reflectivity in a Ni/C multilayer coating at 0.709 Å: 10 bilayers (left) and 40 bilayers (right). The increase in the bilayer number has improved the reflectivity at the Bragg peaks and it has made them narrower. The secondary peaks are strongly reduced because of the increased number of interfering phases.

Far from the Bragg peak, the reflectivity is almost-zero if:

$$2dN_{max}\sin\theta = m\lambda \tag{3.45}$$

where $m \neq kN_{max}$ for all k: in fact, in this case the reflected waves by the layers where the reflection takes place have phases which form an almost-closed polygon, so the resulting amplitude is almost-zero[8]. This means that there must be $N_{max} - 1$ minima between two consecutive Bragg peaks, and consequently $N_{max} - 2$ secondary maxima (and this suggests a method to estimate N_{max}).

Note that the presence of clear secondary peaks is usually an index of a good regularity in the periodic structure and of a good single-boundary reflectivity[9]. The distance between the first zeroes ($m = N_{max}k \pm 1$) around the first Bragg peak is thus

$$\Delta\theta = \frac{\lambda}{dN_{max}\cos\theta} \tag{3.46}$$

as a consequence, the resolving power will be the same as that of diffraction grating:

$$\frac{\lambda}{\Delta\lambda} = \frac{\lambda}{\Delta\theta}\frac{\Delta\theta}{\Delta\lambda} = \frac{1}{2}N_{max}k \tag{3.47}$$

we can conclude that *a large number of effective bilayers reduces the peak width* both in energy and angular scan. This in turn increases its resolving power. Multilayers with a high resolving power must so have a single boundary reflectivity r very poor in order to keep a large number of effective bilayers (e.g. C/C multilayers (see bibl. [67]). For astrophysics applications, the mirrors must instead have a good reflectivity rather than a good resolution: in their design it is important to choose a couple of materials that guarantees a high single-boundary reflectivity.

[8] this can be seen using the formalism showed in the last paragraph: in this case the recursive formula becomes $\alpha_n = \gamma - \alpha_{n-1}$. Hence, α_N oscillates between α_0 and $\gamma - \alpha_0$ for increasing N, so reflectivity oscillates between the substrate' and $r^2\sin^2[\pi\Gamma(k+1/2)]$

[9] even if they are difficult to be detected when N is large, since their distance can be less than the instrument angular resolution

Finally, the condition to have high-reflectivity multilayers is

$$N_{min} < N \ll N_{max} \tag{3.48}$$

where N_{min} is intended as order of magnitude. These inequalities are usually verified for the first peak if the incident photons are far from absorption edges of both absorber and spacer: for the higher order peaks, the situation is quite different because they require a much larger bilayer number than the first one.

This fact is easily explained by the fall of the single-boundary reflectivity r, which decreases approximately as $\sin^{-2}\theta_i$ in grazing incidence (see eq. A.20). Without taking into account the Γ factor effect, in order to reach a (theoretical) reflectivity of about 1 at the kth Bragg peak a larger bilayer number N^k_{min} would be required:

$$\frac{N^k_{min}}{N^1_{min}} \simeq \frac{r(\theta_1)}{r(\theta_k)} \simeq \frac{\sin^2\theta_k}{\sin^2\theta_1} \simeq k^2 \tag{3.49}$$

this is, by the way, the reason why the higher order peaks are narrower than the first one. Thus, the inequality $N^k_{min} < N$ can be no longer satisfied. Supposing, however, that the bilayer number is large, the beam will travel across $k^2 N^1_{min}$ absorbing layers. The crossed absorbing thickness L_k will then be, as $\sin\theta_k \approx k \sin\theta_1$,

$$L_k \simeq \frac{N^k_{min} d_h}{\sin\theta_k} \simeq \frac{N^1_{min} d_h}{\sin\theta_1} k = k L_1 \tag{3.50}$$

that is, at the kth Bragg peak the photons travel through an absorbing path k times larger: consequently, considering also the eq. 3.44, the attenuation at the kth Bragg peak is roughly

$$R \simeq R_N e^{-\frac{N^1_{min}}{N_{max}} k} \tag{3.51}$$

where R_N is the absorption-free reflectivity. The absorption is thus larger for increasing k peak order[10], contributing to the decrease of the peak reflectivity with increasing k.

Considering the case of the reflectivity model in fig. 3.6 for the 1^{st} peak with $\Gamma = 0.375$ (blue line), and assuming for Nickel at 8.05 keV the value $\beta_h = 5.1 \times 10^{-7}$, we obtain from the eq. 3.36, $N_{min} \simeq 24$, from the eq. 3.44 $N_{max} \simeq 319$, the eq. 3.51 returns a reflectivity R $\simeq$ 92 % in the saturation region at the first peak, in good agreement with the numerical calculation. At the second peak (green line), with the same Γ value, $N_{min} \simeq 96$, $N_{max} \simeq 638$ and the achievable saturation reflectivity is R $\simeq$ 84%.

[10]However, *another cause of the decay of a real multilayer reflectivity decrease with increasing peak order is the X-ray scattering caused by interfacial microroughness* (see sect. 3.5.2, page 66). From the eq. 2.21 formula it follows that the higher-order peaks are more sensitive to the roughness, because they are located at larger grazing incidence angles.

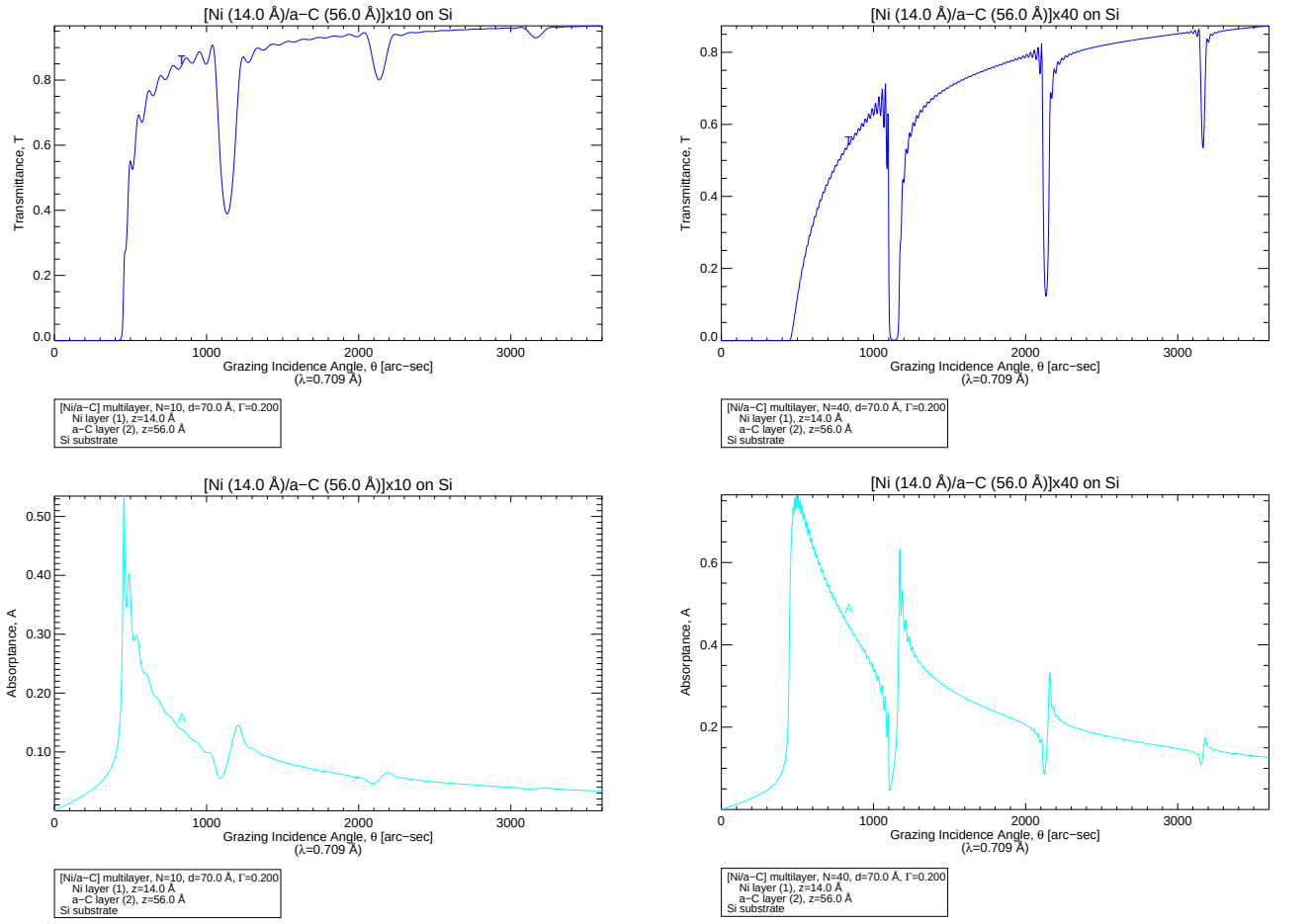

Figure 3.8: IMD simulation of transmissivity (top), absorbance (bottom) in a Ni/C multilayer coating at 0.709 Å: 10 bilayers (left) and 40 bilayers (right). The transmitted beam in correspondence of the Bragg peaks is less intense but it is larger for higher peak order. The absorbed beam decreases with the incidence angle but it is more intense at high order Bragg peaks.

The dependence of N_{max} on Γ^{-1} explains why quarter-wave stacks ($\Gamma = 0.5$) are seldom used as X-ray multilayers: in quarter-wave structures the absorber thickness is so large that the beam absorption is often too intense to reach high reflectivities, even if all the wavelets reflected by all the boundaries would be added in phase (see eq. 3.35). For instance the optimal Γ value in *normal incidence* is given by the analytical formula (Vinogradov and Zeldovich 1977):

$$\tan \pi\Gamma = \pi \left[\Gamma + \frac{\beta_l}{\beta_h - \beta_l} \right] \tag{3.52}$$

(see bibl. [44]). True quarter-wave stack are instead the natural crystals, as their reflecting boundaries are the atomic planes in vacuum (the only non-absorbing medium).

Detailed calculations can be done numerically (e.g. with IMD) by taking into account the X-ray absorption (using the complete recursion method including also the imaginary part of the refractive indexes) and some results are shown in fig. 3.7: it is interesting to observe how the absorption is important especially immediately *after* the Bragg peaks. The observation of reflectivity at many peaks gives so very useful clues in the understanding of the multilayer coating structure in its depth.

3.3.3 Electric fields in a periodic X-ray multilayer

The reflection taking place in a multilayer coating is different from the reflection process in a single, thick layer. The reflection does not take place at the interface vacuum-mirror but in a large fraction of the multilayer stack, and the multilayer behaviour is strongly conditioned by the distribution of electromagnetic energy in the multilayer depth.

The figure 3.9 shows a simulation of electric field intensity distribution in an example multilayer in Mo/Si with 100 bilayers, $d = 6.9nm$ and $\Gamma = 0.4$, at the first Bragg peak incidence. The most relevant feature is the formation of a *standing wave* in the ambient and in the stack with a variable amplitude, as the amplitudes of the incident and reflected wave change at every layer. The standing wave is very important in the ambient where the wave is reflected, and its amplitude is an index of an effective reflection.

An analytical expression for the electric fields in a multilayer stack may be found in the literature (see e.g. Vinogradov, Kozhevnikov, Zeldovich, see bibl. [68]). In particular, we may expect that in the Bragg reflection conditions the incident beam intensity will be reduced by the progressive reflection taking place at each interface (and, in a lesser extent, by the photoabsorption). In the approximation of an infinite number of bilayers the Floquet's theorem holds (the analogous of the Block's theorem for massless particles) and it states that in a periodic potential with period d the wave function may be written as:

$$E(z) = e^{i\eta z} u(z) \tag{3.53}$$

where u(z) *is a periodic function of d*, and the wavenumber η is complex. This result is valid in approximation of an *infinite* multilayer. In particular, the imaginary part of η is responsible for the extinction of the electric field while travelling through the multilayer stack; the real part of η is instead the phase shift of waves reflected by two boundaries at a distance d; if the Bragg condition is satisfied, $2Re(\eta)d$ is an integer multiple of 2π.

In the following we will derive a very approximate (but very practice) expression for the functions u(z) and η in Bragg incidence. Let us orient the x-axis parallel to the multilayer surface and the z-axis normal to surface, pointing in the stack: the X-rays incide in the xz plane, at the k^{th} Bragg incidence angle; the interference of the incident and reflected radiation field (neglecting the refractive correction) is then:

$$\underline{E}(x,y,z,t) = \underline{E}_n^+ e^{i\omega t - \frac{2\pi i}{\lambda}(x\cos\theta_i + z\sin\theta_i)} + \underline{E}_n^- e^{i\omega t + \frac{2\pi i}{\lambda}(x\cos\theta_i - z\sin\theta_i)} \tag{3.54}$$

where $\underline{E}_n^+$ (incident) and $\underline{E}_n^-$ (reflected) are complex vectors (in order to account for the phase shift between them, also variable with the layer number n). We choose the s-polarization, so that the electric field is continuous at all the interfaces and the incident and reflected field are parallel: their interference is obtained from the sum

$$E^s(x,y,z,t) = e^{i\omega t - \frac{2\pi i}{\lambda} x\cos\theta_i}\left[E_n^{s+} e^{-\frac{2\pi i}{\lambda} z\sin\theta_i} + E_n^{s-} e^{+\frac{2\pi i}{\lambda} z\sin\theta_i}\right] \tag{3.55}$$

the overall field varies sinusoidally in the x direction, but it varies also in the z direction with intensity

$$I^s(z) = |E_n^{s+}|^2 + |E_n^{s-}|^2 + 2Re\left[E_n^{s+} E_n^{s-*} e^{-\frac{2\pi i}{\lambda_z} z}\right] \tag{3.56}$$

describing a partial standing wave with a wavelength

$$\lambda_z = \frac{\lambda}{2\sin\theta_i} \tag{3.57}$$

thus, the Bragg law takes the form $k\lambda_z = d$.

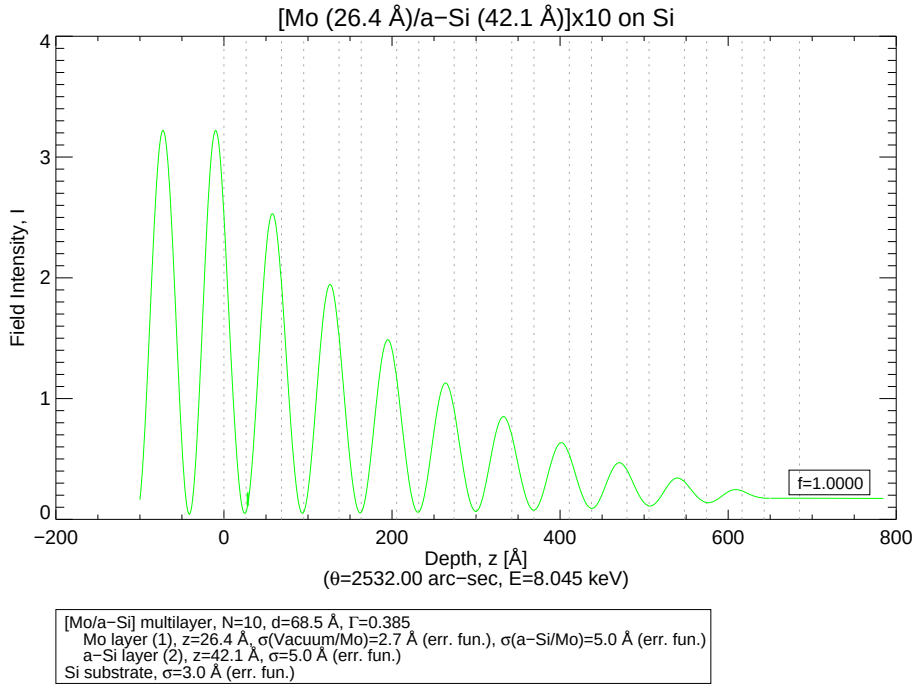

Figure 3.9: IMD simulation of the X-ray electric field intensity at 1.541 $\AA$ (s-polarized) in a Mo/Si multilayer film with 10 bilayers, d=68.5 Å, $\Gamma = 0.4$, at the first Bragg peak (2532"). The X-rays incide from the left.

The field distribution is determinated by the values of E_n^{s+} and E_n^{s-} in every layer. However, we know that the ratio of the reflected and incident amplitude at the kth Bragg peak in the (n+1)th bilayer is $\mathcal{R}_n^s$, as in the equation 3.33, in a non-absorbing multilayer with a high bilayer number N:

$$\frac{E_{n+1}^{s-}}{E_{n+1}^{s+}} = \mathcal{R}_n^s = ie^{-i\pi k\Gamma}\tanh(n\xi) \tag{3.58}$$

where $\xi = 2r\sin(\pi k\Gamma)$, if n is not too small. We can so write that in the (n+1)th spacer layer the s-polarized field amplitude at the kth Bragg peak is

$$E_l^s(z) = E_{n+1,l}^{s+}\left[e^{-\frac{\pi i}{d}kz} + i\tanh(n\xi)e^{+\frac{\pi i}{d}kz - i\pi k\Gamma}\right] \qquad \textit{(spacer)} \tag{3.59}$$

in the assumed approximations a similar behaviour may be assumed in the absorber, considering the multilayer as the succession of spacer/absorber layers instead of absorber/spacer[11]: the reflectivity calculation may be done simply substituting $\Gamma \to 1-\Gamma$, $r \to -r$ and

$$E_h^s(z) = E_{n+1,h}^{s+}\left[e^{-\frac{\pi i}{d}kz} + i\tanh[(n+1)\xi]e^{+\frac{\pi i}{d}kz - i\pi k\Gamma}\right] \qquad \textit{(absorber)} \tag{3.60}$$

the reflected ray is enhanced by the addition of the n+1th absorber layer, which is the true responsible for the reflectivity increase, then the tanh function has now the argument $(n+1)\xi$ instead of $n\xi$.

[11]The difference is negligible if the transmitted wave vanishes before reaching the substrate of the multilayer film.

For the following spacer layer a similar equation as the eq. 3.59 holds. From the field continuity at the absorber/spacer boundary it follows $E^{s+}_{n,h} = E^{s+}_{n+1,l}$: we can indicate by I^{s+}_n the common value of the transmitted electric field in the n^{th} absorbing layer and in the following spacer (n^{th} bilayer). The spacer/absorber transition, i.e. the transition from the $n/n+1^{th}$ bilayer, must also satisfy the energy conservation:

$$I^{s+}_{n+1} - I^{s+}_{n+1}\tanh^2[(n+1)\xi] = I^{s+}_n - I^{s+}_n \tanh^2(n\xi) \tag{3.61}$$

which is simply the equality of the energy inlet and outlet in the nth bilayer. This equation is the same as:

$$\frac{I^{s+}_{n+1}}{I^{s+}_n} = \frac{\cosh^2[(n+1)\xi]}{\cosh^2(n\xi)} \tag{3.62}$$

if N is very large, and $n \gg \xi^{-1}$, $\cosh(n\xi) \approx e^{n\xi}$, thus

$$\frac{I^{s+}_{n+1}}{I^{s+}_n} = e^{2\xi} \tag{3.63}$$

by recursion it is easy to arrive in N-n+1 steps to $I^{s+}_{N+1} = I^s_0$ (the incident, s-polarized beam), and

$$I^{s+}_n = I^s_0 e^{-2(N-n+1)\xi} \tag{3.64}$$

and the s-polarized field amplitude in the nth bilayer can be represented by the equation (neglecting a phase factor)

$$E^s(z) = E^s_0 \left\{ e^{-\frac{\pi i}{d}kz} + i\tanh[(n+1)\xi] e^{+\frac{\pi i}{d}kz - i\pi k\Gamma} \right\} e^{-(N-n+1)\xi} \tag{3.65}$$

as the expression in the { } brackets is a periodic function with period d, if we set $Im(\eta) = \frac{\xi}{d}$ and $Re(\eta) = \frac{\pi k}{d}$, we recover the Floquet's theorem (see eq. 3.53).

The s-polarized field intensity in the stack has the approximate expression

$$I^s(z) = I^s_0 \left[1 + \tanh^2(n\xi) - 2\tanh(n\xi)\sin\frac{2\pi}{d}k\left(z - \frac{\Gamma d}{2}\right)\right]^2 e^{-2(N-n+1)\xi} \tag{3.66}$$

the minima of intensity are so located at

$$z_m = \frac{\Gamma d}{2} + (4m+1)\frac{d}{4k} \tag{3.67}$$

in the last bilayers $\tanh(n\xi) \approx 1$, thus the minima are very near to 0. The intensity maxima are located in the middle of two consecutive minima: in every bilayer the field has so k maxima and k minima, see fig. 3.9: the standing wave has a larger amplitude at the surface and decays exponentially in depth. An increase of the standing wave minima indicates that a significant fraction of the incident beam is transmitted through the stack.

For the p-polarization the calculation may be repeated, remembering that in this case the electric field is not continuous at the interfaces, but the normal component of $\underline{D}$ is: nevertheless, as ϵ_r differs very slightly from 1, the discontinuity at the boundaries is usually small. In this case (in grazing incidence, $\theta_i < \theta_{pol}$) r is to be replaced with -r and the eq. 3.67 locates the intensity maxima.

As the p and s intensity do not interfere but simply sum, the resulting electric field pattern for a non-polarized X-ray reflected in grazing incidence ($I^s_0 = I^p_0 = I_0/2$) is

$$I_n = \frac{I_0}{2}2[1+\tanh^2(n\xi)]e^{-2(N-n+1)\xi} \approx^{n\gg\xi^{-1}} 2I_0 e^{-2(N-n+1)\xi} \tag{3.68}$$

since the interference terms are cancelled in the sum and $\tanh^2(n\xi) \approx 1$ for $n \gg \xi^{-1}$. In this approximation the field intensity is constant in every bilayer and decays exponentially in the stack in a typical bilayer number of $(2\xi)^{-1}$.

In normal incidence the incidence angle is larger than the Brewster angle and the phase inversion rules are the same for both polarizations: as a consequence, also a non-polarized beam will be described by the eq. 3.66[12], with the typical succession of maxima and minima.

3.4 Graded multilayers

3.4.1 Supermirrors

Multilayer mirrors for astrophysical use must have a wide band of reflection : this may be obtained by varying the thickness of the layers along the stack (*graded multilayers*). In such a way, for every wavelength in the reflected band the Bragg law is approximately satisfied in a different fraction of bilayers of the coating (see fig. 3.11), so that the narrow and high peak, typical of periodic multilayers, disappear, but the reflectivity is considerable in an angular/energy band which can be 3-4 times larger than the achievable ons with single-layer coating. Graded multilayers (in visible wavelengths) and many other interferential optical coatings are fairly common in nature (in plants, butterflies, birds... see e.g. bibl. [47]).

The reflectivity of a graded multilayer can be calculated using the recursive theory (see sect. 3.3, page 47) using numerical methods or a specific code (e.g. IMD). The inverse problem (that is, the determination of the structure that returns a definite reflectivity curve) is, indeed, much more complex.

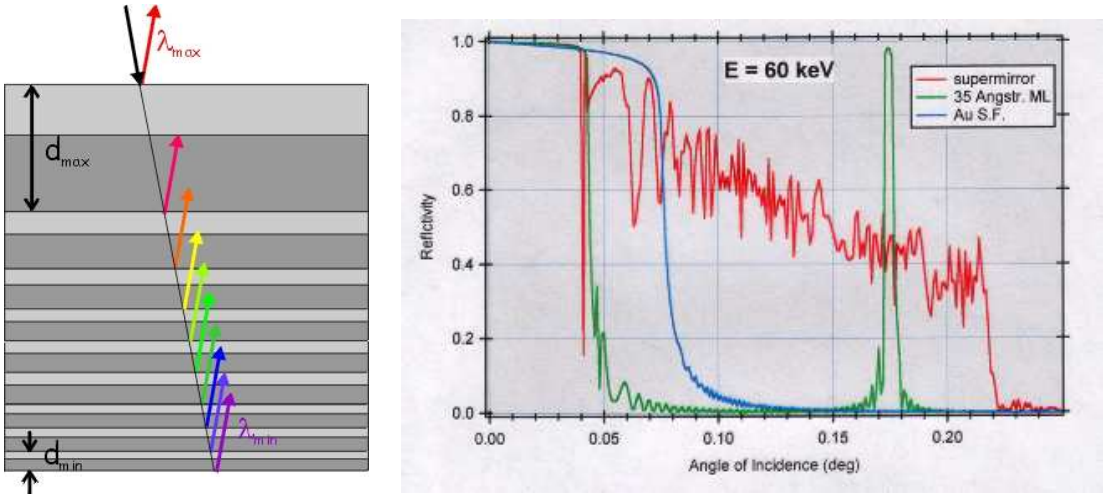

Figure 3.10: (left) Scheme of a graded multilayer: the bilayer thickness (d-spacing) is decreased going from the top to the bottom of the stack: the shortest wavelength are reflected in the deepest bilayers (credits: *D. Windt*).
(right) A comparison of the angular reflectivity plot of multilayer mirrors at 60 keV. The green line represents the reflectivity of a periodic Ni/C multilayer with period 3.5 nm: beyond the total reflection regime, the reflectivity is large only at the Bragg angles. The red line is the reflectivity of a graded multilayer (supermirror): in this case the reflectivity is good in a wide angular range.

[12]Note that the high reflectance of a multilayer coatings depends on the ability of placing the absorbing layers in the nodes of the standing wave so that the absorbed power is minimum, and filling the remaining space with a low-absorption material (as suggested first by Spiller in 1972).

The design of a broad-band reflecting X-ray mirror depends on the chosen *figure of merit* (FOM). In our design the figure of merit is the integrated effective area in a definite band, starting to a typical design aimed to obtain a as more as possible *flat* reflectivity as a function of the incident energy.

For simplicity, the Γ factor is kept constant and the d-spacing trend in the stack $d = d(k)$ (where k is the bilayer index from the top of the stack) may be assumed to be monotonic: it is evident, moreover, that the thinnest layer will be the most deep in the stack, because the hardest X-rays are less affected by the photoabsorption and they can better stand the crossing of the first layers, which may be devoted to the softer X-rays reflection. The function d(k) must so be *decreasing*.

The most simple assumption for d(k) could be linear: but, as a consequence of the equation 3.35 the number of necessary bilayers to reflect a wavelength λ is proportional to $r(\lambda)^{-1} \propto \lambda^{-2}$, roughly; thus, for a fixed N and Γ, the number of thin layers has to be larger than that of thick layers. The d function must so deviate from the linear trend and be a convex function: the most simple function is then a *power-law* (Joensen, 1995):

$$d(k) = \frac{a}{(b+k)^c} \tag{3.69}$$

with a, b, c variable parameters: the eq. 3.69 defines a *supermirror*, concept introduced first for the neutron mirrors[13] by Mezei in 1988 (see bibl. [60]) and after developed by Joensen et al. (1993) for X-ray astrophysics. The parameter a is usually determined by the maximum wavelength to be reflected: in particular, from the Bragg law, a may be estimated approximately as $a \simeq \frac{\lambda_{max}}{2\sin\theta}$. The b and c parameters are obtained from the maximization of the figure of merit: in our optimization study for the XEUS mirrors we obtained $-1 < b < 0$ and $c \simeq 0.25$ (see bibl. [95]). The number of bilayers (> 100) is obviously often much larger for graded multilayers than for the periodic ones. Consequently, supermirrors are a viable solution only provided that the photoelectric absorption is not too high (only over 10 keV).

3.4.2 Multilayer design and optimization

A simple way to design broadband mirrors is based on making a superposition of some periodic multilayer stacks for different wavelengths. If the blocks are well designed good optical performances may also be reached (see bibl. [44]). If, instead, the energy band is very wide and the number of bilayers cannot be kept too large, a numerical calculation is necessary in order to find the maximum performance with the minimum number of bilayers.

The problem of the *optimization of multilayers* can be faced with the numerical approach; the multilayer structure is determined by a number of free parameters. The reflectivity curve is so obviously function of these parameters, which in turn affect the figure of merit (FOM): if our aim is the maximization of the effective Wolter I area in the hard X-rays, the FOM will be the integrated squared reflectivity between e.g. 20 keV and 50 keV, so (provided that we adopted the supermirror design) we have to find the parameter set value a, b, c, Γ which *maximizes* the FOM. If we are instead interested in achieving a precise reflectivity pattern (e.g. a flat reflectivity between 20 keV and 50 keV), the supermirror design is not suitable and we must take as free parameters the thickness of every layer of the stack. In this case, the aim of returning a as-flat-as-possible reflectance is translated in the *minimization* of a FOM which is the χ^2 of the modeled reflectivity compared to the desired one. If the reflectivity pattern R_m to be reached is complex (top-hat,

[13] Multilayer coatings ^{58}Ni/Ti are widely used in nuclear physics to reflect thermal neutrons ($E_K \sim 1eV$), that have a De Broglie wavelength in the range of hard X-rays

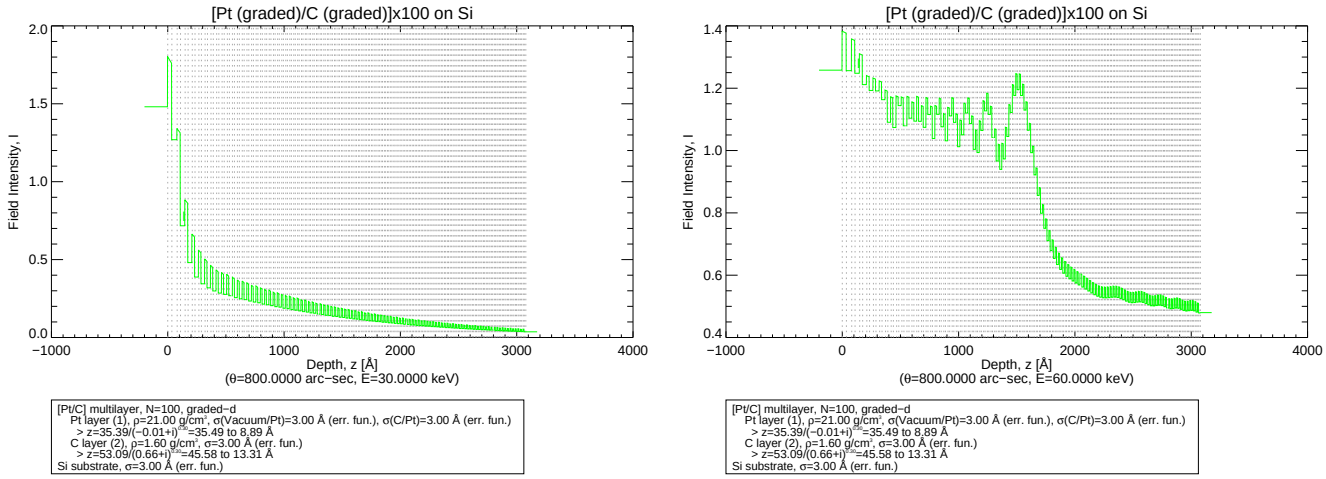

Figure 3.11: IMD simulation of the Electric field trend in a supermirror Pt/C multilayer film with a=35.39 Å, b = -0.1 c =0.3 for the Pt and a = 53.09 b=0.66 c=0.3 for the C. The X-ray beam is non-polarized and incides from the left, at a 800" grazing angle. The photon energies are 30 keV (left) and 60 keV (right). The ray propagates almost unperturbed since it encounters layers satisfying the Bragg law, and it is back-reflected. The intensity drops steeply in correspondence of the reflection point: the 60 keV beam is reflected in deeper regions of the stack.

gaussian, notch filters) a similar FOM can be adopted using the logarithm of the reflectivities:

$$\chi^2 = \sum_i \frac{(\ln R_i - \ln R_m)^2}{\ln R_m} \tag{3.70}$$

in all cases the problem is reduced to a multi-parametric minimization or maximization procedure, for which many algorithms have been developed, based on many different approaches, each according to a different FOM definition.

This way of facing the problem is in principle very fruitful as a very wide set of possible solution can be explored, but it is complex to be implemented:

1. first of all, the reflectivity derived from the multilayer structure must be performed with some assumptions about some layer features (like the material density, microroughness, interdiffusion..., see sect. 3.5, page 63) that strongly affect the mirror performances and which are seldom predictable;

2. the FOM usually depends on a number N of parameters: this means that the minimization takes place in a N dimensional space and the search for the minima will be very time-consuming. A well known minimization method is the *amoeba* algorithm, or *downhill simplex* (see e.g. bibl. [105]), consisting in a series of partially random moves of a set of N+1 points in the N-dimensional space, following the "FOM gradient", step after step;

3. the numerical codes are usually able to find the *local minima*: the programs are usually designed to converge along the FOM gradient, but once found a convergence point, they cannot escape from the found minimum. We cannot so be sure that a lower minimum has been neglected, that is, that a best fitting solution than the found one exists.

The problem of local minimization is a very common problem, and a number of codes has been developed to reduce this risk. In particular, we cite the *iterated simplex* (see bibl. [105], bibl. [74]), consisting in a

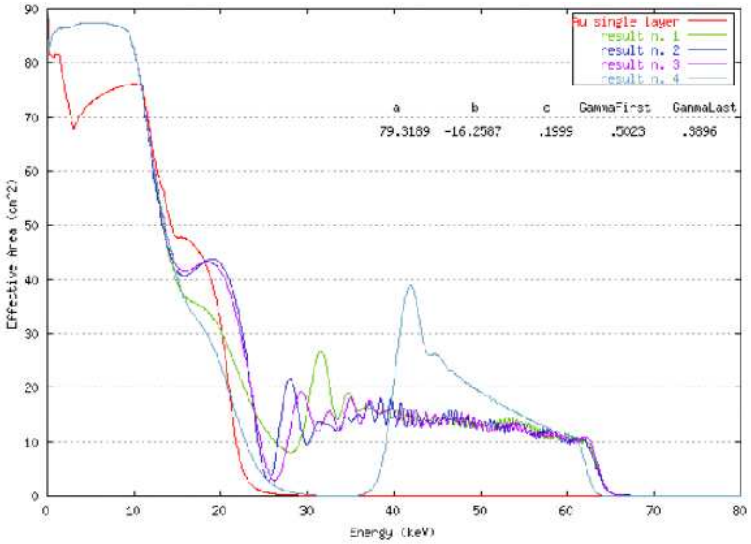

Figure 3.12: Optimization of a W/Si multilayer coating for a mirror shell for the XEUS optics (see sect. 3.7.4, page 87). The baseline for the design is a *supermirror* described by the parameters a, b, c and Γ (this is assumed to be slowly drifting along the stack). The incidence angle is fixed at 779" and the roughness rms is assumed to be 4.5 Å, and different solutions are found for the effective area as a function of the photon energy. The showed solutions (marked as result 1..4), representing different minima for the chosen FOM (the collected photon energy in the 0 ÷ 70 keV energy range), are obtained from the *iterated simplex* procedure: every minimum has been obtained starting from very different initial parameters, so that the likelihood of falling in the same local minimum is strongly reduced. The effective areas are compared to the achievable ones with a single Au layer. The most performant solution parameters are reported in figure (credits: bibl. [105]).

restart of the amoeba algorithm with different initial parameters when a local solution has been found: this method has been used to find a multilayer design for the HEXIT and for the XEUS optics (see fig. 3.12); another global minimization method is the *downhill annealing* (see bibl. [106]), which is described in the chapter 9. The downhill annealing has been also implemented in the reflectivity-fitting program PPM (see bibl. [141]) with very good results. A further approach has been done with the implementation of *genetic algorithms* (see fig.3.13, see e.g. bibl. [108], bibl. [109]), a very powerful algorithm family, successfully used in many domains of Science.

The problem of multilayer optimization is very similar to the problem of *fitting* an X-ray reflectivity scan of an existing multilayer structure: this task can be non trivial in real cases since the all the parameters (densities, thickness, roughness) may vary along the stack in a non-foreseeable way: usually code like IMD (see bibl. [103]) is used for the modelization of a multilayer structure to be compared to the experimental curve, but the modelization leaves room to a large ambiguity since the number of involved parameters may be very large. A more powerful code like PPM allows the exploration of a much larger set of possible solutions, using an optimization approach. The set of stack parameters is fully explored in order to minimize the FOM (eq. 3.70) and find so a solution that reproduces well the experimental reflectivity scan.

It is worth noting, indeed, that the problem of local minimization can be much more critical in the case of fitting than in optimization; not only because the optimization usually operates on the supermirror model, described by a small number of parameters, but also because also a local minimum can return a satisfactory solution, even if it is not the best one. When fitting an existing multilayer, instead, a local minima can return a similar plot to the experimental one adopting non-realistic parameter values.

Finally, we note that in order to avoid the risk of local minimization and since the layer distribution (as computed by the numerical procedures) is often strongly oscillating, a different, *analytical* approach has been recently offered by Kozhevnikov (see bibl. [69], bibl. [71]).

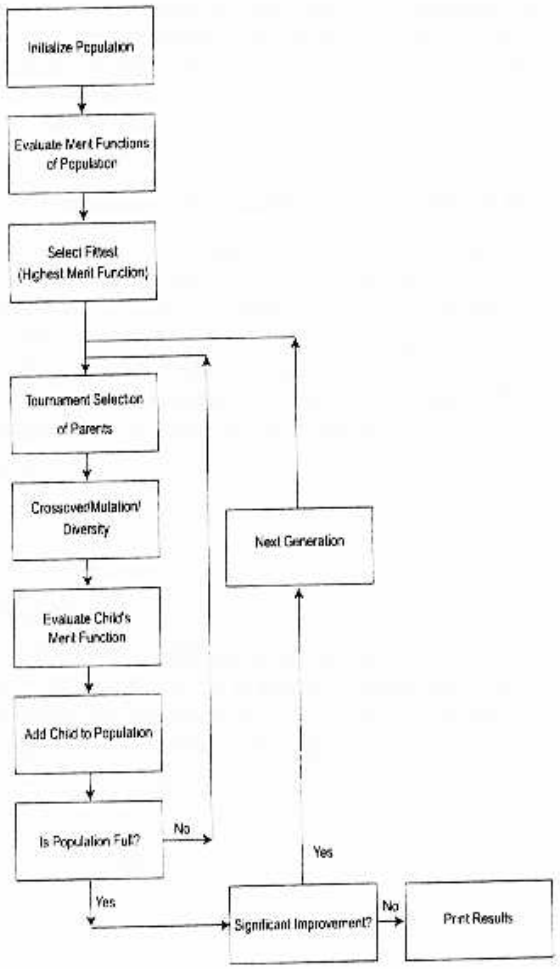

Figure 3.13: A general scheme for Genetic Algorithms. The problem is at first encoded is a chromosome or a a system of chromosomes. Every chromosome takes a set of genes, each representing a problem parameter, to be optimized. Every gene carries a character (its value) and the selection of the most performant problem solution (on the basis of the FOM maximization/minimization) is translated to the selection of the most fitted individuals, that are destinated to survive, from a Darwinian viewpoint. Starting from an initial random solution of individuals (random values for the parameters), some genetic operators (selection, crossover, mutation) are used to process the population and to select those individuals that at each iteration represent the better solution. The following combination, selection and mutation of the survivors converge to the global minimum by improving the genetic pool (credits: bibl. [107]).

3.5 Multilayer films defects

The exposed results in the previous sections supposed the multilayers to be constituted by ideal structures (homogeneous films, either single-crystalline or amorphous, abrupt and smooth film boundaries): however, we have already seen in the sect. 2.2.4 (on page 24) that the surface microroughness is able to destroy a single-layer X-ray reflective coating, and this is even more true for interferential coatings like multilayers; the interlayer microroughness has analogous effects to the X-ray reflectivity (see fig. 3.17) and this is only one of the problems to be faced when we are dealing with *real* multilayers. The development of multilayer defects mainly arises during the deposition: however, the film quality is degraded with time after the deposition: this process is called film *ageing* and it can be accelerated by thermal, electrical, mechanical shocks, or by exposition to radiation. The film quality, indeed, is strongly influenced by the chosen deposition method and, in a large extent, depends on the operational parameter set (pressure, temperature, deposition rate, reactive environment, beam directionality,...).

In fact, thin film growth is a very wide and complex field, and growth process is very difficult to be fully understood, even more to be kept under control; as thin films have applications in virtually all the optical technology fields and in the nanoelectronics (see sect. 3.8, page 92), and since the conflict of the theory with real coating performances are caused by the non-ideal coating structure, the thin film defects reduction is one of the most challenging problems of the next years optical technology development.

A first classification of the thin film deposition method may be done as *Physical Vapour Deposition* (PVD) whenever the film deposition is produced by the condensation of a vapour in supersaturation conditions on a substrate, and *Chemical Vapour Deposition* (CVD) when the film formation is produced by chemical reactions, activated by the contact to the substrate. In the chapter 4 some thin film deposition methods will be exposed: the choice of a suitable deposition method is crucial in the determination of the final coating properties. Some outlines of the general features of the thin film growth defects will be provided in the next pages.

3.5.1 Bulk defects

The film deposition under vacuum is a non-equilibrium and unstable process, in presence of impurity atoms (the residual atmosphere) at almost the same concentrations as the depositing atoms. The properties of the deposited material may so be very different from the bulk properties of the same material, and they are strongly influenced by the deposition temperature T_s and deposition pressure p_v. The temperature and pressure scales are fixed by the film melting temperature T_m and by the saturation vapour pressure p_s at the substrate temperature T_s:

$$T^* = \frac{T_s}{T_m} \qquad\qquad R = \frac{p_v}{p_s} \tag{3.71}$$

In real cases, the vapour condensation is very quick (R$\sim 10^5 - 10^6$) and as the deposition beginning the atoms cannot rearrange in a stable, crystalline structure with a minimum energy: they find so an amorphous, metastable state in *nucleation islands*: when the film reaches a critical thickness (*percolation length*, between 1 and 20 nm), the islands come into contact and an explosive crystallization occurs.

After this phase transition, films take a *polycrystalline* structure (visible with high resolution TEM images), where every crystal is often surrounded by impurity atoms. The atoms often enclose also voids, filled with air or water or hydrocarbons, thus the film takes a *porous* structure and its density will be often

less than the bulk value. The density of voids is often expressed by the *packing coefficient*:

$$p = \frac{\rho_f}{\rho_b} \tag{3.72}$$

where ρ_f i the film density and ρ_b is the material bulk density. For X-ray coatings, if the film is porous but isotropic, the film refractive index $\delta_f = 1 - n_f$ is simply proportional to the actual density, that is, to the p parameter: it is possible to include the effect of the finite refractive index of voids n_v (Kinosita and Nishibori, 1969, see bibl. [44]):

$$n_f = (1 - p)n_v + pn_b \tag{3.73}$$

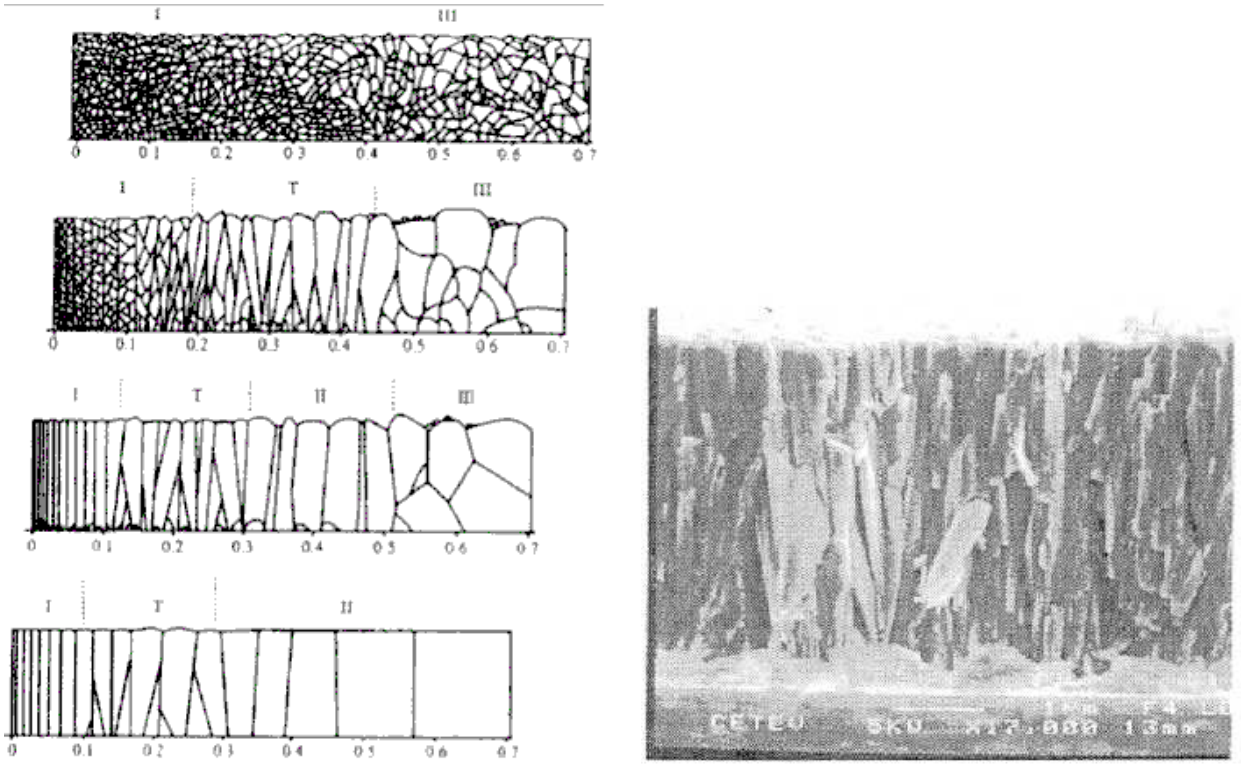

Figure 3.14: (left) Transition scheme from the polycrystalline to the columnar regime, according the Movchan and Demichisin model, 1969 (credits: bibl. [43]). The temperature is increased from left to right; the impurity concentration is decreased from the top to the bottom: low temperature and impurities enhances small polycrystalline film growth.
(right) SEM image showing the columnar growth in a Titanium Nitride layer (credits: Ce.Te.V., Carsoli, Italy).

Often, the polycrystalline growth takes a preferential direction: in this case the sticking atoms on the substrate or on the layer form *columnar structures* (see fig. 3.15); in this growth model, widely studied with the fractal formalism, the adatoms tend to stick more easily at the peaks of the surface features than in the valleys. The result is an amplification of the surface defects and a consequent surface roughness increase. The roughness amplification is a very common process in the multilayer deposition, and this is the reason why it is essential to start from superpolished substrates when depositing smooth, thin films. The amount of columnar growth may be very large in some pressure and substrate temperature ranges; also the irradiation with energetic particles may severely change the film compactness, adhesion, crystallization state.

The formation of columnar structures changes the dependence of the refractive index on the packing

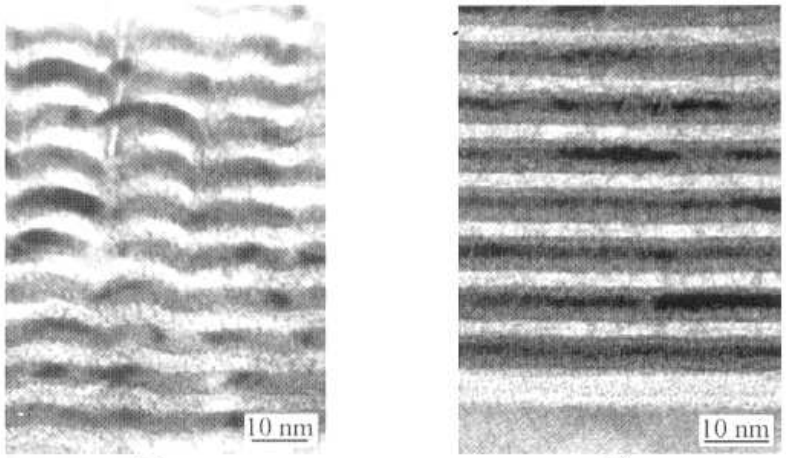

Figure 3.15: TEM images of a Mo/Si multilayer deposited by magnetron sputtering at pressures of 12 mTorr (left) and 2 mTorr (right). In the first case the film shows a strong columnar growth, whereas at lower pressure the layers are continuous; this is probably due to the low energy of the incoming adatoms that do not allow a sufficient surface mobility (from bibl. [43]).

coefficient: a satisfactory model for not-too-packed columns is given by the formula (see bibl. [43])

$$n_f^2 = (1-p)n_v^2 + pn_b^2 \tag{3.74}$$

The crystallization process is only one of the physical processes that occur during the film deposition; the thickness growth is the result of three more factors:

1. *Shadowing:* it is caused by the existing surface roughness, that geometrically interacts with the arriving atoms avoiding the deposition in the regions hidden to the vapour source: the directionality of the vapour flow is typical of the evaporation in vacuum, as the free mean path is usually larger than the distance source-substrate; an high vapour flow directionality is important to obtain smooth and films, because the non-directionality forms shadows, peaks, and voids inclusions. In order to reduce the shadowing effect, the substrate must be *perpendicular* to the atomic flow and the flow divergence must be limited to few degrees with *equalization masks*. This effect dominates at low substrate temperature, $T^* < 0.3$, and leads to the formation of a grained, porous structure;

2. *Surface diffusion:* for $0.3 < T^* < 0.5$, the mobility of the atoms may be larger and they can move along the surface, for instance from a peak to the next valley: high substrate temperature are used to reduce the film roughness, but the mobility does not involve the bulk material, that forms a columnar structure;

3. *Bulk diffusion:* for $T^* > 0.5$, the diffusion involves the bulk material and the film takes a grained structure, supporting amorphous structures with a possible recrystallization: columnar structures are destroyed, and the same occurs when the kinetic energy of the adatoms are larger than 0.3 eV.

The deposition rate also plays an important role; high deposition rate form a large number of fine grains, while a slow deposition produces a rough texture with few, large nuclei. The crystallization is also favoured by decreasing residual gas pressure. Finally, substrate defects act as seeds of rough defects and the presence of impurities has the effect of simulating lower substrate temperatures, with the formation of a rough, polycrystalline, fragmented structure.

3.5.2 Imperfect boundaries: roughness and diffuseness

The bulk defect have an important role in the optical, mechanical performances of thin films: in particular, during the deposition of multilayer films, they result in an increase of the interfacial *roughness* absorber/spacer (see fig. 3.15). The surface microroughness is responsible, as we have seen, for the reduction of the reflectivity of thin film coatings (sect. 2.2.4, page 24) in the specular direction: for multilayer coatings the problem is even more important, as the number of reflecting layers is much larger and the preservation of the phase coherence between layers (which depends on the interface sharpness) is fundamental in order to build up a high reflectivity at large incidence angles.

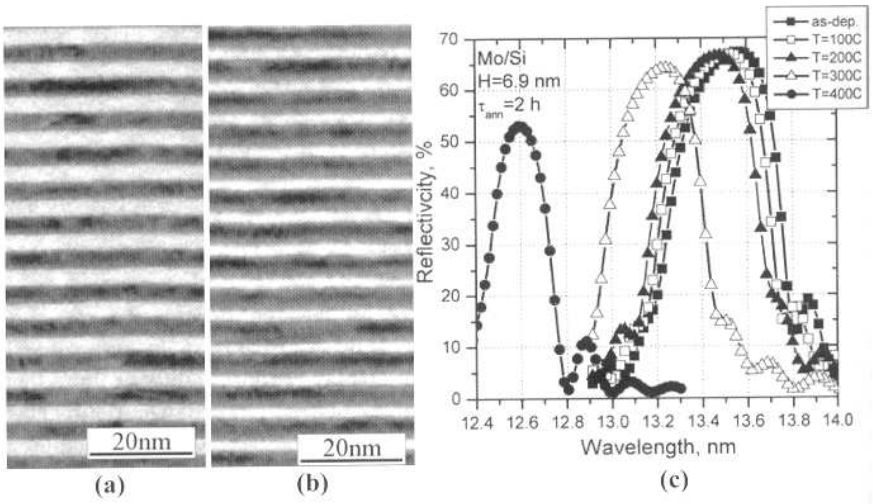

Figure 3.16: TEM sections of a 6.9 nm Mo/Si multilayer after deposition (a) and after a 400 °C for 2 hours (b). After the heating the layers have diffused with formation of Molybdenum Silicide at the boundaries. The optical performances are consequently degradated (c) (from bibl. [44]).

The interface sharpness may be reduced also by the layer *interdiffusion*, a dynamical process that takes place at the layer interface and that creates a intermixing layer between absorber and spacer (see fig. 3.16): typical diffusive processes occur in Mo/Si multilayers, that are used in extreme UV reflectors (see e.g. bibl. [121]). The interdiffusion process has in this case typical time-scales of several days, but it can be accelerated by external factors (like the multilayer overheating). The interdiffusion is often caused by slow chemical reactions at the interlayer boundary.

Multilayer roughness and diffusion have the same effect of reducing the multilayer specular reflectivity. In real multilayer coatings, both roughness and interdiffusion occur, we can define a surface roughness rms σ_r and an interdiffusion rms σ_d: the interface "uncertainty" at each boundary absorber/spacer may be assumed to be

$$\sigma^2 \simeq \sigma_r^2 + \sigma_d^2 \tag{3.75}$$

the σ for diffuse/rough interfaces may be defined as the rms of the variation of the refractive index $n(x, y, z)$ in the multilayer volume. This definition allows to include also the diffusion effects in a generalized form of the reflectivity in grazing incidence (see bibl. [32]):

$$r(z) \simeq \frac{1}{2\sin^2\theta_i}\frac{dn(z)}{dz} \tag{3.76}$$

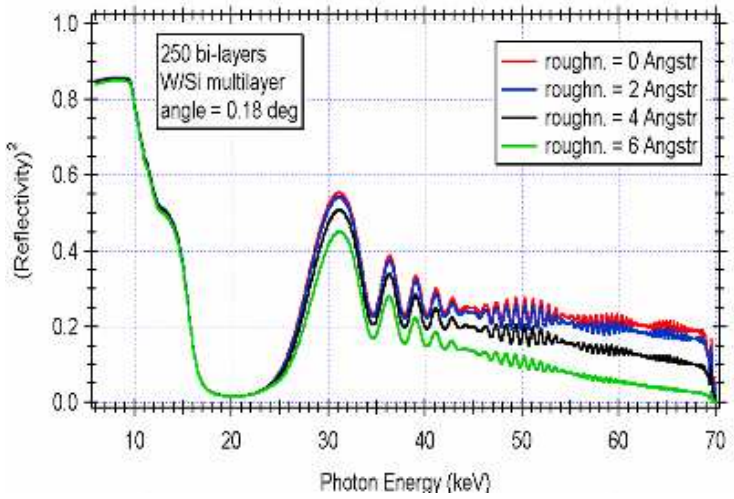

Figure 3.17: Simulation of the roughness action on a W/Si graded multilayer (250 bilayers) reflectivity; for increasing roughness values the reflectivity is affected especially at large photon energies, in agreement with the eq. 3.77

in this case the reflection takes place in a layer around the ideal boundary as a consequence of the refractive index variation: an abrupt variation of the refractive index (no diffusion) will return a delta-like r(z) function whose amplitude is the $\Delta\delta$, the refractive index contrast (and the Fresnel equation for grazing incidence A.20 is recovered).

Moreover, it is possible to derive the reflectivity reduction at *every bilayer* of a multilayer coating with roughness/diffusion σ, absorber/spacer refractive indexes n_h, n_l and incidence angles in absorber and spacer θ_h and θ_l (see bibl. [32]),

$$R_\sigma = R_0 exp\left[-\left(\frac{8\pi^2}{\lambda^2}\sigma^2 n_h n_l \sin\theta_h \sin\theta_l\right)\right] \tag{3.77}$$

called *Névot-Croce formula*. This result is the analogous to the Debye-Waller formula and can be easily derived under the same smooth-surface hypothesis[14], provided that we take the refraction into account (and this is the reason for the presence of the refractive indexes of the two materials).

The effects of the roughness/interdiffusion are thus very similar to those seen in the sect. 2.2.4 in the single-layer case: in this case, however, the Névot-Croce factor is enhanced at the N^{th} power for a multilayer with N bilayers! The reflectivity reduction may compromise seriously the multilayer performance, even in those cases where the single-layer roughness seems to be acceptable. From the eq. 3.77 it is evident, moreover, that the roughness effect is important especially at large incidence angles, i.e. when using *very thin periods*, and *at high photon energies* (see fig. 3.17). The reflectivity reduction is another factor (in addition to the photoabsorption, see sect. 3.3.1, page 48) contributing to the decrease of the Bragg peaks height with increasing k order. A reflection at very shallow angles using large period multilayers may help to reduce the roughness consequences: nevertheless, the use of too shallow angles reduces in turn the mirror effective area, a severe limitation for grazing incidence X-ray telescopes.

Although the roughness and the diffuseness have the same effect of reducing the reflectivity according the eq. 3.77, there are some methods to discriminate their contribution:

[14] this hypothesis allows us to assume that the electric field in the multilayer has not been altered by the presence of the roughness.

1. the presence of rough interfaces destroys the spatial coherence of wavefront sections reflected from different points of the same boundary: as we have seen in sect. 2.2.4, this results in the wave *scattering*. However, the X-ray scattering in a periodic multilayer has different features from the scattering pattern from a single surface, due to the interference of the scattered waves. The scattering is, indeed, a powerful tool to compute the surface roughness PSD of a single surface or that of a multilayer film (see sect. 5.3.1, sect. 5.3.2);

2. the diffusion layer may be though to be the continuous limit of very high frequency roughness; as frequencies over $2/\lambda$ do not scatter (see sect. 5.3.1), the interlayer diffusion does not cause a beam scattering. Consequently, the loss in reflectivity will be compensated by an increase in the transmission; in practice, the single-bilayer reflectivity will be less effective and the reflectivity loss may be *partly* compensated increasing the number of bilayers;

3. a topographic observation of the multilayer surface allows to discover the roughness features that appear at the top of the stack: because of the *roughness growth* from the substrate to the outer surface, the measured roughness with (e.g. an AFM microscope) is an upper limit to the multilayer roughness, but it gives no information about the interdiffusion: the observation of the latter is possible with a TEM section;

4. the interdiffusion *usually* increases in time faster than roughness. The roughness increase with time (multilayer ageing) is mainly caused by *stresses* in the stack (see sect. 3.5.3, page 71).

The case of the Mo/Si multilayer is especially interesting (see fig. 3.16) because of the great interest of this kind of coating in the nanoelectronic component EUV lithography. Even multilayers with very smooth interfaces will always present Mo_xSi_y intermixing layers: a large research of the optimization parameters (see bibl. [121]) has permitted to minimize (1 nm for the Mo-on-Si interface, 0.5 nm for the Si-on-Mo interface) the diffusion but not to eliminate it. The diffusion represents nowadays an intrinsic limit to Mo/Si multilayer reflectivity: a further possibility may be the insertion of ultrathin (few Å) barrier layers (e.g. B_4C, see bibl. [44]) that avoids the contact between the two materials: this design was implemented by several groups, but at the expense of reflectivity.

Roughness growth in a multilayer coating The multilayer growth is characterized by an increase of the interlayer roughness; this is due to both replication of the substrate roughness and a stochastic roughness that takes place during the film growth process. As a consequence, the profile of each profiles will, in a large extent, replicate that of previously deposited layers: however, the interface conformality is not complete.

To understand this point, let us consider at first the growth of a single layer. The roughness growth in a multilayer structure may be expressed by the interface power spectral density (PSD) evolution along the stack (see app. B for the definition and the properties of the PSD), that can be provided by a *growth model* during the deposition or the erosion. Many growth model for a single layer assume a descriptive PSD model, defined by a limited number of parameters: in particular, the observation has lead to the *K-correlation model* (see eq. B.35), mainly based upon the self-similarity, or fractal, theories. This PSD model (see bibl. [79]), may be written as

$$P(f) = \frac{A}{[1 + (Bf)^2]^{C/2}} \tag{3.78}$$

where A is related to the rms roughness and the correlation length l_c is related to B; Note that the PSD is flat up to the corresponding frequency to the correlation length, and after it falls down as a power law.

In an alternative approach (see bibl. [88], bibl. [77], bibl. [78]), the surface profile of a single layer may be described during the growth as a function $z(x, y, \tau)$, obeying to the linear differential equation:

$$\frac{\partial z}{\partial \tau} = -\nu|\nabla^n z| + \frac{\partial \eta}{\partial \tau} \tag{3.79}$$

this equation describes the evolution of the surface profile $z(x, y, \tau)$ as the film thickness τ is increased: the first term is proportional to the n^{th} order derivatives of the surface profile, with a proportionality constant ν that, if positive, tends to smooth the surface profile. The exponent n depend on the considered self-smoothing mechanism (n=1 for viscous flow, n=2 for the condensation of the evaporate, n=3 for bulk diffusion and n=4 for the surface diffusion). A negative value of ν would mean a surface roughening via the growth of the condensation nuclei during the deposition. The η is instead a random shot noise term, responsible for the thickness and roughness increase for increasing τ.

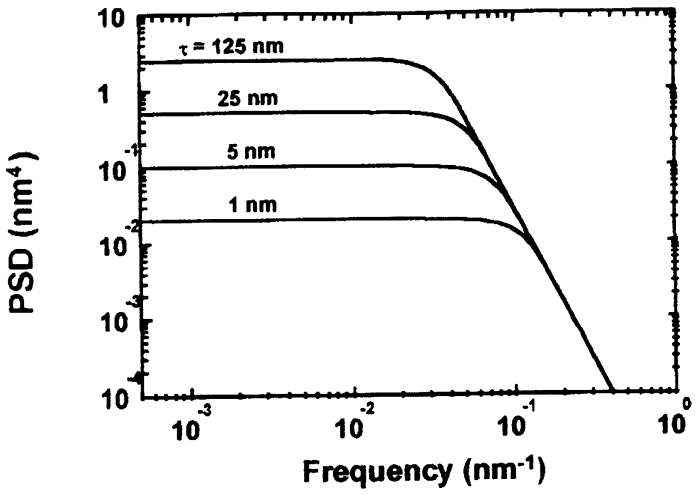

Figure 3.18: Simulation of the evolution of the PSD of a single film during the deposition for increasing film thickness, according the kinetic model. The substrate was supposed completely smooth. The parameters values are $\Omega = 0.02\ nm^3$, $\nu = 2.5\ nm^3$, n=4 (credits: bibl. [78].

A solution of this differential equation may be obtained (see bibl. [88]-app. A) in terms of the surface PSD:

$$PSD(f) = \Omega \frac{1 - exp[-2\nu|2\pi f|^n \tau]}{2\nu|2\pi f|^n} \tag{3.80}$$

where Ω is the volume of the depositing particle during the growth process. An example of a PSD for a layer growing on an ideally smooth substrate is shown in fig. 3.18: the shapes of the fig. 3.18 are substantially the same as the eq. B.35 with n = C. The transition from the flat region (low frequencies) to the power-law regime (high frequencies) is determined by the correlation length $l_c = (\nu\tau)^{1/n}$. The corresponding frequency moves to lower frequencies as the film thickness increases. Only in the limit of an infinite film the PSD becomes a pure power law (purely fractal surface). This result may be physically interpreted as a domination in the flat region by the random deposition roughening process (white noise): at high frequencies the surface relaxation modify the spectrum and smoothen all the surface features with size less than l_c.

This model may be extended to multilayer coatings considering that the layers sequence deposition is a succession of steps where every layer finds the previous one as its substrate. The deposition process of

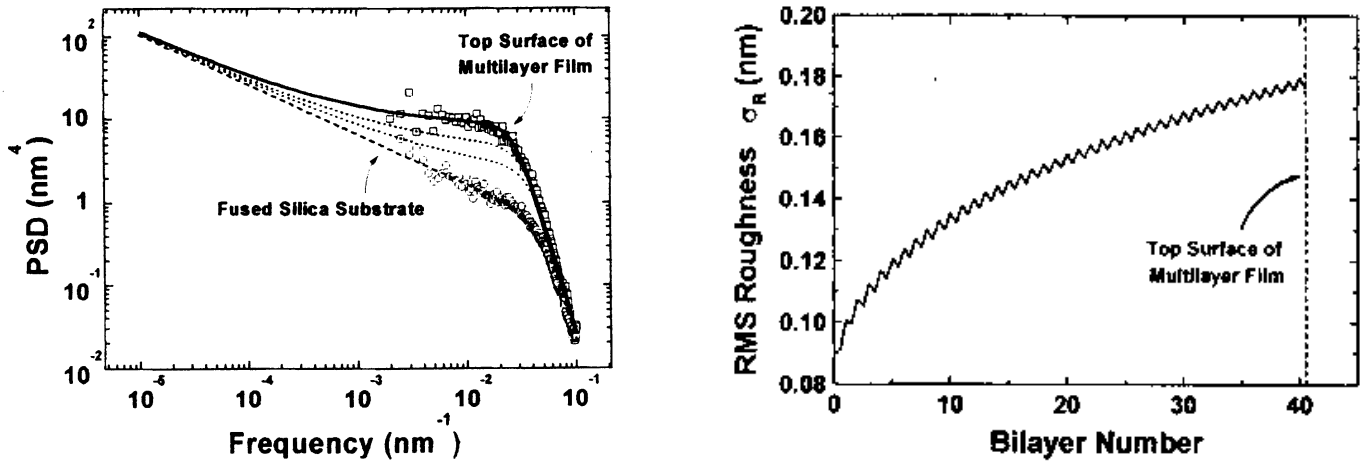

Figure 3.19: Modelization for the roughness growth in a magnetron-sputtered Mo/Si multilayer with 40 periods (credits: bibl. [78]).
(left) PSD evolution (dashed lines) layer by layer. The PSD values have increased from the substrate to the top of the multilayer film, and the simulation was compared to the Atomic Force Microscope data taken before and after the deposition. The data can be fitted to the model assuming $\nu = 2.5$ nm^3, $\Omega = 0.05$ nm^3 and n=4. The large value of Ω, three times the Mo atomic value, indicates that the Molybdenum layers have assumed a polycrystalline texture. This suggests that the multilayer roughness might be reduced by increasing the surface diffusion, that is, by heating the substrate or ion bombardment.
(right) Variation of the σ roughness rms, obtained by integration of the PSDs. The roughness value (0.18 nm) has doubled during the film deposition with respect to the substrate value (0.09 nm).

the i^{th} layer will produce an intrinsic noise roughness PSD $\gamma_i(f)$ and a partial replication of the underlying layer PSD P_{i-1}: thus, the PSD of the i^{th} layer upper surface will be

$$P_i(f) = \gamma_i(f) + a_i(f)P_{i-1}(f) \tag{3.81}$$

where $a_i(f) = exp[-\nu_i|2\pi f|^n\tau_i]$ is the *replication fraction* of the underlying profile (that can be derived in a similar fashion as the eq. 3.80, see bibl. [88]-app. A). Using recursive methods it is possible to compute the final multilayer PSD, and for a periodic multilayer it is possible to derive an expression for the multilayer surface after N bilayers, as the recursion is reduced to a geometric series:

$$P_N = \frac{1-(a_h^2a_l^2)^N}{1-a_h^2a_l^2}(P_{int}^l + a_l^2P_{int}^h) + (a_h^2a_l^2)^N P_{sub} \tag{3.82}$$

where a_l and a_h are the replication factors of the spacer and of the absorber, respectively, and $P_{int}^{l,h}$ are the PSD of the two materials if they were deposited alone on a ideally smooth substrate. P_{sub} is, finally, the substrate PSD. These predictions may be fitted to experimental data (see bibl. [78]), taken from AFM measurements performed on Mo/Si multilayers (40 periods) deposited with magnetron sputtering on a fused Silica substrate (see fig. 3.19). The evolution of the PSD after/before the deposition is quite evident: the increase of the surface roughness is thus an intrinsic process, that cannot be simply ascribed to the substrate roughness replication, although the substrate polishing state remains a crucial point.

The PSD evolves according three different regimes:

1. the low spatial frequencies regime ($l > 10\ \mu m$): in this case the substrate roughness is simply replicated by the multilayer: the roughness will be purely *conformal*, or *correlated*;

2. the intermediate frequencies regime (0.01 $\mu m < l < 10$ μm): the multilayer film is rougher than the substrate, as a result of the random and smoothening processes acting during the deposition;

3. the high frequency regime, ($l < 0.01$ μm): the substrate features are damped by the film smoothening process and the roughness is purely *unconformal*: in particular, the multilayer film may have a lower roughness than the substrate.

Note that the PSD growth is large especially in the intermediate regime, at spatial wavelengths from 0.05 μm to 1 μm; this wavelength range is is also *crucial* in X-ray grazing-incidence scattering (see sect. 5.3.1, page 120), and thus it is a critical point in the reflectivity of X-ray multilayers for hard X-ray telescopes.

3.5.3 Multilayer stresses

The deposition of an heterogeneous structure, like multilayers, on a substrate, produces *stresses*: stresses in multilayer coatings are easily observable when they are deposited on thin, planar substrates: after coating, the mirror takes a convex or concave shape, depending on the thickness, the materials, and on the deposition conditions.

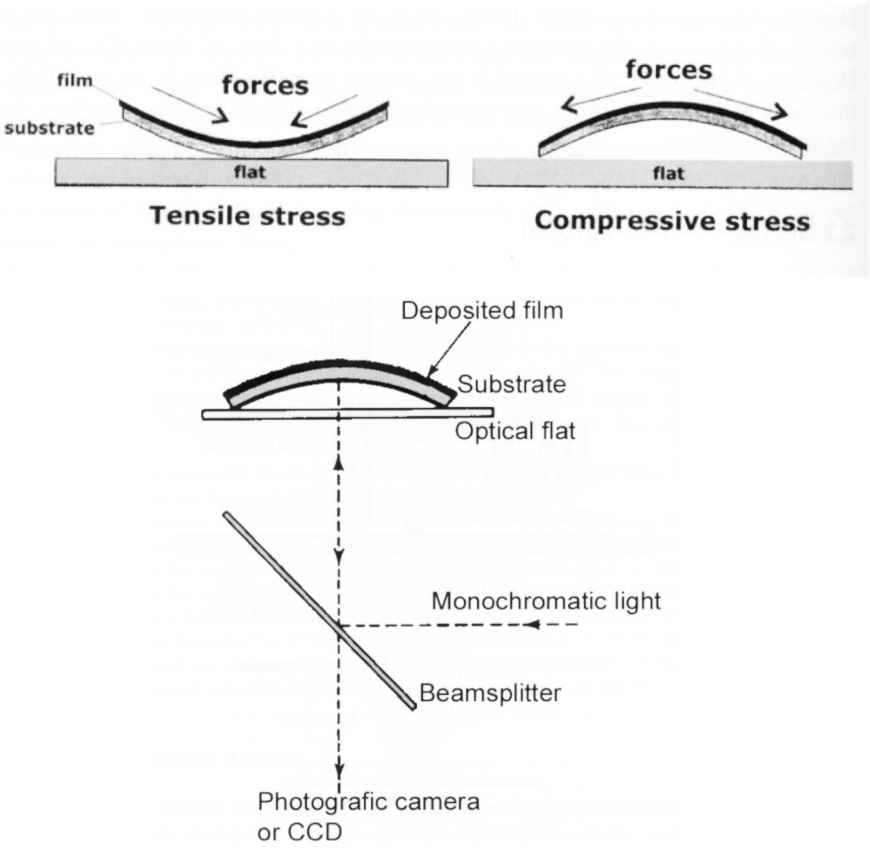

Figure 3.20: (top) Tensile and compressive stresses in a coated substrate (credits: bibl. [44]).
(bottom) A method to measure the stress: the observation of the interference fringes formed by the reflected light by the curved substrate and a reference plane allows to recover the substrate curvature and the stress value from the eq. 3.83 (credits: bibl. [45]).

The thin film stress is an important aspect to be considered in the development of X-rays reflective coatings for X-rays telescopes that have to operate in orbital conditions: the coating must be long-lived and it must keep the same properties, even if a slow degradation is unavoidable, as effect of the strong thermal excursions, the aggression of the atomic oxygen of the residual atmosphere, the degradation of the layer structure operated by the solar wind and by cosmic rays. The role of the stresses in multilayer coatings ageing is known: the substrate can be deformed, with consequent degradation of the focusing performance; as effect of the small-scale stresses the film can loose the contact to the substrate (*delamination*) and become unstable, uneven, and rough: the multilayer reflectivity will thus decrease in time.

In order to minimise the stress in multilayer coatings, a careful study has to be dealt: the material choice, the multilayer design, the deposition method, rate and parameters, the following manipulation has to be optimized.

The stress rise on a multilayer sample may be measured during or after the deposition with various methods (see bibl. [45]): a practical method consists in the measurement of the curvature radius assumed by the substrate, initially flat and optically reflective (for instance by observing the Newton's rings formed by interference with a reference plane). Another method to evaluate the substrate deformation, used in the stress measurements performed at INAF-OAB, is the profile tracing with the Long Trace Profilometer (LTP, see sect. 5.1.3, page 110). These method allows to evaluate the overall stress exerted by the whole coating: once measured the radius R, the stress can be evaluated with the *Stoney equation* (1909):

$$\sigma = \pm \frac{Y_s t_s^2}{6(1-\nu) t_f R} \tag{3.83}$$

where Y_s is the substrate Young's modulus, ν is the substrate Poisson's coefficient, t_f and t_s are the film and substrate thickness, respectively[15] ; σ can be positive (coated side is concave) and the stress is said *tensile*, or negative (coated side convex) and the stress is called *compressive*. Typical stress values range from tenth to hundreds of MPa. An example of evaluation of stress in a W/Si multilayer is reported in fig. 3.21.

The overall stress is the sum of three terms (see bibl. [45]):

$$\sigma = \sigma_{ext} + \sigma_{therm} + \sigma_{int} \tag{3.84}$$

the σ_{ext} is the stress produced by external forces, e.g. when the mirror walls are electroformed on an X-ray reflective coating to produce a mirror shell by replication (see sect. 2.3.3, page 29).

σ_{therm} is the *thermal stress* that arise when the coating is subjected to strong temperature changes, as effect of the difference in the CTEs of the substrate and that of the film. In the case of a multilayer coating, the absorber and the spacer have usually a different CTE and stress arise also *inside* the multilayer structure. Strong stresses may occur during the multilayer deposition, but also during the film cooling or during the next production steps (like e.g. the Nickel electroforming, taking place at $\sim 50^o$): in the case of a single, thin film the thermal stress can be written as:

$$\sigma_{therm} = Y_f(\alpha_f - \alpha_s)\Delta T \tag{3.85}$$

where $\alpha_{f,s}$ are the film and substrate CTEs, respectively, and ΔT is the temperature variation from the deposition to the measurement. For a multilayer film the thermal stress depends also on the period and on the Γ factor (the dependence on the number of bilayers seems to be much less important, see bibl. [120]). The analysis of the thermal stresses are *fundamental* in the multilayer coated X-ray optics for space telescopes

[15] if the substrate was not initially flat, the curvature 1/R is to be replaced with the curvature variation $\Delta(1/R)$.

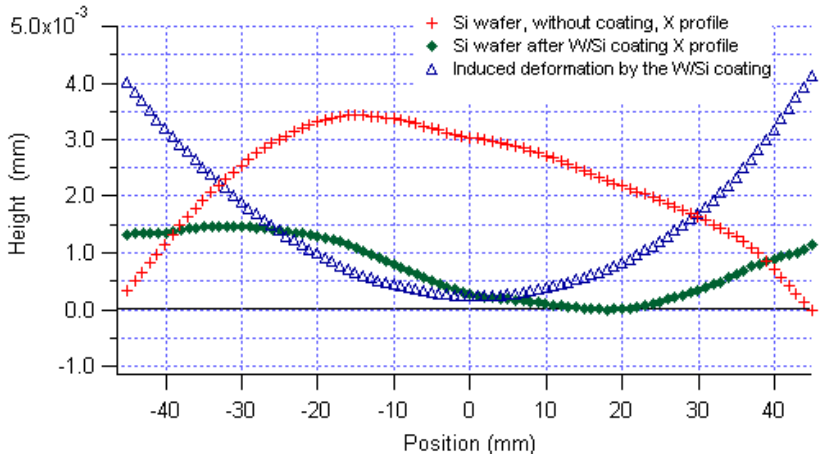

Figure 3.21: Stress measurement on a W/Si multilayer film (40 bilayers, d= 51 Å, $\Gamma = 0.4$) deposited on a Silicon Wafer substrate. The multilayer was deposited by e-beam. The substrate profile measured with the LTP before the deposition is shown in red: the profile of the same substrate after the deposition is the green plot. The initial substrate convexity has been strongly reduced, indicating a tensile multilayer stress. The local stress was evaluated from the variation of curvature $\Delta(1/R)$, obtained as the second derivative of the profiles difference (blue plot). In this case the profile difference is very well approximated by a parabola, indicating that the stress is uniform. The Stoney equation thus returns $\sigma \approx 285MPa$ assuming $Y_s = 170$ GPa, $\nu = 0.25$, $t_s = 0.65mm$ for the Silicon wafer.

because the temperature changes in orbit are sudden and intense: the stress may seriously compromise the optics performances, especially when the optics have large curvature radius and the substrates must be thin in order to fullfill the mass requirements. A very detailed analysis of the thermal stress using the elasticity theory has been performed by Ryutov (see bibl. [86]).

The *intrinsic stress* σ_{int} is the most important part, and it is strictly related to the film microstructure (see sect.3.5.1). It is caused by formation of voids, lattice disorders, variation of the interatomic spacing, atomic rearrangements, amorphous/polycrystalline phase transitions, gas incorporation or chemical reaction which can take place during the film deposition and compromise its stability.

Columnar structures are very often strongly stressed. Recrystallization can, indeed, lead to a strong mitigation of the intrinsic stress. At this step, the grain size appears as to be the dominant parameter that establishes the stress value; large grain sizes usually produce low stresses and small grain sizes are associated to high stresses levels. An alternance of compressive and tensile stresses can, moreover, develop during the growth, especially at the moment of the coalescence of the initial condensation islands (see bibl. [45]). In general, metal films develop tensile stresses; tensile stresses are also typical of e-beam deposited films (see fig. 3.21), with an open columnar microstructure and a low density. Sputtered and evaporated with ion-assistance films have instead an high packing density and show compressive stress.

In order to avoid the film cracking (tensile stress taking over the film breaking strength) and the film delamination (compressive stress taking over the film-substrate adhesion), stress mitigation methods are under study. Some results seem to show that evaporated Mo/Si multilayer show lower stress levels than those deposited by magnetron sputtering (see bibl. [120]). Also the ion polishing/assistance (see chapt. 4) is able to reduce the tensile *interlayer stresses* (see bibl. [45]) due to the increase of the grain sizes: the insertion between the Si and Mo layers of some intermediate layers (used also to avoid the Mo/Si interdiffusion), can mitigate the interlayer stresses, but they affect also the final peak reflectivity. Finally, a Mo/Si multilayer design with a proper Γ value can reduce or even nullify the overall multilayer stress (see bibl. [120]): however,

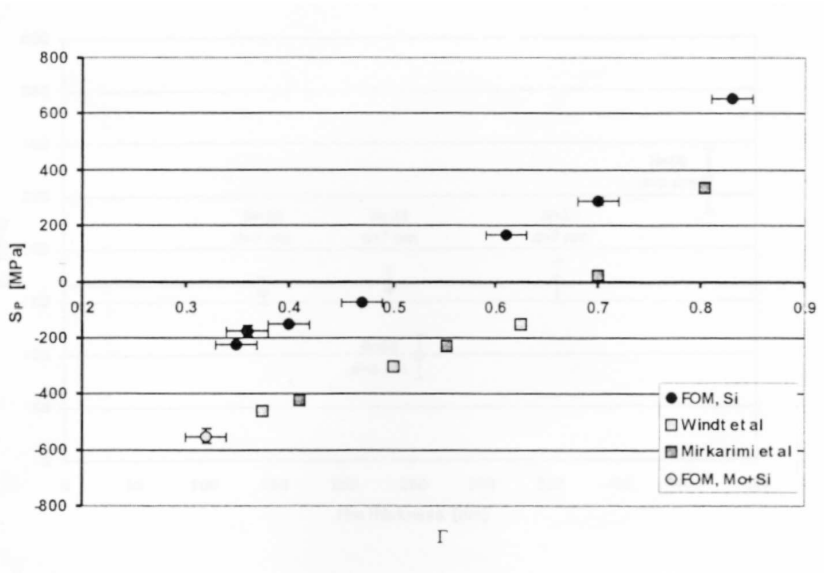

Figure 3.22: Stress mitigation in a Mo/Si multilayer (credits: bibl. [120]). The stress measurements are reported as a function of the Γ factor. There is a linear increase of the tensile stress with increasing Γ: the black circles are produced with e-beam and ion assistance on the Si layers, the squares have been produced by magnetron sputtering.

the Γ value that would nullify the stress (0.65) would provide a too large absorption to return the desired high peak reflectance (70%).

Some progresses (see bibl. [120]) have been done by the insertion of an ASL (*Anti Stress Layer*) under a Mo/Si multilayer optimized for high reflectance. The ASL is simply a Mo/Si multilayer with a reduced number of periods, but with a stress value *opposite* to that of the reflecting multilayer; the reflectivity of the reflecting multilayer is not affected, but the overall multilayer stress is considerably reduced.

The multilayer stress mitigation is a very important item in the development of the optics for the XEUS mission (see sect. 3.7.4, page 87).

3.6 Enhancement of low-energy multilayer reflectivity

Multilayer mirrors can be used not only to extend the sensitivity window of X-ray focusing optics over 10 keV, but also to increase the effective area of X-ray telescopes in the soft X-rays band ($0.1 \div 10$ keV), as it has been already suggested by Catura et al. (see bibl. [62]) and Joensen et al. (see bibl. [61]). In this case it is possible to use *multilayers with a constant or almost constant d-spacing and a limited number of bilayers*: by means of this layered structure broad reflectivity Bragg peaks can be obtained (see eq. 3.47), with a good reflectivity since the single boundary reflectivity at so low energies is still appreciable (see eq. 3.12) and since the loss due to the photoelectric effect internal absorption is low as the reflection takes place in the first layers.

A further reflectivity enhancement (mainly restricted, indeed, to the $0.5 \div 5$ keV energy region) can be achieved by *using the low density material of the bilayer couple as a first layer of the stack* (Carbon is one of the most performing materials for the scope, see the sect. 2.2.1, page 18): the low-density coating reduces the effect of the photoelectric absorption when the mirror acts in total-reflection regime, improving the reflection efficiency with respect to usual single-layers made of a high density material.

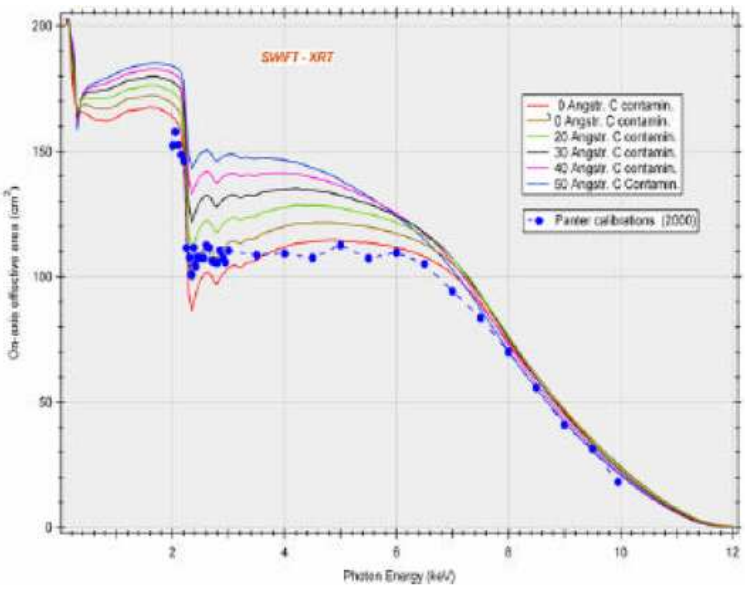

Figure 3.23: Experimental on-axis effective area of the JET-X/SWIFT telescope, as measured at the PANTER-MPE facility, compared to the theoretical profiles expected by assuming a contamination by a Carbon overlayer of different thickness. The increase of effective area in the 0.5 6 keV region of lower energies is evident (credits: bibl. [95]).

Soft X-ray multilayers have the advantage of reflecting at relatively large incidence angles, thus they could be used to coat Wolter I mirrors with a great increase in mirror efficiency, a gain that would in turn allow to reduce its critical dimensions of the optics (focal length and maximum diameter). As it will be presented in the section 3.7.5, this would have important impact also in the case of the XEUS mission (see sect. 3.7.4, page 87). By coating with soft X-ray multilayer reflectors with an appropriate structure the outer shells of the telescope it is theoretically possible to achieve a gain in effective area up to 25% at 1 keV, and up to 50% at 4 keV.

3.6.1 Effect of the low density material overcoating on the single-layer coated X-ray mirrors

A mirror coating made of a high-density material (e.g. Au, Ir, Pt, W or Ni) capped by a thin layer (20 ÷ 120 Å) of a low-density material as Carbon is theoretically able to provide a much better reflection efficiency than usual single-layer mirrors in the soft X-ray energy range between 0.5 and 5 keV, assuming the typical reflection angles of a classical X-ray telescope (0.2 ÷ 1.5 deg).

This effect is caused by a *much lower photoabsorption of Carbon in total reflection regime*, in correspondence of the energetic ranges where the absorption edges of the high density materials are located (see sect. 2.2.1, app. A.1). On the other hand, the reflectivity response of the high-density coating at higher energies (> 5 keV) is not affected by the presence of the Carbon layer, almost transparent to the high energies and with a negligible absorption. This effect has been already experimentally observed in the past as a change of the effective area of X-ray telescopes once in orbit, with *an increase with respect to the ground calibrations*. This phenomenon is in general explained (e.g. also for Chandra) as a contamination by a hydrocarbon film (CH_4) of the mirror surface. In the case of Chandra the presence of this effect was predicted before the launch of the satellite, and an extensive X-ray reflectivity testing campaign was been performed using flat Iridium coated samples contaminated with thin (100 $\mathring{A}$ or less) polyethylene films.

In figure 3.23 the experimental on-axis effective area of the JET-X/SWIFT (see tab. 2.3, bibl. [39]) telescope is reported, compared to the theoretical behaviour expected by a contamination by a Carbon overlayer of variable thickness. Note *the increase in effective area due to the Carbon overcoating.*

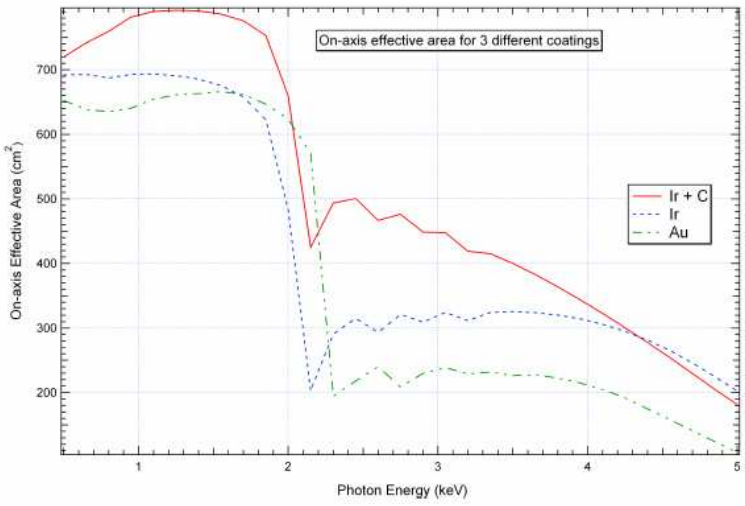

Figure 3.24: On-axis mirror effective area of the ASTER-X telescope for different coating materials, including Iridium plus a Carbon overcoating (credits: bibl. [95]).

In figure 3.24 it is instead shown the theoretical effective area expected for the wide-field ASTER-X mission concept (see bibl. [99]) assuming different kinds of reflecting coatings: Ir monolayer, Au monolayer, Ir monolayer plus a C overcoating. The project is based on two mirror modules of 12 shells each, and a focal length of 7 m. It was designed with the specific aim to efficiently perform a deep all sky survey in the $0.3 \div 10$ keV X-ray band. The mirror profiles of the ASTER-X optics do not follow the Wolter I geometry, but they are instead based on *polynomial* surfaces (see e.g. bibl. [65]), whose coefficients are optimised to get a correct Point Spread Function (HEW better than 5") for focused photons over a field of view of 30' in radius. The outermost shell has a diameter of 1020 mm and length of 485 mm, while the innermost shell has a diameter of 690 mm and length of 330 mm. Also in this case the benefit given by the Carbon overcoated Ir reflector with respect to the other two cases is clear.

3.6.2 Effect of the low density material overcoating on multilayer coated X-ray mirrors

As already mentioned, while hard X-ray optics ($10 \div 80$ keV) with relatively small incidence angles make use of depth-graded multilayer structures (see sect. 3.4.1, page 58) with a wide-band response, their use is not viable below 10 keV, due to the strong photoelectric absorption felt by X-rays passing through the stack of bilayers with a variable d-spacing. However, the use of multilayer films with proper structure can evenly be an interesting option to be explored in order to increase the effective area of an X-ray telescope in the classical $0.1 \div 10$ keV energy band.

In this case the better performing structures are characterized by:

1. periodic (or almost-periodic) multilayer stacks, formed by a small number of bilayers, able to provide high-reflectivity Bragg peaks in the soft X-ray region;

2. a thick top-layer of the *high density material* of the bilayer couple to improve the reflectivity by widening the total reflection regime energetic range;

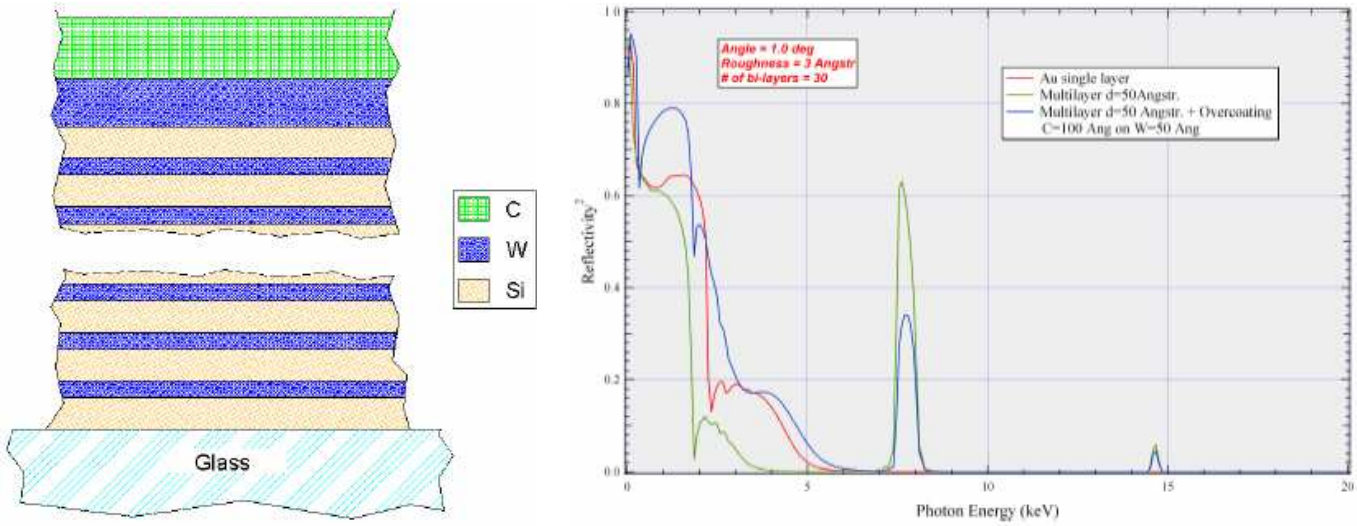

Figure 3.25: (left) Scheme of a multilayer coating for low energies: a constant W/Si multilayer, with a capping film formed by a thick layer of W plus an overcoating of C (credits: bibl. [95]).
(right) Theoretical reflectivity to the square as a function of photon energy at 1^oangular incidence for: i) an Au single layer; ii) a W/Si 50 $\AA$ constant d-spacing multilayer made of 30 bilayers; iii) a W/Si 50 $\AA$ constant d-spacing multilayer formed by 30 bilayers plus two additional top layers of W (50 Å) and C (100 Å) (credits: bibl. [95]).

3. a top external layer formed by a *low-density material* overcoating (e.g. Carbon), as described in the previous section, in order to further on reducing the photoelectric absorption for total reflection at very low energies.

As an example of a similar structure, a W/Si multilayer with Carbon overcoating is represented in fig. 3.25 (left), while in fig. 3.25 (right) the reflectivity-to-the-square (accounting for the two reflections of a Wolter I system) versus the photon energy profiles at the incidence angle of 1^o are shown for three different coatings for comparison:

1. an Au single layer;
2. a constant d-spacing W/Si multilayer made of 30 bi-layers, with period 50 $\AA$ and $\Gamma = 0.35$;
3. the same as for 2) plus an overcoating formed by 50 $\AA$ of W plus 100 $\AA$ of C.

As can be seen, the third case represents the best trade-off to get a high response beyond the total reflection region (with a first-order Bragg peak at $\sim$ 7.5 keV) without a strong decrease of the reflection efficiency at low energy. In this case, the Carbon overcoating clearly determines a significant improvement between 0.5 and 2 keV.

3.7 Future hard X-ray missions involving multilayer coatings

A number of future hard X-ray telescopes are at present time being conceived: most of them will implement multilayer coatings in order to extend the X-ray focusing technique to the hard X-ray band: in the following we will describe some missions of the next (or remote) future that include in their trade-off the implementation of multilayer coatings, each of them with the related, specific mission requirements.

3.7.1 HEXIT/HEXIT-SAT

The HEXIT (High Energy X-ray Imaging Telescope) balloon-borne experiment is devoted to the validation of the new-generation hard X-ray ($20 \div 70$ keV) telescopes based on focusing multilayer optics and high Z solid state detectors. The unprecedented application of concentration techniques to the hard X-ray band will allow the observation with the best angular resolution and flux sensitivity (see fig. 1.1).

The HEXIT mission is in a phase study and it is funded by ASI (the Italian Space Agency). The development project involves a consortium of Italian institutes (Brera Astronomical Observatory, IASF/CNR in Bologna and Palermo, IPCF/CNR in Ferrara, University of Ferrara, see bibl. [93]), and its flight is foreseen from the Trapani/Milo (Sicily) base operated by ASI.

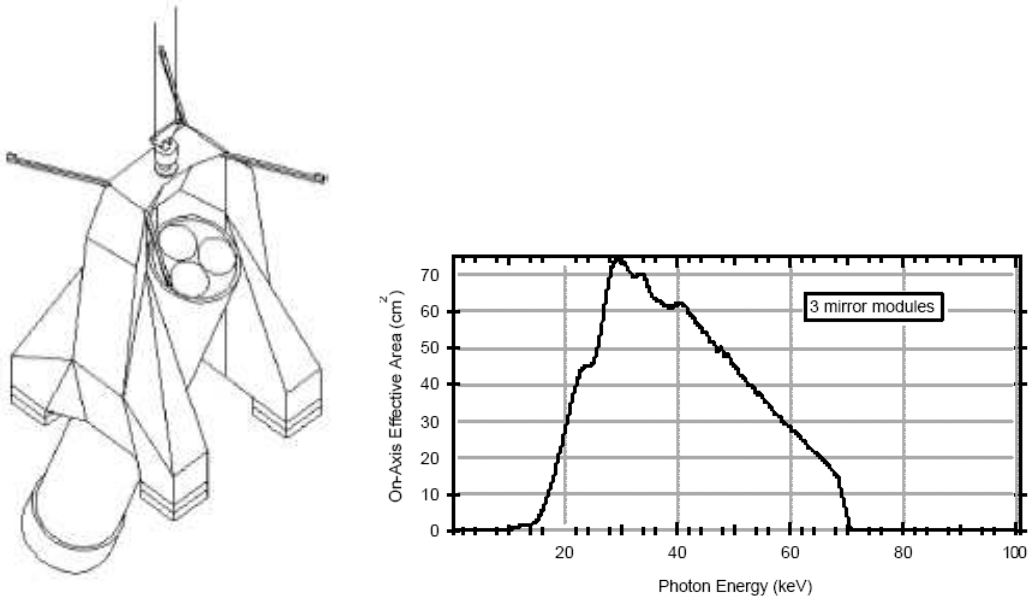

Figure 3.26: (left) Scheme of the HEXIT telescope gondola. (right) The HEXIT on-axis effective area for three multilayer mirror modules (including the reduction due to the atmospheric absorption (credits: bibl. [93]).

HEXIT will fly in the stratosphere (40 Km height), where the X-ray atmospheric absorption is remarkably less than on ground: at such altitudes, 20 keV X-rays are reduced to 40% and 50 keV are reduced to 60% of the initial value in space. During the flight, HEXIT will mainly observe the hard X-ray Background in the peak region.

HEXIT is based on 3 grazing-incidence multilayer focusing optic and will cover the band from 20 up to 70 keV. The lower limit of this band is imposed by the residual atmosphere absorption above the stratosphere: the upper band is set by the extreme difficulty of producing multilayers with period less than some nanometer (see sect. 3.5.2, page 66), but also by the K-edge of the Tungsten used as multilayer absorber: however, an extension is possible up to 140 keV by using a Mosaic Crystal Laue concentrator (see below). The optics will have a Wolter I linear approximation and will be produced by replication, using the Ni electroforming technique (see sect. 2.3.3, page 29): this technique will allow the HEXIT optics to fit in the mission mass limits (30 Kg) while keeping good optical performances ($HPD \simeq 30$", see tab. 3.1). The telescope is supported by a azimuth-zenith mount (see fig. 3.26) in Titanium (a metal that joins good mechanical stability and a low weight), to be integrated in a Aluminium gondola structure which will include all the electronics, the attitude control systems, for an overall weight of 1500 Kg. The positioning is demanded

to a star/Sun sensor (operating in the visible wavelengths) that will be able to determine the positioning offset during the balloon flights (1 day duration). Longer flights (from the Milo base to the USA east coast) will successively give HEXIT the possibility of longer observation time ($\sim$ 1 week), with a large increase in sensitivity that will give HEXIT a chance to resolve the XRB for the first time over 20 keV (see chapt. 1).

Number of modules	3
N. of shells per module	30
Max. diameter	230 mm
Min. diameter	115 mm
Focal length	6 m
Number of W/Si bilayers	150
Min. incidence angle	0.13^o
Max. incidence angle	0.28^o
Wall thickness	0.2-0.3 mm
Field Of View	15'
Single module effective area	23 cm^2 @ 30 keV

Table 3.1: Some characteristics of the HEXIT mission (credits: bibl. [93]). Note in particular the very small wall thickness of the shells, necessary to keep a low weight, compared e.g. to those of XMM (see tab. 2.3). The thinnest walls are those of the inner shells as their lower diameter guarantees a larger shape stability. Note also the very shallow incidence angles (much more grazing than XMM).

The high reflectivity in hard X-rays will be permitted by the deposition of graded multilayers (W/Si, 150 bilayers) according to the *supermirror* designs, whose parameters have been optimized (see sect. 3.4.1, page 58) following an *Iterated Simplex procedure* (see bibl. [74], bibl. [105]), assuming as Figure of Merit the integrated effective area in the band 20 -70 keV (see fig. 3.26). The practical multilayer development is in progress and a mirror shell with a Pt/C multilayer coating has been produced by e-beam deposition and Ni electroforming by INAF-OAB and Media-Lario: the mirror shell has already been tested at the PANTER facility (see sect. 7, page 139).

The possibility of extending the HEXIT operational band up to 140 keV is also considered: the extension may be done with Cu(111) *Mosaic Crystals* in the Laue configuration (see bibl. [134]). Mosaic crystals are constituted of many perfect micro-crystals, each of them having a misaligned lattice orientation with respect to the outer, reflecting crystal surface. The orientation dispersion $\delta\theta$ usually follow a Gaussian profile: when an X-ray incides on the crystal with an incidence angle θ_i, the Bragg condition for reflection $2d\sin(\theta_i \pm \delta\theta) = k\lambda$ is satisfied for a broad energy band, as different wavelengths are reflected by different micro-crystals having the proper orientation.

In spite of the limited imaging performances of Mosaic Crystals (some arcmin HPD), they allow to operate at very large incidence angles due to the very small lattice spacing (some Å): the development activities to design a Laue concentrator are on-going at the University of Ferrara.

A position sensitive detector will be located in the HEXIT focal plane. The requirements to this detector are quite strict: the 30 arcsec angular resolution require a detector spatial resolution better than 500 μm and a broad energy response, with an excellent energy resolution and quantum efficiency. A good candidate

is the CdZnTe (CZT) solid state detector. CZT detectors have spectroscopic performances similar as the Ge or Si detectors, but they take the advantage of the room temperature operation: the possibility of avoiding the implementation of cryogenic systems implies obviously a saving of cost, weight, and instrumentational complexity. Typical energy resolution values for a CZT detector are less than 10% at 60 keV and less than 12% at 40 keV. The quantum efficiency is also very good (99% at 55 keV, for a 1 mm thick crystal) due to the high atomic number of the componing elements and the high density (6.1 g/cm^3). CZT detectors find applications also in high energy X-ray medical applications (see sect. 3.8.2, page 94) and their use is foreseen in the future hard X-ray mission Constellation-X (see sect. 3.7.3, page 85).

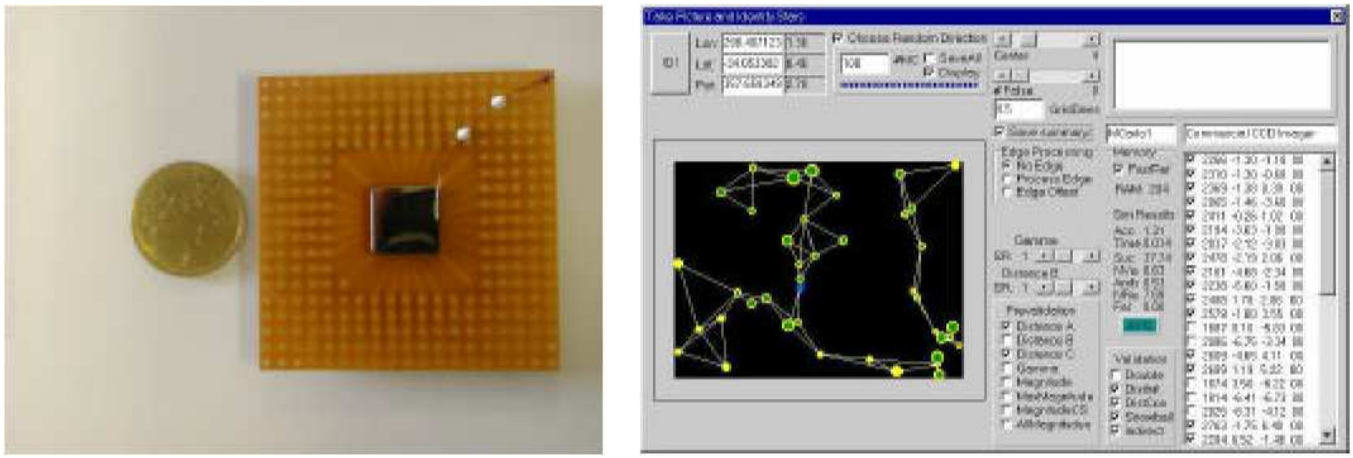

Figure 3.27: (left) A first, reduced size, prototype for the HEXIT telescope detector: a 1 cm × 1 cm size pixeled CZT array. (right) An example of the real-time processing to correct the telescope attitude (credits: bibl. [93]).

The detector design foresees the adoption of a CZT pixel array with 64 × 64 pixels with a 38 mm × 38 mm × 1 mm size. Each pixel has a 500μm size with a 100 μm pitch (the distance between two adjacent pixels). In figure 3.27 a detector prototype with a reduced size (10 mm × 10 mm × 1 mm) is showed and it is currently under test. The detector will be shielded with an anticoincidence system with 3 cm thick CsI scintillators, devoted to the background rejection.

The overall telescope will provide a on-axis 3σ sensitivity in 2×10^4 sec of observing time at 40 keV, better than 0.2 mCrab (see fig. 1.1): this performance is due to the strong photon concentration that allows a large intrinsic background reduction (see sect. 2.1.2, page 16).

It is worth noting that the first satellite hosting focusing hard X-ray optics will be the Japanese mission NEXT, whose launch is foreseen for 2012. HEXIT will serve as a pathfinder for satellite missions before this date, operating in parallel with other balloon-borne missions, like InFocus (see bibl. [51]), HERO (see bibl. [49]), and HEFT (see bibl. [50]).

The HEXIT-SAT mission (see fig. 3.28) is the spacecraft follow-up of the HEXIT mission. Many of the optical payload characteristics will inherit the HEXIT corresponding ones, but with some powered features: in space, no residual atmosphere limits the sensitivity band and HEXIT-SAT will cover the energy range 0.1 ÷ 70 keV. HEXIT-SAT will implement 4 mirror modules with graded multilayer coatings (see tab. 3.2), 50 mirror shells per module, 8 m focal length, obtained with an extendible optical bench. The angular resolution will be 30 arcsec, as in the HEXIT case. A view of the HEXIT-SAT scheme is shown in fig. 3.28.

The mirror manufacturing technique will be, again, the mandrel replication by Ni electroforming (each

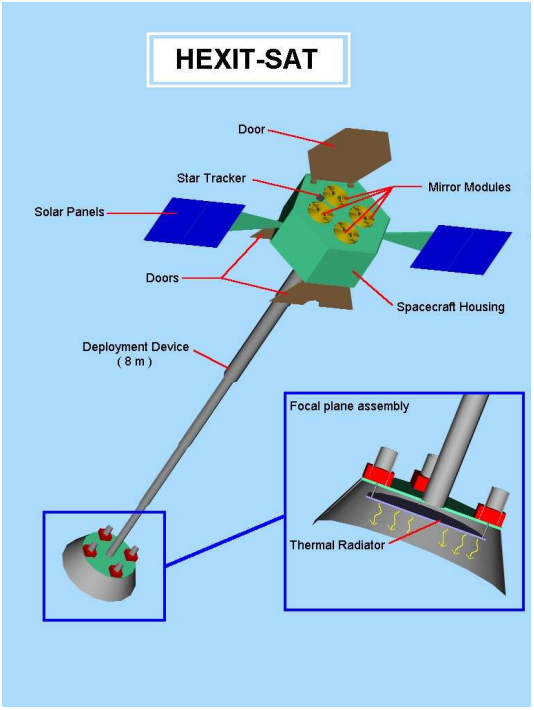

Figure 3.28: A scheme of the HEXIT-SAT mission (credits: S. Basso).

Number of modules	4
N. of shells per module	50
Max. diameter	330 mm
Min. diameter	112 mm
Mirror height	80 cm
Focal length	8 m
Number of W/Si bilayers	200
Min. incidence angle	0.120^o
Max. incidence angle	0.295^o
Wall thickness	0.12-0.35 mm
Field Of View	15'
Pointing accuracy	2"
Single module effective area	75 cm^2 @ 40 keV

Table 3.2: Some characteristics of the HEXIT-SAT mission (credits: bibl. [48]).

module will have, including the mechanical support, a 65 Kg weight). The large effective area in hard X-rays will be permitted by *graded W/Si multilayer coatings* (200 bilayers): in the HEXIT-SAT case, however, the energy band is also very extended in the soft region (down to 0.1 keV), that cannot be easily reflected by W/Si multilayer coatings, due to the strong photoabsorption of high-Z elements like Tungsten. A viable solution may be the overcoating of the W/Si multilayer with a low-Z layer like Carbon, that would reflect in grazing incidence the softest X-rays (up to 1 keV) without affecting the harder X-ray multilayer reflectivity (see sect. 3.6 on page 74, bibl. [95]).

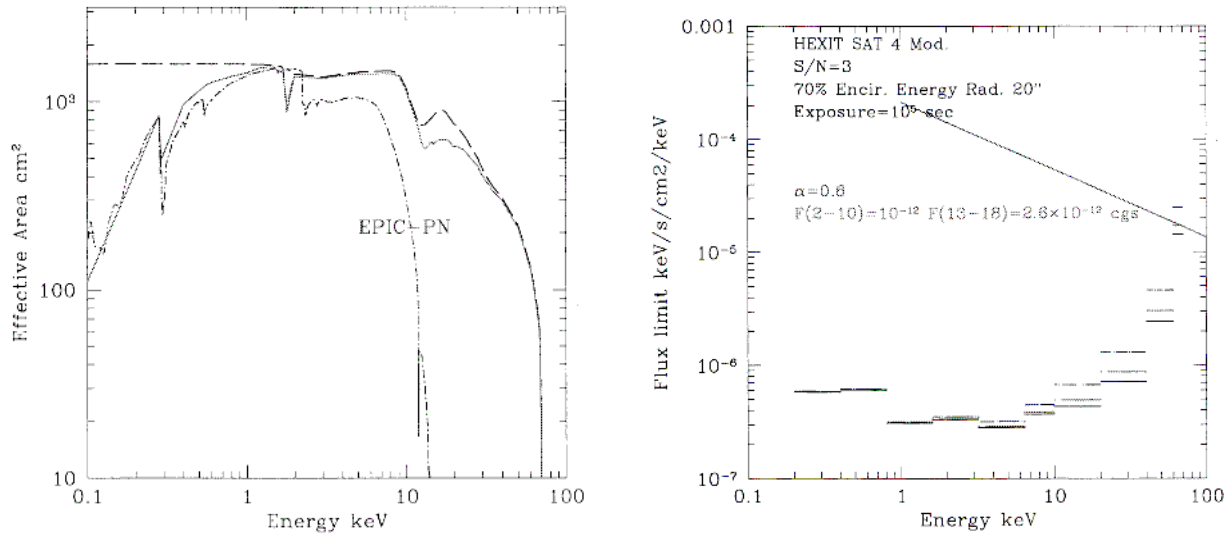

Figure 3.29: (left) HEXIT-SAT effective area. The dashed line is the mirror (4 modules) effective area: the solid line is the effective area multiplied by the detector efficiency. The HEXIT-SAT effective area is compared to that of XMM-EPIC-PN camera (dot-dashed line). The low energy cut-off is caused by the CsI active shields used to reject the background. (right) HEXIT-SAT flux limit as a function of energy. The solid line is the mCrab limit. Three background values are assumed: B= 3×10^{-4} counts sec^{-1}, cm^{-2} B= 10^{-4} counts sec^{-1} cm^{-2}, B= 5×10^{-5} counts sec^{-1} cm^{-2} (credits: bibl. [48]).

As in the HEXIT case, the choice of a detector that matches the hard X-ray mirror response is fundamental. In particular, the efficiency of a CZT detector as the one of HEXIT would be insufficient in the soft band (< 15 keV). Two solutions are possible:

- the use of a CZT detector (15-70 keV) in to be used in series to a Silicon pn-CCD (0.1-15 keV, similar to that used for XMM): in this configuration, the CCD is the first detecting element: it is almost transparent to the hard X-rays, that can be detected by the CZT underlying detector. The pn-CCD used for XMM is slightly oversized (60 mm $\times$ 60 mm instead of the required 35 mm $\times$ 35 mm), but it is very densely pixeled and does not degrade the telescope PSF;
- the use of Silicon Drift Chambers (SDC) with scintillating crystals (CsI); SDC are a Silicon device that can be used as photodiodes. The advantage is the very low noise and the consequent improvement in energy resolution. SDC are also capable of direct radiation detection in soft X-rays, so the energy range can be extended. This kind of devices are under study at the Politecnico di Milano, the IASF in Milano and Bologna.

HEXIT-SAT represents a transfer of the planned HEXIT technologies to the space environment: HEXIT-SAT will achieve, in the $0.1 \div 70$ keV, an effective area comparable to the reached one by Newton-XMM

in the soft band (see fig. 3.29); this will in turn imply a large increase in sensitivity (a 5σ sensitivity of 0.05 mCrab with 10^4 sec integration time, assuming a background B= 10^{-4}counts sec^{-1} cm^{-2} in a Low Earth Orbit): in the band 0.1-70 keV HEXIT-SAT will be 100-200 times more sensitive than SWIFT/BAT, 10 times more sensitive than EXIST, without mentioning the improvement in angular resolution (that for coded masks equipped telescopes cannot be better than some arcmin).

A mission like HEXIT-SAT would be able, in particular, to resolve much more deeply the hard CXB: it is possible to calculate that (see bibl. [48]) the exposure time necessary to detect at 3σ a 10-100 μCrab source in the band 20-40 keV would be respectively 22 ksec and 16 ksec. In 1 Msec it could be possible to observe 2.2 or 30 deg^2 finding 23 and 12 sources in hard X-rays over the 3σ flux limit. In some months it could be possible to collect a number of object sufficient to test the CXB paradigm in the peak region and to put strong constraints about the CXB synthesis model. Also the observation of other hard X-ray targets will give new, fundamental insights to the Astrophysics of these objects.

3.7.2 SIMBOL-X

SIMBOL-X(see fig. 3.30) is a mission concept promoted by CNES (*Centre national d'Etudes Spatiaux*, France): the SIMBOL-X mission (see bibl. [52]) is designed (see tab. 3.3) to be the first hard X-ray telescope to achieve a suitable effective area with large focal length (30 m) while keeping the optics size at the same level as Newton-XMM (but with 1 module only): the effective area achievable with a so large focal length permits the use of a single film coating (Ir, Au or Pt).

The adoption of a 30 m focal length is possible only if the detector and the optics are on two different spacecrafts: the *Mirror SpaceCraft* (MSC) and the *Detector SpaceCraft* (DSC), kept at the right focal length distance by a tracking system (*formation flight principle*). The SIMBOL-X mission sensitivity in the hard X-rays (0.5 ÷ 70 keV, see fig. 3.30) will permit the imaging and spectroscopic observations of the Galactic

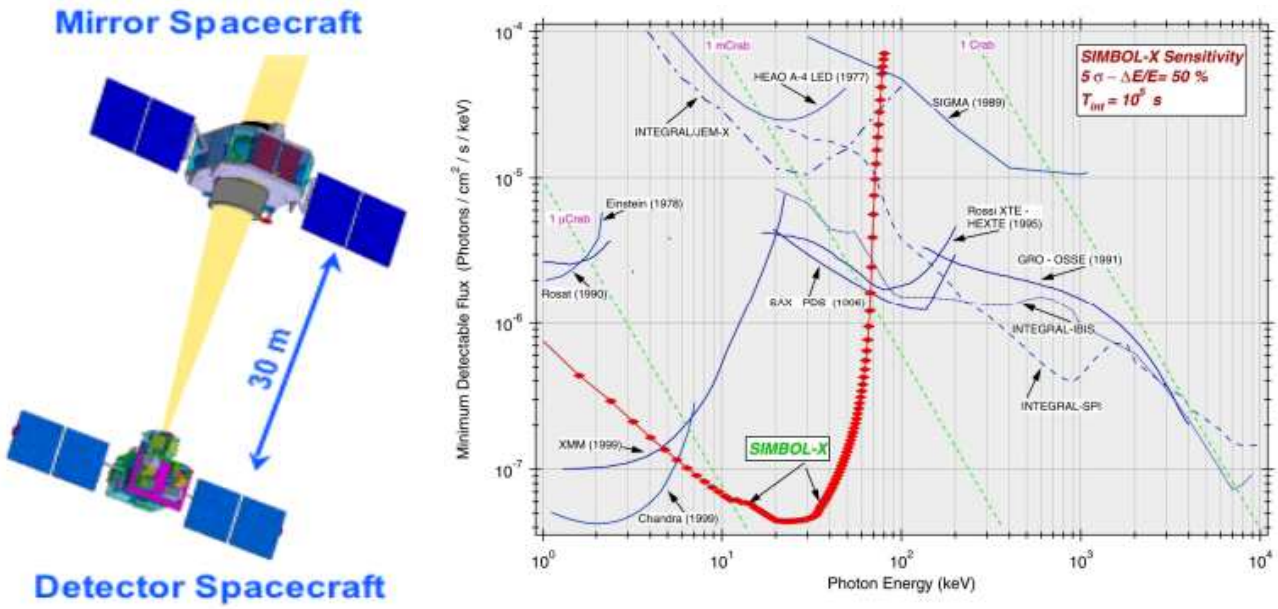

Figure 3.30: (left)A scheme of the SIMBOL-X telescope. The detector and the optics payload are two different spacecraft, operating in formation flight at a 30 m distance/focal length (credits: CNES).
(right) The SIMBOL-X sensitivity (red line) compared to those of other missions of the present and of the past.

Center: other possible targets are young SNR (Cas A, Tycho, Kepler..), AGNs, the hard XRB, flaring stars, X-ray novae, QSO jets. SIMBOL-X will also give an answer about the existence of non-thermal emission in the Galaxy Clusters. The launch is foreseen for 2008.

The formation flight is a principle that will be widely exploited in the X-ray telescopes of the future; SIMBOL-X will be a pathfinder for XEUS as it will experience a set of problems that may derive from the adoption of these "tubeless" telescopes. In particular, in order to make sure the image integrity, the formation flight requirements for SIMBOL-X are:

1. the distance between the MSC and DSC must be kept within 2 cm;
2. the focal plane must be perpendicular to the optical axis within 1';
3. the optical axis must be centered on the detector within 1 cm.

the formation stability is also favoured by the SIMBOL-X location in the Sun-Earth Lagrangian Point L2: this permits to reduce the fuel consumption necessary for the corrections that would be necessary in a near-Earth orbit. Moreover, the Earth will serve as a natural shade from the Sun radiation, making easier the passive detector cooling and permitting long, undisturbed observations of faint objects.

Bandwidth	0.570 keV
Effective area	600 cm^2 ($E < 35keV$)
Field Of View	5 arcmin
Maximum mirror diameter	60 cm
Focal length	30 m
Energy resolution	$<$ 130 eV @ 6 keV, 1 % @ 60 keV
Angular resolution (HEW)	$<$ 30 arcsec (local. $<$ 3 arcsec)
Effective area	$>$ 550 cm^2 E $<$ 35 keV, 150 cm^2 @ 50 keV
Flux sensitivity (5σ, 100 ksec, ΔE = E/2)	5×10^{-8} ph cm$^{-2}sec^{-1}keV^{-1}$ (E $<$ 40 keV)
Soft X-ray detectors	Si SDD Detector (0.5 $\div$ 10 keV)
Hard X-ray detectors	CZT detector (10 $\div$ 70 keV)

Table 3.3: Some SIMBOL-X mission parameters

In the production of SIMBOL-X prototype, the Brera Astronomical Observatory will provide the X-ray optics. As the mirror size is the same as that of XMM, the optics may be produced by Nickel electroforming: if a single coating will be implemented, the achievable effective area with a mirror with 100 shells will be 600 cm^2 up to 35 keV, and decreasing with energy after this limit. The angular resolution will be 20 arcsec HEW. The possibility of implementing multilayer coatings on the SIMBOL-X optics is also considered: this upgrade would allow to increase even more the sensitivity around 70 keV: this would in turn allow the detection of the ^{44}Ti X-ray lines from SNR.

The detector in focal plane is under the CNES responsibility: it must cover the whole mirror FOV (6', corresponding to 5.2 cm of diameter): the possible oscillations in formation flights suggested to take the detector size to 6 cm. The size of the focal spot on the detector (20", corresponding to 2.9 mm) must be

oversampled with a enough large number of pixels in order to avoid the degradation of the image quality: adopting an oversampling factor of 4 (like EPIC and XMM), the pixels will have a maximum size of 750 μm (70 $\times$ 70 pixels minimum). The energy resolution of the detector must also be good (150 eV) in order to achieve precise spectroscopic measurements (able, e.g., to resolve the profile of broad X-rays lines in AGNs).

The detectors will be conceived essentially as those foreseen for HEXIT-SAT: a Si CCD for soft X-rays ($<$ 15 keV) superposed to a CZT detector for hard X-rays ($>$ 15 keV), surrounded by anticoincidence shields. The Si CCD is quite thick (250 μm) in order to assure a good quantum efficiency. Its work temperature is -100 ^{o}C to reduce the intrinsic background: the cooling, indeed, will be obtained passively and will not need any cryogenic system: a prototype (12.7 $\times$ 8.5 mm size, with 22 $\times$ 22 μm) is under test: the CZT detector foreseen for SIMBOL-X will be a pixeled array (500 $\times$ 500 μm), working at room temperature. Its thickness (2 mm) guarantees a total X-ray absorption up to 80 keV.

3.7.3 CONSTELLATION-X

Constellation-X (see fig. 3.31) is a very ambitious NASA project conceived to extend the energy range of the imaging telescopes to the hard X-ray band: it represents a possible alternative to the technological problem of increasing the mirror effective area by adopting large diameter mirrors.

If Con-X will be launched (2013), it will have a sensitivity of some 10^{-8} ph sec^{-1} sec^{-2} keV^{-1} (under the μ Crab) up to 40 keV, and decreasing up to 70 keV (see fig. 1.1. To achieve this sensitivity, an overall effective area larger than 1500 cm^2 (@ 40 keV) is necessary: this will be possible using *four* complete, identical X-ray telescopes on-board four identical spacecrafts in formation flight. Each telescope will have, moreover, focusing optics constituted by three modules. An overall set of 12 identical modules will so be able to give Con-X an exceptional spectroscopic and imaging capability. A large part of the Con-X activity will be devoted to a detailed analysis of the AGN spectra, and to derive important informations about their Black Holes (mass, spin) and about their accreting environments.

Con-X will be able, for instance, to disentangle the physical contributions (Doppler effect, gravitational redshift, ...) that broaden the X-ray emission lines near to the event horizon of Supermassive Black Holes. Other targets include the measurements of the abundances of metals in the IntraCluster Galaxy medium, out to large distances; the high-resolution study of the binary systems dynamics, often uncertain due to the interstellar absorption (see bibl. [53]); a sensitive telescope over a wide band of energy is essential in these observations, as such objects show a set of correlated phenomenologies from the soft to the hard X-rays (radiation reprocessing, hard continuum reflection, ...). Moreover, large effective area is essential in measurements of rapidly variable emission (some hours in AGN), where the integration time has to be only some ksec in order to follow the timing evolution.

Each Con-X spacecraft is constituted of two telescopes: the *Soft X-ray Telescope* (SXT) and the *Hard X-ray Telescope* (HXT). The SXT is devoted to a very sensitive observation of the soft X-ray sky, and it uses wide soft X-ray, single Ir (or Au) coated mirrors: the aperture diameter for each SXT measures 1.3 m. The HXT (6-70 keV) optics have instead a more compact diameter (35 -28 cm) with a slightly larger focal length than SXT (9 m): this allows to operate at shallower angles, where the mirror reflectivity is larger. The HXT reflective coatings will be (W/Si, Ni/C, Pt/C,..) graded multilayers: a possible alternative for the inner mirror shells is a single Ir coating.

The construction of four identical satellites, with three identical modules each, is very expensive and time consuming as a number of identical (12 + 2 spare modules) set of shells have to be produced. From this viewpoint, the replication technique from a superpolished mandrel is a very good candidate, as it allows

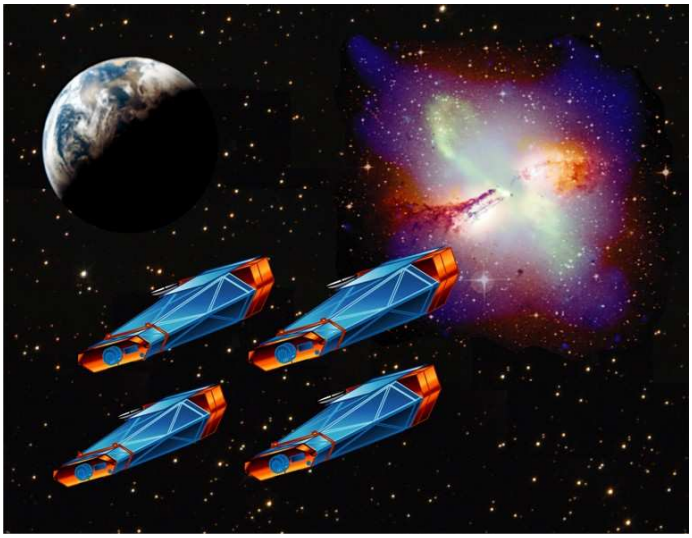

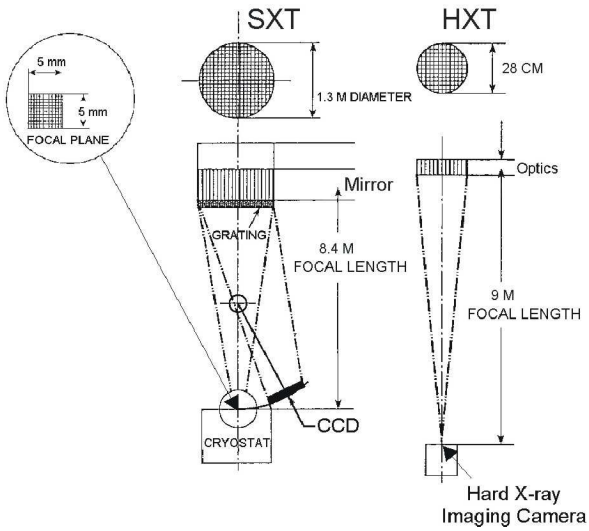

Figure 3.31: (left) Operative scenario of the Constellation-X mission. Four spacecrafts are operating in parallel observing the same X-ray target (credits: NASA). (right) Optical scheme of the SXT and the HXT telescope in each Con-X spacecraft (credits: NASA).

to produce monolithic mirror shells with a great simplification of the mirror assembly process and returns very good optical performances (see bibl. [90]). Moreover, every set of shells that constitute a module can be produced using the same set of mandrels, with an evident saving of costs and time. Another proposed method is, indeed, the replication of thin foils (see bibl. [54], see sect. 2.3.2, page 28), using the epoxy replication on an Aluminium foils. The use of a new type of glass, the DESAG, has also been proposed due to its allowance to be easily bent. Unfortunately, the thin glass approach has to be improved by a sixfold factor in order to reach the HPD required by the Con-X science goals.

Bandwidth (SXT)	$0.25 \div 10$ keV
Bandwidth (HXT)	$6 \div 70$ keV
Focal length (HXT)	9 m
Field Of View	10 arcmin
Maximum diameter (HXT, single mod.)	35 cm
Grazing angles (HXT)	$0.25^o \div 0.1^o$
Angular resolution (HXT)	< 60" (HEW, goal: 25")
Effective area (SXT)	15000 cm^2 @ 1.25 keV
Effective area (HXT)	> 1500 cm^2 @ 40 keV
Spectral resolution (SXT)	$(E/\Delta E)$ 1000
Spectral resolution (HXT)	$(E/\Delta E)$ 10

Table 3.4: Some Con-X mission parameters

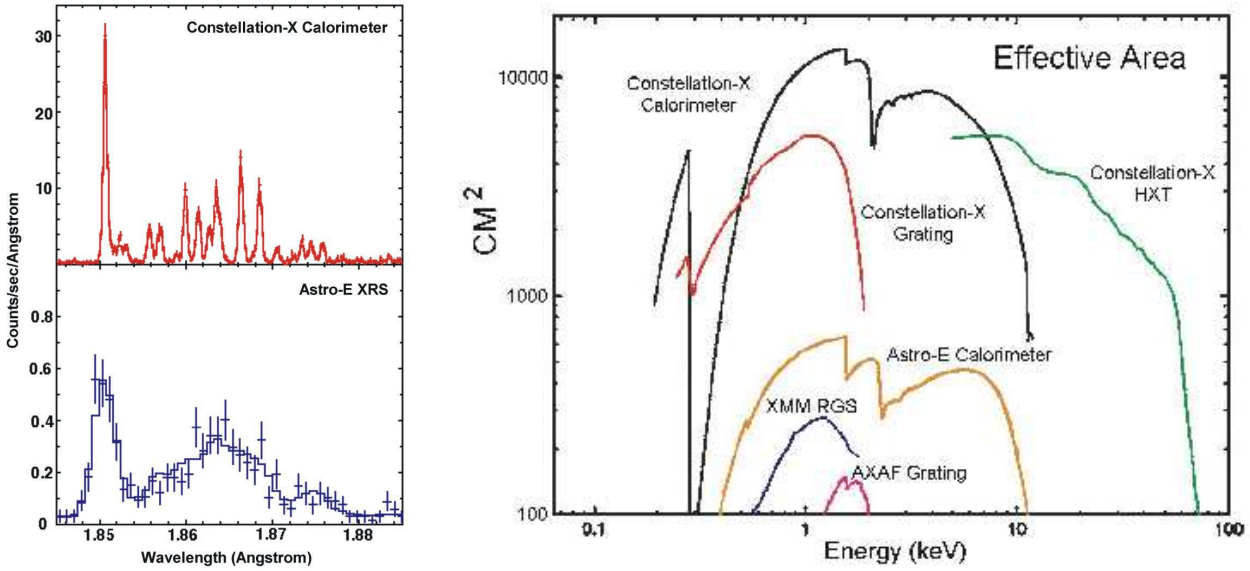

Figure 3.32: (left) Simulations of helium-like iron (Fe XXV) emission from a $\sim$ 20 million degree plasma. The top panel shows the spectrum from the Constellation-X calorimeter, which is currently under development. The bottom panel shows the spectrum from the microcalorimeter to be flown on Astro-E. Con-X has a larger capability to resolve single lines, that would be blended with the the limited Astro-E resolution (credits: NASA). (right) Con-X effective area, as a function of the energy (credits: NASA).

After the SXT mirror, a system of Reflective Diffraction Gratings (more complex than the RGS on-board XMM) deviates a part of the focused beam to a off-axis CCD in the focal plane ($E < 2keV$, 8.4 m far from the mirror) for dispersive X-ray spectroscopy. The zero-order sky image is observed by a devoted camera (ZOC) for non-dispersed imaging. This low-energy capability is particularly important for high-redshift objects, for which line-rich regions (moved into this lower energy band) would be completely blended and could not be measured individually (see fig. 3.32).

However, the grating spectroscopy has very limited capabilities in the observation of extended objects, and it cannot be used in a wide spectral range. So, the X-rays passing through the grating incide on a microcalorimeter (2 -10 keV, 5 $\times$ 5 mm size, 2.5' field of view), a spectroscopy device with excellent energy resolution (2 to 4 eV). A microcalorimeter detects the micro-heat pulses produced by the X-rays when they are absorbed by the sensitive detector element: the system is cooled down to 0.1 K, so that the thermal capacity is so low that the absorption of every photon is traduced to a measurable temperature pulse. The temperature variation is in turn recorded as a resistivity variation as so it is converted to a voltage pulse, proportional to the incident photon energy. This detector combines high efficiency and high energy resolution. In the Con-X case, the microcalorimeter will be superconducting in order to achieve a better stability and a faster detection.

The HXT detectors will be likely in CZT (see bibl. [54]), with sub-millimeter spatial resolution and high quantum efficiency up to 100 keV. The development and test of these detectors are in progress.

3.7.4 XEUS

XEUS (*X-ray Evolving Universe Spectroscopy*) is the potential successor to ESA Newton-XMM (see bibl. [55]): it is a very ambitious mission, aimed to carry the X-ray astronomy to unprecedented sensitivity performances. The scientific XEUS goals are the study of the evolution of the hot baryons in the Universe by the observa-

tion of the earliest AGN ($z > 5$): XEUS will be able to observe their black holes and will estimate their mass, redshift and angular momentum by observing the Fe-K line profile and the continuum. XEUS will be able to detect the first Galaxy Clusters bound by the dark matter, and to perform spectroscopic measurement in order to determine the intracluster medium density, temperature, composition (see bibl. [56]).

The sensitivity required to XEUS can be achieved with a focusing optics with a mirror area of 30 m^2, implying (see eqs. 2.12 and 2.13) a focal length of 50 m $\pm 0.1mm$. This would in turn make impossible to fit detector and optics on a single spacecraft, thus XEUS will consist of two different spacecrafts, the *Mirror SpaceCraft* (MSC) and the *Detector SpaceCraft* (DSC), in formation flight at a distance of 50 m (see fig. 3.33). The MSC remains passive, while the DSC is charged to follow the MSC focal point. The production of an optic with a final diameter of 10 m (see tab. 3.5) is very challenging.

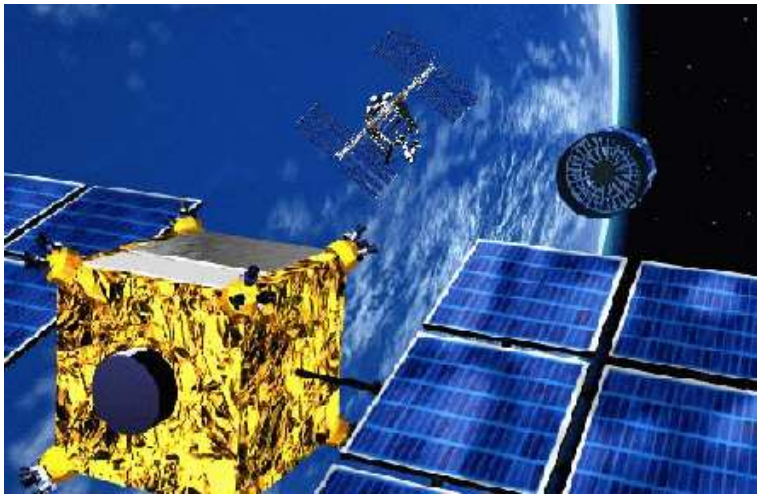

Figure 3.33: Operative scenario of the XEUS mission. The detector and the optics payload are two different spacecraft, orbiting in flight formation at a 50 m distance/focal length (credits: ESA).

The Nickel electroforming used for XMM (see bibl. [102]) has been considered as a theoretical possibility for XEUS: with so large diameters, however, the segmented structure is mandatory: the segments may be rectangular segments of $1m \times 0.5m$ size, a series of them will be assembled in 562 *petals* and the petals assembled in the final telescope optics. In the first phase (XEUS I), 266 petals would be assembled in a 5 m diameter module (see fig. 3.34), to be assembled on ground and launched. The remaining 269 would be assembled after 4-6 years of operation by the robotic arm of the ISS, taking so the diameter to 10 m.

In this design, the optical assembly has to be excellent in order to guarantee the goal angular resolution (2") and the gravity effect on the mirror structure deformations have to be carefully studied. The XEUS I effective area in hard X-rays could be improved by the adoption of W/Si graded multilayer coatings: in this case a careful study of mechanical stresses is to be dealt (see sect. 3.5.3, page 71). Moreover, the size and number of plates to be coated would be very large (17500, for a total area to be covered of 8750 m^2), so the necessity to coat large surfaces requires a suitable (and industrializable) multilayer deposition method. For the outermost shells, indeed, the grazing angles would be so large that the multilayer d-spacing would be too small in comparison to the achievable roughness level (see sect. 3.5.2, page 66). The outermost shells would be so devoted to the soft X-ray reflection, that could be achieved simply with some couples of bilayers (to minimize the photoelectric absorption) or by single Au-layers with Carbon overcoating (see sect. 3.6, page 74).

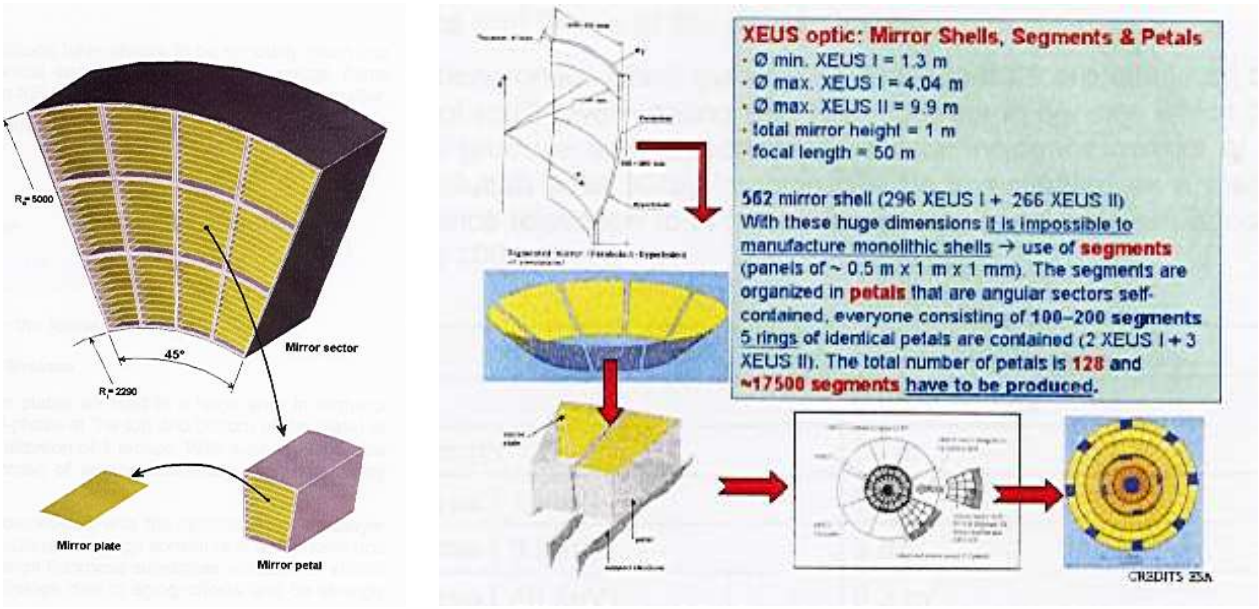

Figure 3.34: (left) Scheme of a petal of the XEUS optic module. The mirror plates segments are assembled at the respective incidence angles in a single petal (credits: Media-Lario s.r.l.).
(right) The circular disposition of a number of identical petals constitutes the XEUS telescope optic (credits: Media-Lario s.r.l.).

The extremely strict XEUS requirements in angular resolution imply that the mirror wall need to have a sufficient stiffness (some mm) to resist to the deformation factors. On the other side, the mass limit of the optics (25 tons) implies that the ratio mass/geometric area must be exceptionally low, 0.08 Kg/m^2 (for comparison, for XMM was 0.22 Kg/m^2, see fig. 2.10).

Even in this case, the overall optic mass would be probably too large to be carried to orbit by an Ariane V vector: an alternative technique for the production of replicated optics with a lower weight could be considered, using as substrates ceramic materials (SiC, Alumina, see sect. 2.3.3, page 33), figured Si wafers, thermally formed Borosilicate glass plates (Borofloat^{TM}). The epoxy replication is instead ruled out due to the CTE mismatch of the resin with the substrate: the thermal variations due to the MSC rotation (-30 ^{o}C $\div$ -40 ^{o}C) would thus produce strong optics deformations and degrade the optical resolution.

Another problem is the XEUS orbit: the LEO (Low Earth Orbit) could seem the most simple choice as the aperture background is effectively shielded by the Earth magnetosphere, since the orbit deployment would seem simpler, and in view of the XEUS II phase, This choice, indeed, would mean a large number of necessary launches and a reduction of the mission lifetime, because a large amount of fuel expense would be necessary to keep the DSC at the focal point in a non-Keplerian orbit (see bibl. [57]). A more economic eventuality is the possibility to deliver a single, *large payload in the Sun-Earth Lagrangian point L2*. In L2 the propellant usage will be very modest and XEUS could be operational during 15 years.

With a single launch MSC in L2, the "petals" have to be strictly packed within the spacecraft volume: the current design foresees that the mirror will be folded in half and closed in a "canister" for the stowed configuration. Once deployed, the mirrors would be shaded from the Sun radiation by the same halves of the canister: the shading would keep the optics thermalized within 1 K. The DSC will be launched in L2 after the successful deployment of the MSC.

A new solution for the optics technology for XEUS has been proposed (see bibl. [57], bibl. [58], bibl. [59]),

	XMM	XEUS
Focal length	7.5 m	50 m
Number of modules	3	1
Min. diameter	0.3 m	1.3 m
Mirror length	70 cm	1 m
Max. diameter	0.7 m	10 m
Geometric area	0.15 m^2 per mod.	30 m^2
Ang. res. (HEW)	15"	2"
Optics mass	510 Kg (total)	25 tons (Ni)

Table 3.5: Initial baseline for the XEUS mission optics (a single, grazing incidence Wolter I optic module), compared to the corresponding ones for XMM.

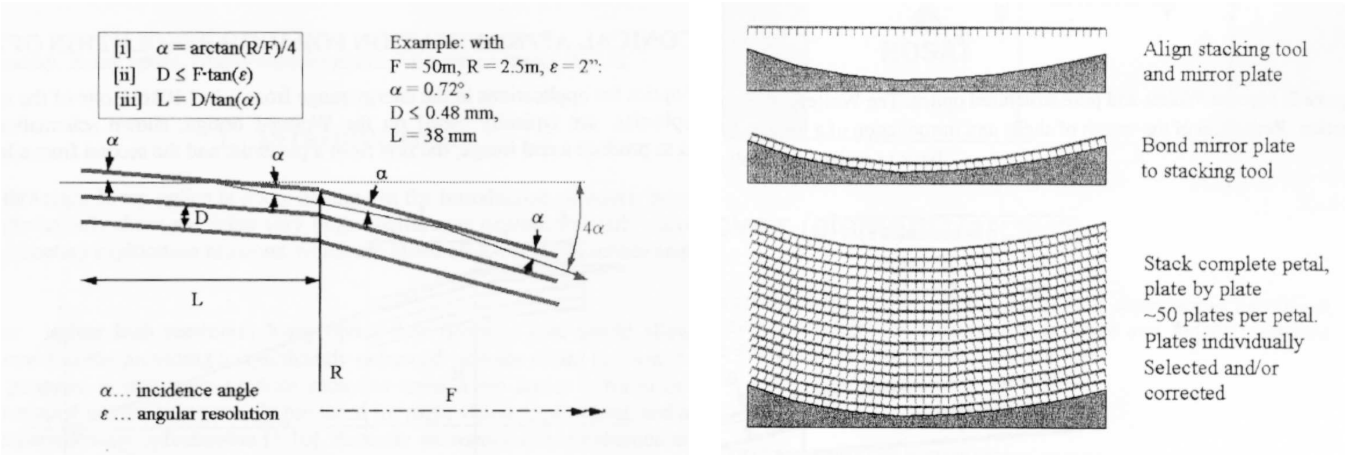

Figure 3.35: (left) Requirements of a double cone surface to replace a Wolter I optic. (right) assembly of the Silicon plates to produce the mirror petals with the right curvature, imposed by a conical, concave mandrel (credits: bibl. [58]).

in order to lower abruptly the ratio mass/geometric area keeping good angular resolution, the *Silicon micropore optics*. They are constituted by Silicon plates with micropores that double-reflect X-rays (see fig. 3.35), providing the focusing geometry: the plates are curved in order to form the mirror petals that are assembled in a circular structure. Two of these structures, once superposed, return a double-cone approximation of the Wolter I geometry (see fig. 3.36).

Silicon wafers can be used as a starting point to produce micropore optics. They are ribbed (with very smooth surfaces) and superposed on a precision Silicon mandrel that gives the curvature for a single conical surface. The ribs form the micropores and the superposed plates form a stiff structure that will be used to assemble the mirror petals (see fig. 3.35). Silicon micropore plates can in principle achieve good angular resolutions, HEW 5.5" with some small (2 cm^2 area) prototypes, with the advantage of a lightweight (200 Kg/m^2 effective area @ 1 keV, to be compared to the 2300 Kg/m^2 effective area for XMM).

The most critical point is, indeed, the alignment process during the mirror integration: measurements in full illumination of the whole stack have returned HEW values of 18". The PSF is, moreover, characterized by relevant X-ray "baffles" (see bibl. [57]).

Finally, we can say that the design of the XEUS MSC is a scientific and technical challenge that will require a considerable effort in the next years. Even if micropore plates have become the official current baseline ESA design for XEUS, studies of other techniques are in progress: multilayer coatings are still considered a viable solutions for the XEUS optics, and in particular the INAF-OAB, in collaboration with Media-Lario, has started a development project to produce W/Si multilayer mirrors deposited on glass/silicon curved substrates to evaluate the feasibility of a multilayer-based design.

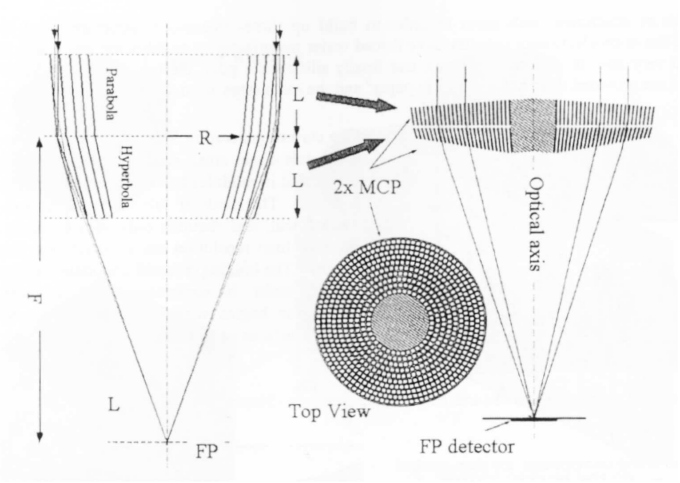

Figure 3.36: Normal Wolter and pore structured optics. The Wolter design employs pairs of hyperboloids and paraboloids. A strong reduction of the shell length with a long focal length allows two set of pores placed in series to reproduce the shell structures (credits: bibl. [58]).

3.7.5 A simulation of soft X-ray multilayer mirrors with Carbon overcoating in XEUS

A preliminary evaluation of the potential increase of effective area achievable with the use of soft X-ray multilayer mirrors discussed in the section 3.6 has been performed also for the case of the XEUS (see sect. 3.7.4, page 87). The results of this evaluation have been obtained assuming the first baseline design of the mission (the change of the XEUS design configuration will be envisaged for future simulations, see sect. 3.7.4, page 87): in performing the simulation for XEUS I, broad-band supermirrors (multilayers with graded structure) have been assumed, while for the XEUS II mirror shells constant d-spacing structures plus Tungsten + Carbon overcoating the reported parameters in tab. 3.6 have been used.

The total XEUS effective area (XEUS-I + XEUS-II) in the 0.1 10 keV energy window after the simulation is showed in fig. 3.37 where, as usual, we also reported for comparison the value achievable with mirror shells coated with a simple Au layer. In figure are also represented the equivalent profiles for the XEUS-I phase alone. In this evaluation we did not consider any reduction of effective area due to the vignetting by the mechanical structure (that should affect this value for less than 10 %). From the fig. 3.37 it seems evident that, with respect to the use of Gold, multilayers would allow to get an important increase in the effective area between 0.5 and 10 keV. This improvement is in part due to the use of the C overcoating (between 0.5 and 3 keV), in part to the Bragg peak of the multilayer mirror (between 3 and 10 keV).

Number of bilayers	30
Couple of Materials	W/Si
Multilayer period	80 $\mathring{A}$
Γ factor	0.35
W capping layer thickness	80 $\mathring{A}$
Thickness of the C overcoating	100 Å

Table 3.6: Multilayer structure adopted for the XEUS-II mirror shells.

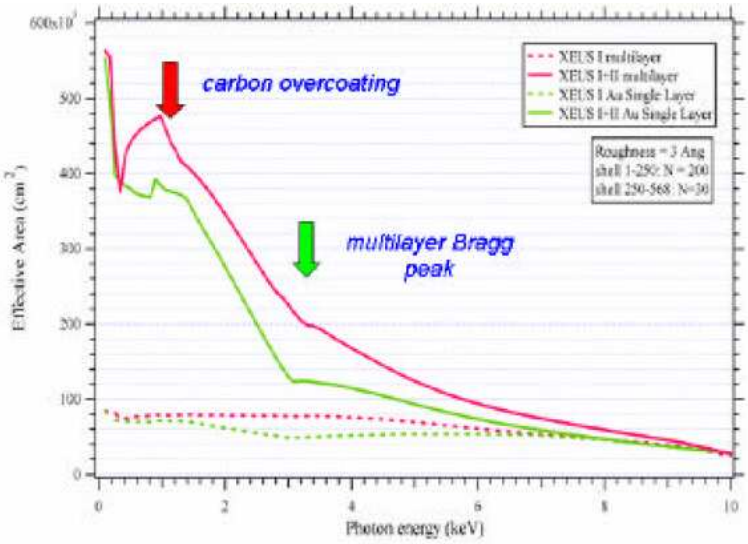

Figure 3.37: The total XEUS theoretical effective area achievable by the use of soft X-ray multilayer mirrors (credits: bibl. [95]).

3.8 Possible spin-off's of the developed activities

3.8.1 EUV and soft X-ray lithography

Mo/Si multilayer coatings have found an application in the EUV nanolithography of electronic components. The lithography of circuits is a procedure very widely used in electronics to print circuits: since some years the performance requirements to the microprocessors have imposed an increasing degree of complexity in the integrated circuits, with a density of components doubled every 18 months, on average (*"Moore law"*): thus, the lithographic technique used to produce them is reaching smaller and smaller sizes. At present time, the integrated circuits to be produced have reached an order of magnitude of the nanometer, and the technological issue to manufacture them is called *nanolithography*.

The lithographic process starts from the deposition of a thin layer of the material to be modeled (called *resist*, doped Si, SiO_2, metal...) on a substrate (usually a Silicon Wafer). The resist is exposed to UV radiation in the points that will be removed from the film: in other words, an UV image reproducing the negative pattern of the nanocircuit is projected on the resist, degrading its chemical resistance to a special solvent.

In the usual lithographic process, the image was obtained by contact of the resist to a quartz mask with a Cr pattern drawn on it: the quartz is transparent to the UV radiation, while Cr is opaque and protects the resist from the irradiation in the points to be kept on the substrate. The points where the resist is irradiated become soluble to the attack of a chemical agent, and can so be removed.

In the nanolithographic process a mask cannot be directly laid on the resist, and the image is obtained by reflection on the mask, traced with an absorber material (see fig. 3.38): the UV pattern is reproduced on the resist with a very reduced size, and the following removal process allows to obtain a nanometric pattern.

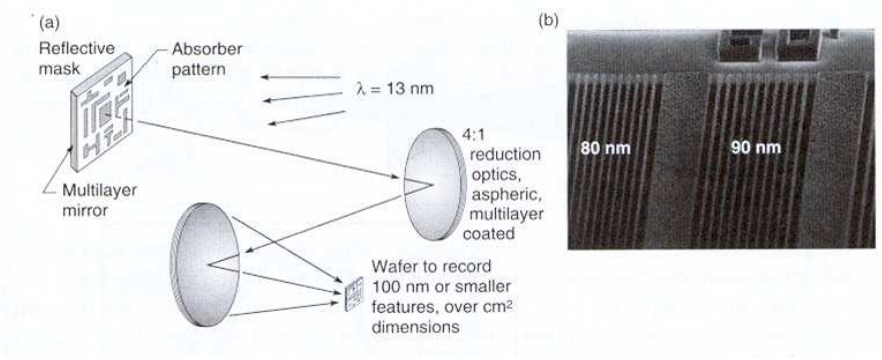

Figure 3.38: The scheme of EUV Silicon lithography. A 13.5 nm source emits UV light in all directions, is collected in almost-normal incidence by a reflector on a mask that reproduces the pattern to be projected on the Silicon film (credits: bibl. [25]).

All the process can properly work (i.e. reproducing the mask pattern with a nanometric precision) only if the diffraction effects can be neglected. This aim may be pursued by adopting EUV (Extreme Ultra Violet) radiation: the recent developments of the nanolithography suggested to use the Silicon emission line at 13.4 nm. The problem of the nanolithography is so reduced to the capability of collecting, reflecting and focusing the EUV radiation on the resist, that is, the reflection and focusing very soft X-rays (0.09 keV).

At the Si-L line energy (13.4 nm), two solutions are possible:

1. grazing incidence optics, single-layer coated;

2. normal incidence optics, Mo/Si multilayer coated.

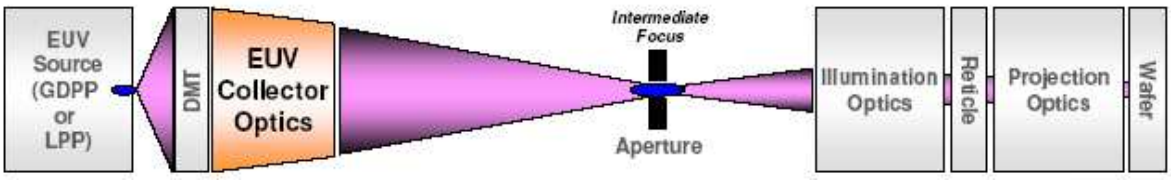

Figure 3.39: The Zeiss optical arrangement for nanolithography. The EUV collector is a grazing incidence optic with Wolter-1 geometry nested shells that focuses the EUV rays in an intermediate focus: the successive optics are a system of 6 normal-incidence Mo/Si reflectors. Due to the high number of reflections, the multilayer coated mirror reflectivity must be high in order to have a sufficient EUV flux on the resist surface (credits: ZEISS).

Single-layer coated optics may be used as *collector* of the EUV light from the source. The collector is usually conical, with the EUV source in a focus, and its task is the collection of the light from a wide solid angle to the elements that have to focus the radiation on the resist. Mo/Si periodic multilayer (40 bilayers, d=69.4 Å, Γ =0.39) optics are instead used to produce the image on the resist, and they are designed in order to provide the maximum reflectivity (near 74%) at 13.4 nm.

The multilayer development activity will so find a natural spin-off in the development of high reflectivity multilayer for EUV: in particular, the adopted deposition method (the e-beam evaporation) will take the advantage of a fast deposition on large mirrors.

3.8.2 Radiology and X-ray therapy

A large benefit of optics with multilayer coatings could also come to medical applications, especially in radiology. Radiographies exploit X-rays with energies over 15 keV, because soft tissues are almost opaque under this limit. Bones and hard tissues are instead opaque for much larger energies, so they appear clearly visible in a photographic plate, but anomalies in soft tissues (like a cancer) cannot be seen in the early development phases with sufficient image contrast to allow an early diagnosis. On the other side, the X-ray dose absorption limitation do not allow a too large integration time.

This is especially the case of mammographies, as human breast is constituted completely by fat tissues and fiber-gland tissues: the identification of the structures present in the breast is possible due to the different attenuation in X-rays, which is very similar in the case of cancers, non-patologic microcalcification, and normal tissues. The optical contrast between a cancer and benign microcalcification is, indeed, larger in soft X-rays: that makes, considering the lower energy limit of 15 keV, an optimum photon energy around 18 keV for maximum image contrast. Even with this choice, an high-contrast and detailed mammography very difficult to obtain, unless we adopt unacceptable dose expositions.

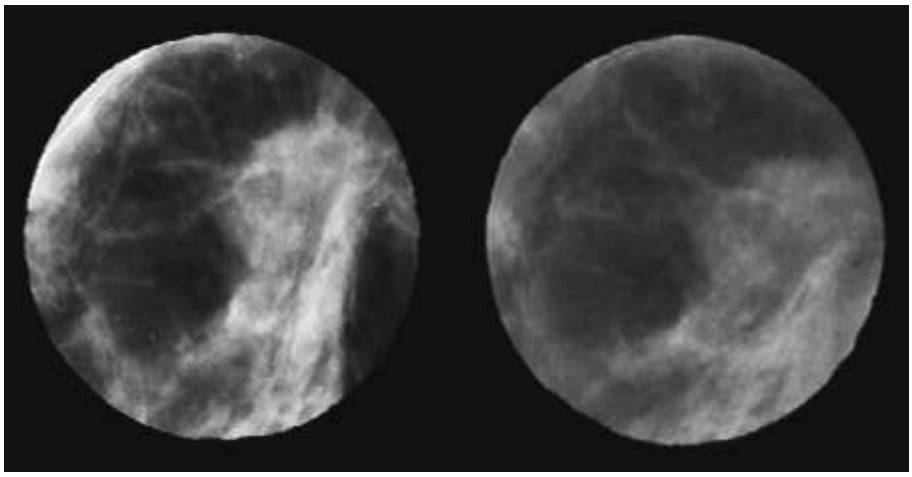

Figure 3.40: Radiographies of the same breast, take with two different sources: (left) Synchrotron radiation at 18 keV, (right) a conventional X-ray tube with a Molybdenum anode and a Molybdenum filter (credits: Burattini et al., see bibl. [131]).

A conventional X-ray source for mammographies is the X-ray tube with a Molybdenum anode and a Molybdenum filter with accelerating power of 28 kV. The filtration of the 17.4 keV from the bremsstrahlung continuum is necessary, because the softest X-rays would be completely absorbed, with a dose increase without image benefits: the hardest photons are not selective between tissues and do not improve the image

contrast, and moreover they are easily Compton scattered in soft tissues; the presence of a diffuse radiation considerably degrade the radiographic contrast. Thus in order to achieve an high quality image, it would be essential to discard completely the X-ray continuum, a task that is been pursued by improving the filter, but without an ultimate, satisfactory result.

The radiation collimation is also an important parameter: X-ray beam has to be wide to fill the radiography field, but the use of wide sources would return a poorly directional beam with the formation of shadows without clear boundaries: the image would be degradated, especially in details that could reveal early, small tissue anomalies.

We can so conclude that adopting a highly *collimated and monochromatic 16-20 keV X-ray radiation* more contrasted mammographies could be obtained (see bibl. [131]) taking also the advantage of a dose reduction: such X-ray sources are available, for instance, as synchrotron light. Some mammographies taken in synchrotron light (see bibl. [131]) have showed very satisfactory results (see fig. 3.40), but the use of a synchrotron in the medical practice is unlikely adoptable.

An adoptable solution can be the realization of a monochromator to be use with a conventional X-ray tube. Monochromators used in X-ray diffractometers use Silicon crystals that reflect according to the Bragg law, and due to the very large crystalline plane number involved, they can achieve a very good resolution. Some prototypes implementing mosaic crystals (HOPG) have been, indeed, produced (see bibl. [131], bibl. [132]), with a flux gain with respect to usual crystals, a good monochromatization (12%) and large field (10.5×12.0 cm^2).

Here we want to observe that an X-ray optic may be used to both monochromate and collimate the radiation from a conventional X-ray tube with Mo anode, and so the multilayer development activity may find an interesting spin-off in this field. The optic may be constituted of nested shells (with Wolter I profile or a conical approximation) coated with multilayer coatings with *constant* period along the stack, and the X-ray source could be put in the optic focus. If the multilayer period is properly tuned to the incident energy and the incidence angle on every shell, the optic would produce a *monochromatic* beam with the desired energy and would absorb all the other wavelengths. Moreover, as the optical profile is very sharp (enough to satisfy the astronomical requirements), the outgoing beam would be *highly directional and collimated*, and would permit radiographies with clear and defined shadows. A similar technology could probably be used also for radiotherapy, with the advantage of a better dose control and spatial precision in the tissues irradiation.

Chapter 4

Thin-layer deposition methods

In this chapter some outlines of the deposition methods that can be followed to produce multilayer coatings will be provided. Not all the approaches will be suitable for the multilayer implementation with respect to the possible industrialization of the process, the reliability in terms of internal micro-roughness and stress, the fast and large surface covering necessary, e.g., to cover the very large XEUS surface. A particular attention will be paid to the methods that will be likely used for the future development of the hard X-ray coatings of future telescopes.

4.1 Thermal (or Joule) evaporation

In this classical and old PVD (Physical Vapour Deposition) technique, a material is placed in a refractory crucible, heated by an electrical resistance. The crucible is kept under vacuum (10^{-6} torr) and as the material temperature is raised, the contained material is evaporated and condenses on the substrate. This basis technique is not widely exploitable because the rate of deposition requires an high level of vacuum and the deposition of heat in the target is not very effective. Moreover, the chamber walls are often heated too, causing the release of some of their adsorbed gases and water vapour at the time of coating deposition. The film may so include residual gases, and it results in porous, low-durability, soft films. This method is not suitable for astronomical space X-ray optics.

4.2 Electron beam evaporation

A very diffuse PVD technique which allows the fast deposition of thin films is the *e-beam* evaporation (see fig. 4.1). This process, like the thermal evaporation, is based on the heating of a material placed in a refractory crucible, but in this case the heating is produced by an high-energy (5-15 keV) and high-current (several ampere) *electron gun*, focused on the surface of the charge, while the crucible is water-cooled. The energy transfer ratio of the electrons is low enough to convert almost all the energy in local raise in temperature, leading to the local evaporation of the target. The walls are much less heated and we can evaporate also refractory materials, the evaporation point of which exceeds that of tungsten resistance.

The heating process is in this case very efficient and allows a very fast deposition way for single-layer thin films. However, the evaporated atoms have a thermal spectrum with average energy 0.1 eV. This energy is insufficient to cause the surface diffusion of the growing film: consequently, evaporated films will have

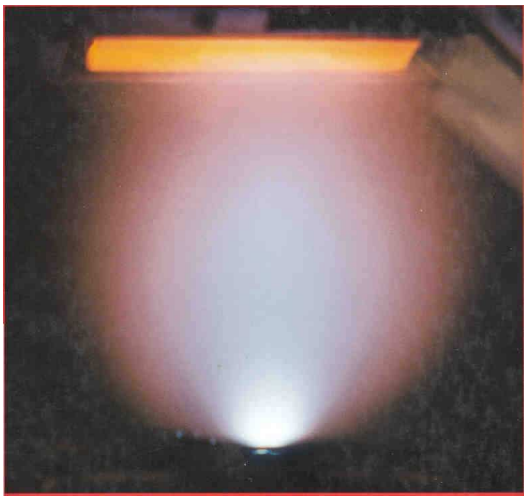

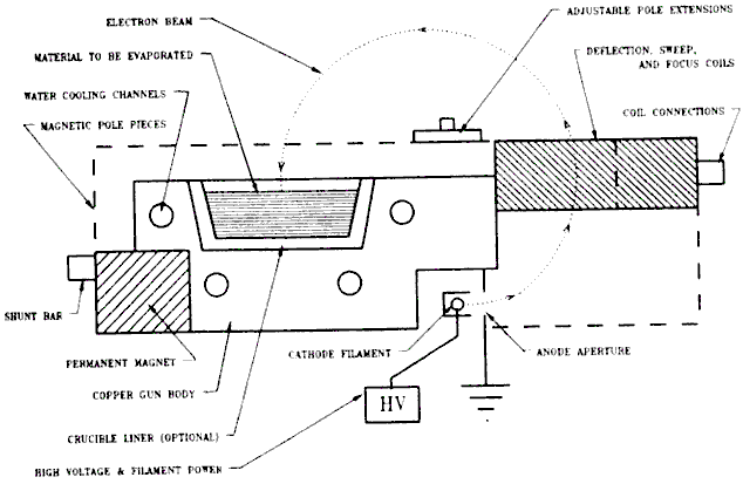

Figure 4.1: (left) Image of a deposition by thermal evaporation (credits: bibl. [116]). This vaporization (in this case, an high-temperature superconductor) is obtained with a pulsed laser (an alternative and effective method to evaporate the target). The substrate heating (750 ^{o}C) is evident, a positive factor to improve the smoothness, but a negative one for the thermal stresses. Also the visible beam divergence, typical of the thermal (and e-beam evaporation), is to be corrected using *equalization masks* with rotating substrates. The equalization mask improves the film uniformity and the beam directionality, reducing so the flow *shadowing* (see sect. 3.5.1, page 63) that is in a large extent responsible for the roughness growth during the film growth .
(right)Schematic of a typical electron beam source: the e-beam is deviated of 270^o by a magnetic field that drives it on the target (credits: bibl. [118]).

a low density and are relatively soft. On the other side, the e-beam is a method that allows the uniform deposition on large surfaces (see bibl. [32]), a good advantage when X-ray mirrors have to be produced.

The layer thickness of the deposited film has to be monitored with *quartz microbalances*, i.e., piezoelectric quartz exposed to the evaporating flux and connected to a frequencymeter: the oscillation frequency of the quartz (some MHz) is slowly decreased when some material is deposited on it: the balance is very sensitive to the deposition of some $\mathring{A}$ per second or less and it is also very fast, so it can be used to monitor in real-time the evaporation rate. However, being the evaporation very anisotropic, the real thickness deposited on the substrate will be different from the value recorded by the quartz probe, unless they are placed very near. Moreover, the quartz is sensitive to the density fluctuations of the depositing material because the frequency decrease depends on the deposited *mass*, and the frequency is also affected by the thermal irradiation from the source. This problem is important especially when evaporating low-density materials, when the frequency decrease per second is modest.

It should be noted that the e-beam approach has been successfully used by Media-Lario for the deposition of the Au reflecting coatings on the XMM mandrels. Concerning the deposition of thin multilayer films for EUV and X-ray applications, which require a very small internal roughness and a density for deposited layers close to their bulk values, it it convenient to provide specific energy to the atoms deposited by e-beam. The energy can be provided by an ion-beam striking the surface at a grazing incidence (several hundred eV) after the deposition of each layer (*Ion Etching*) or striking the surface at 30 degrees off-normal (*Ion Assistance*) at 25 $\div$ 100 eV. The incoming energy helps the relaxation process in the film microstructure, improving smoothness, adhesion, stability, durability, density, similar properties as sputtered films (also the stress values become similar as those of magnetron sputtered films: see bibl. [120]).

4.3 Sputtering

The process in which fast ions bombard a sample, with its consequent evaporation, is called *sputtering*. Physically, incident atoms collide elastically with the target atoms, without chemical reactions (the used ions are always inert gases, Ar^+ or Kr^+). The ions transfer their momentum to target atoms, so they leave the surface. The emission of target material is connected to secondary electron emission, ion reflection at the target surface, ion implantation, emission of photons, structural changes in the target. Flowing water keeps the target cool, so that thermal evaporation does not occur.

The properties of the emitted particles depend on the bombarding ions, their kinetic energy, incidence angle, atomic mass, target material and its structure. The maximum energy transfer rate is reached when the atomic mass of the target and the ions is the same.

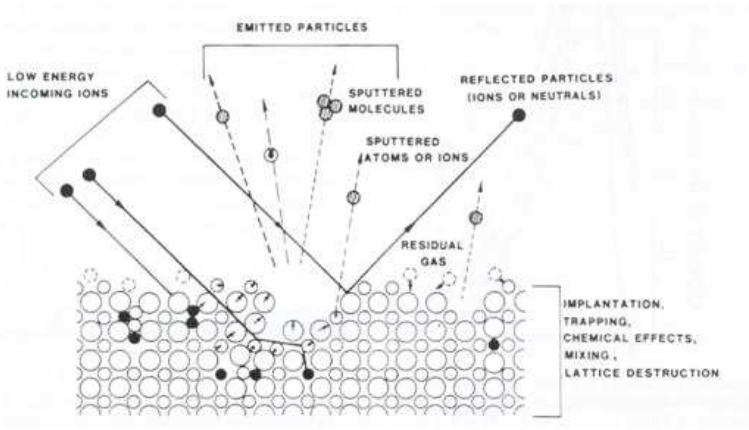

Figure 4.2: General interaction processes related to ion-sputtering taking place in proximity of the target surface (credits: bibl. [119]).

The *sputtering yield* (the number of emitted atoms per incident ion) varies with the energy of the incident ions (see fig. 4.4). Sputtering starts at energies approximately equal to the heat of sublimation (tens of eV). Above this threshold, the yield increases and reaches a maximum at 10 keV. For higher energies the penetration depth causes ion implantation and less effective momentum to the target atoms. For incident angles below 60^o the sputtering yield increases with increasing angle with an inverse cosine law ($\propto (cos\theta)^{-1}$) because the penetration depth is reduced. It reaches a maximum for angles between 60^o and 80^o, then it sharply decreases as *ion reflection* increases.

The sputtered atoms have kinetic energies with a non-thermal spectrum, and typically (1-10 eV) they are of an order of magnitude higher than in the case of thermal evaporation. The high energies lead to formation of very dense films with high refractive indices and low environmental shifts, in addition to a good smoothness. Moreover, the evaporation rate is physically related to the ion flux and is very stable: the thickness control is even obtained by time calibration, without any need of quartz probes.

4.3.1 Diode/Triode Sputtering

The conventional technique for sputtering (the glow discharge) is produced applying a strong enough electric field between an anode and the target. The ions of the inner gas are accelerated and collide on the cathode: this results in erosion with emission of atoms. This simple process is called *diode sputtering*.

Sputtering	Thermal Evaporation
Very stable rates	Deposition rate can fluctuate
Thickness control by timing	Needs error compensating in-situ thickness monitor
Substrate holder rotates past sputter sources	Shutter in front of sources
Good uniformity requires large deposition system chamber diameter >3 × mirror	Good uniformity over large areas Diameter > mirror diameter
Might run unattended at high deposition rate	Speed limited by thickness monitoring system
Kinetic energy of deposition usually larger than 100eV can be adjusted	Kinetic energy smaller than 0.5eV not adjustable
Film surface bombarded by sputter gas ions	Ion polishing added for smoother boundaries
	Laser plasma source has higher kinetic energy than conventional thermal source, adjustable

Figure 4.3: Some general differences between a sputter deposition system and a thermal evaporation system for the fabrication of X-ray multilayer mirrors (credits: bibl. [32]).

The diode sputtering guarantees an high sputtering rate, but it is not considered as a suitable solution, because the energy of the ions as well as their incidence angles are difficult to control. Sometimes, a grid is included in the system to help stabilize the discharge, and these are called *triode sputtering*. This arrangement is suitable when the target is an insulator. Because of the very high capacitive impedance of the plasma, very high voltages are necessary to sustain the discharge. As the spatial closeness of target to substrate is required, interactions between plasma and growing film cannot be avoided: even if we use a RF voltage to reduce the necessary voltage to few hundreds of volt, high deposition rates imply an electron bombardment leading to an unacceptable substrate heating (500 ^{o}C).

4.3.2 Ion Beam Sputtering (IBS)

The IBS (*Ion Beam Sputtering*) arrangement uses an ion-gun to produce an accelerated ion beam. Using this method, the ion energy and their angle of incidence may be sharply defined, and there is no substrate bombardment. A beam neutralisation is necessary to avoid the electrostatic divergence of the beam, as well as the repulsion between the charged substrate and the ion-beam. The achievable deposition rate is proportional to the sputtering yield and to the ion current: it is, indeed, considerably less than the achievable one by e-beam evaporation (see fig. 4.3).

The beam must erode evenly the target and the layer has to be deposited uniformly, therefore the beam has to be large: the area of a sputtering target has then to be of *an order of magnitude larger than an equivalent evaporation source*. A satisfactory design is provided by a *Kaufman-type source*: an Argon atmosphere is ionised by electrons produced by an hot filament and accelerated by a moderate voltage. Two grids capture the electrons and accelerate the ions: this design allows beam sizes of 20 cm diameter,

with currents up to 20 mA/cm^2 and energies in the range 500 ÷ 2000 keV. This design has however some disadvantages, like lifetime problems or sputtering on the walls of the ion-generating chamber, leading to contamination of the ion-beam.

The neutralisation of the beam (but without ion recombination) may be obtained using an hot filament: the filament, indeed, is sputtered by the ion-beam, and the ion beam may in turn be contaminated by the filament material. An hollow cathode is then suitable, or a shielding of the filament using a non-ionised gas (Plasma Bridge Neutraliser). The resulting beam plasma interacts weakly with the residual gas in the chamber.

In the IBS setting, the gas pressure in a sputtering system is relatively high compared with that in an evaporation system (10^{-4} mbar vs. 10^{-6} mbar), therefore, the mean free path of a sputtered particle is one-hundredth of that in an evaporation system: for the target atoms, to avoid the loss of much of their energy, the distance between target and substrate must be as small as possible. Inert gases (Ar,Kr) are usually used since chemical reactions are unwanted: if instead the compound coatings deposition is desired, reactive gazes like Nitrogen are used. In this case the process is called *reactive sputtering* (it used to produce TiN coatings, see sect. 6, page 129).

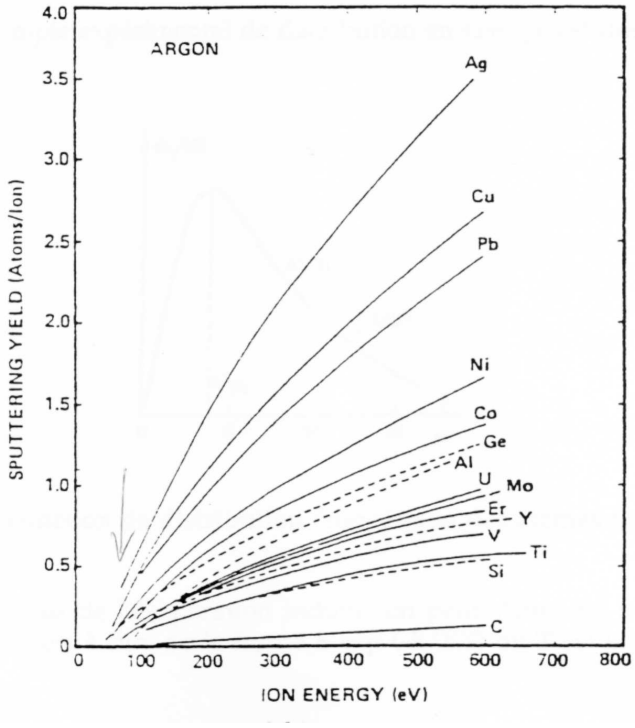

Figure 4.4: Sputtering yields for some materials, as a function of incident ion energy. .

The IBS takes the advantage of a more directional deposition compared with other methods (evaporation, magnetron sputtering), which in turn permits the deposition on the substrate at near-normal angles: the lack of directionality causes a strong increase of shadowing effect, responsible for a large part of the multilayer roughness amplification (see sect. 3.5.1, page 63). The degradation of the multilayer caused by poor sputtering directionality as well as off-normal incidence is dramatic (see fig. 4.7).

As natural extension of the IBS, a further ion-etching (see above) on the deposited layer can be used, combining the benefits of both methods (very hard and durable films, low interface roughness).

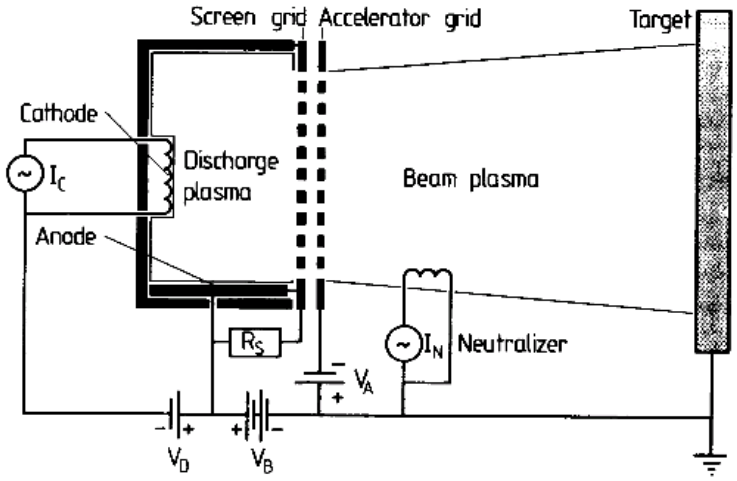

Figure 4.5: Scheme of a Kaufman-type ion beam source (credits: bibl. [117].) .

4.3.3 DC Magnetron Sputtering

Magnetron sputtering is a technique that was developed to reduce the substrate heating and to improve the deposition rate at moderate voltages. The concept is that the free electrons can be trapped by magnetic fields and controlled. The magnetic fields are weak enough so that the paths of heavy ions and charged sputtered atoms are not significantly affected, but the electrons are confined in vicinity of the target, and do not bombard the substrate. Moreover, the electrons are trapped in a close race-track without touching the solid surfaces, so that they can ionize the gas more efficiently, and a lower pressure (10^{-3} mbar) is necessary to sustain the plasma: a further advantage is the lower number of collisions between the sputtered atoms and the plasma ions, which results in higher energy of sputtered particles.

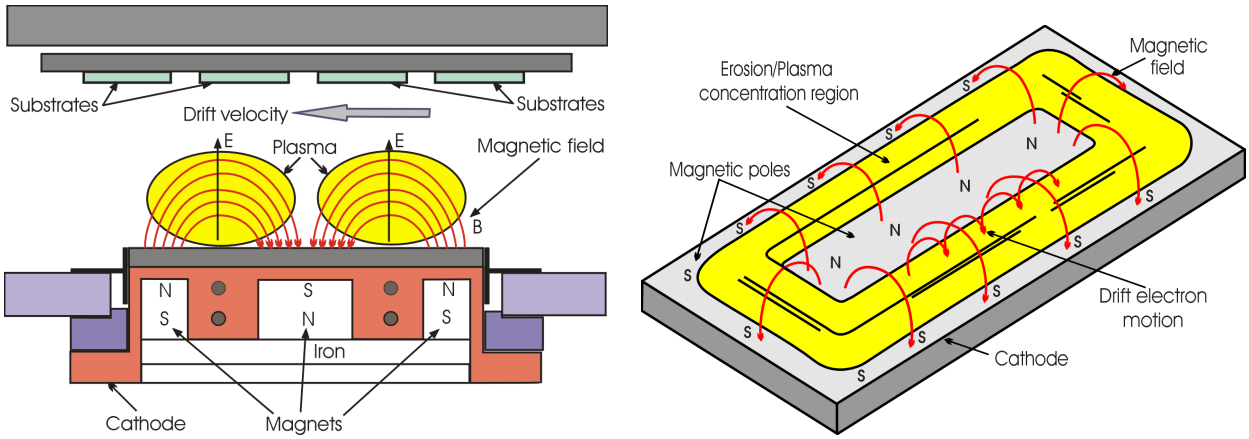

Figure 4.6: A typical arrangement for Magnetron Sputtering deposition method: (left) side view, (right) top view.

One of the most effective arrangements is the planar magnetron (see fig. 4.6). It consists of a copper body with a plane front surface to which the target plate is attached. Magnets inserted into the copper body from the back side create a toroidal-shaped magnetic field in front of the target. Many arrangements and designs are possible, provided that the magnetic field (200-500 G) is perpendicular to the electric field along a closed path. In such conditions the drift velocity of electrons is perpendicular to both fields, and

so they follow a closed path. The plasma impedance is substantially reduced (the voltage required is about 300-700 V), and current densities of 60 mA/cm^2 can occur at power densities of 40 W/cm^2.

The magnetic field may be generated by electromagnets (this offers the advantage of being tunable) or (usually preferred) by permanent magnets. In the case of a circular cathode, the magnets may be assembled to form a ring around a central magnet with inverted pole orientation. The magnets are back-shunted by an iron pole piece.

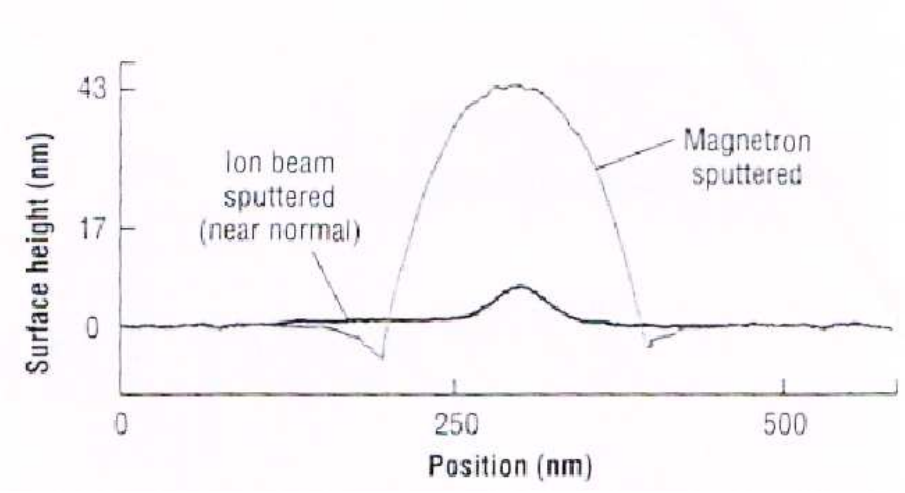

Figure 4.7: Surface topography from AFM scans for Mo/si multilayer films deposited by magnetron sputtering and near-normal incidence ion-beam sputtering on 50 nm Au nanosphere (credits: bibl. [113]) .

The distance between target and substrates is usually larger than the extension of the plasma cloud so that the substrates are not directly in contact with the plasma: the extension of the plasma lobes may be controlled varying the magnetic field. The more the extension is close to substrate, the more the ions condense at high energies. The properties of the film may then be varied tuning the magnetic field.

The erosion of the material is, however, non uniform. Most of the erosion occurs in the high-density plasma regions: directly connected is the low uniformity (5%) of the deposited layer. The bombardment of fast electrons is also non uniform, the substrate is heated at higher temperatures where the magnetic field is weaker. These effects may be reduced by spinning the substrate (the uniformity may then be improved to 1%). The deposition rate depends solely on the delivered power. Nevertheless, magnetron sputtering can produce films with significantly large roughness than IBS deposited films. This is due to an higher particulate emission during the deposition process, probably due to the poor flux directionality of magnetron sputtering (see fig. 4.7).

4.4 Ion Etching and Ion Beam Assisted deposition (IBAD)

As already mentioned, the e-beam evaporation may be improved by use of the ion-etching (see bibl. [130], bibl. [127]). An important parameter in order to reduce the roughness is the temperature of the substrate. With Mo/Si multilayers, the reflectivity is almost two times higher at deposition temperatures around 200 ^{o}C than an analogous multilayer deposited at room temperature(see bibl. [129]) and it stabilises itself along the process deposition (but with the risk of an interdiffusion increase). However, the thermal control of substrate is not always applicable in deposition facility.

The use of an *ion beam* incident on every deposited layer *has the effect of smoothing the peaks of the surfaces*. Substantially, it acts like an internal sputtering. Physically, this process is not completely understood. In fact, the collision of an high-energy ion locally raises the temperature, so that the surface behaves like a viscous, self-smoothening liquid. Very good results have been obtained with Mo/Si multilayer and a beam of 2 keV (see bibl. [129]) of Kr^+ ions at 50^o of angle of incidence, but every case requires a detailed study and optimisation of the ion energy and angle of incidence. The smoothing is, in fact, superposed to a statistical roughening caused by the same ion-etching, and may be analyzed with mathematical methods analogous to those used to study the roughness growth (see sect. 3.5.2, page 68). With others typologies of multilayer better results have been obtained by using grazing ions (see fig. 4.10): in this case, the reflection of bombarding ions is favoured and the ion implantation in the multilayer structure is reduced.

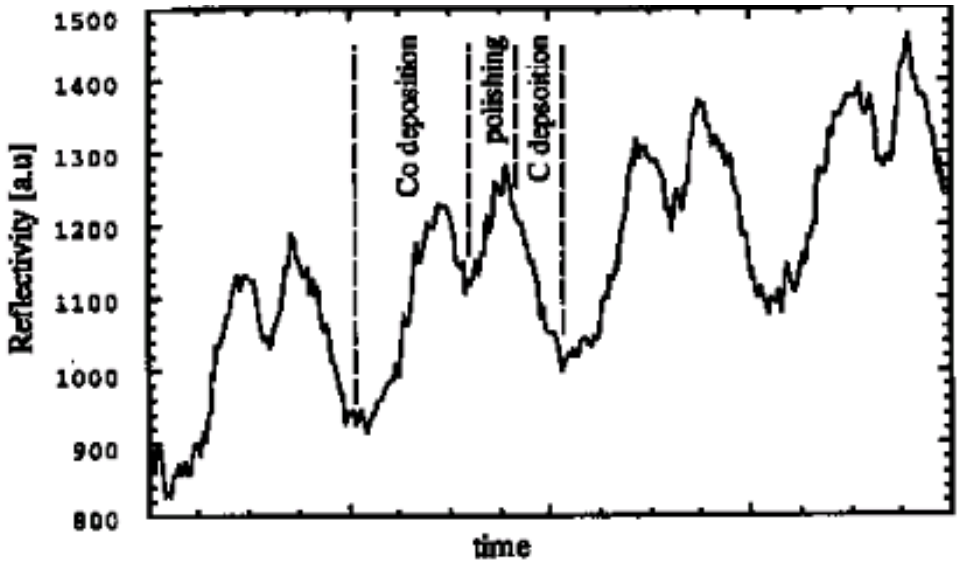

Figure 4.8: A polishing cycle in the Co/C multilayer deposition. The small gain of reflectivity at each cycle allow to reach a large reflectivity gain at the end of the deposition (credits: bibl. [75]) .

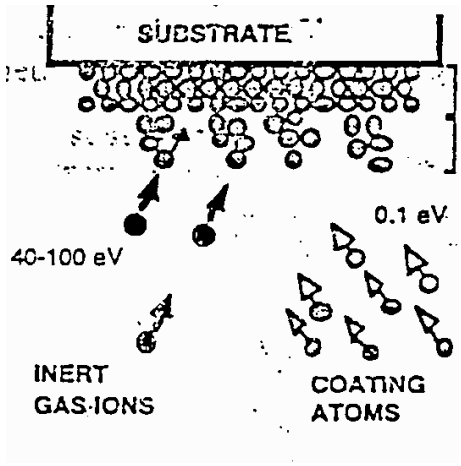

Figure 4.9: Scheme of the Ion assistance in e-beam film deposition (credits: bibl. [126]) .

The atom removal rate can be monitored real-time *in situ* evaluating the change in reflectivity on multilayer of an X-ray beam. This method is very practical but it is not always possible implement an X-ray diffractometer in the evaporation chamber. A further possibility is, indeed, the use of the *e-beam colliding on the target as a bremsstrahlung X-ray source* that can be used to monitor *in situ* the multilayer deposition and the reflectivity enhancement by ion etching or assistance, without an external X-ray source (see bibl. [110]).

A large enhancement of reflectivity of Co/C multilayer is reported using the ion etching (see bibl. [75]). During the deposition of Co the reflectivity is increased until it reaches the "resonance thickness", corresponding to a maximum: instead of stopping, a further layer is deposited and so the reflectivity is lowered. Then, the ion etching erodes the deposited Co until it removes the excess layer: the reflectivity is improved at each deposition cycle, over the maximum reached at deposition of Co. This is due to roughness reduction by ion etching, and even if the improvement of reflectivity might seem rather poor (some %), it is worth noting that every improvement in single-layer roughness implies a larger improvement in next layers: as a multilayer is typically obtained as superposition of hundreds of bilayers, every gain in smoothness may strongly enhance the overall multilayer reflectivity.

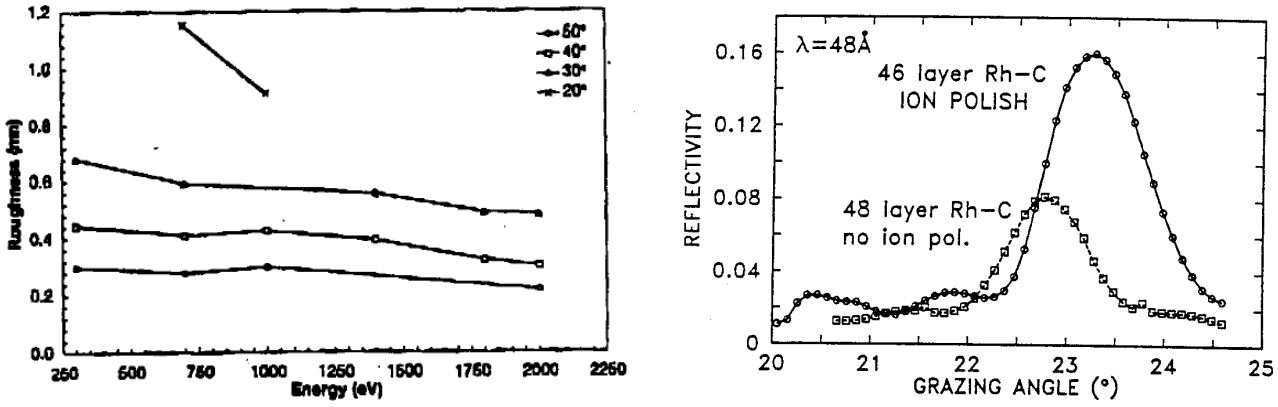

Figure 4.10: (left) An example of roughness reduction effect by ion polishing used to assist the e-beam deposition of Mo/Si multilayers, as function of ion energy and grazing incidence angle. The used ions were Kr^+ with a current of 19 mA. The roughness data are derived from the specular reflectivity at 1.541 $\AA$ (credits: bibl. [129]).
(right) An example of peak reflectivity enhancement (at 48 Å, synchrotron radiation) by ion-polishing on a Rh/C multilayer for a UV telescope. The use of an Ar ion polishing flux at 500 eV and 5^o incidence degrees has doubled the reflectivity with respect to a simple e-beam evaporated multilayer (with a roughness reduction from 9.5 $\AA$ to 6.3 Å). The Bragg peak is shifted because the ion polishing has reduced the multilayer period. Only the Carbon layers have been polished in order to avoid the Rh crystallization. (credits: bibl. [130]).

If the *in-situ* monitoring is not viable, it is possible to calibrate first the facility by monitoring the removal rate on a sample test of the same type. After the deposition, the layer will be exposed to the ion flux for the necessary time. As in the most deposition techniques, the substrate is spun to improve the coating uniformity. An other advantage of the ion-etching technique is that almost any layer thickness error may be corrected after the deposition of the layer.

The existing facility at Media-Lario (the vacuum chamber shown in fig. 7.4) is suitable to host an ion gun in its upper part, and then a ion-polishing system is feasible. The distance between the source and the substrate is large enough to improve the coating uniformity. The ion gun (Ar^+) installed in the coating chamber is more suitable for IBAD (Ion Beam Assisted Deposition, see fig. 4.9): the IBAD is produced with

a ion flux with an energy of $70 \div 150$ eV (considerably less than the used energies for ion polishing) with incidence angles of 30^o off-normal, and a rate ion/atom $0.6 \div 1.3$: the IBAD gives mobility and compactness to the surface without atom removal and ion implantation, improving density, smoothness, spectral stability and durability of coatings (see bibl. [126]).

IBAD coatings are also more resistant to the action of the oxygen and water absorption: metal coating, in particular, tend to show larger crystallite sizes when deposited with IBAD (see bibl. [128]), a feature allowing a reduction of intrinsic stress (see sect. 3.5.3, page 71).

4.5 Other methods

4.5.1 CVD and PECVD methods

In CVD (*Chemical Vapour Deposition*) the deposition is supplied by a reactive gas or vapour. A gas is adsorbed by the substrate (often heated to enhance the reaction) or by the previously coated substrate, and the reaction alters the substrate, developing a thin film. In other cases, the contact with a hot surface allows the decomposition of the gas, which in turn releases the element to be deposited (e.g. the contact of methane gas with an hot surface deposits a thin graphite film).

The CVD process may be assisted by a plasma. In this case the process is said PECVD (*Plasma Enhanced Chemical Vapour Deposition*), because the deposition is produced by reactions where the plasma is a catalyzer. For instance, the reaction

$$SiH_4 + O_2 \overset{Ar\ plasma}{\Longrightarrow} Si + 2H_2O$$

is a PECVD reaction where the Silane SiH_4 reacts with the Oxygen depositing a Silicon layer. The reaction, that would be too slow, is enhanced by the Ar plasma without substrate heating. SiC coatings may be deposited by PECVD (before being polished with diamond powders, however: see sect. 6, page 129).

These methods allow good deposition rates, and the gas do not react with the chamber walls. The gas flow is, indeed, difficult to manage; the convection can be non uniform. Moreover, the interface roughness id difficult to test. Finally, not all materials are suitable for CVD deposition.

4.5.2 MBE

The *Molecular Beam Epitaxy* is an improvement of the CVD technique, consisting in the direct deposition of the element by a reactive molecule. The molecule is chosen so that the deposited element grows in a crystalline lattice that fits the substrate lattice. The interface is sharp and with good adhesion. The MBE is often used in the semiconductor industries because it generates very thin films at lower temperatures than CVD: on the other hand, even if the interface is sharp, it is seldom uniform. Moreover, the crystalline growth often causes the formation of peaks and columnar features that destroy the uniformity that is necessary to deposit multilayer films. Finally, the deposition rate is usually very low.

Chapter 5

Substrate and multilayer characterization

In evaluation of the multilayer coatings quality and that of the substrates the tests involve some parameters (roughness rms, slope rms, curvature rms, correlation length, mean wavelength), the most significant among them with respect to reflectivity improvement and scattering being the roughness rms (see app. B). Also the distribution of roughness over the frequency window (the PSD Power Spectral Density, see app. B) gives useful hints about the diagnostics, evaluation and reduction of surface defects. We are mainly interested in frequencies which could degrade the reflectivity of the coating, that is the wavelength range $0.1 \div 100$ μm (see sect. 3.5.2, page 68 and app. C).

In order to determine the surface parameters, some tests are performed using topographic and X-ray facilities. In each measurement method, some points have to be taken into account:

1. the surface parameters describe a sample (or a set of samples) of the surface, assumed as representative,

2. each measurement covers only a limited range of spatial frequencies: the limits are determined by the Nyquist criterion (see app. B). This is the reason why the values of surface parameters are not unique, but depends on the window sensitivity of the used instrument,

3. the accuracy and precision are limited by instrumental and environmental noise.

A short description of instruments and used procedure follows.

5.1 Instruments for topographic measurements

The topographic instruments (PROMAP/WYKO, AFM, LTP) return direct informations about the 1-D or 2-D surface profile: they are usually designed to have an high precision level in a limited frequency range. However, they are switchable on some different windows. The sampled area at each scan is only a small fraction of the whole surface. Analysis routines are always included in these instruments. At the INAF-OAB also an *azimuthal profilometer* to measure the roundness of the replicated shells is available, but it will not be described here.

5.1.1 Phase contrast Nomarski microscope

The Nomarski microscope returns a surface image and it does not permit roughness measurements. Nevertheless, is it widely used to see the roughness of polished samples, and to understand the size and origin of surface defects.

The Nomarski microscope produces a polarized, polychromatic light beam, which is splitted by a Wollaston Prism, producing two correlated beams with perpendicular polarizations. A lens focuses the two beams at two positions on the surface under test, separated by one-micron distance. If a surface defect is present, the two beams will be reflected with two different phase changes. After a further polarization plane rotation, the beams interfere in the image plane. The phase variation appears in the variable brightness of the image, returning a surface map with a sensitivity of 1 nm. The space resolution is near to the used light wavelength, i.e. 0.22 μm.

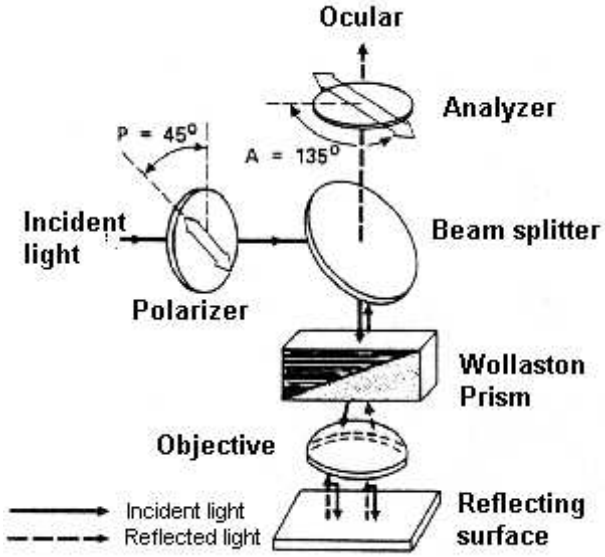

Figure 5.1: Scheme of the Nomarski phase contrast microscope.

Many magnifications are selectable (from 5x up to 100x) and the phase difference may be shifted in order to highlight the features at the most interesting height.

5.1.2 Atomic Force Microscope (AFM) and WYKO profilometer

The direct measurement of roughness at INAF-OAB is mainly performed using:

1. the WYKO (PROMAP) optical profilometer in the range $1 \div 300$ μm, eventually switchable to lower frequencies, but not of great interest for our purposes.

2. The AFM (Atomic Force Microscope), which is sensitive to higher frequencies, corresponding to a wavelength range $0.01 \div 50$ mm

The WYKO (see fig. 5.2) is an interferometric optical profilometer: it uses a polychromatic light source, splitted by an interferometer. One beam is sent to a known surface used as reference, while the other is focused on the sample. The reflected rays then interfere and from the interference fringes shape (that

would be parallel, dark bands if the surface were perfectly smooth) the instrument records the phase shift while scanning the sample length, and thus it returns a monodimensional profile of the sampled surface. The WYKO scans 1024 points with a 0.66 (20x) or 6.6 mm (2.5x) scan length. Usually the first setting is adopted (sample bin: 0.6 μm): it provides information on the lowest frequencies involved in the X-rays reflection, going from hundred micron up to 1 micron (Nyquist's limits), with a few angstroms height accuracy. The instrumental noise limits the effective lowest wavelength to 3 μm. A fitting of rough profile is necessary to subtract the misalignment of sample: the facility includes code for automatic roughness and slope calculation, profile drawing and fitting. We also deal in parallel with an analysis of the PSD.

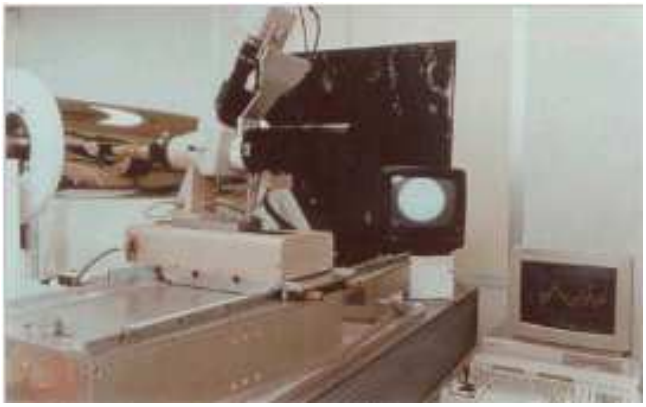

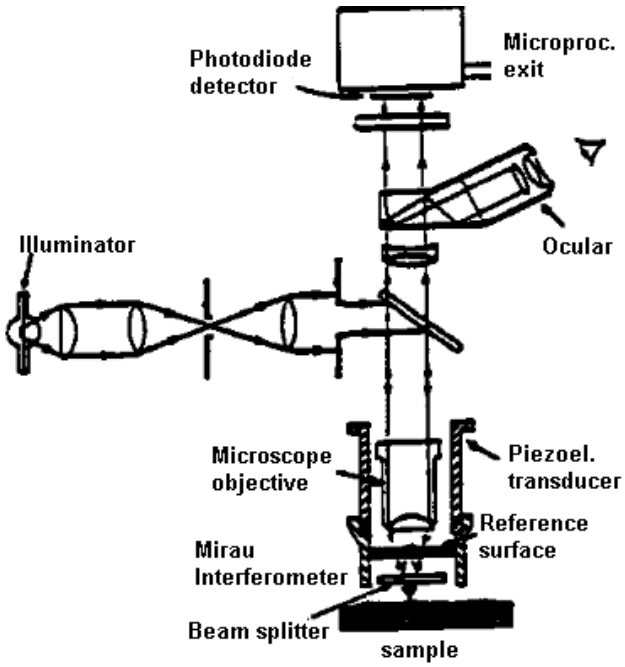

Figure 5.2: (left) Photo and (right) scheme of the WYKO profilometer. In the photo the WYKO is tracing a 0.6 mm long, 1-D profile of the surface of a superpolished mandrel for a shell replication.

The AFM (see fig. 5.3) is a "contact" instrument: it uses a probe (some microns) which, by means of careful computer controls, is approached to a position on the sample: the interaction forces between the probe and the atoms of the surface under test (some nN) cause a deflection of the cantilever where the probe is mounted on. At each height change, the probe changes position/oscillation frequency and phase, and this change may be monitored by a laser lever that amplificates the oscillation. By scanning the sample surface, the AFM reconstructs the height 3-D profile, with a few angstroms accuracy in height, and an horizontal accuracy up to 20-30 Å. The AFM can work either in "contact mode" (the interaction of the tip to the surface is stronger and the instrument has a better resolution but the surface can be damaged) or in "non-contact" (*tapping*) mode.

The installed AFM at INAF-OAB is a "stand-alone" instrument: the AFM head, where the probe is hosted, has reduced dimensions and can be put inside curved mirror shells to measure the roughness of the reflecting layer or be laid upon mandrels. The width (and the resolution) of the scans can be set at 100 μm, 10 μm, 1 μm. Every scan covers a 512x512 pixel matrix, so that the scan resolution varies between 0.2 μm and 20 Å. This instrument is then used to extend the PSD spectral analysis to higher spatial frequencies than WYKO, taking care of the filtering of the aliases in the spectrum (see app. B).

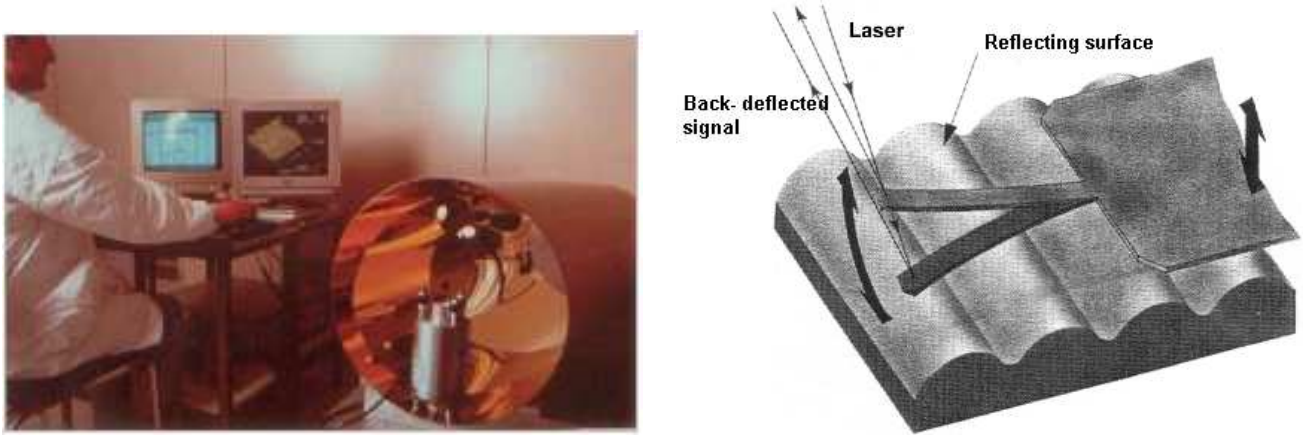

Figure 5.3: (left) Photo and (right) scheme of the cantilever of the Atomic Force Microscope. In the photo the AFM head is tracing a 2-D profile of the inner, Au-coated surface of a Nickel electroformed X-ray mirror shell.

5.1.3 The Long Trace Profilometer (LTP)

The LTP is a sensitive slope-angle-measuring instrument, based on the original concept of the pencil-beam interferometer of Von Bieren, and developed by P. Tackacs et al.

The LTP measurement principle is simple: two pencil Ne-He laser beams are scan the surface of a mirror and the reflected beam direction changes according to the local surface slope at that position. A Fourier transform lens converts the angle variation of the reflected beam in a variation of position in its focal plane. Another part of the beam is focused on reference surface, in order to subtract the tilting and rotation of the optical head. An advantage of such a configuration is a significant weight reduction of the movable part of the interferometer (with an obvious decrease of mechanical flexure of the scanning slide), and a side-mounting configuration for the surface under test (that greatly reduces the gravity induced deformation on the optical element under test).

The focused laser beam position is recorded by a linear array detector and, after a proper fit, the local slope of the mirror under test is obtained. With proper environmental conditions and periodic and precise calibrations of the instrument, LTP is able to measure slope profiles, with an accuracy better then 1 mrad rms.

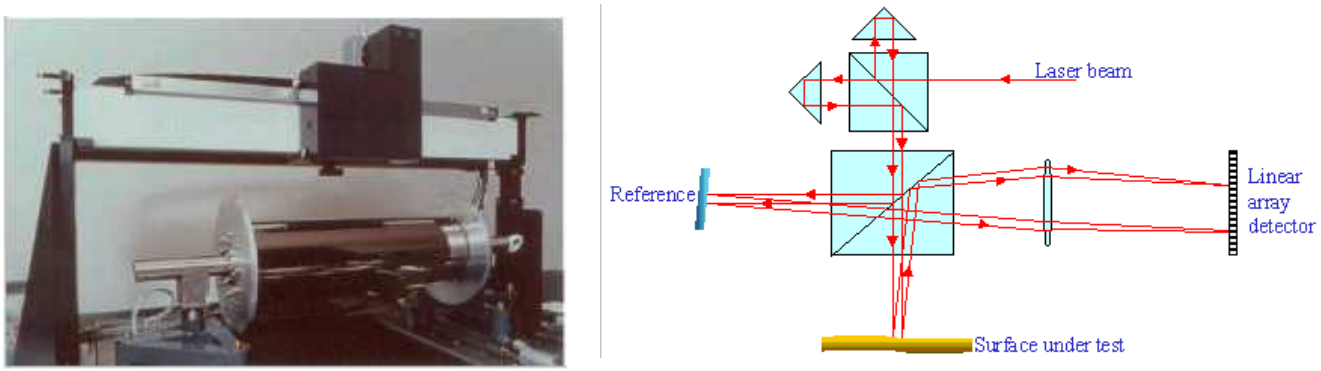

Figure 5.4: Image (left) and scheme (right: credits: ELETTRA Synchrotron, Trieste) of the Long Trace Profilometer at INAF-OAB. In the photo the LTP is tracing a profile of a superpolished mandrel.

Even if this instrument has a sensitivity to wavelength in the range from meters to millimeters and then cannot really measure the surface roughness, it is very useful in mirror realization as it is able to detect the shape imperfection of mirrors. It turns also to be a basic tool to measure the mirror substrate curvature (e.g. produced by multilayer stresses, that can be so evaluated using the eq. 3.83).

The parameters to be optimized are related to environmental changes while measuring (mainly temperature stability and air turbulence along the laser beam path). The whole instrument is mounted on self-stabilizing, air-suspensions. These are necessary for isolation from the sound waves, propagating from the ground. This limitation affects, indeed, all the microtopographic instruments.

5.2 X-ray reflectivity (XRR) measurements

The X-ray reflectivity is obviously a basic test to understand the properties of a multilayer coating. X-ray grazing incidence multilayers may be directly tested in the spectral bandwidth in which they have to operate, but also multilayer coatings designed for the extreme UV in normal incidence may be deeply characterized by an X-ray reflectivity measurement. The X-ray reflectivity provides informations about the thickness of the deposited materials,it is sensitive to the interface roughness and diffuseness and to the optical constants and density of the used materials: every feature of the specular reflectivity scan reflects a property of the multilayer stack.

The reflectivity measurements may be divided into two groups:

1. *angular scans*: in this measurement the energy of a thin incident beam is kept constant and the reflectivity is recorded while the sample under test is rotated under different grazing incidence angles. The reflected beam is followed and measured by a co-rotating detector (usually a scintillator with photomultiplier). The angular scan does not require a very complex apparatus, because the detector may be sensitive only to the energy to be used, and the measurement resolution is determined only by the incident beam divergence, which can be controlled using a system of microslits. Moreover, for fixed energy the optical constants are fixed in the scans, and the reflectivity plot is easier to be modeled and interpreted.

   Terrestrial X-ray sources suitable for these measurements are commercially available as X-ray tubes. They emit a continuous bremsstrahlung spectrum (with a cut-off maximum energy proportional to the accelerating power) superposed to the X-ray emission lines of the anode material. In such low-power sources, usually an emission line is selected in order to provide a sufficient flux to improve the signal/noise ratio.

   As the multilayer structure is always characterized by a large number of parameters, a single-energy scan leaves room to some ambiguity in the scan interpretation: for example, a low peak reflectivity might be attributed to a low density contrast or to interfacial roughness. To reduce the ambiguity, the measurements are performed at more than one energy. The cross-test allow to discard some parameters combinations,(due to the different dependence of reflectivity on them for different energies) and to find the exact distribution of thicknesses, densities, roughnesses. The BEDE-D1 Diffractometer installed at INAF-OAB we used to perform almost all measurements in this Ph.D. thesis may operate at 8.05 keV (1.541 Å, Cu Kα line) or at 17.4 keV (0.709 Å, Mo Kα line): in particular the latter is interesting because it is situated in the hard X-ray range and allows to test the behaviour of hard X-ray with multilayer designed to extend the mirror reflectivity in that band.

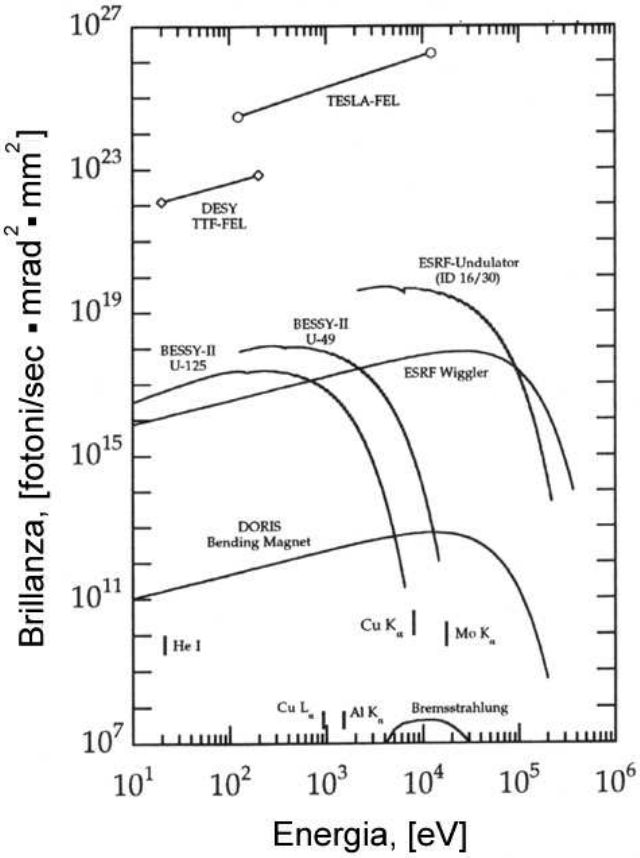

Figure 5.5: Spectra of terrestrial X-ray sources. The X-ray tubes are the most widely used sources, especially to perform angular scans at a fixed energy (usually an X-ray fluorescence line). Synchrotrons emit X-rays in a continuous spectrum with a much larger efficiency and in a continuous spectrum up the hundreds of keV (credits: bibl. [112]).

2. *energy scans*: in this case the incidence angle is constant and the multilayer is illuminated by a broad spectral beam: the reflected beam must be collected by a multi-channel detector which is able to discriminate the energy of the reflected photons: from a measurement of the incident spectrum the reflectivity is computed (eventually the covered beam area must be taken into account). The energy scan shows the Bragg peaks like the angular scan, but in addition it reveals the variation of the optical constants with the energy. This kind of measurement allows an immediate view of the behaviour of the mirror in the spectral range where it has to operate, but it requires an expensive detector with a very good spectral resolution and a very low-divergence beam. Moreover, a broad-band beam have often to operate in vacuum: an example of such a source is the *PANTER* facility in Neuried (DE), which emits a parallel-beam in an energy range up to 50 keV (see bibl. [100], see sect. 8.1, page 163) using an high-power X-ray tube. In this case, either the bremsstrahlung continuum or the X-ray emission lines may be used for the XRR measurement. Also when using such a facility, repeated measurements at some different angles may help to determine the stack parameters.

Using both scan methods, the XRR allows to characterize a multilayer stack in depth, while the topographic measurements give access only to the outer surface; the parameters resulting from the XRR provide an independent measurement of some topographic parameters and may be used in interaction with them. A

multilayer characterization that includes the spectral distribution of the roughness may be done, however, only by observing also the non-specular reflected beam, i.e. the scattered beam (see sect. 5.3.1, page 120).

A special class of X-ray sources is represented by the Synchrotron Facilities (like the ESRF). Their minimum beam divergence, their wide energy range and their intensity make them ideal sources to perform scattering measurements, X-ray microscopy and dispersive spectrography, but also to measure X-ray reflectivity of low-reflection samples (e.g., high-order multilayer peaks).

5.2.1 The BEDE-D1 Diffractometer

The X-ray diffractometer BEDE-D1 (see bibl. [70]) installed at INAF-OAB consists of an X-ray shield, which contains an X-ray tube, a Si crystal monochromator, a sample carrier and an X-ray detector, both equipped with precision goniometers (res. 1"). All of these elements are positioned and moved by micrometric motors, driven by an external computer code. The same code traces the rocking curves, and records them onto the hard drives.

The X-ray tube (equipped with a copper anode) generates a bremsstrahlung spectrum, superposed to characteristic fluorescence lines of Cu. In particular the Kα1 line (8.05 keV, 1.541 Å) is selected because of its intensity and sharpness (typically it has a 1eV equivalent width). The line intensity may be changed by external power controls. The X-ray tube is easily removable in order to change the target anode. Different tubes are available: the tube with a target anode in Molybdenum (Kα, 0.709 $\mathring{A}$ 17.4 keV) is implemented to perform measures in harder X-rays.

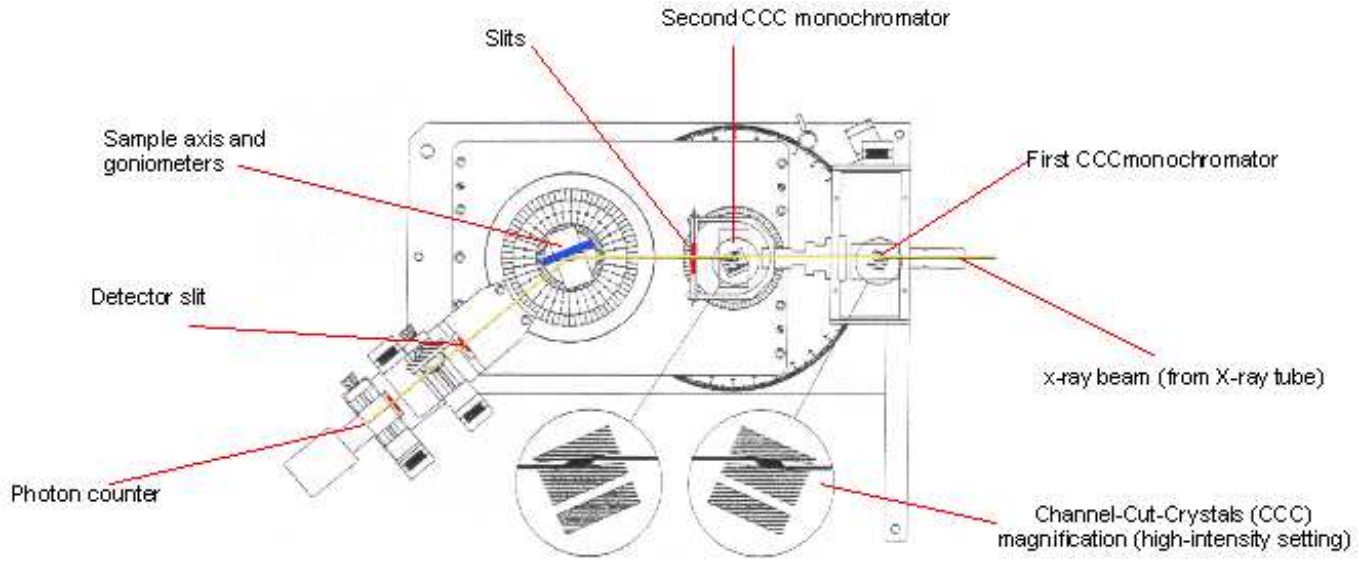

Figure 5.6: Scheme of the BEDE-D1 diffractometer (credits: BEDE Scientific).

The (Cu or Mo) fluorescence line is then filtered an collimated. A Channel-Cut-Crystal (CCC) in Silicon, properly cut, disposed and aligned as in figure 5.6, reflects X-rays incident from various angles with the crystal planes, only if they satisfy the Bragg law. The X-rays are then partially reflected two times and are then dispersed out of the channel according their each wavelength.

The Kα1 line may then be found and isolated by a narrow (50 μm) slit as a peak of beam intensity. According to the chosen channel in the CCC (and consequent Bragg reflection angle) we may reach a divergence beam of 12" (high-resolution, low-intensity channel) or 25" (low-resolution, high-intensity channel).

A second CCC may be mounted in order to improve monochromaticity and collimation. A further system of slits can be used to improve the angular resolution and the beam width to 0.07 mm (but at expenses of the photon flux), so that the reflectivity of short samples (some cm) can also be measured.

The emerging beam finally incides on the sample (usually in grazing incidence), mounted on the goniometer. The reflected/scattered rays are collected by a photoelectric detector: both angles (sample and detector) are measured and recorded by the goniometer, as well as the corresponding reflected/scattered beam. A camera is also available to verify the incidence of the beam on the sample. The BEDE D1 can be also used in energy-dispersive mode, using the polychromatic beam and upgrading the detector with a CZT detector.

The BEDE-D1 is a general purpose instrument: it allows X-ray diffraction, reflectance, scattering measurements. For XRR measurements the achievable photon fluxes are $N \approx 10^4 \div 5 \times 10^5$, depending on the desired angular resolution, beam width and the used X-ray tube. Very thin beams have to be used when the samples have a very limited size, while a very high angular resolution is adopted when the reflectance scans have important details to be resolved. In XRR measurements the precision limiting factor is the *detector noise*, whose counts are around 1 cps (8.05 keV line, rejection photomultiplier parameters correctly set), leading to a reflectivity determination error of $10^{-4} \div 10^{-5}$: this error source is important only where the reflectivity falls under this limit. Another error is caused by the Poissonian source fluctuation $N^{-1/2} \approx 1\% \div 0.05\%$. Both errors can be reduced by the increase of the integration time as $t^{-1/2}$, but at the risk of long-term source instability.

Some examples of measurements are presented afterwards.

5.2.2 Single-layer thickness, density, roughness measurements

The most simple measurement after the measurement of a single substrate is the characterization of a single layer, deposited on a substrate. Typical substrates are common glass for microscopy tests ($\sigma \approx 10 \div 20\mathring{A}$), superpolished fused silica ($\sigma \approx 1\mathring{A}$), superpolished silicon wafers ($\sigma \approx 3-4\mathring{A}$). The reflectivity scan of a thin layer shows a typical alternance of maxima and minima caused by the interference of the X-ray reflected by the two boundaries ambient/layer and layer/substrate (see sect. 3.1, page 42).

At very small angles the X-rays are completely reflected by the layer, decreasing slowly by effect of the increasing penetration depth of the X-rays. At the layer critical angle $\theta_c \simeq \sqrt{2\delta}$ (see eq. 2.7) the reflectivity drops and the interference fringes start to appear. An example of a thin Platinum layer thickness measurement is shown in fig. 5.7. If the substrate is denser than the layer, the interference occurs in total reflection regime for the substrate, and very intense interference fringes appear (see sect. 5.2.3, page 115).

The critical angle is proportional to the actual material density, i.e. on the packing coefficient (see sect. 3.5.1, page 63). Over the critical angles, the amplitude of the interference fringes is influenced by the $\Delta\delta$ of the layer/vacuum and layer/substrates and by the layer/substrate roughness. From the Bragg law (see eq. 3.9)it is easy to derive that the interfringe $\Delta\theta$ depends instead essentially on the film thickness d,

$$d \approx \frac{\lambda}{2\Delta\theta} \tag{5.1}$$

and this suggests a method to measure it. The refraction effects may be, indeed important. From the Snell law and the Bragg law, it is easy to derive the following expression for the measured position of two successive maxima (or minima, if the layer is denser than the substrate):

$$\sin\theta \simeq 2\delta + \frac{k\lambda}{2d} \tag{5.2}$$

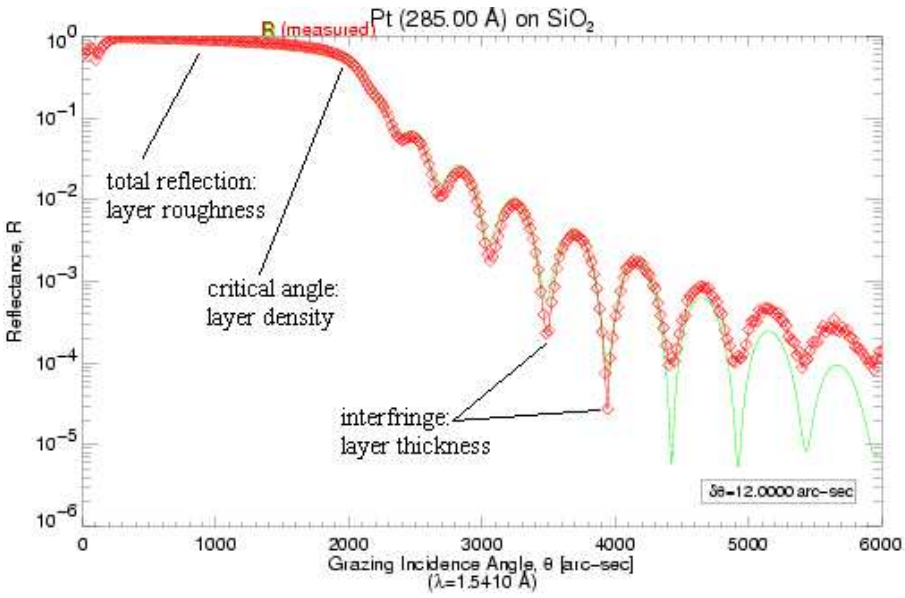

Figure 5.7: Thickness derivation of a thin Pt layer deposited on glass substrate by e-beam, from the interfringe of an X-ray reflectivity scan at 8.05 keV. The inferred thickness from the Bragg law (refraction corrected) is 28.5 nm.

this equation shows that the effect of an increasing density is not only a shift of the critical angle, but also a shift of the whole interference pattern to larger incidence angles. The effect is negligible for large interference orders, but this refraction effect may be important at very small angles, where usually the reflectivity is larger and interference fringes are easier to be detected; interference features can be observed up to a maximum angle, where the reflected beam falls down the instrumental noise limit.

Usually, thicknesses down to $5 \div 10$ nm can be measured with the BEDE-D1, depending on the deposited material. Once found a good estimate for the thickness, the fit of the critical angle determines the material density and the whole reflectivity pattern intensity determines substrate and layer roughness. A code like IMD (see bibl. [103]) is very useful to perform the reflectance scan fit.The single layer thickness measurement is essential to calibrate deposition facilities to produce multilayer coatings.

5.2.3 Double layer thickness, density, roughness measurements

The double layer reflectivity pattern is more complicate than the single layer, as it is caused by the interference of three reflected rays. Depending on the density contrasts, the reflectivity scans can have different appearances, resulting from the modulation of the two interference patterns.

Double layers are used to measure layer thickness of materials having very similar densities as the substrate (e.g., Al, MgF_2, C, Si,... on glass substrate) and the interference fringes would be too weak to be fitted to derive the layer thickness. In this case a thin layer of a denser material (Ni, Pt, Mo, W,...) is inserted between the substrate and the layer to be measured. The contrast density is enhanced and the interference is important in the angular range between the two critical angles (see fig. 5.8), as the X-rays penetrate the layer to be measured, but they are reflected by the high-density material. In this regime the position of the maxima depends only on the low density, upper layer thickness.

In practice, the denser layer is deposited first and a preliminary X-ray reflection scan allow to measure its thickness, density and roughness. After the deposition of the low-density layers, these data are useful to

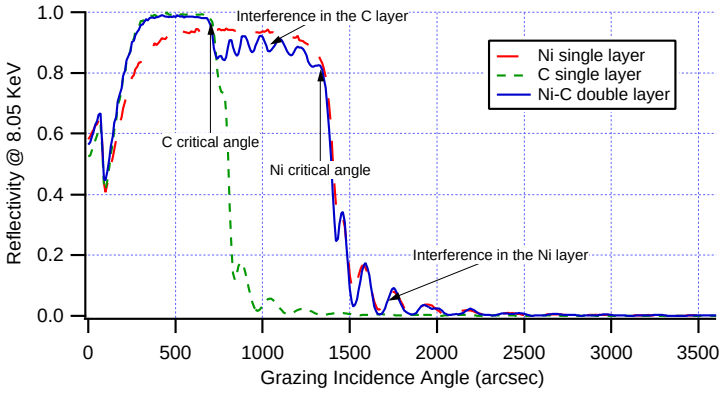

Figure 5.8: Thickness measurement of single Ni-layer (dashed line), single C-layer (short-dashed line) and a double Ni-C layer (solid line) at 8.05 keV, e-beam deposited. For grazing angles less than the Carbon critical angle, the reflectivity of the double layer is almost the same as the single Carbon layer: in the same range the reflectivity is higher than Nickel. The interference pattern of the Carbon layer alone is included between the critical angles of Carbon ($\sim 800''$) and that of Nickel ($\sim 1430''$).

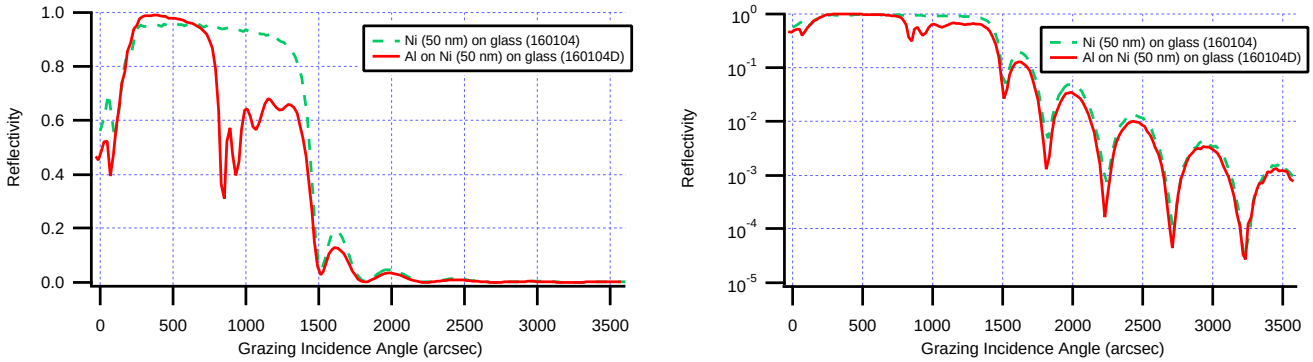

Figure 5.9: Thickness measurement of a single Ni-layer (dashed line) and a double Ni-Al layer e-beam deposited (solid line) at 8.05 keV: linear plot (left) and log -linear plot (right). At very small incidence reflection angles the Aluminium better reflects than Nickel, due to a lower photoelectric cross-section ($\propto Z^5$). The interference pattern in the Aluminium layer alone is included between the critical angles of Nickel ($\sim 1430''$) and that of Aluminium ($\sim 800''$). Over the critical angle of Nickel the Aluminium thin layer is almost X-ray transparent.

perform the fit of the whole reflectivity scan. Also the region over both critical angles is useful to verify the found value for the layer thickness in the region between the two critical angles. Another example of double layer Ni-Al XRR characterization is reported in fig. 5.9.

There are obvious thickness limitations to the use of the X-ray interference in thickness measurements: if the layer is too thin (1-2 nm) the period can be so long that the reflectivity falls down the detection limits before reaching two successive maxima or minima: if the layer is too thick (some hundred nm) the distance between two maxima can be shorter than the instrument angular resolution (which is determined by the X-ray source divergence). Such thick layers are often rough and absorbing, thus the interference cannot often be observed (even if the X-ray lines are very monochromatic): some constraints about the layer thickness can be derived, indeed, from the extinction measurements between the two critical angles: since the outer layer roughness affects much less the transmitted ray than the reflected one (see eq. 2.22) an outer roughness estimate is not so essential, even if it would be preferable: a solid density estimate is very important, instead. An example of such an evaluation is reported in fig. 5.10.

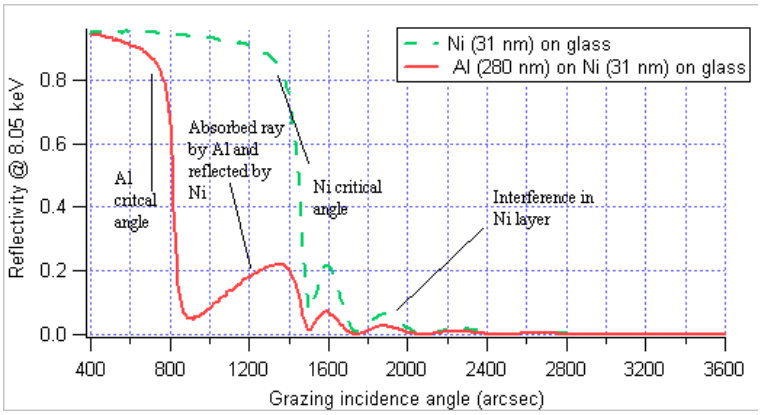

Figure 5.10: Measurement of an Aluminium layer deposited on a glass substrate with a 30 nm-thick Nickel layer. The reflectivity scan at 8.05 keV shows in the region between the Aluminium critical angle ($\sim$ 800") and that of Nickel ($\sim$ 1430") no evident interference patterns, completely erased by the Aluminium surface roughness (7 nm) and by the Aluminium layer thickness: the apparent increase of reflectivity with the incidence angle is caused by the reduction of the crossed absorbing thickness: the absorption amount can lead to a thickness estimate of 270 $\div$ 280 nm, assuming from the Al critical angle, that $\rho_{Al} = 2.6$ g/cm^3.

5.2.4 Multilayer thickness, density, roughness measurements

A characterization of the multilayer XRR is quite complex since the expected structure may differ from the designed one in many respects, reflecting the practical, intrinsic difficulty of producing this kind of coatings for X-ray/EUV mirrors:

1. the layer thicknesses (of some nm) are difficult to control with a good precision (1 $\div$ 2 Å, the order of magnitude of the atomic size. The thickness control is difficult especially when techniques like the e-beam evaporation are adopted, since the evaporation rate is unstable and depends on many factors (chamber pressure, e-gun settings, source distance, crucible preparation, ...). Deposition methods like sputtering allow instead a more precise control on the layer thickness (on the other side, they do not allow a large, uniform surface coating) as the atomic flux is simply related to the sputtering ionic flux;

2. the materials densities may differ from the natural ones. Usually deposited layers by evaporation have densities values less than the bulk values, due to the low kinetic energies of the evaporate, leading to a low atomic packing state (see chapt. 4). Sputtered films are usually denser, as well as evaporated films with ion assistance. The density may also vary during the deposition as a result of instability in the environmental conditions;

3. the layer roughness evolves along the stack (see sect. 3.5.2), page 68;

4. if the multilayer has to be graded, the interpretation of the XRR is not trivial at all.

It is then difficult to model an XRR scan with a limited number of parameters. For a fast multilayer modelization we have always used the code IMD (see bibl. [103] that allows the modelization of periodic and graded multilayers. An automatic fitting procedure, very promising, to explore the multiparametric set of solutions that can be used to structure a multilayer coatings is the numeric code PPM, described in the chapt. 9.

A periodic (or almost periodic) multilayer scan can indeed lead to a quick "diagnostic" from some clues (the number of bilayers is assumed to be a known parameter, as well as the presence of capping layers):

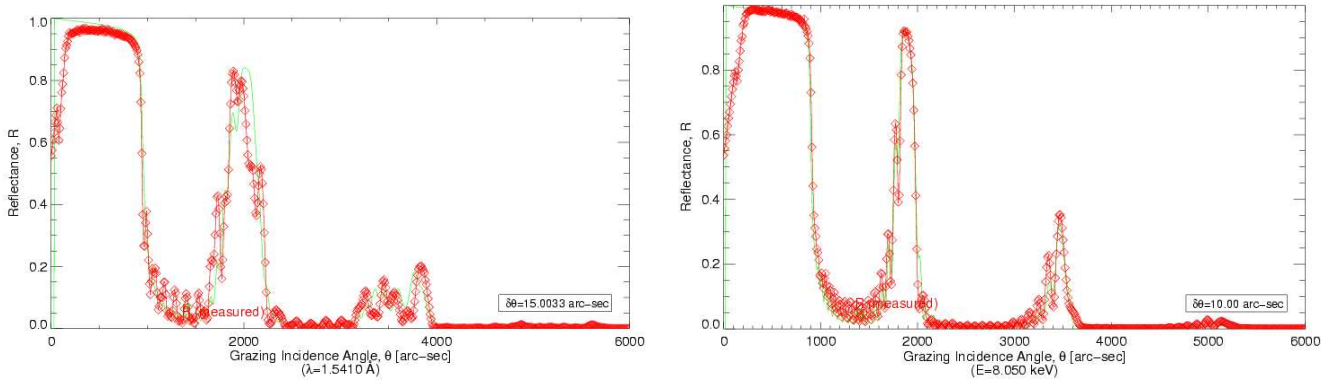

Figure 5.11: Reflectivity scan at 8.05 keV of two quasi-periodic Ni/C multilayers, with the same number of bilayers (20), e-beam evaporated.
(left) The multilayer is characterized by a undesired, strong variation of the period along the stack (8 ÷ 10 nm, with a $\Gamma \sim 0.4$), visible from the large width of the 1^{st} Bragg peak, and from the almost complete absence of the second. The roughness that can be inferred is good, indeed: 3 Å, similar as the Si wafer where the multilayer was deposited.
(right) The multilayer has a more constant period, visible also from the presence of clear secondary peaks. Their anomalous height, indeed, is a clue of an increase of the thickness approaching to the multilayer outer surface (with a variation still too large: from 10 to 9.3 nm, $\Gamma \sim 0.2$). The large roughness inferred from the fit (7 Å) may be due to the substrate roughness (a common glass).

1. *clear, defined, narrow peaks are an index of the constance of the period along the stack*. Very periodic and smooth multilayer show also clear secondary peaks, as described in the sect. 3.3.1, page 48, between the main Bragg peaks: in these multilayers also a large number of Bragg peaks are observable, depending on the roughness and on the total number of periods; *the inconstancy of the period is marked instead by a dispersion of the Bragg peaks*: the period variation is concentrated in the medium/innermost layers if the higher peak order are dispersed, it is located mainly in the uppermost layers if the dispersion regards the lowest peak orders;

2. *the position of the peaks, if well defined, allows to determine the multilayer period* using the *refraction-corrected* Bragg law, eq. 3.21. A difficulty to find a period in agreement with all the observed Bragg peaks can indicate an angle offset error;

3. *the* Γ *factor is responsible for the relative peak height*: the peak orders near to $m\Gamma^{-1}$ (m integer) tend to be suppressed, those near to $(m + 1/2)\Gamma^{-1}$ are enhanced. Peaks falling exactly at Γ^{-1} are almost cancelled. Moreover, when no peak falls near to the Γ^{-1}, it is often possible to find some very low reflectivity angular regions in vicinities of the incidence angle Θ_m, where also the secondary peaks are almost invisible. This low-reflectivity zone is due to the destructive interference of the reflected rays from the interfaces absorber/spacer and spacer/absorber, that are phase-delayed by π (see sect. 3.3.1, page 48). This condition is verified when the incidence angle is roughly

$$2d\Gamma \sin \Theta_m \simeq m\lambda \tag{5.3}$$

with m integer. From the first Bragg angle θ_1 and the Θ_m measurement we can so estimate

$$\Gamma \approx m \frac{\sin \theta_1}{\sin \Theta_m} \tag{5.4}$$

An increase of the Γ factor is responsible also for a slight positive shift of the whole XRR scan, as well as the cut-off angle. This can be produced, indeed, also by increasing the material density;

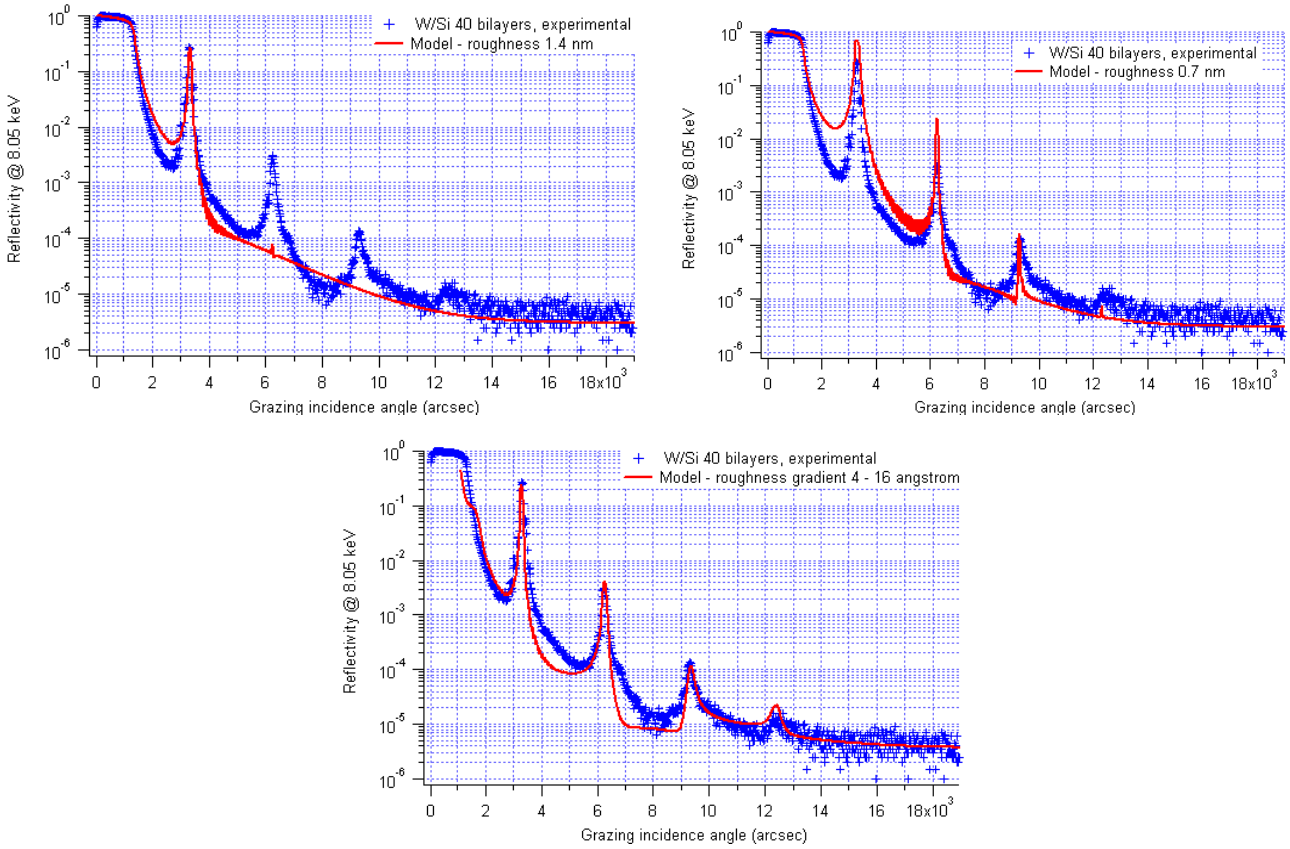

Figure 5.12: Evidence of roughness evolution from a 8.05 keV XRR scans of a W/Si multilayer with 40 bilayers (d = 51 Å, $\Gamma = 0.4$).
(above, left)The experimental curve cannot be fitted by a model with a single roughness value of 14 Å, necessary to fit the first peak, because it would make the observed higher order to disappear.
(above, right) It can not be fitted as well by a single roughness value of 7 Å, value suggested by the third peak height, as it would overestimate the first and second peak reflectivities.
(bottom) The best fitting model can only assume a roughness gradient in the stack: the fitting curve was derived assuming that σ drifts linearly from 4 $\mathring{A}$ on the substrate up to 16 $\mathring{A}$ on the outer surface. The above reported values of 14 $\mathring{A}$ is the average roughness value of the first bilayers, involved in the 1^{st} peak reflection, whereas the 7 $\mathring{A}$ value represents the average stack roughness (since at the 3^{rd} peak all the multilayer is effective) and it can indicate that the roughness drift is not so linear.

4. the interlayer roughness may be evaluated from the primary and secondary peak height, from the external reflection region intensity (but also the presence of low-density capping layers enhances the reflectivity in this region (see sect. 3.6, page 74). The higher order Bragg peaks are more sensitive to the interface roughness: however, by fitting the XRR scan with a *single roughness* value it is common to find that the higher orders reflect better than in the model: this may be due to the better smoothness of the innermost layers, involved in the high order Bragg reflection: this effect may be more easily observed with multilayers with a large bilayer number (see fig. 5.12). Finally, the roughnesses of the absorber/spacer and spacer/absorber may be different as a result of the different crystallization state of the two materials;

5. the material density *contrast* may sometimes be suggested from the peak heights: the absolute density value can be suggested by the cut-off angle and from an overall shift of the XRR scan to the larger

angles for larger materials density, provided that we have a solid Γ estimate and we can be confident that the angular offset is negligible.

The ambiguity coming from similar effects of the parameter variation may be reduced by performing XRR angular scans at more than one energy, or energy scans at more than one angle. For instance, as the X-ray refractive index of materials scale as $\rho\lambda^2$ (far from absorption edges, see app. A.1) and the roughness effect in peaks (see sect. 3.5.2, page 66) scales as $e^{-2\pi^2\sigma^2k^2}$, the contributions of the two factors in determining the peak height may be disentangled.

It is worth noting that when modelling/fitting XRR reflectivities the roughness measurements can be underestimated since the experimental data are assumed to be the specular reflectivity data alone (obeying to the Névot-Croce formula, see eq. 3.77), without any contribution from the scattered beam. Since the detector has always a finite angular acceptance, the collected data are the specular reflected beam *plus* the scattered beam fraction falling in the detector, usually caused by the low-frequency roughness. The apparent increase in reflectivity can exclude the low-frequency component of the surface roughness (see sect. 5.3.1, page 120): in particular, it is possible to see (see app. C) that the maximum spatial wavelength contributing to the measured reflectivity reduction is (see page 216) $\frac{2\lambda}{\sin\theta_i\Delta\theta}$, where $\Delta\theta$ is the detector angular acceptance, thus the measured roughness σ^* from the XRR scan is

$$\sigma_*^2 = \sigma^2 - \int_0^{\frac{\sin\theta_i\Delta\theta}{2\lambda}} PSD(f)df \tag{5.5}$$

leading to an underestimation of σ.

5.3 X-ray scattering (XRS) measurements

The reflectivity in the specular direction is related to the surface/interfacial σ roughness (see sect. 2.2.4, page 24), but it does not allow a complete characterization of the surface. The exhaustive description of the surface profile is given by the *non-specular reflectance*, that is, the *scattering* in directions other than the specular one, being related to the *power spectral density* (PSD) of the surface (see appendix B). PSD single surface are simply obtained from a single scattering scan, whereas the interpretation of scattering from layered structures is much more complex (see bibl. [68]).

5.3.1 Scattering from a single boundary

The perturbation theory allows to explain the PSD-scattering link (see bibl. [66], bibl. [79]): the main theory result is a simple proportionality relationship between the scattered intensity distribution and the surface PSD, expressed as a function of the *surface spatial wavelength*. The σ roughness is obtained, in particular, from the integrated scattered power: it is worth noting that most of obtained results are valid not only for X-ray scattering but also for every light scattering from a reflecting surface.

A typical arrangement for a surface scattering experiment is depicted in fig. 5.13: the beam incides on the sample under test at the angle θ_i and, provided that the smooth-surface condition

$$2\sigma\sin\theta_i \ll \lambda \tag{5.6}$$

is satisfied, is mainly reflected in the specular direction. The presence of the surface irregularities cause the scattering of the beam in the surrounding directions (θ_s, φ_s); a detailed calculation of the distribution is performed in the app. C, and the recovered, classical results (see also bibl. [82], bibl. [83], bibl. [84]) are:

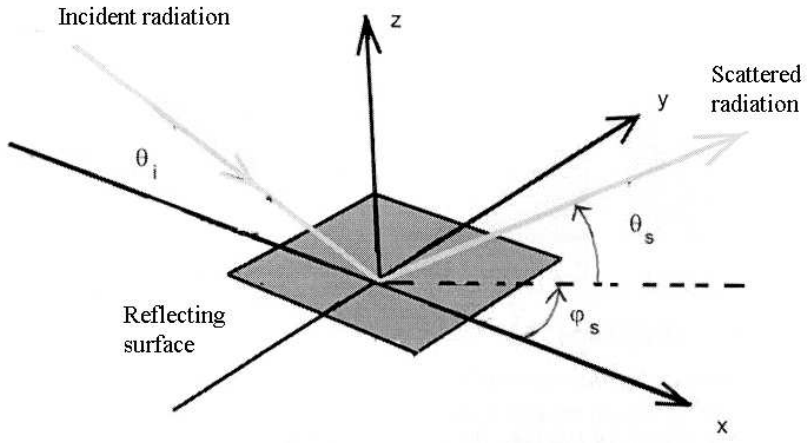

Figure 5.13: Geometry of the X-ray scattering from a rough surface. The angle ϕ_s is included between the x axis and the projection of the scattering direction on the surface. The surface lies in the xy plane.

1. the bidimensional X-ray scattering diagram, intended as the scattered fraction of the incident power per solid angle at the angles (θ_s, φ_s) *is proportional to the bidimensional surface PSD* $P(f_x, f_y)$:

2. if the surface is *isotropic*, in grazing incidence the scattering in the incidence plane (θ_s direction) is $100 \div 1000$ times more effective than in the normal plane (φ_s direction): the scattered power in the φ_s direction may be so easily integrated to derive the scattered power per angle unit at the angle θ_s (see eq. C.36):
$$\frac{1}{I_0}\frac{dI_s}{d\theta_s} = \frac{16\pi^2}{\lambda^3} Q_{is} \sin^2\theta_s \sin\theta_i P(f) \tag{5.7}$$
where $P(f)$ is the monodimensional surface PSD and Q_{is} is a *polarization factor*, which has the approximate expression:
$$Q_{is} = [R(\theta_i)R(\theta_s)]^{1/2} \tag{5.8}$$
with $R(\theta_i)$ and $R(\theta_s)$ are the Fresnel reflectivity evaluated at the incidence and at the scattering angle:

3. for the scattering from an isotropic surface, every 1-D PSD value evaluated at the scattering angle θ_s is linked to a corresponding *spatial wavelength* as from eq. C.9 with $\phi_s = 0$,
$$l = \frac{1}{f} = \frac{\lambda}{|\cos\theta_s - \cos\theta_i|} \tag{5.9}$$

XRS applications A single XRS scan allows us to compute the PSD for every scattering angle θ_s:
$$P(\theta_s) = 2\pi \frac{1}{I_0}\frac{dI_s}{d\theta_s}[4k^3(R_F(\theta_i)R_F(\theta_s))^{1/2}\sin^2\theta_s \sin\theta_i]^{-1} \tag{5.10}$$
although the PSD is an even function, the asymmetry of the last equation makes the scattering pattern asymmetric: in particular, the dispersion power $\frac{d\theta_s}{dl} = \frac{\sin\theta_s}{\lambda}$ and increases with θ_s: the zero frequency corresponds to the specular reflection $\theta_s = \theta_i$, higher frequencies scatter to larger scattering angles. As the PSD is even function, we can use one-half of the scattering pattern to compute the PSD, usually the one at $\theta_s > \theta_i$, because it has a larger dispersive power. In this case the PSD is to be multiplied by a factor 2 to take into account the negative frequencies contribution. Of course, as the reflected specular ray is never

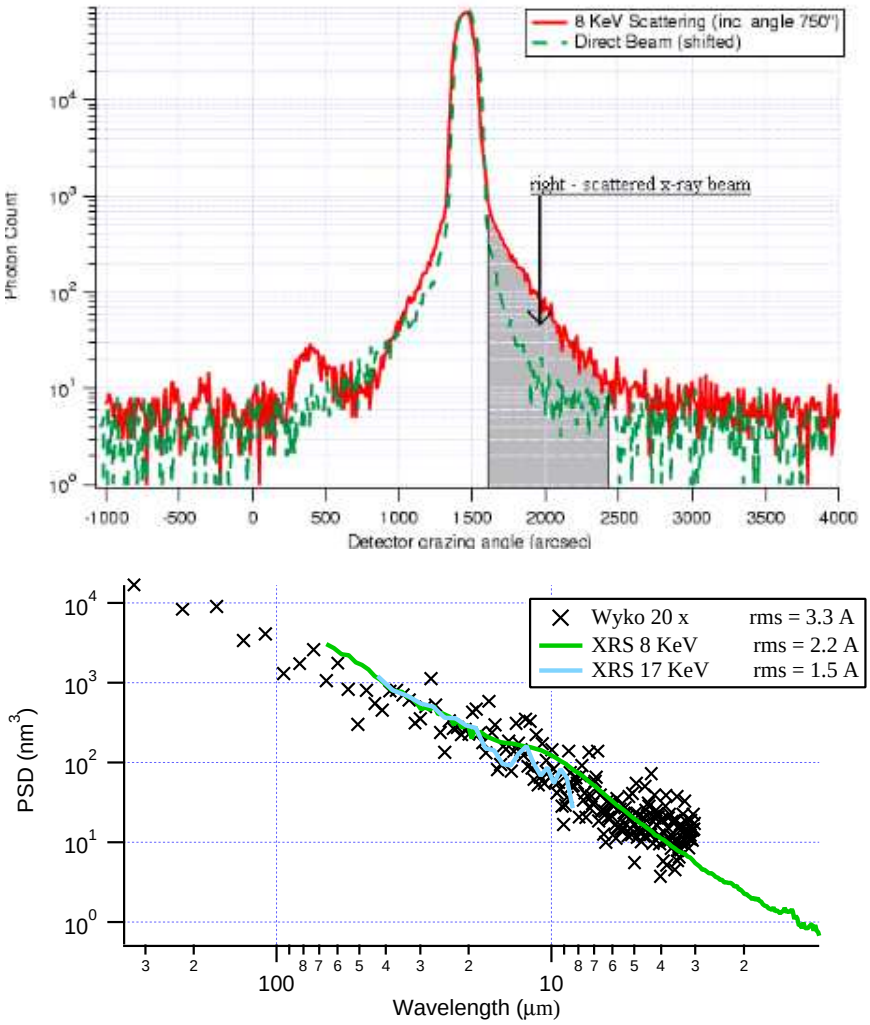

Figure 5.14: Scattering by a TiN superpolished surface with 8.05 keV X-rays (left), in grazing incidence at 750" (solid line). The direct incident beam is superposed (dashed line): the scattered beam is clearly emerging on the right (between the arrows). The computed PSD (at 8.05 and 17 keV) is plotted versus the spatial wavelength (right, solid lines) and it is a clear power-law. The agreement with the WYKO measurement (black crosses) is very good.

delta-like due to the finite instrument angular resolution, the scattering is observable only down to an angle θ_m and the PSD cannot be measured down to the corresponding wavelength f_m: on the other side, the high frequencies are also limited by the instrumental noise, and we can observe scattering up to a maximum angle θ_M which corresponds to a maximum frequency f_M. The PSD is thus computable only within $[f_m, f_M]$ (see fig. 5.14). This limitation, indeed, affects all the topographic measurements (see appendix B).

A scattering measurement provides a complete characterization of the surface and by computing its even moments we obtain some characterizing properties (see the definitions in appendix B):

- the *roughness rms* σ

$$\sigma^2 = \int P(f)df = \frac{\lambda^2}{8I_0 \sin\theta_i R(\theta_i)^{1/2}\pi^2} \int_{\theta_m}^{\theta_M} \frac{1}{R(\theta_s)^{1/2}\sin\theta_s}\left(\frac{dI_s}{d\theta_s}\right) d\theta_s \tag{5.11}$$

- the *slope rms s*

$$s^2 = \int (2\pi f)^2 P(f) df = \frac{1}{2I_0 \sin\theta_i R(\theta_i)^{1/2}} \int_{\theta_m}^{\theta_M} \frac{(\cos\theta_i - \cos\theta_s)^2}{R(\theta_s)^{1/2} \sin\theta_s} \left(\frac{dI_s}{d\theta_s}\right) d\theta_s \tag{5.12}$$

- the *curvature rms* $c = \frac{1}{R_c^2}$

$$c^2 = \int (2\pi f)^4 P(f) df = \frac{2\pi^2}{I_0 \lambda^2 \sin\theta_i R(\theta_i)^{1/2}} \int_{\theta_m}^{\theta_M} \frac{(\cos\theta_i - \cos\theta_s)^4}{R(\theta_s)^{1/2} \sin\theta_s} \left(\frac{dI_s}{d\theta_s}\right) d\theta_s \tag{5.13}$$

- the *correlation length* l_c

$$l_c = \frac{2\pi\sigma}{m} \tag{5.14}$$

the scattering measurement takes the advantage of sampling the properties of a larger surface (some cm^2 with the BEDE-D1 spectrometer) fraction than the AFM (0.01 mm^2) or WYKO (0.6 mm) mapping: the scattering can return a more representative PSD of the surface. Moreover, the signal to noise ratio may be reduced simply by increasing the incident flux and the integration time.

Our scattering measurements are confirmed by the usual topographic methods: in fig. 7.6 a Silicon Wafer superpolished surface measured with LTP / WYKO / AFM, is compared to the PSD computed by 8.05 keV XRS. The measurements in different wavelength ranges are in very good mutual agreement and describe a typical Lorentzian pattern (see appendix B). A different PSD shape is characteristic of metallic surfaces superpolished by diamond-turning: its X-ray scattering pattern shows narrow peaks due to the periodicity of the "scratchy" polishing features (see bibl. [87]). Our substrate measurements will be exposed in detail in the section 6.

XRS scans and trajectories in the reciprocal plane A XRS scan may be performed using different techniques:

- *Detector Scan:* the sample is set at a fixed incidence angle θ_i and the scattered intensity is measured while varying the scattering angle θ_s around the specular reflected ray at $2\theta_i$: the scattering diagram is in this case easier to be interpreted,
- *Rocking Scan:* the detector is fixed at the $2\theta_i$ position and the incidence angle is varied by rotating the sample: the scattering and incidence angle change so together.

The range of spatial frequencies which can be explored by a XRS scan is easily understood if we figure it in the *reciprocal space*. Considering the wave momentum transfer $\vec{q} = \vec{k_i} - \vec{k_s}$, the reciprocal space is the space of the its components. A comparison with the eq. C.9 shows that this coincides with the space $(\omega_x, \omega_y, \alpha)$. For isotropic surfaces all the informations are thus contained in the plane (ω_x, α). Not all the regions of the reciprocal plane are accessible; when either θ_i or θ_s become negative, no scattering is possible: for a detector scan this limiting situation corresponds to

$$q_x < k(1 - \cos\theta_i) \qquad\qquad q_z < k|\sin\theta_i| \tag{5.15}$$

the boundaries of the forbidden regions are inside the circumferences defined by:

$$q_x^2 + q_z^2 \pm 2kq_x \cos\theta_i = k^2 \tag{5.16}$$

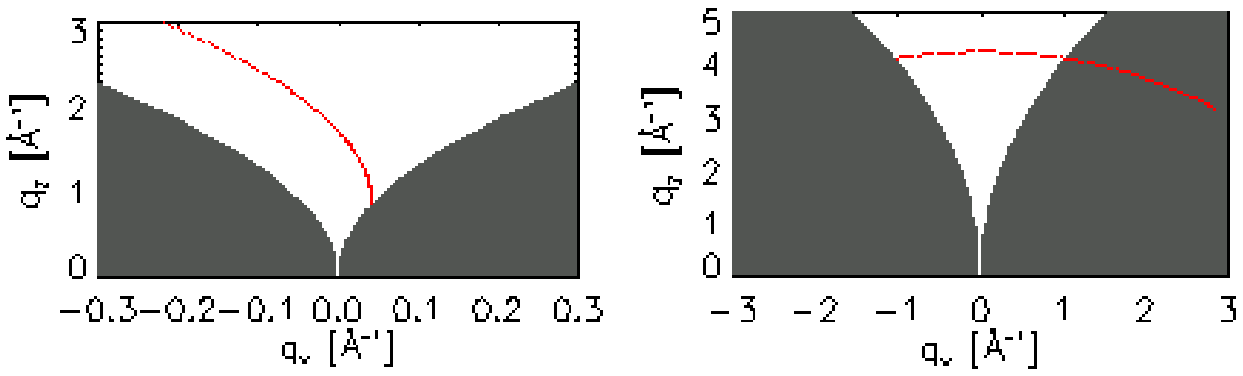

Figure 5.15: A detector scan (left) and a rocking scan (right). The greyed regions are the set of momentum transfer which cannot be explored with a scattering measurement: the scans are represented by the red lines.

the forbidden spheres(the greyed regions in fig. 5.15) are centered in $(\pm\cos\theta_i, 0)$ and they are tangent in $(0, 0)$.

A XRS scan may be seen as a trajectory in the reciprocal space (see fig. 5.15); depending on the scan type, the trajectory will be different: for a detector scan, remembering the eq. C.9 we can fix θ_i and eliminating the parameter $\sin\theta_s$ it is easy to show that detector scans are circumferences with center $(-k\cos\theta_i, +k\sin\theta_i)$ and radius k, so that they all pass by (0,0). Only the arc which does not intersect the Ewald spheres is physically meaningful. The XRR measurement ($\theta_s = \theta_i$) in the reciprocal plane is obviously located in all the points with $(0, 2k\sin\theta_i)$. A rocking scan is instead represented by a circumference in the reciprocal space centered in the plane axis with a radius $2k\sin\theta_0$ (where θ_0 is the initial incidence angle). A very complete reciprocal formalism is explained in bibl. [72].

5.3.2 Scattering by a periodic multilayer-coated surface

A scattering experiment on a rough, multilayer coated surface, usually returns a scattering diagram of difficult interpretation: the reason is that the X-rays are scattered by *all* the multilayer interfaces, and because of the periodic multilayer structure the scattered waves interfere: an extension of the model for the single surface is reported in appendix C.2 showing that, under the same hypothesis, the scattered power per angle unit is expressed as the sum of two terms:

$$\frac{1}{I_0}\frac{dI_s}{d\theta_s} = \frac{16\pi^2}{\lambda^3} Q_{is} \sin\theta_i \sin^2\theta_s [P_{unc}(f) + P_{corr}(f)] \tag{5.17}$$

where $\alpha = 2\pi\lambda^{-1}(\sin\theta_s + \sin\theta_i)$ and

$$P_{unc} = \sum_n T_n^2 P_n(f) \tag{5.18}$$

$$P_{corr} = 2\sum_{n>m} (-1)^{n+m} C_{nm}(f)\, T_n T_m \cos(\alpha\Delta_{nm}) \tag{5.19}$$

having defined $\Delta_{nm} = \langle z_n\rangle - \langle z_m\rangle$, $\alpha = 2\pi\lambda^{-1}(\sin\theta_i + \sin\theta_s)$, T_n the fraction of the transmitted power in the n_{th} layer and

$$P_n = L_1 L_2 |\hat{z}_n|^2 \qquad C_{nm} = L_1 L_2 Re(\hat{z}_n^* \hat{z}_m) \tag{5.20}$$

the P_n are the Power Spectral Density of the interfaces, whereas the C_{nm} are the *crossed spectral densities* of the m_{th} boundary with the n_{th} boundary. The C_{nm} are simply the Fourier Transform of the cross-correlation

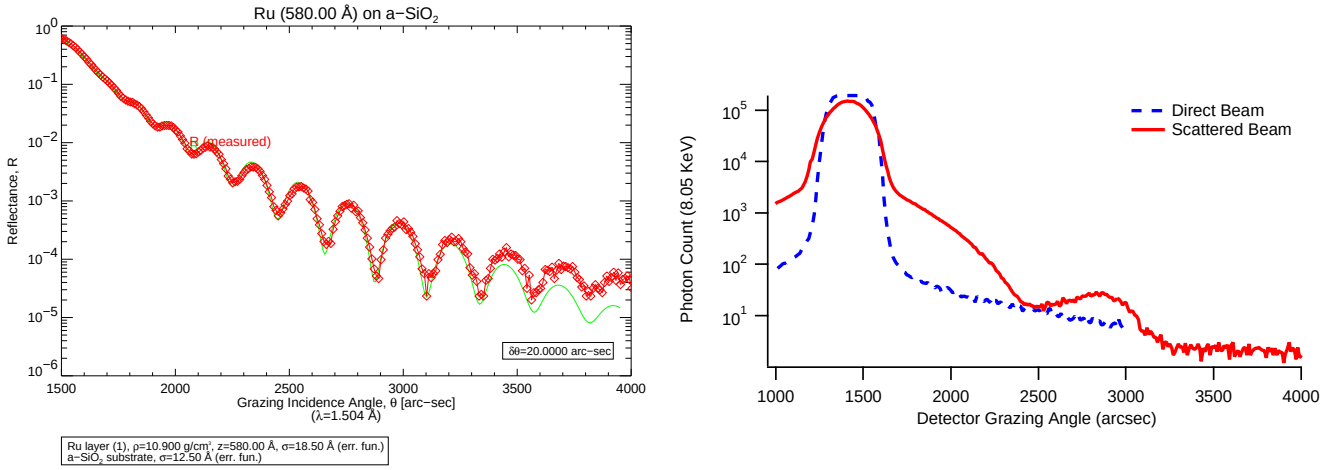

Figure 5.16: Reflectivity (left) and scattering (right) at 8.05 keV from a Ruthenium coated glass. The incidence angle is 700" (in external reflection, interference of the evanescent wave) and the layer thickness is 58 nm. Clear interference fringes arise in the scattering diagram (red solid line) in comparison to the direct incident beam (blue dashed line): this is an evidence of correlation between the substrate and the Ru upper surface. The scattering pattern has as estimated period of 600", about two times larger than the reflectance period, as from equation C.52.

functions of the interfaces: their presence in the scattering pattern indicates that the process is not only a simple *superposition* of scattered rays by each interface, but it is also modulated by their *interference*. This interference is a coherent superposition of scattered waves by the replication in each layer of the underlying roughness features, a very common event in film growths (like in the simple example reported if fig. 5.16, in the case of a single layer of Ruthenium on glass substrate). The scattering caused by the P_n is called *incoherent scattering*, the caused one by the C_{nm} is called *coherent scattering* and the integration of C_{nm} returns the *correlated roughness*.

These equations may be used to compute the interfacial PSDs: in this case a single X-ray scattering scan is not sufficient to extract the characterization of the interfaces: more than one scattering measurement will be necessary. If the multilayer has N layers, it is easily seen that the the number of P_{nm} is

$$\frac{(N+2)(N+1)}{2} \tag{5.21}$$

e.g., for a single layer they will be P_{00}, P_{11}, C_{01} $(= C_{10})$: an equal number of independent measurements will be necessary to resolve the eq. C.52. The measurements may be performed at different incident energies or at different incidence angles: in order to have predictable transmission coefficients and a convenient photon count it is preferable to deal with measurements at the Bragg peaks: a measurement at angles less than the critical one provides simply the outer surface PSD (as the ray do not penetrate the stack), by using the same formula as in the sect. 5.3.1, page 120.

Following the detailed treatement of Kozhevnikov (see bibl. [68]), let us see some properties of this solution: the interference features are caused only by the correlated roughness, and the scattering has peaks where

$$\begin{aligned} \cos(\alpha\Delta_{nm}) &= +1 \qquad \text{for even n+m} \\ \cos(\alpha\Delta_{nm}) &= -1 \qquad \text{for odd n+m} \end{aligned} \tag{5.22}$$

the first solution corresponds to the constructive interference between scattered waves by interfaces at distance equal to $\frac{n+m}{2}d$. It is equivalent, remembering the eqs. C.9, to

$$d(\sin\theta_i + \sin\theta_s) = k\lambda \tag{5.23}$$

this equation locates *quasi-Bragg peaks* as they arise in correspondence to the Bragg peaks which are observed in reflectivity. In fact, if the X-rays strike on the multilayer at the k_i Bragg peak, the condition eq. 5.23 becomes

$$2d \sin\theta_s = (2k - k_i)\lambda \tag{5.24}$$

the scattered peaks fall exactly at the Bragg peaks at order $k_s = 2k - k_i$. It is clear the parity of k_s is the same of k_i, that is, even Bragg peaks are scattered at even peaks and odd Bragg peaks are scattered at odd Bragg peaks. The number of boundaries satisfying the eq. 5.23 is as large as the effective bilayer number and so the quasi Bragg peaks are narrow and high.

The second solution corresponds to the interference of boundaries separated by $l_1 d + l_2 \Gamma d$ and $l_1 d + l_2(1-\Gamma)d$, with l_1, l_2 integers. However, these peaks (which would be located in the middle of the above defined quasi-Bragg peaks) are almost suppressed because in a periodic structure with period d only two boundaries satisfy the condition above.

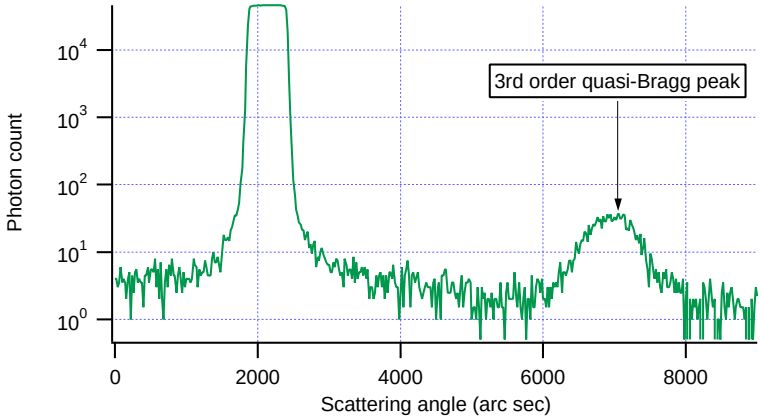

Figure 5.17: Scattering experiment with a Mo/Si multilayer with d= 6.9 nm, $\Gamma = 0.4$ and $\sigma = 5\mathring{A}$: the 8.05 keV beam incides at the first Bragg peak (2150"). The third quasi-Bragg peak, visible on the right, is caused by the constructive interference of scattered waves by all the interfaces.

The exact extraction of the interfacial PSD, however, requires a too large number of independent measurements. In some extreme cases (see also bibl. [68]), these equations can be simplified assuming that:

- the overall electric field in the stack is constant in every bilayer and its relative amplitude decays exponentially (see sect. 3.3.3, page 55) according the law $T_n = 2^{1/2} e^{-(\frac{N}{2}-n+1)\xi}$, with $\xi = 2r\sin(\pi k \Gamma)$ and being n the *bilayer* index,
- for every bilayer, the electric field decay of $e^{-\xi}$ takes place in absorber layers,
- there is no PSD growth, i.e. the PSD is independent on the bilayer index n,
- interfacial PSDs are either
  1. *completely uncorrelated:* the relative phases of the spectral components of interfacial surfaces at any spatial frequency are a random variable of the layer index, hence all interface profiles are completely *different* ($P_n = P(f)$, $C_{nm} = 0$, $\forall n, m$),
  2. *completely correlated:* the relative phases of the spectral components are the same for all layers, hence (since also PSDs are constant) all interface profiles are *identical*, ($P_n = C_{nm} = P(f)$, $\forall n, m$) .

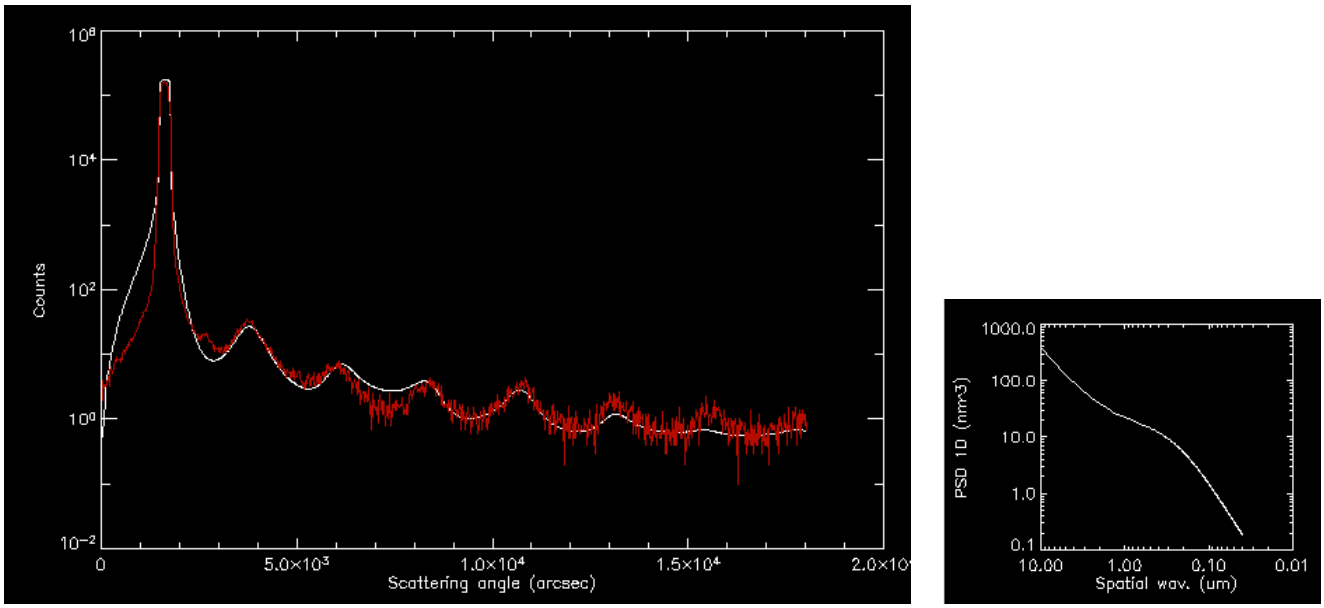

Figure 5.18: (left) Simulation of the XRS diagram at 8.05 keV at the 1st Bragg peak incidence angle of a W/Si multilayer with d = 13.6 nm and $\Gamma = 0.355$ with a roughness of $\sigma = 3.5\mathring{A}$ from 10 μm to 0.04 μm. The multilayer is constituted of 8 bilayers deposited by DC magnetron sputtering onto a superpolished fused silica substrate ($\sigma \approx 1\mathring{A}$), that at the first Bragg peak (1912") are sufficient to saturate the multilayer reflectivity - hence the exponential decay of the electric fields can be considered valid. A correlation degree of 87% has been assumed. The incident flux is 2×10^5 cps and the angular resolution is 250". A low noise level (0.5 cps) is also added to the simulation. (right) The PSD used to compute the XRS diagram: it approximates quite well the measured PSD with AFM on the surface of the multilayer coating: the most prominent feature is the broad peak of PSD growth over 1 μm, a typical feature of multilayer growth (see sect. 3.5.2).

with these assumptions, the C.52 sums can be explicitly performed since they are reduced to geometric sums,

$$\frac{1}{I_0}\frac{dI_s^{unc}}{d\theta_s} \simeq 2K(\theta_i,\theta_s)2P(f)\frac{1-e^{-(N+2)\xi}}{\tanh\xi} \tag{5.25}$$

$$\frac{1}{I_0}\frac{dI_s^{corr}}{d\theta_s} \simeq 4K(\theta_i,\theta_s)P(f)\left|\frac{e^{-\frac{N+2}{2}\xi}-e^{i\frac{N+2}{2}\alpha d}}{1-e^{\xi+i\alpha d}}\right|^2[\cosh(2\xi)-\cos(\alpha\Gamma d)] \tag{5.26}$$

where we have indicated by $K(\theta_i,\theta_s)$ the usual proportionality constant

$$K(\theta_i,\theta_s) = \frac{16\pi^2}{\lambda^3}Q_{is}\sin\theta_i\sin^2\theta_s \tag{5.27}$$

in the limit of a semi-infinite multilayer $N \to \infty$,

$$\frac{1}{I_0}\frac{dI_s^{uncorr}}{d\theta_s} \simeq 2K(\theta_i,\theta_s)P(f)\coth\xi \tag{5.28}$$

$$\frac{1}{I_0}\frac{dI_s^{corr}}{d\theta_s} \simeq 4K(\theta_i,\theta_s)P(f)\frac{\cosh(2\xi)-\cos(\alpha\Gamma d)}{|1-e^{\xi+i\alpha d}|^2} \tag{5.29}$$

these equations are similar to the results which can be found in literature (see bibl. [68], pag. 487). In particular, the eq. 5.29 has maxima in the angular position defined by the eq. 5.23.

These analytical formulae (eqs. 5.25 and 5.26) can be easily written in an IDL routine and can be compared to measured results: for instance, in fig. 5.18 a comparison between 8.05 keV XRS measurements

onto a W/Si multilayer (with d = 13.6 nm and $\Gamma = 0.355$ with a roughness of $\sigma = 3.5\mathring{A}$ in the spatial wavelength window of interest) at the 1^{st} Bragg peak (incidence angle 1912") and theory predictions is shown, with very good agreement: the fit parameter reduced χ^2 equals 0.93 and the ratio of integrated scattering simulated/measured is 1.18. The main discrepancies are at low angles, due to some difficulties in modelization of the polarization factor under the critical angle.

To achieve this agreement, the above XRS diagrams 5.25 and 5.26 have been combined linearly with an amount of 87% of correlation degree, and some reasonable corrections to ξ and α have been adopted to take into account refraction and absorption. The used PSD to model the XRS diagram is also shown (consistent with the PSD measured with AFM). The exposed model can be applicated also at higher order Bragg peaks, provided that the multilayer transmission is negligible, i.e. the multilayer reflects in saturation regime. It can be also applicated (carefully) in the reflection minima, where the electric fields decay is completely determined by photoabsorption (see sect. 3.51).

The intermediate cases are difficult to be evaluated, as they strongly depend on the assumed growth model: usually a larger degree of correlation in the roughness growth is found at the low frequencies of the PSD (see sect. 3.5.2, page 68). The approximations of constant PSDs and constant correlation degree can be considered valid only in a very limited number of cases, mainly because the correlation degree decreases with increasing spatial frequency (see sect. 3.5.2), and because the PSD is different from layer to layer. In the reported example, the final roughness (3.5 $\mathring{A}$)is much larger than the substrate' (1 $\mathring{A}$), hence a roughness growth did take place: however, the roughness increase should have been concentrated in the first deposited layers, to remain constant in the following ones. Further developments are aimed to implement the PSD increase/correlation resulting from a model reported in sect. 3.5.2 in the calculation of the XRS diagram.

Finally, it should be eported that an approach that could describe the scattering from a real multilayer coating is the assumption of a descriptive model (e.g. the Lorentzian, see app. B) for all PSDs: such a scattering model has been already implemented by Christensen et al. (see bibl. [85]) with a two-dimensional scattering model.

Chapter 6

Characterization of Ni/TiN/SiC overcoating for Con-X mandrels

As it was highlighted in the sect. 2.3.3, page 29, the Nickel electroforming replication from shaped mandrels takes the advantage of an high throughput and of good imaging properties. The replication technique allows also the production of monolithic shells, that simplifies the assembly process with respect to techniques based on segmented substrates, it implies a reduction of cost and time and allow the production in an industrial context. Moreover, the case of multimodular telescopes (as it is the case of Constellation-X) it satisfies a large requirement: the possibility of reusing the same mandrel to produce another shell having the same geometric properties. The replication technique, in the traditional version or in the alternative approach of deposition inside a replicated substrate, is a good candidate for the production of the optics of Constellation-X.

As already mentioned, such technique may be extended to replicate multilayer-coated mirrors. On the other hand, it is well known how the microroughness of the reflecting surface hampers the X-ray mirror reflectivity: this is an even more crucial point in multilayer-coated mirrors, because the reflected intensity falls down exponentially at every layer with its interface rms. The interface smoothness is then an essential point to care about. This goal can be reached by a careful study and optimization of the deposition process, but also by depositing the layers onto a mandrel whose surface has been superpolished at excellent level. The film quality is in fact very sensitive to initial defects of the surfaces where they are deposited on, and as long as layers grow, the interface roughness could be amplified up to unacceptable values (see sect. 3.5.2, page 68).

It is then a fundamental step to produce mandrels having a very low surface microroughness. Our requirement to be met is an rms $\sigma < 2.5\mathring{A}$ in the wavelength range $0.1 \div 10$ μm. Such levels are going to be reached with developments performed in our labs by adopting usual Nickel coated mandrels. Another respect has, however, to be taken into account. The replication of a series of shells by using a mandrel tends to *deteriorate* its surface and after a few replication processes the quality of the mandrel surface could be compromised. Moreover, at every replication residual particles of the film usually remain in place onto the mandrel surface and, after a few iterations, must be removed. During this cleaning phase the mandrel may be damaged, and the surface smoothness compromised.

In order to solve these problems and to avoid the repetition of the long and expensive superpolishing process, it is convenient to *overcoat the mandrel with a very hard material, provided that it can be polished at similar levels as electrochemical Nickel.* Due to their very mechanical properties (in particular the hardness), materials like *Titanium Nitride* (TiN) and *Silicon Carbide* (SiC) seem to have the requested properties.

In the following sections the characterization performed on flat prototype mandrels with TiN and SiC overcoatings in the framework of the Constellation-X development project will be described, showing that they can be superpolished at microroughness levels comparable to the usual Ni mandrels. These materials are therefore optimal candidate to be used in the realization of master mandrels for future hard X-ray optics.

6.1 Ni coated mandrel superpolishing

As already discussed, it is essential to start the deposition from a superpolished mandrel. Therefore, the mandrel has to be polished at a roughness level much better than in the case of simple Au-coated optics used for soft X-ray optics. This is due to the amplification of roughness at each layer in multilayer growth. At INAF-OAB we developed a new lapping process in the aim of enabling superpolishing of mandrels at the requested level: currently, this process is achieved with the Zeiss superpolishing machines (used for the XMM mandrels fabrication, see sect. 2.3.3, page 29) now installed at INAF-OAB (see fig. 6.1). In tab. 6.1 the microroughness (rms values) for a mandrel taken from the BeppoSAX series and a prototype polished with the new technology are reported. The gain is evident.

Figure 6.1: A Zeiss superpolishing machine at work on a Ni-coated mandrel.

Scanning instrument	Scan Length (μm)	σ (rms) mandrel SAX n.12 (Å)	σ (rms) Ni superpolished mandrel (Å)
WYKO 20 X	660	7.6	3.0
AFM	10	6.2	2.4
AFM	1	3.4	1.8

Table 6.1: Roughness levels (rms) at different scan lengths as measured for the mandrel n. 12 of the Beppo-SAX series, compared to a Ni coated mandrel, superpolished with the new procedure.

6.2 Characterization of hard prototypes with hard overcoating

We have characterized two flat prototypes made of Aluminium, at which a TiN and a SiC overcoating were respectively applied. In the first case (TiN) the sample was first overcoated with electroless Nickel, which was polished before the overcoating of the hard material at a level of ten angstrom rms as measured with a WYKO 20x optical profilometer, in order to avoid print-through effects in the final superpolished phase. This prototype is a 10 cm diameter disk, coated by a few microns TiN layer by reactive sputtering (see sect. 4.3, page 99), and then superpolished (at INAF-OAB) again down to few angstroms of rms.

The SiC prototype is instead a 2.5 cm diameter Aluminium disk, coated with a 18 μm SiC layer at Ce.Te.V. by PECVD method (see sect. 4.5.1, page 106) and then superpolished at ZEISS (Germany) by using diamond powders, needed due to the extreme hardness of the material.

Parameter	Nickel	Titanium Nitride	Silicon Carbide
Vicker Hardness (Kgf/mm^2)	721	1300 ÷ 2000	2500 ÷ 3100
Density (g/cm^3)	8.9	5.22	3.1
Young's modulus (GPa)	214	600	200 ÷ 400 (ceramic)
Melting point (^{o}C)	1455	2930	2650 ÷ 2950

Table 6.2: Comparison between properties of suitable materials for mandrel coatings (data taken from www.goodfellow.com and www.brycoat.com).

One of the mainly relevant properties of TiN and SiC are their extreme hardness and stability (see tab. 6.2) and for these reasons they are optimal candidates for the overcoating of mandrels to be used in X-ray mirror replication. Moreover, TiN (a conductor) and SiC (an insulator) are excellent non-sticky materials, which makes easier the mirror separation at the last step of the replication procedure. They are also inert to acids, bases, solvents, caustic.

For the characterization of our samples we used topographic instruments and X-ray scattering (using the equations 5.7 and 5.9, as explained in the sect. 5.3.1, page 120). The topographic measurements were performed by using the stand-alone Atomic Force Microscope with scan length of 100, 10, 1 μm, and the WYKO optical profilometer TOPO 2D in the 20x magnification which provides monodimensional 600 μm-wide scans with 1024 sampled points. Finally, in these study, we even made use of Nomarski Contrast Phase Microscopy, which allowed us to acquire a direct optical images of the surfaces. Concerning the X-ray scattering measurements we used the BEDE X-ray Diffractometer (see sect. 5.2.1, page 113) at the wavelength of 1.541 $\mathring{A}$ (Cu Kα1 line) and 0.709 $\mathring{A}$ (Mo Kα1 line).

6.2.1 Titanium Nitride

The TiN sample at the Nomarski Microscope showed some point-like defects in ejection with typical diameter of a few microns and a typical height of 20 nm (they are also noticeable in (100 μm)^2 scan of AFM), which cover a fraction of the surface depending on the considered point (1% at least, but in some points they are much more numerous): these defects and their polishing are still under investigation. There are also some scratches due to the powder-lapping process, but not affecting in a sensitive way the microroughness level of the surface.

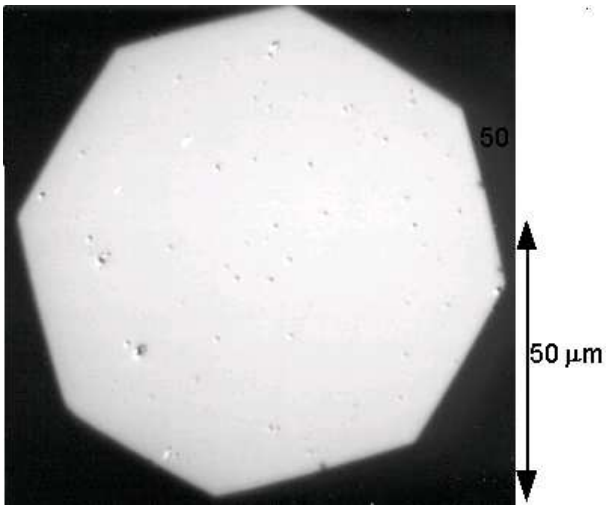

Figure 6.2: A 50x magnification of the surface of the TiN superpolished sample. The point-like defects are visible.

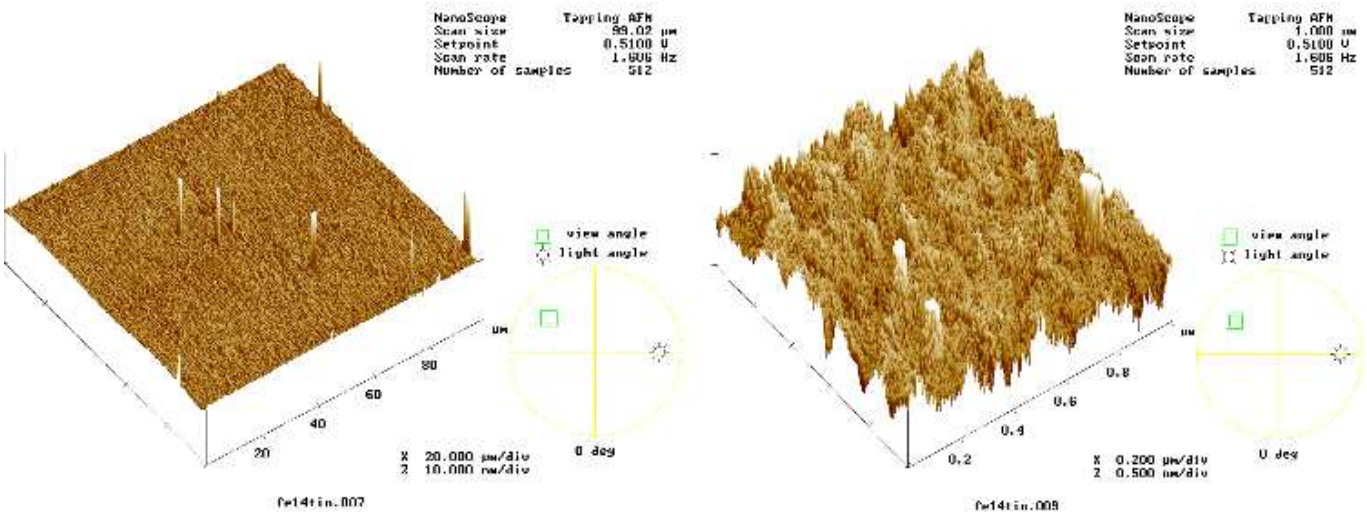

Figure 6.3: AFM digital maps images of the TiN superpolished sample. (left) 100 μm scan length, the scale for the ordinate axis is 10 nm/div. (right) 1 μm scan length, the scale for the ordinate axis is 0.5 nm/div.

In order to get a quantitative topographic surface analysis, AFM scans have been taken in various surface points. The defects visible in the Nomarski image (see fig. 6.2) are evident also in the 100 μm scan (fig. 6.3, left : $\sigma = 2.7$ Å), while the background surface seems to be quite smooth. A 10 μm and 1 μm scan (fig. 6.3, right: $\sigma = 0.8$ Å) show the nature of the low-amplitude roughness. These roughness value show a good improvement in smoothness with respect to the previously reached smoothness with Beppo-SAX (see tab. 6.1). The same improvement is observed also in the WYKO 20x profiles ($\sigma = 3.3$ Å). Moreover, by computing the 1-D PSD of these scans (which approximate power laws, as predicted by the theory for fractal surfaces, see app. B), we can also conclude that the measurements are in agreement each other (see fig. 6.4) as the PSD are superposed.

As explained in the section 5.3.1, another valuable method we have used is the X-ray scattering analysis. The scattering measurements allow us to measure the surface PSD without informations about the chemical composition of the sample. The performed scattering measurements are shown in fig. 6.4: the measured PSD by XRS (either at 8.05 or 17.4 keV) are in a good agreement with the WYKO and AFM data.

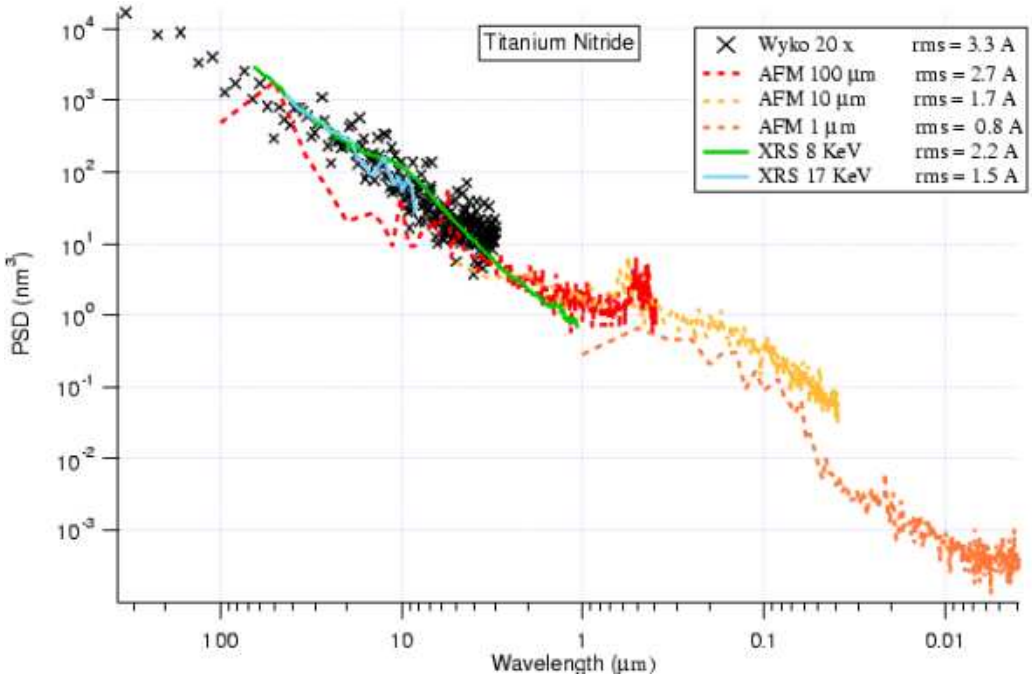

Figure 6.4: PSD results from 8.05 and 17.4 keV X-ray scattering (solid lines), from AFM scans (dashed lines) and from WYKO profilometer (black crosses)

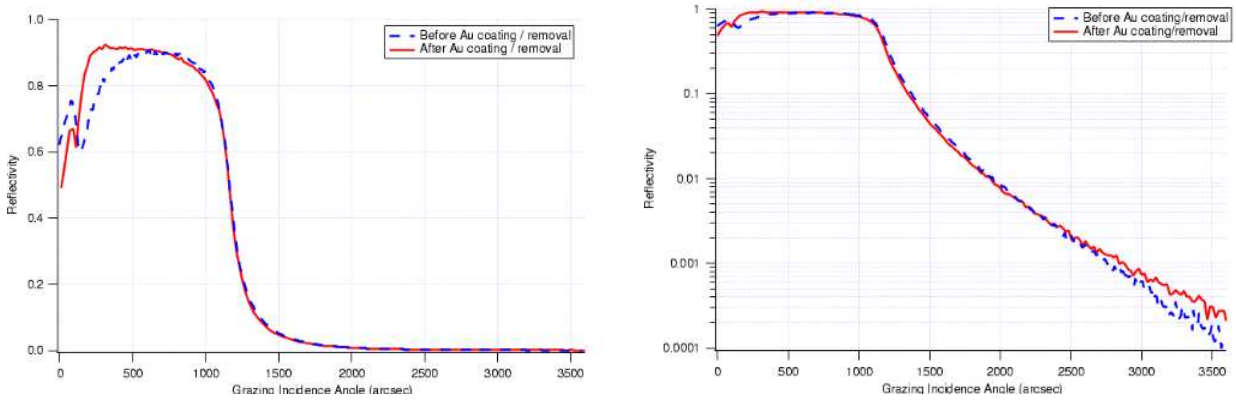

Figure 6.5: TiN 8.05 keV reflectivity profiles before (dashed line) and after (solid line) the deposition and removal (by tape lift) of the Au layer. Linear plot (left) and logarithmic plot (right)

As already mentioned, the adoption of hard overcoatings is suggested by the need of reusing the same mandrel to replicate a mirror shell many times as the requested number of X-ray mirror modules. At the end of some replication the residual particles of the deposited film must be removed in order to avoid the reflectivity degradation in following replications. In order to understand whether our coating can effectively stand the deposition followed by a removal of the deposit, the TiN sample has been coated with a 300 Å-

thick gold layer by e-beam deposition (at Media-Lario, Bosisio Parini, Italy). This Au layer has then been removed from the sample by tape lift. The residuals of gold and tape have then been ultimately removed with an Acetone cleaning. After these steps, we have measured again the sample by X-ray reflectivity and scattering.

The reflectivity results are shown in figure 6.5: the reflectivities before and after the Au coating and removal are identical[1], up to thousands of arcsec grazing incidence angles. As the reflectivity of a superpolished surface is strongly determinated by the its roughness state, we can conclude that the smoothness of the sample was not damaged by a deposition and separation of a layer which simulate, in fact, the operative conditions of mandrel replication. Future measurements will help us to understand whether repeated Au removals do not change the TiN surface smoothness.

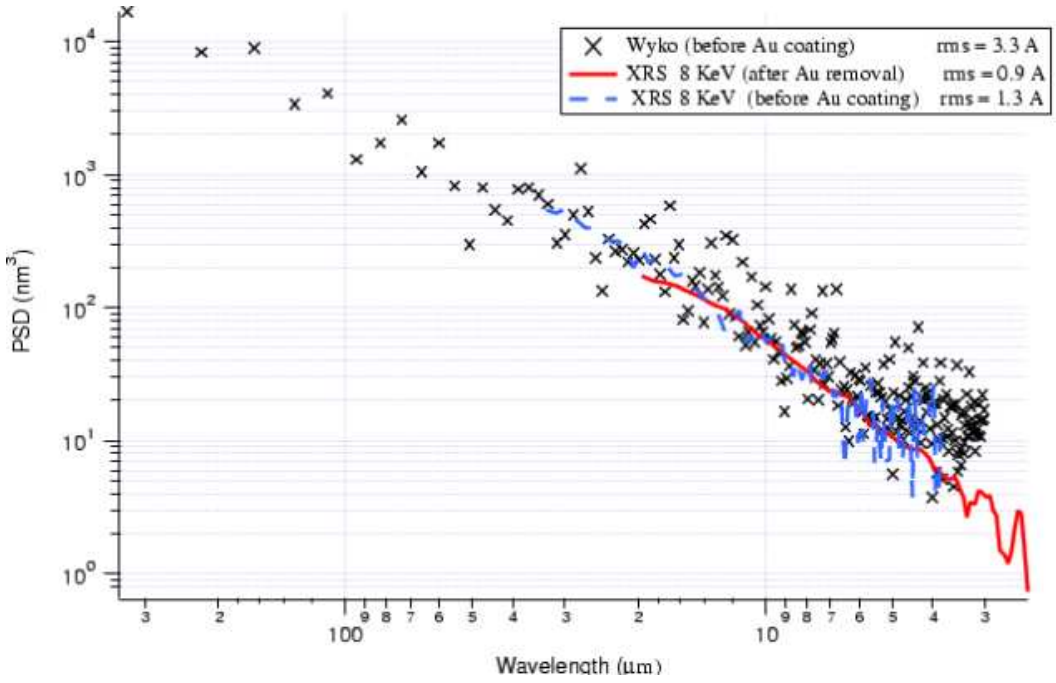

Figure 6.6: PSD comparison in TiN before (dashed line) and after (solid line) the Au coating deposition and removal. The black crosses represent the WYKO measurements before the deposition.

A further confirmation of the resistance of TiN overcoating to the separation of a deposited layer comes from the PSD comparison. The X-ray scattering at 8.05 keV has been measured on the surface after Au removal and compared to the surface PSD before the deposition. The result is plotted in fig. 6.6. The two PSDs are almost superposed, and at no measured wavelength the PSD of the surface after deposition has a larger value than the PSD previously measured. This is another evidence that the surface characteristics were unchanged following the deposition/removal process.

[1]except in the very low angle region: the discrepancy is simply a footprint effect, i.e. due to the incomplete X-ray beam covering at very small angles, see sect. 3.1, page 42. This difference is a purely instrumental effect and it is not related to any surface feature.

6.2.2 Silicon Carbide

The SiC sample images show a less number of point-like defects than TiN. Only very weak scratches due to the diamond powder used for the superpolishing are visible in the Nomarski photos. On the other hand, AFM 10 μm scans show (see fig. 6.7) some undulations in the surface of 2-3 μm wavelength, superposed to some low point-like defects. However, the height of these features is less than 2 nm. The roughness rms is 3.7 σ with a 10 μm scan and 0.8 $\AA$ with a 1 μm scan. The PSD measured by the AFM scans are confirmed by their good superposition. Because of the limited sample size, the performed X-ray measurements allow us to explore only the largest spatial wavelength window (the lower limit is 20 μm). Within this limit, the X-ray scattering measurement superposes quite well to the 100 μm AFM PSD (see fig. 6.8).

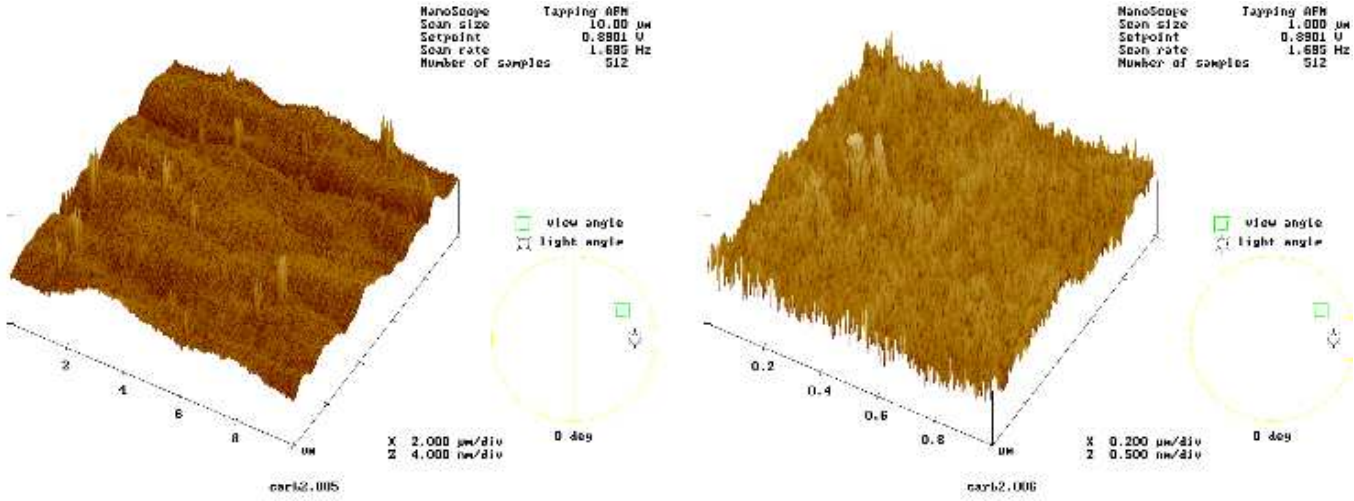

Figure 6.7: AFM digital maps images of the SiC superpolished sample. (left) 10 μm scan length, the scale for the ordinate axis is 4 nm/div. (right) 1 μm scan length, the scale for the ordinate axis is 0.5 nm/div.

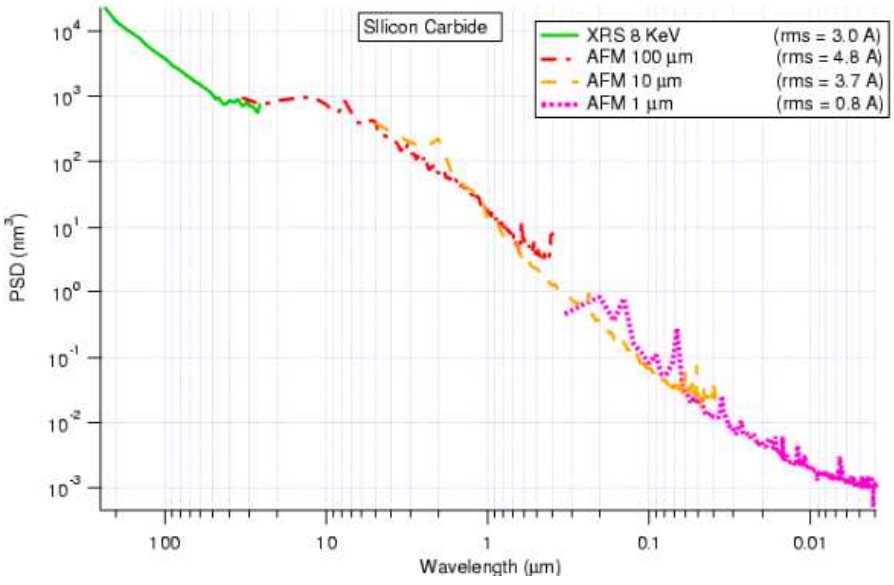

Figure 6.8: SiC PSD results from 8 keV X-ray scattering (solid lines) and from AFM scans (dashed lines).

The absence of peaks (in the explored wavelength range) indicates that the the diamond superpolishing has not left significant periodic features that would scatter strongly the incident radiation (see bibl. [87]). Future planned measurements ought to allow us the extension of the XRS measurements at larger angles, which could give us a confirmation of the topographic measurements at lower spatial wavelength.

6.3 Conclusions

The characterization of two flat superpolished samples with hard overcoating material in TiN and SiC allowed to determine the achieved smoothness of its surface. These tests allow us to understand the effectiveness of the polishing procedure onto hard materials.

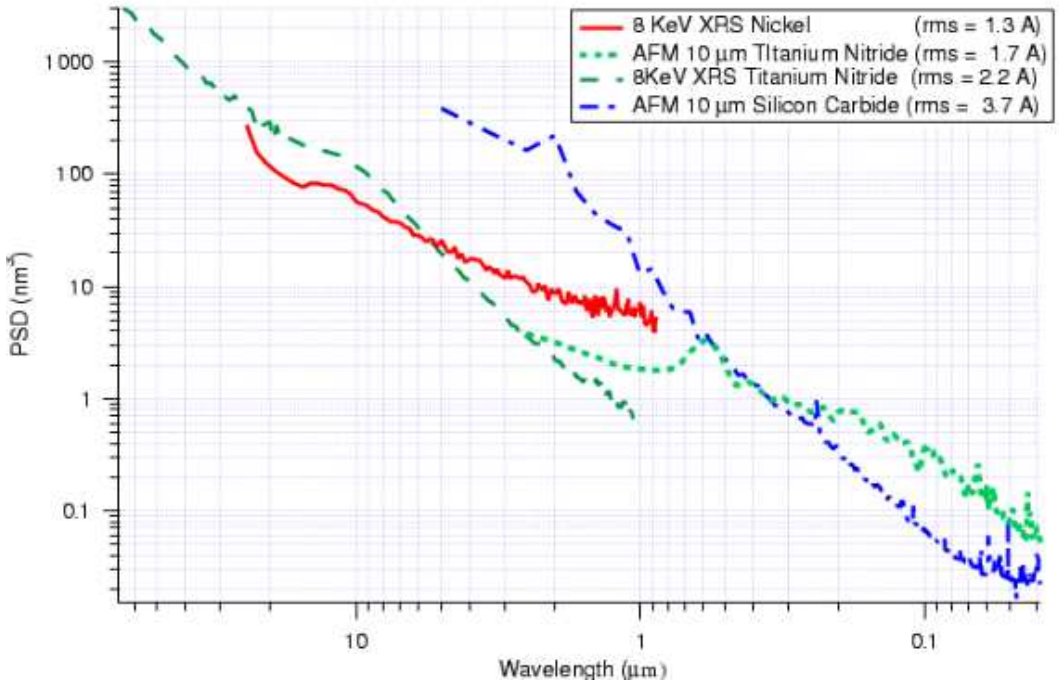

Figure 6.9: Some PSD results with superpolished TiN sample (dashed line) and SiC sample (dashed-dot line) compared to a Ni sample (solid line).

The microroughness measurements performed on the flat samples showed that a multi-instrument analysis lead us to a coherent result: *the TiN and SiC samples can be polished at comparable levels as the already experimented Nickel* (the usual external material of replication mandrels), see tab. 6.3, and due to their hardness properties they are suitable materials for the mandrel replication. The X-ray scattering test has been done also on a Nickel flat sample superpolished following the same superpolishing procedure adopted for TiN. The resulting PSD is plotted in figure 6.9 in comparison to some PSD for TiN and SiC. Although the roughness rms might seem less for Ni than for TiN, the PSD are similar. The better apparent smoothness of Ni is mainly due to the less extent of spatial frequency of the measurement. Moreover, we can observe that the PSD values of TiN are less than Ni in the region around 1 μm, which is the wavelength range that mainly amplifies the surface defect growth in multilayer coatings (see sect. 3.5.2, page 68). We can conclude that the superpolishing procedure works well for TiN as for Ni (at least in the explored frequency range), which was since now the ideal surface coater that could be polished at the requested levels by X-ray optics.

Used Instrument	Nickel (Å)	Titanium Nitride (Å)	Silicon Carbide (Å)
WYKO	3.0	3.3	N.A.
AFM 100 μm	N.A.	2.7	4.8
AFM 10 μm	2.4	1.7	3.7
AFM 1 μm	1.8	0.8	0.8

Table 6.3: Comparison among the obtained microroughness of our flat samples. The XRS measurement rms are not directly comparable because each of then is referred to a different frequency range.

The SiC PSD is not still at the same level as the Ni. The PSD comparison shows that in the 1-5 μm wavelengths range the SiC has a higher roughness than Ni and TiN. The situation changes, however, around some tenth of micron, where the SiC PSD falls down the TiN. This means that it is possible to attain superpolishing levels in SiC which are comparable to TiN at least in the $0.1 \div 0.5$ μm wavelengths. In the SiC case an improvement of the superpolishing method is then necessary, in order to lower the PSD level in the 1 μm region as done with TiN.

Chapter 7

Multilayer development by e-beam evaporation

Multilayer coatings (see chapt. 3) which is foreseen in a number of future hard X-ray telescopes (see sect. 3.7.1, 3.7.3, 3.7.2) can be used to extend the technology of traditional, single layer coated, replicated optics (see sect. 2.3.3, page 29). The advantages of this choice are the very good optical performances and the low mass/geometric area achievable with such a manufacturing technique: the application of graded multilayer coatings to replicated mirror shells would extend beyond 10 keV the capabilities (angular resolution, sensitivity) of optics like those of Newton-XMM, since now limited to the soft X-ray band ($1 \div 10$ keV).

The upgrade of the replication technique to the case of multilayer coatings can be done following two distinct approaches (see fig. 7.1). The first approach is an extension of the usual replication by Ni electroforming, depositing on the master mandrel the multilayer instead of a simple Au layer: this method takes the advantage of returning a multilayer coating with a very similar roughness as the mandrel, but the delicate multilayer structure has to outstand electroforming and replication, delicate processes that can degrade the optics performance. The second method allows the deposition of a multilayer on a previously replicated substrate and does not need a multilayer replication, but it is limited by the practical available length of the linear source. Moreover, the reflecting layer would be sensitively rougher than the replicated substrate (see sect. 3.5.2, page 68).

We are exploring both approaches: the direct method is being studied in the framework of the ASI preliminary project (see this chapter); the second method is explored in the developments of the Con-X/XHT optics, and it is being pursued in a collaboration with the CfA (*Center for Astrophysics* in Boston, US), where W/Si multilayers are deposited by Magnetron sputtering (see chapt. 4) onto replicated mirror shell substrates at INAF-OAB/Media-Lario, as described in the sect. 8.2, page 167.

The development of X-ray multilayers following the first approach is in progress in the framework of the "High energy payload preliminary project" funded by ASI (the Italian Space Agency), that involves INAF/Brera Astronomical Observatory, Media-Lario s.r.l, IASF, Politecnico di Milano, LABEN. This project is aimed to the production of a prototype of an hard X-ray telescope with multilayer-coated optics in view of the construction of the Balloon-borne hard X-ray telescope HEXIT (see sect. 3.7.1, page 78): the technique we are developing is the deposition of multilayer coatings directly on a superpolished Ni-coated mandrel, followed by the deposition of the mirror walls by Nickel electroforming.

In the following sections the adopted coating facility will be described and the results we obtained during the first developments of this activity.

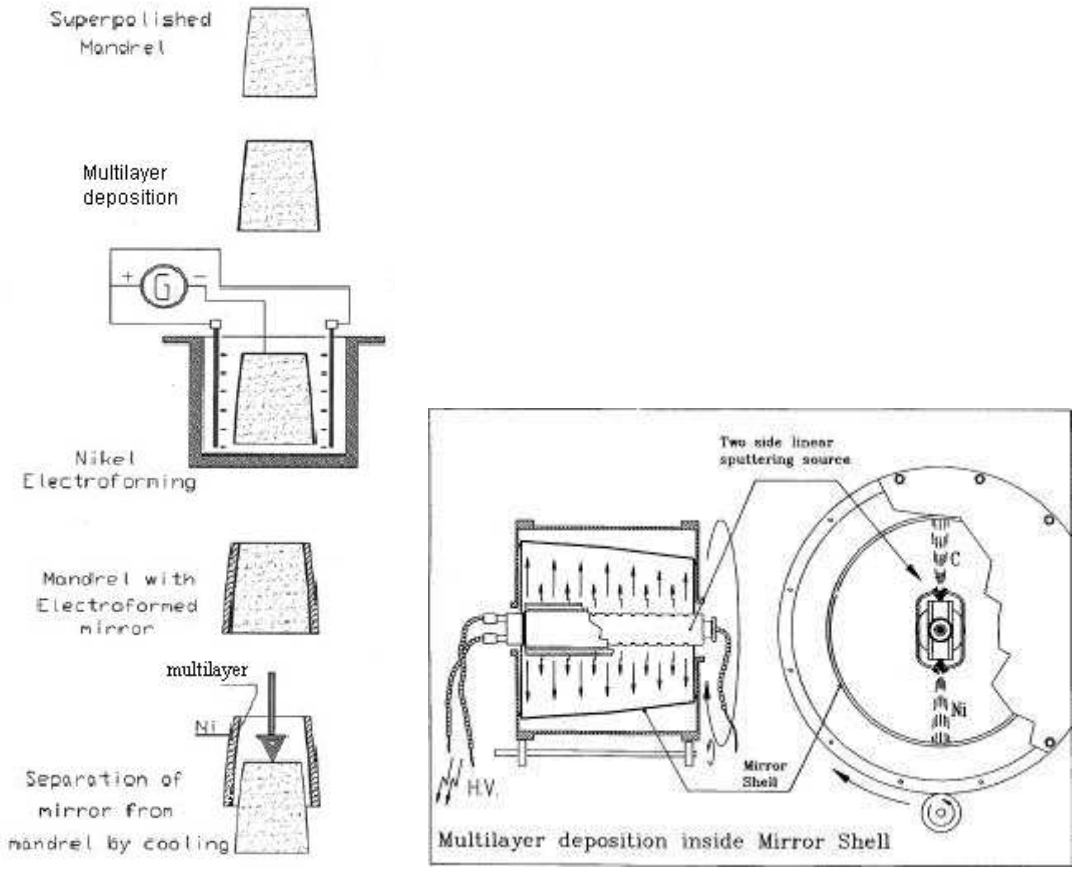

Figure 7.1: The Ni electroforming technique, upgraded for multilayer coatings. (left) First approach: a superpolished mandrel with a negative Wolter I profile is produced, then the multilayer coating is directly deposited onto the mandrel surface superpolished mandrel and the replication by Ni electroforming follows as usual.
(right) Second approach: application of the multilayer coating onto the surface of a *previously Ni replicated Au-coated substrate* by using a vacuum deposition system based on a linear source.

7.1 Multilayer materials choice

The production of multilayer coatings for astronomical applications requires to pay attention to a number of factors. The multilayer has to be wide-band (see sect. 3.4.1, page 58) and it must have an high reflectivity, thus it has to be graded with an high number of bilayers (>100). In order to reduce as possible the number of bilayers, the materials that compose the multilayer coating must have an high density contrast, and their photoelectric extinction in the X-ray band to be reflected must be low.

Moreover, the roughness growth must be checked (see sect. 3.5.2 on page 66, 3.5.2 on page 68) and kept at a low level as well as the layer interdiffusion. It is well known, furthermore, that interlayer stresses arise due to the mismatch of the CTEs of substrate and of the two layers forming the multilayer stack (see sect. 3.5.3, page 71).

To minimize the impact of thermal stress, the multilayer coating can be designed with a proper Γ ratio (see sect. 3.5.3, page 71), but, since this parameter determines also the film optical performances, this parameter cannot be freely varied.

The multilayer design has then to satisfy the following requirements (see fig. 7.2, page 141):

1. the materials (substrate, absorber and spacer) should have a similar thermal expansion coefficient;
2. the Young's modulus of the materials should be high enough to reduce optics deformations;
3. all the foreseen (differential and absolute) stresses should be below the breaking strength.

Material	*Young's Modulus (GPa)*	*Thermal Expansion coefficient ($10^6 \times K^{-1}$) @ 25 °C*	*Breaking strength (Mpa)*	*Sputtering Yield*	*Temperature at vapour pressure $10^{-4}/10^{-6}$ torr*	*Possible coupling*
Ni	200	13.0	Not available	1.3	*1270/1072*	*C*
C	6.5 ÷ 9 (graphite)	7.1	8 ÷ 15 (graphite)	0.36	*2015/1872*	*Ni, Pt*
Pt	168	8.8	Not available	1.1	*1750/1492*	*C*
W	411	4.5	Not available	0.60	*2800/2407*	*Si*
Mo	329	4.8	1930	0.70	*2150/1822*	*Si*
Si	47 ÷ 131	2.6	120	0.5	*1340/1147*	*Mo, W*

Figure 7.2: a comparison of the properties of some materials used to produce multilayer coatings

A good couple of material that approximately satisfies these requirement may be the couple Pt/C (fig. 7.2) that, in addition to a good chemical stability (suitable to make stable, abrupt interfaces) and a very high contrast density (Pt: 21.1 g/cm^3, C 2.3 g/cm^3) that allows to minimise the number of necessary bilayers and the consequent interlayer stresses, have also a very similar thermal behaviour. Furthermore, C is a spacer with a minimal X-ray photoelectric absorption coefficient and Pt has the K-edge at the energy of 80 keV, so they can be used to reflect X-rays in the band 10 -70 keV (covering the whole X-ray band of HEXIT, see sect. 3.7.1, page 78) without an excessive photoelectric loss.

Our final project foresees in the framework of this preliminary project the deposition of graded multilayer with $\sim$ 150 bilayer: in this first phase, however, we will produce a mirror shell with a constant period multilayer. This first step will allow us the calibration and the evaluation of the deposition method.

7.2 The deposition facility

The capability of deposition on large surfaces is an important requirement in order to industrialise the multilayer coating process. The deposition rate has to be large enough to coat a number of mirrors (or master mandrels) in a reasonable time and the deposition has to cover the whole surface with an uniform film. For these reasons, we are concentrating on the *e-beam deposition*: it is known that this deposition method allows the coverage of large surfaces (see chapt. 4) and the evaporating crucible can be much smaller

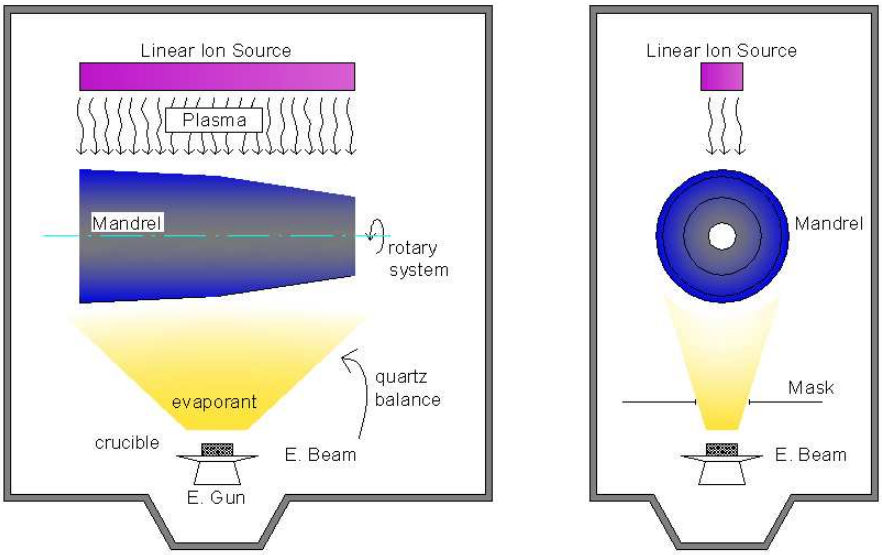

Figure 7.3: Scheme of the implemented coating facility: front view (left) and side view (right): the evaporating e-beam device is located in the lower part of the vacuum chamber, where some crucibles mounted on a carousel carry the materials to be evaporated (Pt, C, Ni, Mo, Si ...). The evaporate condenses on the rotating mandrel, after passing through an equalization mask that allows an uniform coating upon the whole mandrel length. The thickness growth is monitored by a quartz microbalance device: the layer thickness and the evaporation rate are managed by a control electronics and by a system of shutters. In the upper part of the chamber, a Linear Ion Source (LIS) provides an homogeneous Ar ion flux on the deposited layer while the mandrel rotates, in order to improve the film properties.

than the substrate size (see e.g. bibl. [32]): moreover, some vacuum chambers (mod. *Balzers*) equipped with an e-beam evaporator (8.1 ÷ 11 kV) are already installed at Media-Lario (see fig. 7.3), and were already used to make the Au coating of the XMM mirrors (see sect. 2.3.3, page 29 and fig. 7.4).

These vacuum (residual pressure $\sim 10^{-6}$ mbar, obtained with cryopumps) chambers host a set of crucibles mounted on a carousel that can be used to host and switch the materials to be evaporated in vacuum (Pt, C, Ni, ...): the evaporates condense on a rotating mandrel, or upon open substrates (those often used used for calibration). The deposition rate may be of 0.2 nm/sec or more (on non-rotating samples). Eventually, a lower rate may be also chosen, provided that the incident power is large enough to keep the crucible hot, and obtain a steady evaporation rate.

The thickness monitoring and control are demanded to a power feed-back system and to a system of shutters controlled by a quartz microbalance: a specially designed software varies the e-gun settings in order to keep the evaporation rate stable: many parameters (film density, beam size/sweeping path on crucible, quartz response time/gain...) have to be set and optimized by the operator: all these parameters are fundamental in order to obtain repeatable films, and have turned out to be basic in determining the multilayer characteristics.

In order to check the absence of contaminating agents, the residual gas in the deposition chamber is analyzed by a *mass spectrometer* mod. *Quadstar*: this device is able to ionize and measure the concentration of molecules present in the chamber, discriminating them from their mass/charge ratio. Usually the residual atmosphere is analyzed immediately before and after every evaporation.

These coating chambers are thus perfectly suitable to deposit multilayer coatings, and the results we have obtained with flat substrates are very promising (see sect. 7.3 on page 147, sect. 7.4 on page 152).

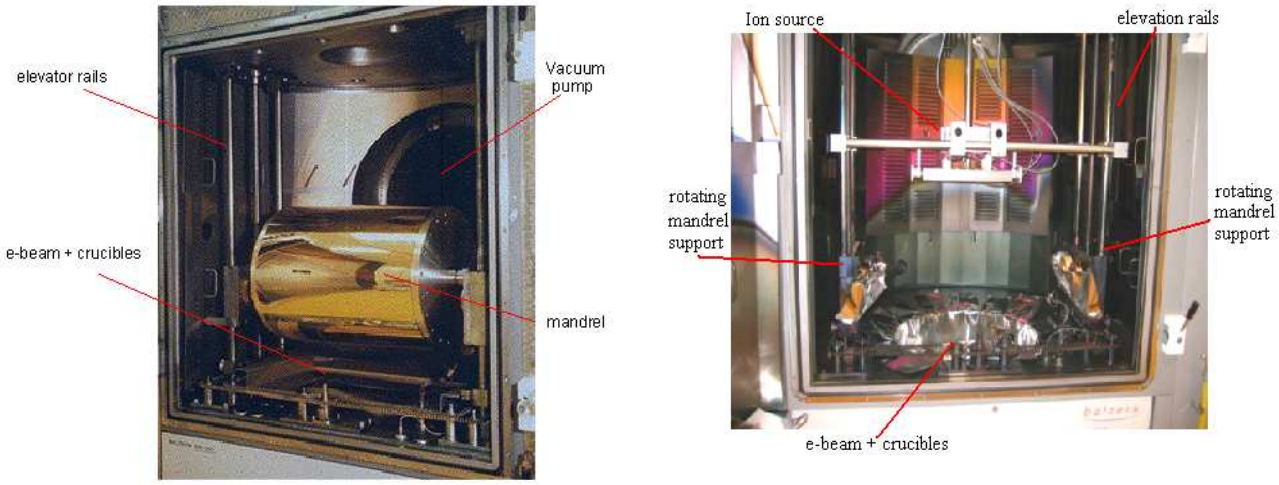

Figure 7.4: The coating chambers installed at Media-Lario.
(left) The open chamber with a Gold coated XMM mandrel mounted on the rotary system: the Balzers chambers are large enough (vol. 1.5 m^3) to host large mandrels to produce large, monolithic mirror shells, like e.g. those of the SIMBOL-X optics. They can be used, indeed, to coat also large (planar or curved) masters or substrates like the segments of the XEUS mirrors (credits: Media-Lario s.r.l.).
(right) a coating chamber of the same model after the installation of the ion source, visible in the upper part of the chamber: the e-beam evaporator + crucibles are located in the cavity in the lower part of the image (credits: Media-Lario s.r.l.).

A typical problem of the e-beam is, however, the evaporation rate instability (see chapt. 4); this is especially true for Carbon: a large part of my activity was the search for a parameter combination that could allow the stabilization of the Carbon evaporation, but now we think we have achieved a steady deposition rate. Another possible problem is the sensitivity of the *quartz microbalance* devoted to the thickness monitoring, to the deposited material density fluctuations. This might cause in turn an uncertainty in the thickness determination: a large number of trials have been done, leading to some possible solutions.

In order to improve smoothness, adhesion, hardness, durability of the film, a Linear Ion Source has been installed in one of the coating chambers (see fig. 7.3, fig. 7.4). This source provides an homogeneous Ar ion flux on the whole mandrel length while the multilayer coating is grown by e-beam evaporation: the Ar ions transfer a part of their energy and momentum to the atoms constituting the layer and they increase their mobility: the result is a smoothing of the structures that cause most of the film microroughness, and a consequent improvement of the multilayer reflectivity (see chapt. 4).

The ion assistance has been also reported to enhance the film mechanical resistance and the durability against environmental agents, an important requirement for coatings which have to operate on-board an orbiting spacecraft, where the residual atmosphere, mainly constituted of atomic oxygen, causes a rapid film aging.

The installed Linear Ion Source (LIS) is able to produce an Ar ion flow upon a length of 40 cm, sufficient for the ion polishing/assistance on a mandrel. A scheme and an image of the ion source are showed in fig. 7.5. The LIS (unlike the Kaufman-type source in figure 4.5) is a metallic box with electrodes connected to an high (100 ÷ 2000 V) voltage generator. An Ar inlet enters the box and, when the pressure reaches the limit to produce a glow discharge, it is strongly ionized. The strong electric field in the box accelerates the ions, that emerge from two slits in the lower part of the LIS, while the electrons are trapped by a magnetic field produced by permanent magnets. The longer electron path helps the Ar ionization and to sustain the

discharge, even at voltages of some hundred volt. Most of the Ar flow is, indeed, not ionized and simply flows in the vacuum chamber, where it is pumped out by the cryopump. The regulation of the Ar flow (that can be varied with a precision of cm^3/min) may be used to stabilize the chamber pressure.

The energy of the incident ions may be tuned by varying the source voltage: the current may also be varied as a function of the voltage or by varying the pressure with a variation of the Ar inlet. A larger pressure than the used one in the simple e-beam evaporation (some 10^{-5} mbar) provides a larger spatial charge density, allowing the discharge also at lower voltages ($100 \div 150$ eV) with high current fluxes. This condition is desirable for ion assistance, as the ion energy has to be low enough to avoid the film sputtering and the ion implantation: the ion polishing in more grazing incidence is also possible at higher energies and lower pressures (> 500 eV).

The angle of incidence of the Ar ions may be varied simply by tilting the whole source: a contribution to the incidence angle variation is also given by the mandrel roundness. The distance of the source from the mandrel may, similarly, be varied ($10 \div 35$ cm).

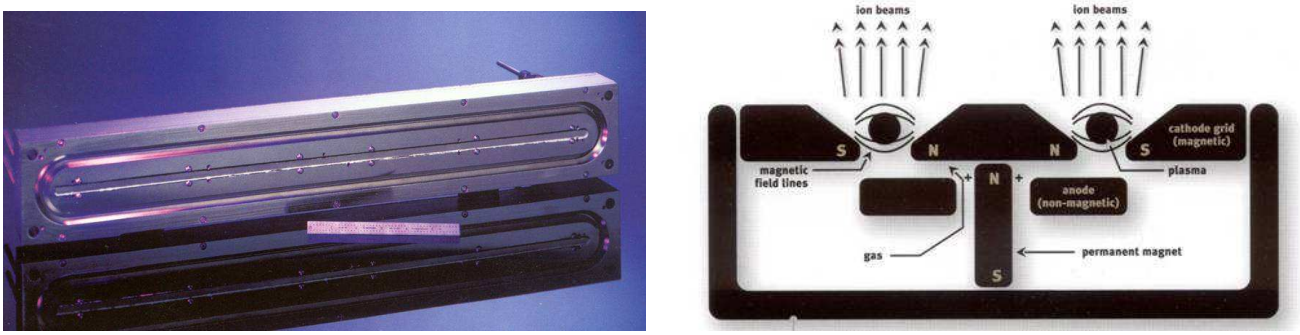

Figure 7.5: (left) A view of the Linear Ion Source installed in the coating facility. The plasma is generated inside the box. (right) A scheme of the Linear Ion Source (credits: Advanced Energy).

The use of an ion-source with the e-beam method is not simple, since the working pressure range of the e-beam ($10^{-6} \div 10^{-7}$ mbar) does not overlap that of the ion beams ($10^{-4} \div 10^{-5}$ mbar). At too low pressures the ion beam provides a too small ion flux (or none at all) but at higher pressures the e-beam could produce a short-circuit, and the film quality could be compromise by the inclusion of Ar gas. An intermediate pressure range has to be adopted, in order to permit the operation of both devices, while the ion assistance is expected to give a large return in the film properties.

Most of the developed activities were centered on the stabilization of the thickness in order to achieve the capability to produce multilayers according the foreseen design (a supermirror). A preliminary result is being pursued and a Ni electroformed mirror shell with 20 Pt/C bilayers (periodic) has been produced and has been characterized at the PANTER facility in full illumination setup (see sect. 7.6, page 156). The period of this mirror shell is thin enough to make us understand whether the cited control has been achieved: on the other side, the number of deposited layers (20) is small enough to avoid a large roughness growth, thus, in this phase we used the e-beam evaporation alone: the problem of roughness will, indeed, emerge in the next future, when we will deposit graded multilayers, since the number of necessary bilayers will be larger of an order of magnitude: the calibration of the ion assistance followed by its use will be absolutely necessary.

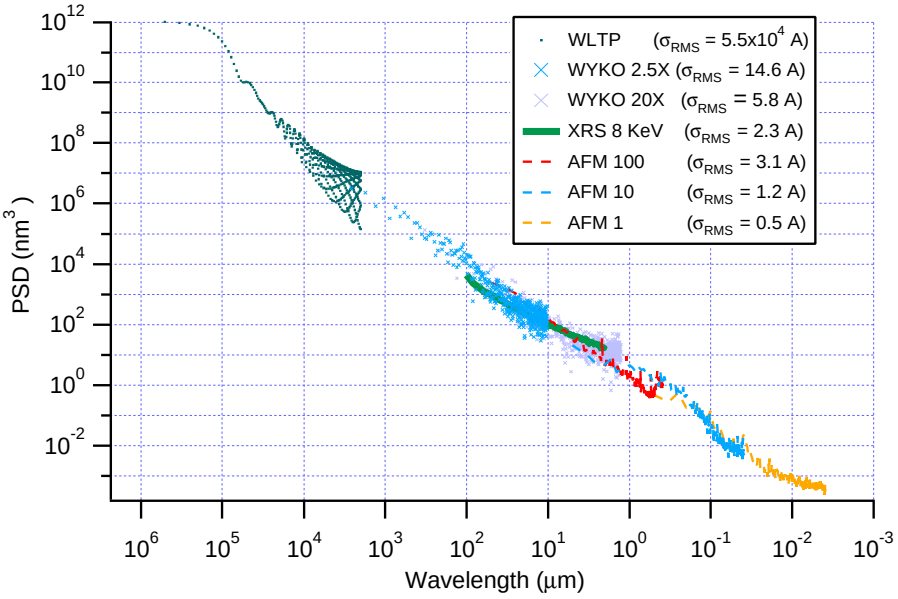

Figure 7.6: PSD measurement on a Si superpolished surface (*courtesy of D. Vernani*). The PSD are computed by all of available instruments, each covering its sensitivity wavelength band: all the measurements are in very good agreement and describe a Lorentzian profile, as predicted by the theory. The "knee" is located in the LTP range (left) whereas the WYKO is a power law (typical of fractal surfaces) and superposes very well to the 8.05 keV scattering measurement. The AFM covers the $0.01 \div 100$ μm and it is a power-law as well.

7.2.1 Used substrates and single layer deposition

The multilayer development project has been started by the deposition of coatings with constant period by simple e-beam evaporation in order to check the process control, with the substrate placed *opposite* the evaporating target and without any beam masking. The first tests performed had the aim of understanding the e-gun parameters necessary to guarantee a steady evaporation; we have started to deposit single layers various elements (Ni, C, Pt, Si, some 10 nm thick) on simple glasses and we have measured the thicknesses with the X-ray diffractometer at INAF-OAB (see the examples in sects. 3.1, 5.2.3 page 115), providing so a first calibration for the quartz microbalance. Simple glasses could be used for simple trials, but to understand the intrinsic deposition characteristics process smoother substrates have to be used.

Smooth substrates and not so expensive are *Silicon wafers*, used as substrates in nanoelectronics: they are thin (some mm) slices of crystalline Silicon superpolished to σ levels of $3 \div 4$ Å: they are also hard and abrasion resistance, so they can be cleaned if necessary. A PSD characterization of a Si wafer is presented in fig. 7.6. Other substrates we used were fused silica disks ($\sigma \sim 1 \div 2\mathring{A}$), Nickel Kanigen superpolished disks ($2 \div 3\mathring{A}$): the deposition on Nickel Kanigen (the same material used to coat the mandrels used for the shell mirror electroforming) is a basic step in order to understand the replicability of the deposited coatings.

7.3 Ni/C multilayers

The first attempts have been done in order to test the coating facility reprogramming oriented to multilayer deposition: a set of tests has been done with Ni/C multilayers, that allowed us to learn more about the Carbon evaporation (the spacer to be used in our final deposition) while using Nickel as absorber (a much cheaper material than Platinum). After finding the parameters necessary to guarantee a steady Carbon

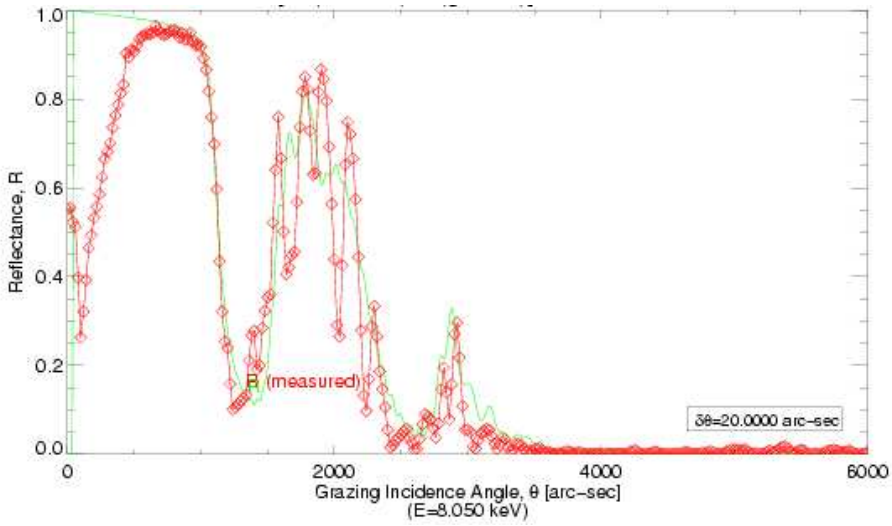

Figure 7.7: Reflectivity scan at 8.05 keV of the first Ni/C multilayer with 20 bilayers. The peak is very broad and it can be fitted assuming a variation of the period of 8 nm along the stack (with an average period of 20 nm, much larger than programmed). The period drift is likely caused by a variation of the shape of the Carbon target, layer after layer, that caused a modification of the ratio of the thickness deposited at the quartz microbalance to the deposited one on the sample (the so-called tooling factor).

evaporation, a deposition of a 20 bilayers Ni/C multilayer, aimed to the calibration of the multilayer period, has highlighted some critical points in the deposition of Ni/C multilayers (see fig. 7.7):

- the 8.05 keV reflectivity scan shows that the first Bragg peak is extremely large, and dispersed in a set of secondary peaks: this dispersion is due to the period instability and, since the Nickel deposition has never shown any instability in the previous tests (in a Ni/Al multilayer, e.g.), the cause is probably to be searched in the Carbon;

- the peak reflectivity is indeed, large (83 %), indicating that the deposition has good properties with low roughness (4-5 Å):

The reason of the lack of thickness control in the Carbon deposition may be searched in the fact that Carbon does not melt and the shape of the evaporation cone is varied when the Carbon target shape changes (as effect of the evaporation itself). In these tests the quartz microbalance was located in an angular position far from the substrate, so the ratio between the Carbon thickness at the probe and that on the sample changes, with a consequent increase of the Carbon layer grown at every cycle (this was evident also from the increase of necessary power to evaporate at a constant rate).

We have deposited Ni/C multilayers with unchanged settings with respect to the previous one, but with the quartz microbalance near to the Silicon wafer substrate, and we have reached a very encouraging result from this deposition, even if the e-beam deposition without assistance is commonly believed to be a not optimal deposition method for multilayer coatings. The X-ray reflectivity characterization of an example of deposited Ni/C multilayer prototype at the two standard energies of 8.05 keV and 17.4 keV is shown in fig. 7.8. The reflectivity at the first peak turns out to be very good (95% at 8.05 keV). The average period (110 Å) is indeed much larger than programmed (90 Å).

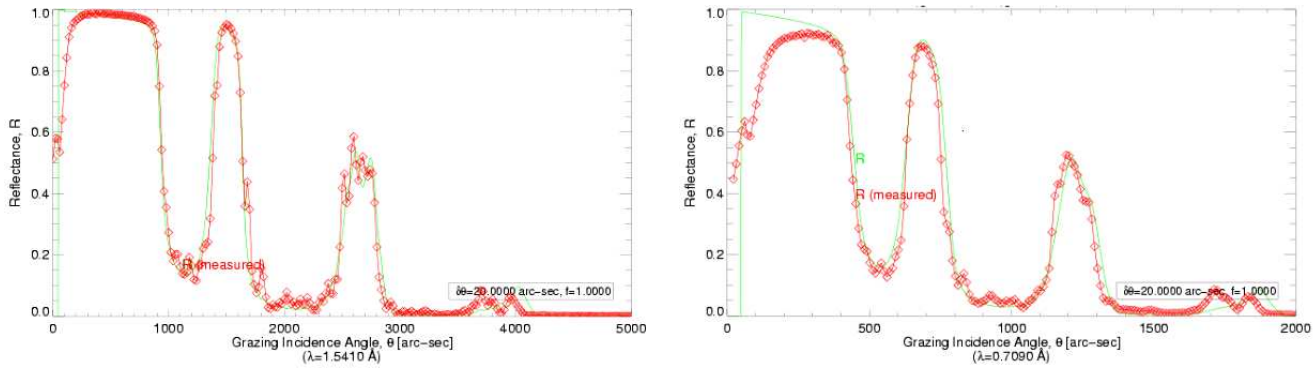

Figure 7.8: Reflectivity scan at 8.05 keV and 17 keV of a Ni/C sample. X-ray reflectivity test at 8.05 keV (left) and 17.4 keV (right) performed on a Ni/C multilayer with 19-bilayers. The reflectivity profile is fitted with IMD. The first peak reflectivity is over 95% @ 8.05 keV. In both cases there is an evidence of layer thickness instability: the period drift has been strongly reduced in the successive multilayers. The roughness value inferred from the model is about 3 Å, assuming the bulk value density for the Carbon (2.3 g/cm^3).

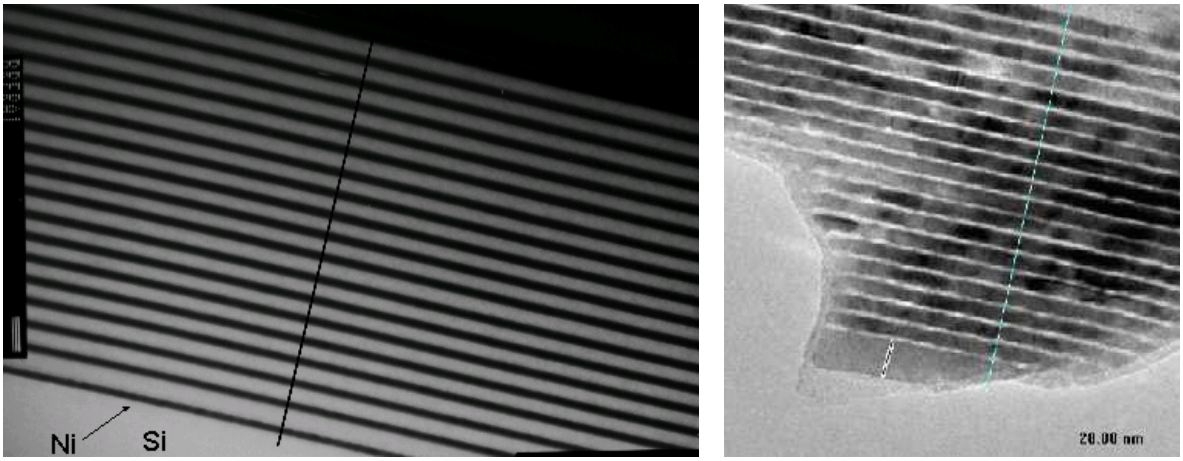

Figure 7.9: (left) TEM section of a Ni/C deposited by e-beam with the Balzers coating chamber at Media-Lario. The dark bands are the Nickel layers, the clear ones are the Carbon layers and the Silicon substrate. Both Carbon and Nickel are completely homogeneous and amorphous: the thickness is variable with the depth. TEM section of the X-ray measured Ni/C multilayer. Overall thickness: 219 nm. The Ni layers are the dark bands, the C or Si are the clear bands. The layers are completely amorphous and homogeneous.
(right) TEM section of a reference Ni/C multilayer deposited by Ion Beam Sputtering (see chapt. 4). In this case a number of crystallites has formed and the layers are less homogeneous than in our case

The reflectivity curve is well fitted with a roughness of 4 $\mathring{A}$ assuming a C density of 1.6 g/cm^3, and 3 $\mathring{A}$ assuming the C bulk value (2.3 g/cm^3), very near to the initial substrate value: the use of the ion assistance is expected to smoothen the film even more.

The 2^{nd} peak dispersion indicates instead a residual drift in the bilayer spacing, that can be estimate with IMD to be of the order of 2 nm: the presence of this period drift is confirmed by a *Transmission Electron Microscope* (TEM) analysis (see fig. 7.9, left), that showed also a very promising film quality as the layers are amorphous and homogeneous.

The absence of crystallites in the structure is very positive also because it lowers the interlayer *intrinsic* stress (see sect. 3.5.3, page 71). A possible cause of the period instability may be the evaporation rate or

density fluctuations: thus, we have in the following paid special attention to the stability of the evaporation conditions. It is worth noting that a part of the reflectivity enhancement is caused by the lower value of the C density, which increases the contrast density absorber/spacer.

On the other side, the large CTE difference between Ni and C (see fig. 7.2 is responsible for large thermal stresses that arise during the deposition and showed an X-ray reflectivity decay some months after the deposition. The multilayer ageing due to thermal stresses will be probably mitigated by the adoption of Pt/C multilayers.

7.3.1 Characterization of Carbon density

The period dispersion observed in the Ni/C multilayer is of course a problem to be corrected. The production of a graded multilayer requires obviously a sharp determination of the d-spacing, and this is impossible without the control on the deposition process. A probable cause of the thickness instability is the Carbon evaporation, as evident from the fig. 7.8. Also the Nickel has a thickness drift, but since our goal is the deposition of Pt/C multilayers, we have started to search for the possible causes of the Carbon thickness drift.

As the evaporation rate measured by the quartz is steady, one possibility is the fluctuation density of the Carbon. This is not so unlike as the C atom sticking on the substrate has a low mass (12 a.u.m.) in comparison to the residual air molecules present in the deposition chamber. As the packing density depends on the energy of the sticking atom (and for the e-beam the energy is already low, 0.1 eV, and as a result the e-beam evaporated films are often lighter than than in the natural conditions), it is possible that an higher chamber pressure increases the number of collision of the adatoms with the air molecules: the result would be a loss of kinetic energy and a reduction of the Carbon density. This can be one of the reasons why the obtained period with the Ni/C multilayer was much larger than programmed.

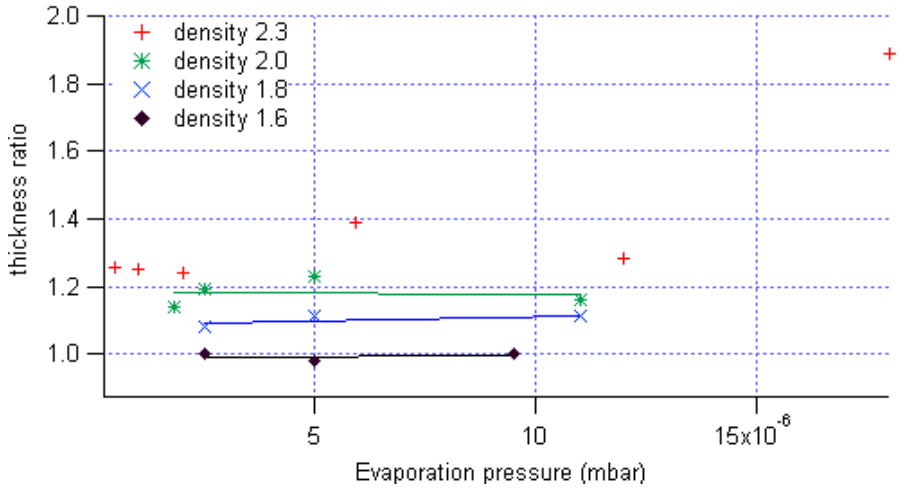

Figure 7.10: Variation of the obtained/expected Carbon thickness deposited by e-beam as a function of the pressure chamber and as a function of the set Carbon density in the quartz microbalance.

To calibrate the quartz microbalance to the deposited Carbon density, we have done some Carbon density measurements, also in order to understand an eventual dependence of density on the deposition pressure. Such a measurement could for instance be done by depositing some thin layers of Carbon on glass samples and deriving the actual density from the Carbon critical angle (see sect. 3.1) in reflectivity scans at 8.05 keV.

However, this method is not suitable since the Carbon critical angle is near to that of glass, so they can be confused. Also by coating the glasses with Ni layers in order to increase the density contrast (as described in the sect. 5.2.3) we could not reach ultimate results because of the difficult of a precise determination of the critical angle, and since angle offsets can be present from the initial sample alignment with respect to the X-ray beam.

Some thin Carbon layer depositions on glass substrates have been done and we have measured their thickness to understand if pressure variation in the coating chamber could cause a density fluctuation: a density fluctuation causes a thickness variation because the quartz microbalance intends the frequency decrease during the deposition on the basis of the depositing material density, whose value has to be entered by the operator. If the assumed density is overestimated, the quartz microbalance (which is sensitive to the deposited mass) will in turn underestimate the deposited thickness, and it will close the shutters later. The result will be an exceeding layer thickness.

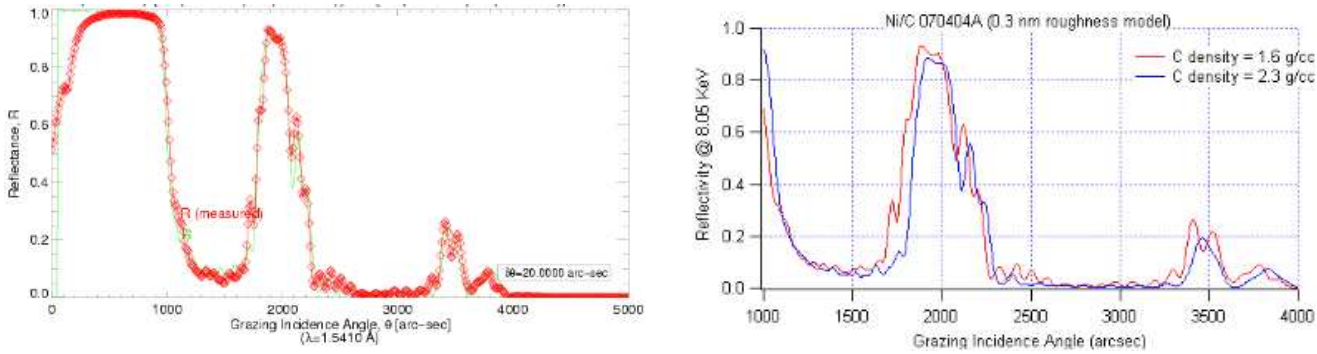

Figure 7.11: (left) 8.05 keV reflectivity scan of a deposited Ni/C multilayer after the C density determination. The period has been kept better constant, but some layers are still different as a result of the ion-gun instability.
(right) a simulation showing how the low carbon density has improved the reflectivity from 88% (blue curve, 2.3 g/cm^3, bulk value) to 93% (red curve, 1.6 g/cm^3, fitting value)

In fig. 7.10 some results are shown: the ratio obtained/expected thickness (measured by XRR reflectance fitting) vs the chamber pressure is usually larger than 1: this indicates that the obtained density was less than expected. We have repeated the depositions for different density setting in the quartz probe (2.3 g/cm^3, 1.8 g/cm^3, 1.6 g/cm^3) and the deposited thickness is equal to the expected one for the density value *1.6 g/cm^3*: this is the probable density value for the deposited Carbon. This value is also in agreement with the value inferred from the Ni/C multilayer fits.

The density seems not to be affected by the chamber pressure, as the thickness are constant with different pressures. Only for the set density value of 2.3 g/cm^3 there is a rough increase, but the correlation is uncertain and it is probably due to a rate instability.

The obtained result has been confirmed by the following Ni/C multilayer deposition: in fig. 7.11 a Ni/C multilayer with 20 bilayers has been deposited after setting the Carbon density value to 1.6 g/cm^3. The XRR curve at 8.05 keV is shown: the first peak reflectivity is high (93%) and the average period is the desired value (9 nm, $\Gamma \sim 0.33$): this means that the main reason to the larger period was the wrong Carbon density assumption.

The period drift, however, has not disappeared: it has been reduced to 1 nm (the Ni/C drift was 2 nm) but it is still present, as can be seen from the first peak width and the very low and dispersed second peak. The IMD modelization has shown that only some layers in the middle of the multilayer are responsible for

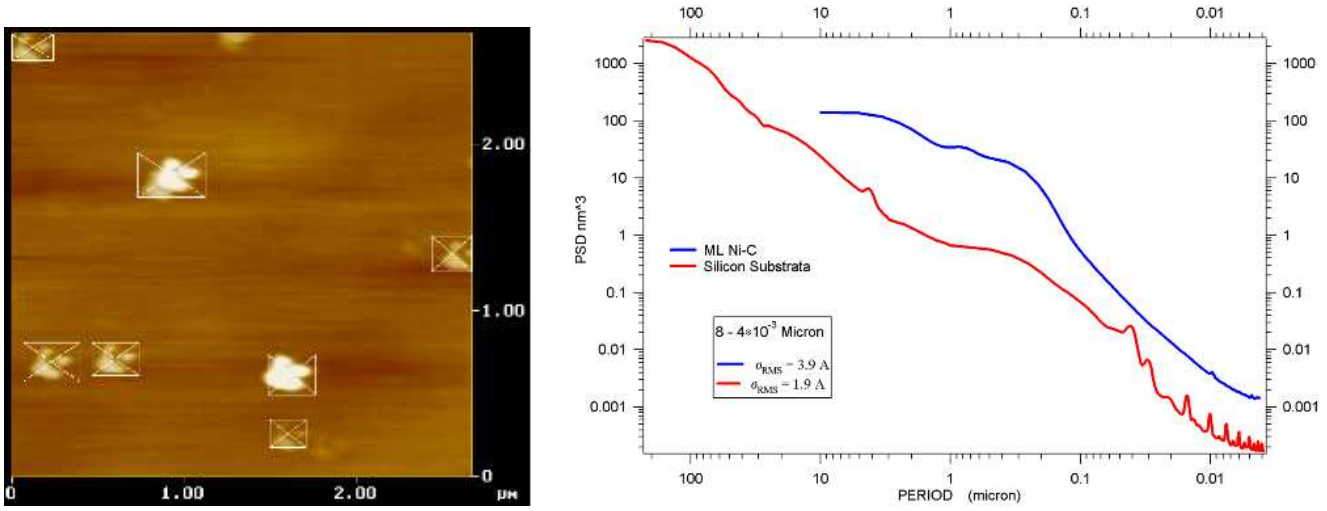

Figure 7.12: (left) AFM scan of the multilayer measured in fig. 7.11. Except some point-like defects (Silicon Wafer defects?) the surface is very smooth.
(right) The spectral analysis of the AFM scan. The roughness growth is evident from the PSD (the point-like defects are excluded from the analysis: *courtesy of D.Vernani*). Note the PSD growth in the intermediate frequency range.

the period variation: this makes only 10 bilayers active in reflection since the deepest 10 are phase shifted, a number sufficient to build a good reflectivity at the first peak, but useless to produce an high second peak.

If the density is essentially constant with pressure variation, the cause of the layer drift must be another one: we have found that the origin is probably the heat emission effect on the probe and in the feedback power system that try to keep the evaporation rate steady: we have obtained good benefits from the stabilization of the e-beam incident power (see sect. 7.3.2, page 150).

It is worth observing that the lighter Carbon contributes to the reflectivity improvement because it enhances the density contrast (see fig. 7.11): were the C density 2.3 g/cm^3 (with all the other parameters unchanged), the first peak would have been high only 88%. This is positive in view of the deposition of the graded multilayers, as in that case every small reflectivity enhancement is important (in graded multilayers a limited number of bilayers reflects a single X-ray wavelength).

The inferred roughness from the XRR fit is $3 \div 4 \mathring{A}$. This is a good result since this value is near to that of the substrate (a Si wafer) and consequently the deposition process does not develop a rough multilayer. The AFM scan of the multilayer surface (see fig. 7.12) shows that, excluding larger point-like defects (probably Silicon wafer defects), the roughness in the wavelength range $10 \div 0.01$ μm is 0.37 nm, in agreement with the XRR measurement. The PSD spectral analysis shows also the roughness increase in all the spectral range (and especially between 10 and 0.1 μm, as expected from the roughness growth models, see sect. 3.5.2, page 68).

7.3.2 Electron gun settings

In the stabilization of the layer thickness an important role is played by the electron gun settings. The energy of the electrons, determined by the accelerating voltage, is not very important from this viewpoint. The *shape and size of the e-beam* is fundamental, instead, in order to obtain repeatable films. This is always true, but especially with Carbon evaporation.

The Carbon evaporation target is constituted by Graphite: the melting temperature of Graphite is very high (3527 ^{o}C at 1 atm pressure, higher than for Tungsten). In high vacuum the melting temperature is lower and could be reached with an e-gun (depending on the incident power), but with Carbon the sublimation temperature is reached first (1867 ^{o}C at 10^{-6} mbar). As a result, Graphite sublimates instead of melting and evaporating (like Ni, Pt, Si, Mo, and so on). The sublimation takes place easily, producing a quick layer deposition. This has, however, two defects:

- the sudden sublimation is larger than the evaporation rate, and the feedback power control system tends to reduce the power very quickly: the resulting rate fall produces a feedback increase of the power, producing an oscillating deposition rate. This may be corrected by setting the gain and the response time of the feedback cycle of power regulation;

- due to the lack of melting, the target consumption is not uniform, as the Graphite target evaporates mainly in the regions "sweeped" by the e-beam. At the center of the target, thus, a "hole" is produced, and consequently, the evaporation cone is shielded by the hole walls. The evaporation takes so place within a narrower solid angle while the target consumption goes on: this may have as a result a non-uniform coating even on small surfaces, but also in an irregularity in the deposited layers if the quartz probe is off-axis as in deposition on rotating mandrels;

For these reasons, a very broad e-beam must be used with a Graphite target. A beam that sweeps all the target enlarges the evaporation hole, allowing a more uniform, repeatable and regular layer deposition. An example (the same plot as in fig.5.11, right) is reported also hereafter in fig. 7.13. The thickness drift is reduced with respect to the example reported in fig. 7.8 from 2 nm to 8 Å: however, the high secondary peaks located at the left of the first and second main peak can be fitted (with IMD) by assuming an *exponential* increase (with a C thickness trend $70.7 + 9.9e^{-0.18i}$) of the period from the deep to the top of the multilayer. This might probably indicate that the period quasi-constance has been kept up to the 10^{th} bilayer within a few angstroms, after that the target was partially consumed and the C thickness has started to increase.

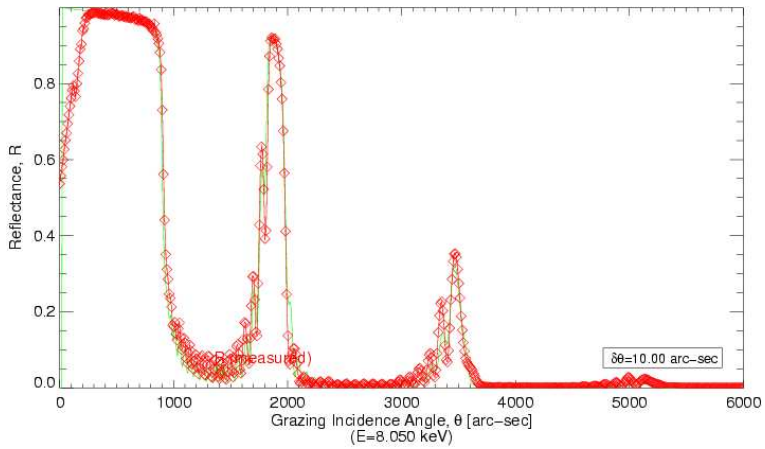

Figure 7.13: Reflectivity plot at 8.05 keV of a Ni/C multilayer (the same as in fig. 5.11, right) with 20 bilayers, evaporated with a broad beam (half the target size). The multilayer has a quite constant period. The anomalous height of the secondary peaks at the *left* of the first peak, indeed, is an index of an increase of the thickness approaching to the multilayer outer surface (with a non linear drift from 93 to 101 Å).

With a broad beam, indeed, a much more intense power is requested to evaporate because the beam is distributed on the target surface, so the evaporation resembles more to the Joule evaporation than to e-beam: in this case, another problem emerges: the sensitivity of the probe to the radiating heat from the target. At the shutter opening, the quartz probe is influenced by two factors: the evaporate deposition, that decreases the oscillation frequency, and the radiated heat, that increases it. With heavy elements, the decrease of frequency is usually much larger than the heat effect, and the deposition rate is recorded and measured since its beginning. With Carbon, however, the low density of the film can be taken over by the strong heat radiated by the target, and the first phases of the evaporation can be not detected by the quartz probe. This problem seems to have been resolved by finding the right power necessary to the evaporation and by setting a maximum power limit slightly larger than the necessary power to produce a steady evaporation.

Finally, the impurities absorbed by Graphite (mainly water vapour) can affect the density and the Carbon film properties. They can be eliminated pre-heating the Graphite target before the deposition.

7.4 Pt/C multilayers

According to our design, we have deposited a number of Pt/C multilayer (constant-period prototypes) on Silicon Wafers that returned very high peak reflectivities. An example is reported in fig. 7.14: the 8.05 keV X-ray reflectivity shows well defined and narrow peaks, with 1st peak reflectivity value of 83%. The peak definiteness indicates that the layer drift has been strongly reduced. The roughness value inferred from the fit is very good (3 Å, starting from a Silicon wafer substrate: the process itself produces small roughness amounts). The Pt layers have a density close to the bulk value (21.1 g/cm^3) whereas the Carbon has deposited at only 1.6 g/cm^3: the high density contrast and the low roughness contribute to build up the observed high reflectivity. For this sample a TEM sections is not yet available.

As a curiosity, the multilayers in fig. 7.8 and 7.14 are located in the first and fourth place in the reflectivity between the worldwide collected multilayer reflectivity data http://www-cxro.lbl.gov/multilayer/survey.html

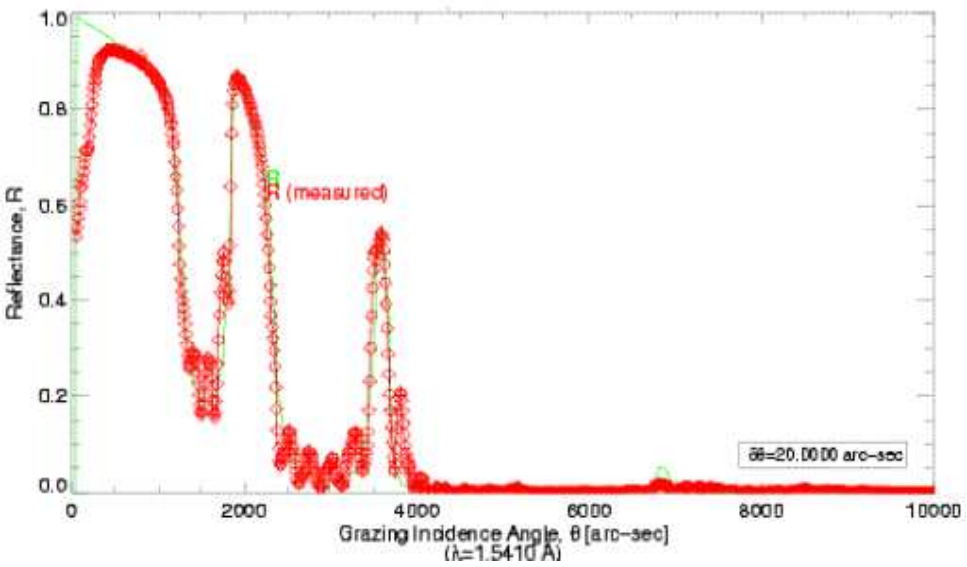

Figure 7.14: A 8.05 keV reflectivity scan of a 20-bilayer Pt/C multilayer on flat Si wafer substrate. The period is about 9.3 nm and $\Gamma \sim 0.33$, modeled with a roughness value $\sigma = 3\mathring{A}$. The peaks are clearly defined as the period is better kept constant.

7.4.1 Replicated Pt/C multilayers flat samples

The replication process feasibility with multilayer coatings is also under investigation. We are performing Ni electroforming and replication tests of 20 Pt/C bilayers on a number of superpolished flat Ni Kanigen sample, the same material which is used to produce the mirror master mandrels. The coating has been Ni electroformed and replicated: the result is a transfer of the multilayer structure on the electroformed Ni mirror (see fig. 7.15). The reflectivity scan shows a clear constant period multilayer, with clear and narrow peaks, meaning that the multilayer structure has not been too stressed following the replica process.

Other tests on rotating, Ni Kanigen flat substrates (a process that simulates the real deposition on mandrel) have been performed. As we will see in the next sections, the last improvements of the deposition technique have allowed to produce thin period multilayers (15 bilayers with d=56 $\mathring{A}$ and $\Gamma \sim 0.38$) with a period instability of only 2 $\mathring{A}$ along the stack. These tests has proven the feasibility of Pt/C multilayer replication from Nickel and, as we will see in the following, using the same setup we could produce a Nickel electroformed mirror shell by mandrel replication coated with a Pt/C periodic multilayer (see sect. 7.6).

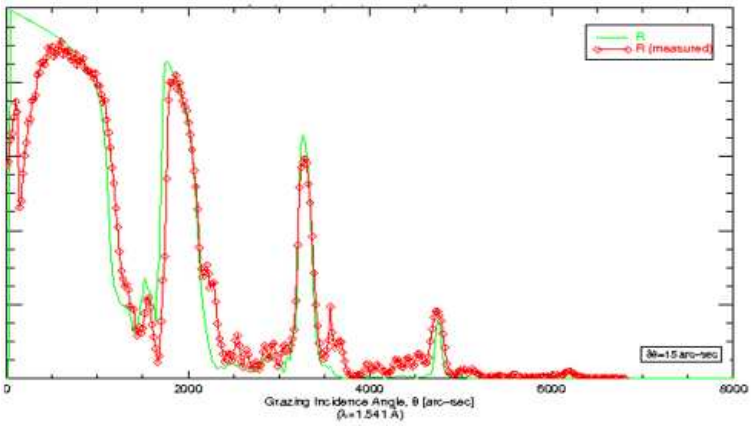

Figure 7.15: A 8.05 keV reflectivity scan of a 20 bilayer Pt/C multilayer, after Nickel electroforming and replication. The multilayer was previously evaporated on a flat superpolished Nickel Kanigen sample. The multilayer structure was preserved after the replication.

7.5 Soft X-rays reflectivity enhancement by Carbon overcoating

In order to obtain an experimental proof regarding the possibility of the employment of soft X-ray multilayer mirrors in future high energy missions (see sect. 3.6, page 74), a few flat prototype samples have been realized and tested with soft X-ray reflectivity scans, using the coating facility described in the previous sections.

1. a bi-layer film based on a first thick (300 Å) layer of Platinum plus a Carbon overlayer (110 $\mathring{A}$ thick);
2. a Pt/C film formed by 20 bilayers (d-spacing of 80 Å), with an overall Platinum overcoating of 80 Å, and a 100 $\mathring{A}$ thick C capping layer;

The substrates used for the deposition were superpolished Si wafers. The reflectivity tests of the samples were performed with monochromatic X-rays using the *soft X-ray reflectivity system* specifically prepared at the XACT (X-ray Astronomy Calibration and Testing) facility operated at INAF-OAPa (Palermo, Italy, web site: http://www.astropa.unipa.it/XACT/index.html).

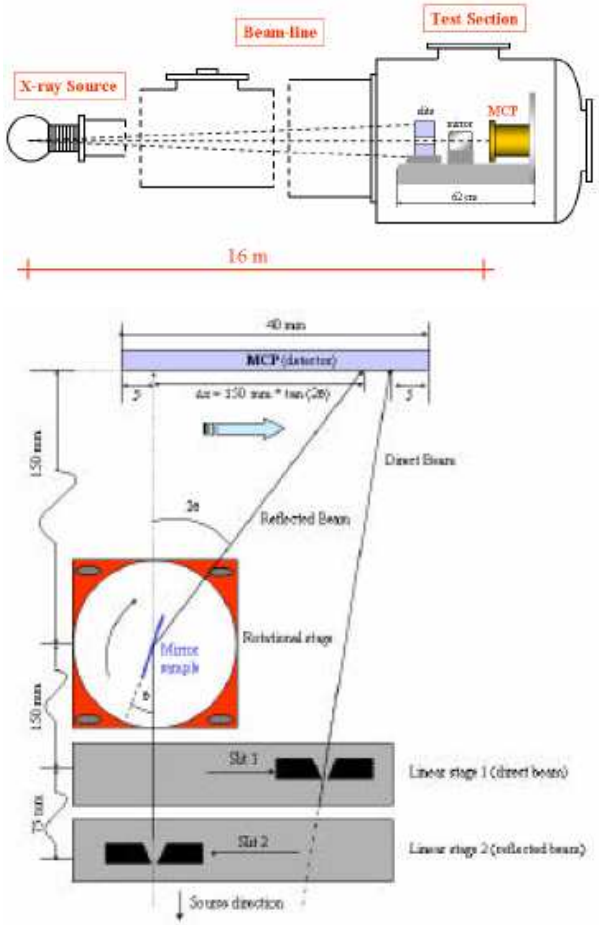

Figure 7.16: Scheme of the set-up used @ XACT for the soft X-ray reflectivity tests. (top) lateral section; (bottom) cross section (credits: INAF/Palermo Astronomical Observatory).

XACT is a general purpose facility realized few years ago for the development and calibration of filters, detectors, and moderate angular resolution grazing incidence optics for astrophysical and laboratory applications. It includes a 16 meter beam-line connecting the X-ray source to the test section, and the test section itself. The beam-line consists of 11 tubes, each 1 or 2 meter long, assembled together to reach the overall length of the pipe. The diameter of the pipe increases from the source end (150 mm) to the test section (630 mm). The test section is a 1 m diameter, 1 m long stainless steel cylinder with several ports for inspection, instruments and feed-troughs, and a door in the back having the same diameter of the chamber that opens inside a class 1000 clean room. The test section can be isolated from the pipe by means of a sliding gate valve with the same diameter of the pipe (630 mm).

The X-ray source is a multi-anode micro-focus Manson model 5 (J.E. Manson CO., Inc. Electrons) which is located at the end of the main X-ray vacuum beam-line. This source is equipped with six different anodes (Mg, Si, Ti, Cr, Fe, Cu) and four different filters that can be selected without breaking the vacuum. The power supply system has been modified to allow X-rays to be emitted up to 20 keV. In particular, the test of the sample n. 1 was performed in monochromatic light at the 1.49 and 1.74 keV photon energies, corresponding to the Kα lines of Al and Si, respectively. The set-up that was used for the reflectivity measurements is represented in fig. 7.16.

It should be noted that the detector for testing was a Multi-Channel Plate imaging system with a sensitive area of 40×40 mm^2. By means of two slits working in parallel, it was possible to simultaneously register the direct beam flux and the one reflected by the sample. During the data analysis we have taken into account the different quantum efficiency of the detector as a function of the angle of the impinging beam and the normal to its surface.

The reflectivity profiles at the photon energies of 1.5 and 1.74 keV performed at the XACT facility on the sample n. 1) (Pt thick layer plus a C overcoating) are shown in fig. 7.17. The two sets of data have been fitted assuming the same model for the bilayer structure, i.e. 300 $\AA$ of Pt plus 110 $\AA$ of amorphous C. The density of Pt and C are assumed to be slightly less than the natural values (18 instead of 21.4 g/cm^3 for Pt, 1.8 instead of 2.2 g/cm^3 for C), while for both materials the microroughness level is 6 Å. The excess due to the presence of the Carbon overcoating with respect to Pt alone up to 1.5^o (a value which can be considered the limit for the angular range of interest for reflection with Wolter I X-ray optics) is apparent.

The advantage is even more important if we consider that the parameter to be used for the evaluation of the effective area of an X-ray telescope is not the simple reflectivity, but instead its value to the square, since each photon undergoes two reflections before being focused in the detector.

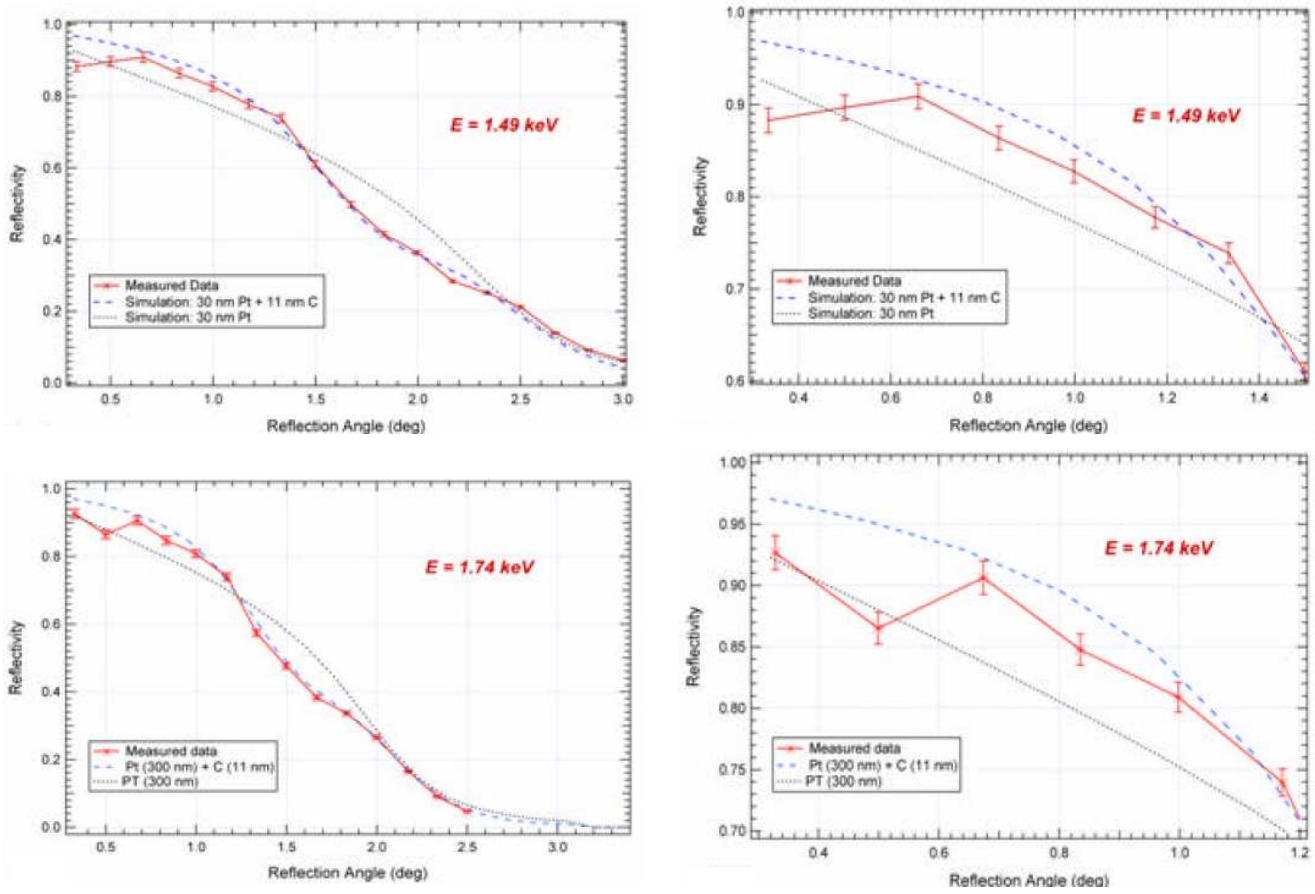

Figure 7.17: (left) Reflectivity profile the Pt film with C overcoating (Sample n. 1) at the photon energies of (top) 1.49 keV and (bottom) 1.74 keV. The model of the data with and without the carbon overcoating are reported. The excess due to the presence of Carbon is apparent.
(right) Expansions of the grids in the typical angular region for reflection of a Wolter I X-ray optics.

The reflectivity profile at 1.49 and 1.74 keV of the Platinum sample with Carbon overcoating presents, as expected, an evident improvement with respect to the theoretical model of Pt alone. On the basis of these encouraging results achieved on preliminary samples, the activity will continue in future to study the assessment and the feasibility of soft X-ray telescopes based on multilayer mirrors. It should be noted that similar studies are currently on going also at the Nagoya University (Japan).

7.6 A Pt/C multilayer coated, Ni electroformed replicated shell

The next step in the multilayer development in the framework of the ASI preliminary project is the deposition of Pt/C *periodic multilayer coatings* on master mandrels having a negative Wolter I profile, which will produce, by Nickel electroforming replication, a Pt/C multilayer coated mirror shell. The extension of the deposition from flat, small substrates is not straightforward: the thickness calibration is to be repeated because during the deposition because the mandrel rotates but the quartz probe (used for thickness monitoring) does not. A special care is to be devoted to the uniformity of the multilayer coating along the mandrel length, because if the coating is non uniform the reflectivity at a given energy will be different according the X-ray impact parameter on the mirror shell surface.

For Wolter I shaped shells, this point is even more critical since the overall shell reflectivity is the product of the hyperboloid and paraboloid single reflectivities (see fig. 2.7). Since X-rays from a celestial source strike in succession on the two revolution surfaces with the same grazing angles, if the multilayer period is constant along the stack but different for the hyperboloid than for the paraboloid, the Bragg peaks will be located at two different energies and product of the two reflectivities will be near zero.

Moreover, the replica process will produce different stresses in a long cylindrical shell structure than in a small, flat sample. From this viewpoint, the replica is much more critical in the case of multilayers than with a single Au coating, as for strong stresses the separation could occur also *inside* the multilayer stack. This risk is to be considered especially for e-beam deposited films, that are quite soft and characterized by a low adhesion. Large improvements in this point are expected also from the use of the ion assistance device.

In spite of these difficulties, we could manufacture a Nickel electroformed mirror shell with a 20 bilayer Pt/C multilayer coating. The replica process has partially failed, in the sense that (likely) *all but the last bilayer has been replicated from the mandrel*: the deposition process also is to be upgraded because the e-beam has been unstable during the deposition of the first C layers, and the surface roughness is too large as a consequence of the replica process. Indeed, *we have succeeded in the ever first production of a hard X-ray Pt/C multilayer coated, integral mirror shell by Nickel electroforming.* This mirror shell, recently (Oct 2004) calibrated at the PANTER facility *in full-illumination setup* (see sect. 8.3, page 176), has shown to have a significant effective area in the hard X-rays. The result is to be improved in both deposition and replica phase, but we have reached a first solid baseline for the next development, aimed to the following replication of graded multilayers.

7.6.1 Deposition on rotating mandrel

The deposition of a multilayer mirror Pt/C has been shown to be possible on flat, Silicon substrates: these multilayers can be replicated and transferred from (see fig. 7.15) flat substrates (Si wafers, flat superpolished Nickel plates) onto Nickel electroformed mirror walls. The technique is now to be extended to cylindrical mandrels overcoated with superpolished Nickel. The main difficulty to be faced is in this case the much longer necessary time to the deposition, as the whole lateral mandrel surface is to be coated. Moreover,

as the quartz microbalance is in a fixed position and in different point than the mandrel, the measured thickness at the probe is to be properly linked to the actual deposited thickness on the mandrel.

The deposition on large substrates like mandrels cannot be done without use of a beam equalization mask. A mask is simply a metal plate in which a special shaped cut is made: the mask is placed between the e-beam source and the substrate to be coated and its cut has a long, double profile along the mandrel length: narrower at the center (near to the evaporating target), and wider at the two sides. The equalization mask has two main tasks:

- to limit the evaporate beam divergence to few degrees in order to avoid the deposition with incidence angles far from the normal, because a divergent beam would deposit with different incidence angles during the rotation: this causes a strong amplification of the roughness by *shadowing* effect (see sect. 3.5.1, page 63);
- to improve the uniformity of the deposited layers along the whole mandrel length, because the evaporation is non-isotropic and tends to deposit a larger thickness at the center of the mandrel; the special shape of the mask (narrower at the center, wider at the sides) reduces the beam section at the center and enhances it at the sides, compensating the evaporation anisotropy;

Even when using equalization masks, however, the deposition uniformity must be verified and corrected, if necessary. This can be done putting some little substrates (glasses, or pieces of Silicon wafers) on the mandrel surface (or a structure that simulates it) at different positions: these substrates are coated and they work as witnesses of the deposition since they can be analyzed separately.

If we define L as the mask width at the center and R is the mandrel radius, it is evident that for every deposited layer with thickness d the apparent thickness D to be programmed at the quartz microbalance has to be:

$$D \approx \frac{d}{t}\frac{2\pi R}{L} \tag{7.1}$$

where t is an instrumental factor (usually $0 < t < 1$), called *tooling factor* that takes into account the different position of the quartz microbalance with respect to the substrates. Usually the quartz probe is aside the mandrel, strongly off-axis with respect to the evaporating beam, so it collects less material than a non-rotating substrate. Eventually, the probe can be put on-axis, near to a substrate, and in this case $t \approx 1$. Seldom the probe can be located nearer to the source than the substrates itself (in this case t can be larger than 1).

The eq. 7.1 is a very first estimate, and the calibration of thickness must be done semi-empirically. Another big problem we had to face was the instability of the Carbon evaporation when the quartz probe was put far from the substrate. We discovered that the evaporation can be kept steady by limiting the e-beam maximum power in the feedback system, and setting the proportional gain at a very low value. Also the response time was set to 2 sec, in order to smoothen sudden target evaporation that would start an unstable feedback cycle. Moreover, the use of a very broad electron beam has permitted (after a lot of failed attempts) to achieve an uniform deposition upon the whole mandrel length.

7.6.2 Multilayer deposition: a preliminary calibration on a flat sample

After all the Pt/C multilayer deposition study described in the chapt. 7, we had to do a final test in order the feasibility of the final deposition on a mirror shell. We have so deposited a 15 bilayers Pt/C on three silicon wafer fixed upon a rotating "dummy" mandrel, at three different positions on the mandrel generator.

If the process parameters are correct, the left, central and right samples must be coated with the same multilayer.

The reflectivity scans of the three samples at 8.05 keV (INAF-OAB) have shown that the multilayer has a constant period (d $\sim$ 55 Å, $\Gamma \sim 0.4$) within 2 $\mathring{A}$ and a low roughness 4$\div$5 Å, considering that we started from a substrate with $\sigma = 3$ $\mathring{A}$ (see fig. 7.18. The process itself, thus, keeps the surface smoothness at an acceptable level. Moreover, the period is almost the same for all three samples (within the 2 $\mathring{A}$ period drift, the constance of the Γ is less important for the present scopes, see tab. 7.1): this should ensure that the deposition on mandrel would produce an uniform coating, a very important requirement since the mirror shell will have the Wolter I shape.

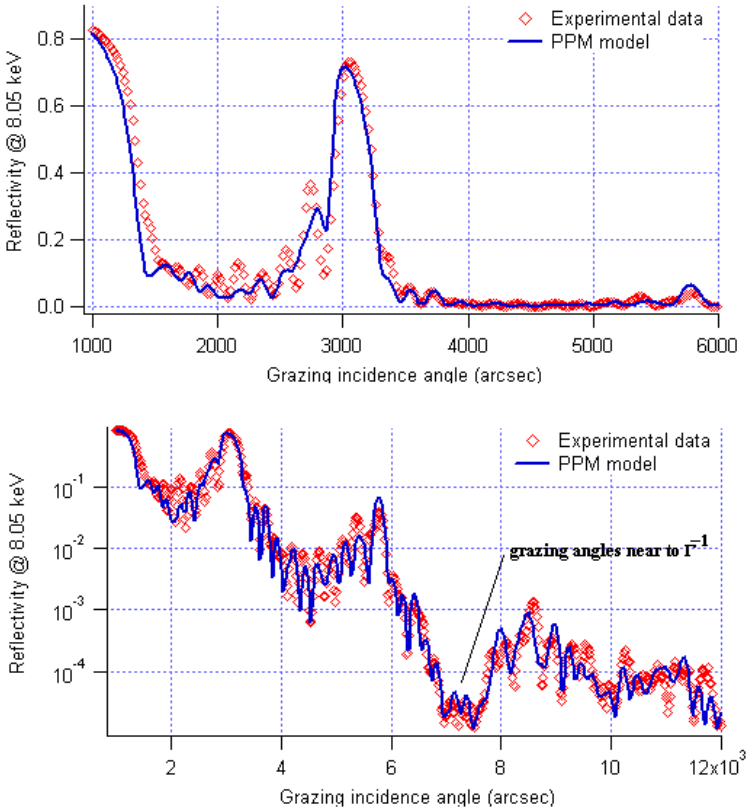

Figure 7.18: Reflectivity plots at 8.05 keV of the central sample used to calibrate the mirror shell deposition: (top) linear plot and (bottom) logarithmic plot. The reflectivity curve was fitted by PPM (see chapt. 9) assuming as free parameters all the d-spacings and Γ factors for all bilayers, with a fixed roughness value for all layers. This run has permitted the localization of a good number of primary secondary peaks. After the peak localization, the layer thicknesses have been fixed and the roughness left free to vary for all layers. The result is a period of $(55 \pm 2)\mathring{A}$, and $\Gamma = 0.40 \pm 0.02$ (this is also visible from the zero-reflectance angles). The roughness σ drifts from 4 to 5 Å.

The deposition has confirmed that we are able to produce almost uniform multilayers along the mandrel length (40 cm) with a quasi-constant period: this precision is still to be improved for future applications (graded multilayers) and the uniformity is to be ensured for even longer optics. This precision is, indeed, acceptable for the present requirements.

The calibration has allowed to deposit on the adopted mandrel (27 cm diameter, 40 cm length) for the mirror shell fabrication a Pt/C multilayer with 20 bilayers, a period of 70 Å, $\Gamma = 0.3$, keeping all the evaporation setup parameters unchanged. The resulting multilayer should have the first Bragg peak at 29

	Left (-20 cm)	Center	Right (+ 20 cm)
Period (Å)	55.9	56.9	55.0
Γ	0.38	0.38	0.42

Table 7.1: Period and Γ factor derived from the witness samples used for calibration of the multilayer to be electroformed and replicated.

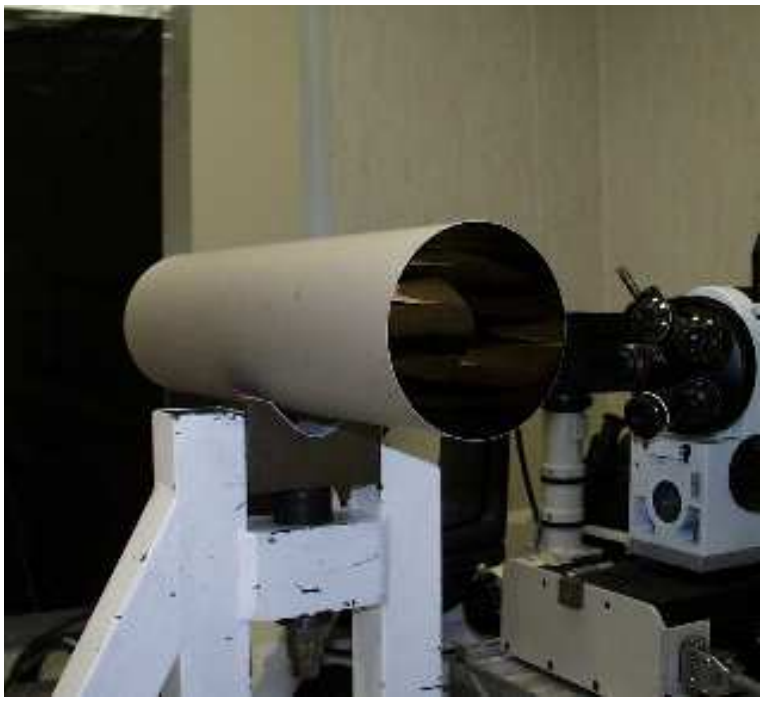

Figure 7.19: A Wolter I, Ni electroformed replicated mirror shell with 70 cm length and 12 cm diameter. The mirror shell has an inner coating of a Pt/C multilayer with 7 nm of capping Au.

keV for a grazing incidence angle of 0.19^o. The deposition has been regular except for the first *two* Carbon deposition cycles, where the e-gun spot was unstable and could not keep the large size required for an uniform rate: as a consequence, the evaporation rate has been larger during the deposition of the first and second layer since the whole electron flux was concentrated in the Carbon target center. We can, hence, expect that the first two carbon layers will be much larger than foreseen.

7.6.3 Application of release/adhesion agents

The release of the Nickel mirror shell (with all the X-ray reflective coating) is a crucial step in the fabrication of replicated optics. The result of a difficult release can return deformation of the mirror shell with consequent degradation of the optical performances, the formation of micro-strains on the surface that can reduce the effective area, the increase of superficial roughness that could increase the scattering. Even worse, the layers that constitute the multilayer could loose their cohesion if mechanical stressed. Hence, the reflective coating adhesion to the mandrel must be low enough to permit the release: on the other side, the multilayer cannot be too loosely bound to the mandrel, since a separation from the mandrel during the deposition (e.g. due to thermal stresses) could occur.

Figure 7.20: (left) *Peelable paint* application to the mandrel after Au + Pt/C multilayer + Cr + Au coating. Some centimeters of mandrel length are covered with a paint that isolates the coating from the electroless Nickel, making easier the release process. (right) The mandrel after the paint application. The visible coating is a 100 nm thick Au layer.

The release of single-layer Au coated mirror shell was not a problem, since Gold fullfills very well these requirements. A thin Au layer (7 nm) can thus be used as a release agent: deposited directly on the mandrel, before the first Pt layer, it can ease the separation of the mandrel from the multilayer coating, and, due to its very low thickness, it would not affect too much the reflectivity, especially at very high energies.

A single Au layer is not sufficient, however, to promote the adhesion of the multilayer to the electroformed Nickel wall. A 100 nm thick Cr layer is then deposited on the mandrel after the last Pt layer: Chromium is a well-known element used to favour the adhesion of evaporated films to their substrates (as for the Chandra Ir coating). Due to the chemical instability of the couple Chromium/Nickel, however, a further Au layer (100 nm thick) is deposited on the Cr layer. The Au layer is well suitable for Nickel electroforming, and the Chromium layer contributes to the consistency of the Au or Pt/C multilayer system.

Following this method we had already produced a 70 cm long, 12 cm of diameter Pt/C multilayer coated, replicated mirror shell (see fig. 7.19). This preliminary result, obtained with a mirror shell with reduced geometric area, has shown the feasibility of the release process, even if the release of the mirror shell which is to be produced (28 cm diameter) will be more difficult.

7.6.4 Mirror shell electroforming, release and integration

After the deposition run in the coating chamber, the mandrel is coated with 7 nm Au, a Pt/C multilayer, 100 nm Cr, 100 nm Au and appears an in fig. 7.20: the external Au coating, where the Nickel mirror wall will be electroformed, is clearly visible.

The usual technique adopted for the mirror electroforming and release (and used also for the XMM mirrors) consists in mounting two cylindrical expansions at the mandrel sides, having the same mandrel radius and connected to the mandrel body but isolated from the lateral mandrel surface. The system mandrel + expansions is put in the electroforming bath, and after the Nickel walls deposition, the shell

is separated from the mandrel by cooling (see sect. 2.3.3): this method allows to produce mirror shells having exactly the same length as the mandrel; however, a part of the electroforming bath can penetrate in the space between mandrel and expansions, and a Nickel layer can be electroformed also at the terminal mandrel surface: the release would be impossible in this case, since the electroformed Nickel would be directly "welded" on some parts of the mandrel.

In order to avoid this danger, an alternative method has been adopted: before the electroforming, a *peelable paint* layer has been applicated on the terminal sides of the mandrel (see fig. 7.20), and on some cm of the multilayer-coated mandrel surface: the paint separates the electroformed Nickel from the mandrel in the terminal points, so the Nickel walls come into contact to the X-ray reflective coating only in the non-covered, central part of the mandrel.

After the electroforming, the Nickel layer deposited on the peelable paint can be easily removed from the mandrel: hence, we can be sure that the remaining mirror wall is separated from the superpolished mandrel surface by the X-ray reflective coating, which is to be replicated. The mandrel, after the Nickel electroforming and the paint removal is shown in fig. 7.21-left. The original superpolished mandrel surface is visible on the mandrel terminals, where the paint was applicated. The figure 7.21-right, shows the usual method for the successive mandrel cooling to ease the mandrel contraction and the consequent Nickel shell release.

Figure 7.21: (left) The coated mandrel as in figure 7.20, after the Nickel electroforming. The Ni mirror wall was been grown on all the mandrel surface, except on the two terminal strips that were covered by the peelable paint (credits: Media-Lario s.r.l., cited with permission).
(right) Cooling of the mandrel with liquid Nitrogen to ease the shell release: the separation is permitted by the CTE difference of Nickel and Aluminium, the material that constitutes the mandrel (credits: Media-Lario s.r.l., cited with permission).

As we will see, the replication has been in this case *almost* complete. In fact, after the replication, a Carbon layer was visible on the mandrel, while the inner mirror shell surface had a metallic colour (Pt). The residuals on the mandrel have been replicated on small glass substrates, and the X-ray reflectivity at 8.05 keV performed on these small samples showed that only *one bilayer* (plus the initial 7 nm thick Au layer), had not been transferred on the mirror shell. In this case, the failed replication of only one bilayer should not degradate too much the multilayer performance (excepting the reflecting surface roughness); thus, in

this preliminary phase the shell can be used to provide an X-ray characterization of the production process. In the next developments, a special care will be devoted to avoid an incomplete replication, since the loss of bilayers could compromise the multilayer reflectivity, especially when they have to be wide-band.

The replicated shell has then been integrated in the *mirror case*; this is a tube (made in stainless steel to match to the Nickel CTE) where a number of holes have been made in order to make it lighter without losses in mechanical stability. The mirror case is used to give the shell a mechanical stiffness and to manipulate the optic. The shell has been glued to the rear spider that constitutes the terminal side of the case: the alignment of the case axis with the shell axis and the deformation of the shell during the integration have been monitored with a UV optical bench installed at INAF-OAB, returning a constant HEW value of 40" in all the process phases. Before, during the integration and the glue polymerization, two stiffening rings applicated to the external shell surface have kept the shell roundness (in case of shell nesting, the rings should be removed after the integration of each shell). Some characteristics of the mirror shell are reported in tab. 8.3, page 177.

Figure 7.22: The integrated mirror shell in the case: the rear spider structure is visible, reflected on the mirror shell. The AFM has been installed on the inner shell surface in order to measure the surface microroughness.

7.7 Conclusions

The developed activity was aimed to the production of a hard X-ray Pt/C multilayer coated mirror shell by e-beam evaporation using the coating facility already installed at Media-Lario, which was previously used for single-layer deposition. The XRR and TEM characterizations of the deposited samples showed that a promising deposition quality is achievable: a further improvement is expected from the future use of the ion assistance. We had some problems in thickness control (typical of e-beam evaporation) and in multilayer replication, but a systematic study has allowed to start to reduce these problems. We could so manufacture a hard X-ray mirror shell by replication of a Pt/C multilayer coated mandrel with Nickel electroforming.

The mirror shell has been characterized at the PANTER facility, obtaining very important indications of the multilayer structure, the optic profile accuracy, the surface state. The characterization has in turn highlighted the critical points that have to be improved in the next activity developments (see sect. 8.3).

Chapter 8

Calibration of multilayer mirror shells at the PANTER facility

A facility suitable to calibrate X-ray optics is the PANTER facility in Neuried (DE), an X-ray tube that permits the optics full-illumination with an almost parallel beam up to 50 keV, thus reproducing the approximate operative conditions of the hard X-ray telescopes. The facility was planned in the late seventies to accompany the development and realization of the ROSAT mirror system. The PANTER facility, able to provide a wide, low-divergence X-ray beam for the characterization of X-ray astronomical optics, can be considered unique in Europe. Soon after its construction it turned out that such a facility is absolutely necessary for realizing X-ray telescopes: so the PANTER facility was used for the calibration of X-ray telescopes optics like EXOSAT, Beppo-SAX, ROSAT, XMM, JET-X/SWIFT (see e.g., bibl. [40]). Also several prototypes of light-weight monolithic X-ray mirror shells made of ceramics materials realized at INAF-OAB have been measured at PANTER (bibl. [102]).

At the PANTER facility we have calibrated the first Nickel electroformed (with multilayer coating) mirror shell prototypes for hard X-rays telescopes. Two of these (see sect. 8.2, page 167) are mirror shells whose Nickel substrate was first electroformed at INAF-OAB/Media-Lario and then multilayer coated by Magnetron sputtering (see chapt. 4) at the *Harvard-Smithsonian Center for Astrophysics* in Boston (US), whereas the third one (see sect. 8.3, page 176) is the replicated mirror shell by Nickel electroforming, Pt/C multilayer coated mirror shell produced in the context of the Italian Space Agency (ASI) "High-energy payload preliminary project" by INAF-OAB and Media-Lario following the direct replication method (see fig. 7.1). The description of the multilayer development and mirror shell fabrication is described in the chapt. 7.

In the following sections we will show a short description of the PANTER facility, followed by the mirror shell X-ray characterization. We will see that the produced mirror shells have highlighted the problems to be resolved in the next activity development, but they constitute also a solid baseline for future hard X-ray focusing optics.

8.1 The PANTER facility

For X-ray telescopes calibration, the ideal situation would be an X-ray source at infinite distance. Being this impossible, a wide, collimated X-ray beam can be approximately obtained placing an X-ray source at very large distance. The PANTER (see fig. 8.1) is constituted by a high vacuum tube 125 m long and 1 m

wide tube connecting an X-ray source (from 4.5 to 50 keV) to a clean room, where experiments are dealt. The possibility of performing full-illumination tests also up to 50 keV is very important to allow reliable and easy to make calibrations of hard X-ray optics. The low divergence achievable (0.064^o for a mirror shell of 300 mm in diameter placed at the entrance window of the testing chamber) is a very important parameter since the typical reflection angles of hard X-ray optics are very small ($0.1^o \div 0.3^o$). The tube length was adapted to the optical properties of ROSAT and was sufficient for the experiments in the 70s, but now the beam divergence has to be taken into account (see sect. 8.3.1, page 178).

The clean room (class 1000, 12.5 m long $\times$ 3.5 m wide) hosts a set of X-ray detectors: the optics under test are placed in the clean room, at the X-ray front end, and their position can be adjusted by a set of manipulators driven by stepper motors that with a precision of 3 μm (lateral shift) and 1" (rotation). Tube, chamber, source are kept under vacuum (10^{-6} mbar, obtained with turbo-molecular pumps located at four distinct pumping stations). Moreover, two cryopumps connected to the clean room reduce the water vapour partial pressure, in order to avoid the formation of ice on the cooled CCD cameras.

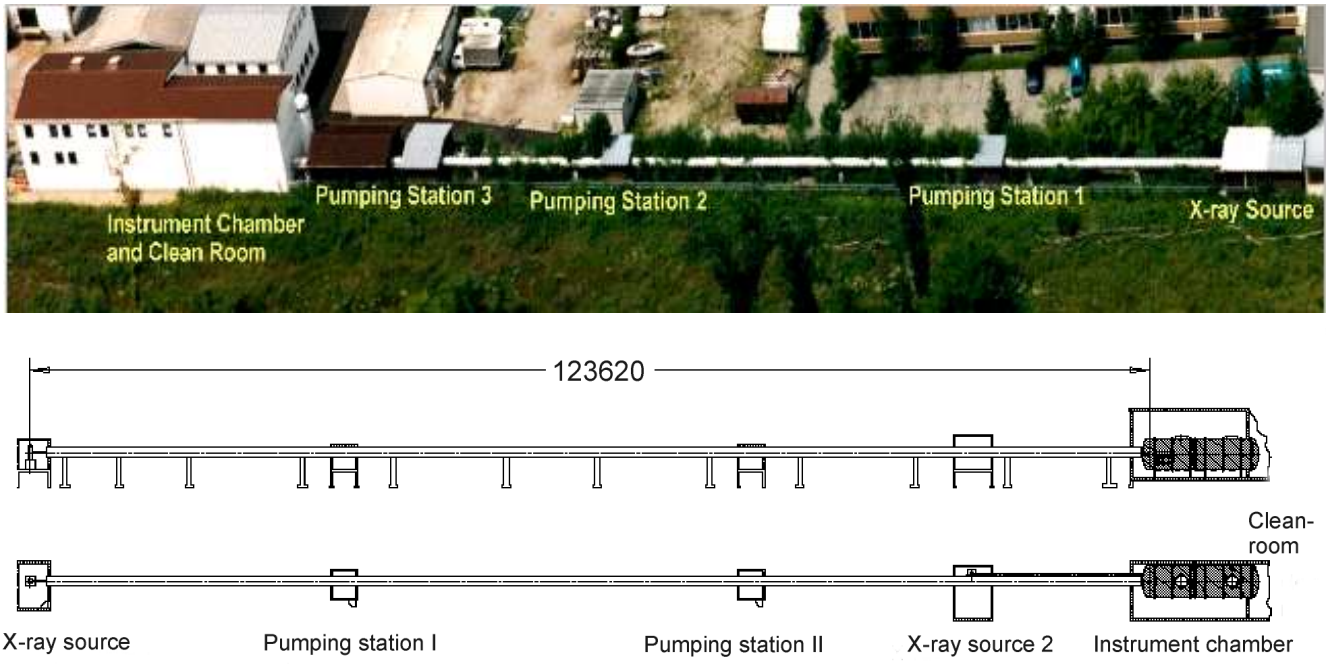

Figure 8.1: (top) Air view of the PANTER facility at MPE (credits: MPE, *Max Planck Institut fur Extraterresrische Physik*). (bottom) Scheme of the X-ray tube of the PANTER facility (side and top view). The tube length is 123620 mm (credits: MPE).

8.1.1 X-ray sources at the PANTER facility

Four different X-ray sources are available at PANTER, with 16 different targets (elements). Typical fluxes are 5000 counts/sec/cm^2 in the chamber, depending on the target material. The spectrum of each source is a typical bremsstrahlung one (with a cut-off energy corresponding to accelerating power of the X-ray tube) superposed to the fluorescence lines typical of the adopted target material between 0.28 and 8.05 keV. By means of different absorption filters, the spectrum can be modified by suppressing some part of the continuum or some X-ray fluorescence lines.

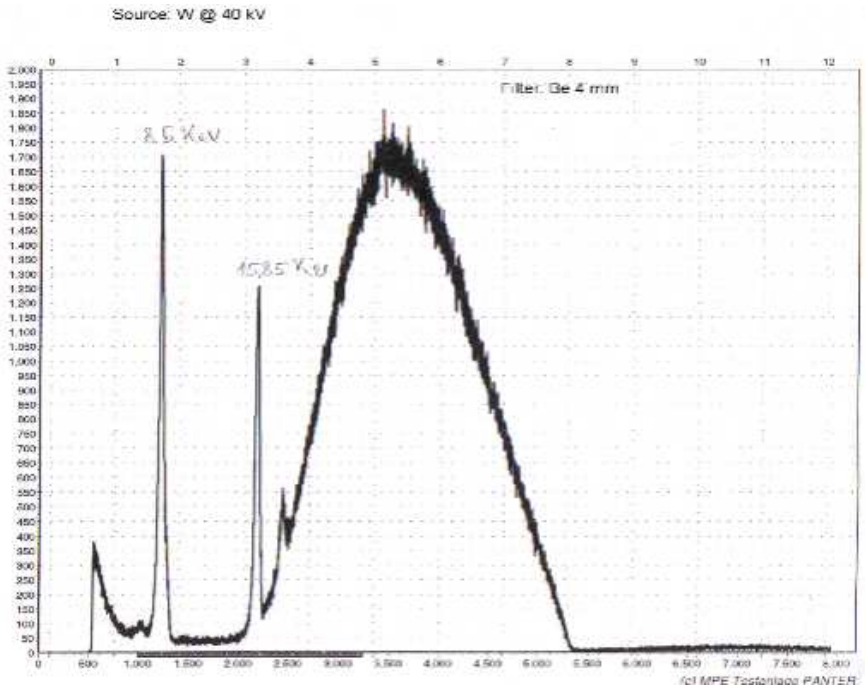

Figure 8.2: A spectrum of an X-ray beam at the PANTER facility, using a W target and a accelerating power of 40 kV (credits: MPE). The typical bremsstrahlung spectrum with fluorescence lines is filtered by a Be window (4 mm).

For very high fluxes, a commercial (sealed) source is also available. This source provides a couple of X-ray lines between 4.5 and 22 keV, plus a bremsstrahlung component that may cover the spectral range from 4.5 and 50 keV. The continuum component source can be measured with the pn-EPIC detector that, considering its good energy resolution, allows a broad-band measurement (*energy-dispersive* mode). In our case, the measurements have been performed using either the emission lines or the continuum (see fig. 8.2).

A preliminary calibration of detectors is usually performed with sharply monochromatic radiation, thus two monochromators are installed at the PANTER facility. One is a tunable reflection grating and is used as a monochromator covering the energy range $0.2 \div 1$ keV (or 2 keV, using the second orders), or a tunable double crystal monochromator from 1.5 up to 25 keV; both filter the continuum radiation coming from a Molybdenum or Copper target of an open X-ray source, with a spectral resolution better than 4% (see below).

8.1.2 X-ray detectors at the PANTER facility

Two energy-sensitive detectors are usually used at the PANTER facility: a model of the ROSAT PSPC (Position Sensitive Proportional Counter, energy resolution 30% at 1.5 keV, spatial resolution 250 μm) working up to 10 keV, and a pn-EPIC CCD camera. The pn-EPIC has a better energy (145 eV @ 6 keV) and spatial resolution (150 μm) than the PSPC and it can operate up to 50 keV. Also a CCD camera with higher spatial resolution may be used (a predecessor of the EPIC MOS camera on-board XMM) but it can operate only up to 8 keV. Others proportional counters are distributed along the vacuum tube in order to monitor the X-ray beam uniformity. For the hard X-rays measurement we have adopted the pn-CCD camera, even if its quantum efficiency rapidly drops after 10 keV (3% at 50 keV) and in spite of its

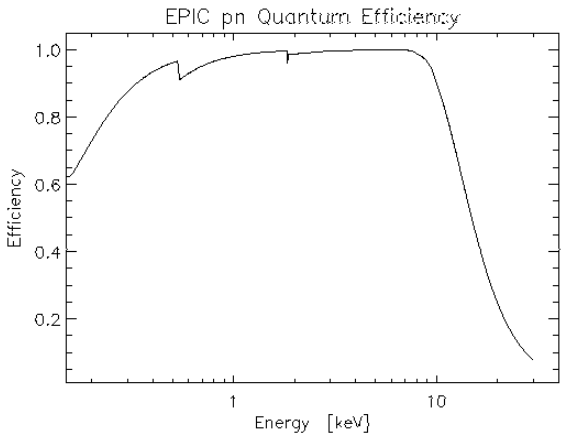

•Photon Energy	•Quantum Efficiency
•10 keV	•89.1 %
•20 keV	•25.1 %
•30 keV	•8.6 %
•40 keV	•4.7 %
•50 keV	3 %

Figure 8.3: The pn-EPIC quantum efficiency (credits: MPE). The sensitivity to hard X-rays is much lower than under 10 keV, but is is significant up to 50 keV, and it can be increased by a long integration time. *The pn-EPIC has been used for the first time up to 45 keV during the following measurements.*

medium spatial resolution, since we were interested mainly in the hard X-ray optics efficiency reflection. The pn-EPIC camera low quantum efficiency beyond 10 keV can be compensated by increasing the exposure time.

It should be noted that for focal lengths larger than $8 \div 9$ m the optics to be tested could be placed directly into the vacuum tube (1 m in diameter) connecting the testing chamber to the X-ray source. It was the case of the Pt/C mirror shell (10 m focal length, see fig. 8.4, page 167), whose characterization is exposed in the sect. 8.3 . Even in this case, if we were interested only in the reflectivity measurements (and not in the image HEW), the detector can be kept at a shorter distance than the focal length provided that all the reflected beam falls into the detector area (36 cm^2 for the pn-EPIC).

A very important point to be checked is the X-ray beam uniformity: four detectors (area 36 cm^2) at the entrance of the tube are thus used to monitor the spatial constance of the count rate (one of them can be even be moved in two dimensions to this aim). Another movable detector (area 2.5 mm^2) is located at the tube end, near to the X-ray source.

8.1.3 Possible PANTER setup for measurements beyond 15 keV

Two possible setup can be used to extend the operative range of the PANTER facility over 15 keV: the *monochromatic X-ray* mode and the *energy-dispersive* mode.

Monochromatic X-ray mode: a monochromatic X-ray source is constituted by a special water-cooled X-ray open tube with changeable anode targets (Cu or Mo), operating up to 50 kV and 60 mA: the size of the anode focus spot is 1 mm diameter, and the emitted X-rays enter the monochromator chamber through a thin Berillum window (thickness 8 μm, diameter 4 mm, usually closed, but manually removable for low-energy operations). The monochromation is devoted to a couple of crystals that can be rotated to tune the reflected energy: the second crystal is shifted parallel to the first one simultaneously to the rotation in order to preserve the beam offset.

The main limitation to the radiation monochromaticity is the beam divergence ($\sim 0.4^o$): the pair of crystals adopted at PANTER are HOPG(002), Si(111). Usually the HOPG crystals are used due to their

lower absorption: they are constituted by mosaic structure with mosaic spread 0.3^o, able to guarantee a very large integral reflectivity. The choice of a mosaic spread smallest as possible allows to obtain a large intensity of the reflected beam while keeping a large intrinsic energy resolution, which is mainly determined by the beam divergence. HOPG crystals are used over 2 keV, while for energies beyond 15 keV the beam is produced with the Mo anode and monochromatized at the 2^{nd} Bragg peak, returning a resolution of 3%: typical intensities provided by the HOPG monochromators are 100 counts sec^{-1} cm^{-2} at 3.5 keV and 600 counts sec^{-1} cm^{-2} at 8 keV for the first order at the entrance of the test chamber.

Figure 8.4: (left) The mirror shell measurement setup for the X-ray optic reflectivity measurement (focal length $< 9m$). The mirror shell is integrated in front of the X-ray beam emerging from a hole in the shutter. A system of screens, driven by motors, can be used to limit the beam. A precision system of motors regulates the optic position with 1" of precision.
(right) The setup for X-ray optic reflectivity measurement with focal length larger than 9 m. The integrated optic has been mounted inside the X-ray tube, together with a special optic manipulator.

Energy-dispersive mode: it is a very practical way to operate in hard X-rays; a broad-band X-ray beam illuminates the optics to be tested, and the focused photons are collected by the pn-CCD camera. The very good energy resolution of this device (2.5 % at 6 keV and improving proportionally to the square root of the photon energy) allows to derive a broad-band mirror reflectivity with a single exposure. The poor quantum efficiency of the pn-CCD camera can be compensated by long integration times and high incident fluxes, like those produced by the X-ray source with Tungsten anode, operating up to 60 kV. The bremsstrahlung component of this source is thus perfectly suitable to cover the hard X-ray spectrum from 4.5 to 50 keV (with achievable fluxes of 3500 photons cm^{-2} sec^{-1} in the 10 40 keV energy range).

8.2 Characterization of a mirror shell prototype for Con-X

The NASA astronomical mission Constellation-X (see sect. 3.7.3, page 85), to be launched around 2013 (and that will operate in the L2 Sun-Earth Lagrangian point), will be one the most sensitive X-ray telescopes ever built. The large sensitivity in soft and hard X-rays will be possible due to the use of a multimodular (12) optics (on-board 4 identical spacecrafts), that will make possible to attain a very large effective area (1500 cm^2 @ 40 keV) avoiding the problem of construction of very large aperture optics.

The section of every Con-X spacecraft devoted to the observation of the hard X-ray sky (HXT, 6-70 keV) will have 3 optics modules with a quite compact diameter (35 cm) and with a focal length of 10 m

in Wolter-1 profile. The eq. 2.13 yields so a grazing incidence with very shallow angles ($0.1^o \div 0.25^o$). A possibility to achieve a large reflectivity with so grazing angles is (apart from the eventuality of a single Ir coating for the innermost shells) the use of graded multilayer coating. The use of mandrel replication is particularly interesting because it offers the possibility of producing all the modules using the same set of mandrels (from this viewpoint we have done a feasibility study, see sect. 6, page 129, see also bibl. [92]).

The application of the replication technique to Con-X/HXT has been studied (see bibl. [90]) leading to the conclusion that the Ni electroforming approach allows the reduction of the ratio geometric area/mass (but keeping good imaging capabilities, $HEW \sim 25$") in order to fullfill the severe mass constraints (195 Kg/satellite). This is due to the stiffness of the monolithic shell (after the integration), whose thickness must be increased going towards the larger shell, but always being very limited ($0.1 \div 0.2$ mm).

In order to verify the feasibility of the extension to the multilayer coatings of the replication technique for Constellation-X, two multilayer coated mirror shell prototype have been produced in the framework of an international collaboration (INAF-OAB and the *Harvard-Smithsonian institute Center for Astrophysics*), following the second approach exposed in fig. 7.1: the mirror shell Nickel substrate, Au coated, is produced and replicated by INAF-OAB at Media-Lario, and the substrate roughness measurement (a W/Si multilayer coating) is deposited at the CfA using a DC magnetron sputtering device (see fig. 8.5).

Figure 8.5: Inside the CfA DC magnetron coating facility. The facility is a cylinder 112 cm high, and 56 cm diameter, cryopumped down to 10^{-7} torr. Two linear cathodes (66 cm) are mounted in the center of the chamber: the optic is mounted around the cathodes. During the sputtering, the cathodes rotate to coat the inner side of the shell. A system of shutters allows the deposition of an element per time (credits: bibl. [89]).

Two mirror shells single-cone (single reflection) shaped have been fabricated at INAF-OAB /Media-Lario and W/Si multilayer coated at the CfA with this approach: a periodic multilayer coated shell and a graded multilayer coated one. The result of the calibration of these mirror shell at the PANTER facility will be exposed in the following of this section. It is worth noting, that this is the *first measurement performed on a multilayer optics with a parallel beam up to 50 keV*. A second part of the tests have been performed at the INAF-OAB, where the X-ray reflectivity has been tested at the BEDE diffractometer at 8.05 and 17.4 keV.

8.2.1 W/Si periodic multilayer coated shell measurement

The first X-ray mirror shell under test was not uniformly coated within a single deposition run, but instead *five different multilayer coatings with distinct structures* and grown with separate deposition cycles were

applied in sectors distributed onto the internal shell surface (see fig. 8.6). In particular, the measurements at PANTER have been dealt on a single sector of the shell coated with a W/Si multilayer coating with the following nominal parameters: 20 bilayers, period 78 $\mathring{A}$, $\Gamma = 0.40$. During the same coating process a *witness multilayer sample* was realized onto a superpolished glass (fused silica, with a surface roughness $\sigma \sim 1\mathring{A}$) 2 inches disk whose nominal parameters are slightly different due to the different placement of the witness flat with respect to the optics: N = 20, period 75 Å, $\Gamma = 0.3$. Also this sample, for comparison, was tested at PANTER. Due to the much better surface smoothness of the witness substrate than the Au layer on the replicated shell (that was measured with a AFM scan and turned out to be 4-5 Å), we can expect that a larger roughness growth has taken place on the shell than on the witness, and consequently the witness will have a better reflectivity than the shell.

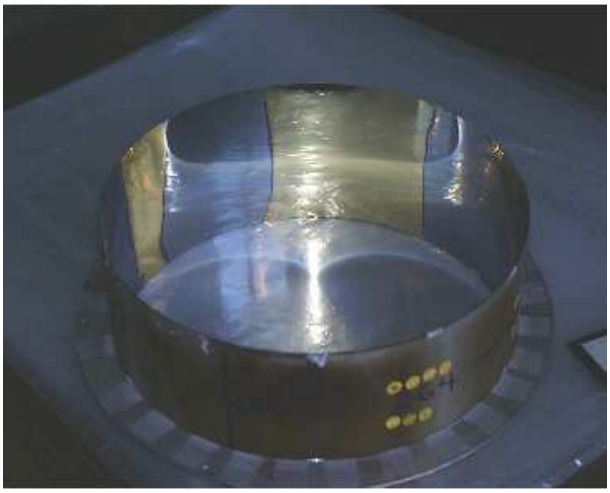

Figure 8.6: The mirror shell produced at the CfA and tested at the PANTER facility. The shell is a single cone with 280 mm maximum diameter, 20 m focal length, 125 mm height. The on-axis incidence angle is 0.21 deg. The coated sectors on the Au background are clearly seen.

The measurements have been performed using the bremsstrahlung continuum (see fig. 8.2) in energy-dispersive mode, using a Tungsten target and a high voltage of 60 kV: the bremsstrahlung spectrum could so be exploited up to 45 keV, and explored by an energy-sensitive detector (the pn-EPIC, in this case).

Once integrated into the mechanical structure, the mirror shell was mounted onto the PANTER manipulator placed at the entrance of the testing chamber. A slit has been machined into an X-ray screen mounted in fixed position to allow a precise illumination of the multilayer-coated sectors of the mirror shell. The rotation of the mirror shell was enabled by a special rotational stage to allow the selection of different coated sectors. The witness flat sample was also mounted in the same basement of the mirror shell. Finally, a hole (3.96 mm in diameter) in the screen was precisely drilled for permitting the measurement of the direct beam flux. A layout of the mounting system used is shown in figure 8.4, left.

The effective area and, as a consequence, also the reflectivity of the multilayer coated sector in the mirror shell was measured from 10 up to 50 keV by means of the energy-dispersive setting described in the previous section. The pn-CCD camera used as a detector was placed at a distance of 8 m from the mirror shell. This is much closer than the nominal position of the focal point expected taking into account the geometric divergence (16.8 m). However, due to the large detection area of the pn-CCD camera, it was possible to collect all the reflected photons (see fig. 8.7) although so far from the focal position, allowing the measurement of the effective area.

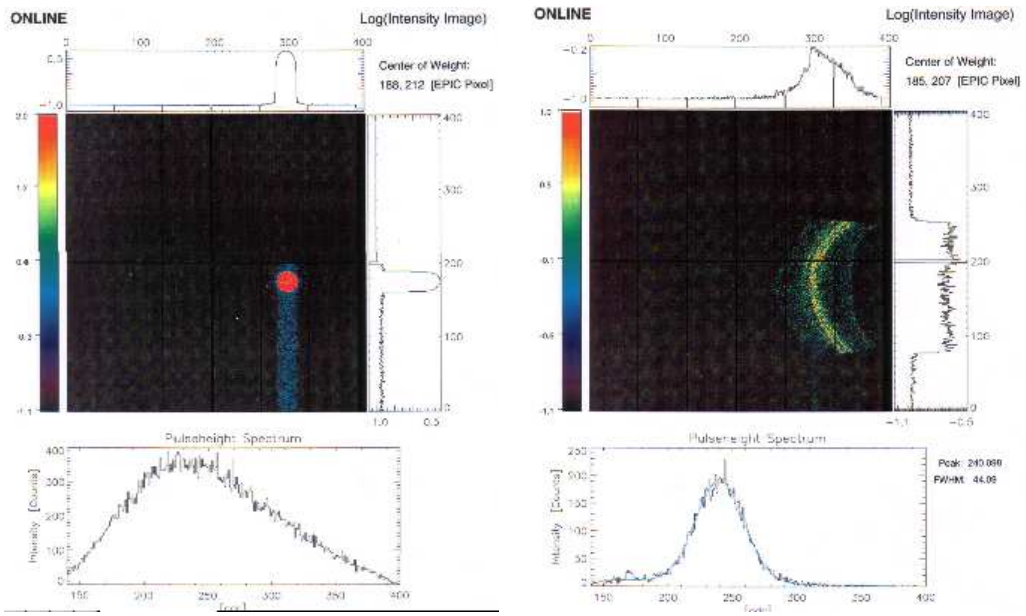

Figure 8.7: (left) The pn-EPIC CCD image of the direct beam emerging from a circular hole, used to compute the incident X-ray brightness.
(right) The pn-CCD image of the beam reflected by the sector of the mirror shell. The circular shape is due to the closeness of the CCD to the mirror, with respect to focal plane. Scattered radiation is also visible in the CCD field.

The reflectivity measurements have been carried out setting the high voltage of the X-ray tube to 50 kV. The surface brightness of the direct beam $B_{inc}(E)$ has been measured by counting the emerging photon rate $C_i(E)$ from the circular hole in the screen (with area A_i), while the mirror sector effective area $A_{eff}(E)$ has been derived from the reflected photon rate C_c integrated on the focal spot:

$$A_{eff}(E) = \frac{C_c(E)}{B_{inc}(E)} \tag{8.1}$$

from the ratio of A_e to the area of the entrance slit (this is equal to the illuminated sector area A_s projected in the normal direction to the beam, $A_s \sin\theta_i$) the reflectivity R(E) can be derived, for every detector energy channel:

$$R(E) = \frac{A_{eff}(E)}{A_s \sin\theta} \tag{8.2}$$

each reflectivity measurement has been repeated at slightly different grazing incidence angles θ_i, to the aim of investigating the change of the reflectivity range according to the Bragg Law. The variation of the incidence angle, in particular, allowed to shift the reflected energy range up to the emergence of the 2^{nd} Bragg peak: the presence of more than one peak is very important in a multilayer reflectivity fit, as higher order peaks are more sensitive to the interface roughness (see sect. 3.5.2, page 66), and because the single peak height is changed also by the Γ factor (with a modulation $\sin(\pi k\Gamma)$, see eq. 3.35). The observation of two or more peaks allows to disentangle the separate effects of the roughness and of the Γ factor.

In figure 8.8 the reflectivity profiles of the multilayer coated Ni mirror and of the flat witness mirror are shown, at an off-axis incidence angle 14.65 arcmin. As expected the reflection efficiency of the flat sample is larger than the mirror shell, due to a lower microroughness of the substrate surface before coating. A model to fit the data (performed by using the IMD software package, see bibl. [103]) is also superimposed to the reflectivity curves.

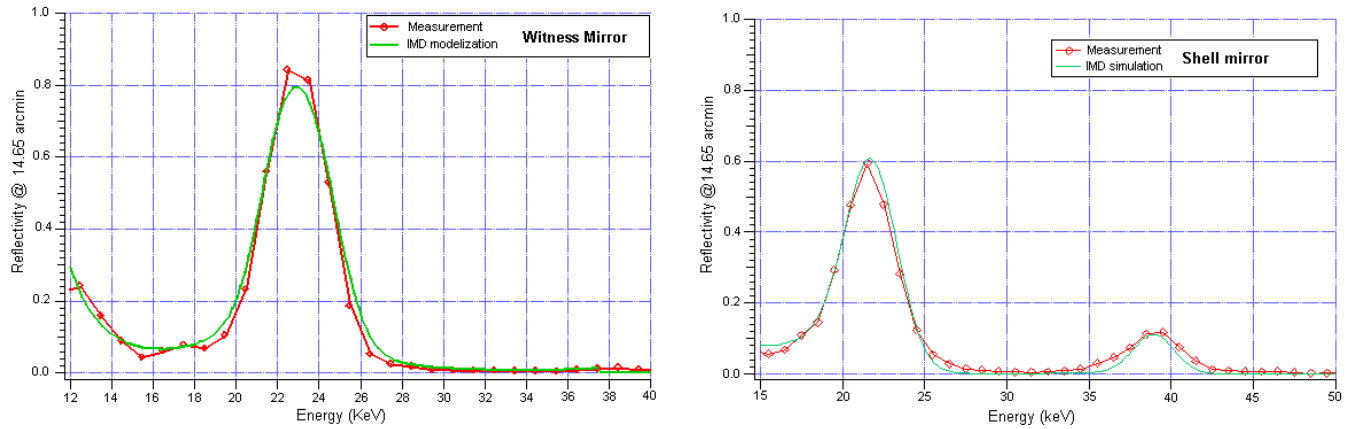

Figure 8.8: Reflectivity profiles taken at the PANTER facility / linear plots. (left) Witness mirror and (right) a sector (named 264) of the shell mirror. The peak reflectivity of the witness (85% @ 23 keV) is considerably larger than that of the shell (60% @ 22.5 keV), indicating a rougher structure in the last case. The peaks also are in different positions, due to a foreseen difference in the multilayer period.

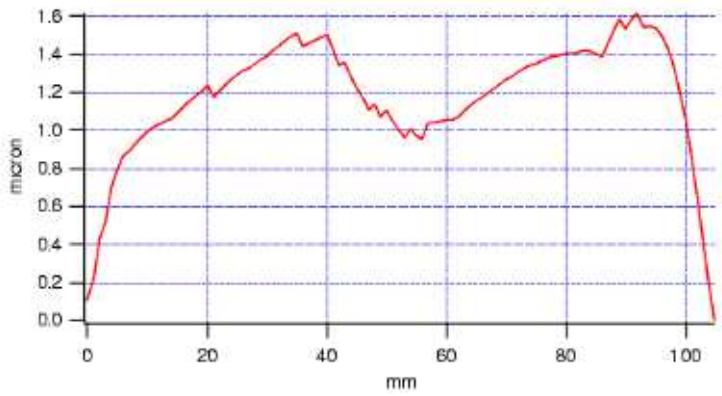

Figure 8.9: The LTP profile of the mirror shell: the multilayer compressive stresses (see sect. 3.5.3, page 71) in the coating have deformed the mirror, whose shape has become convex. The y scale is strongly stretched. The apparent concavity in the profile center is due to the convex shell shape as the LTP measurement was not exactly on-axis.

The possibility of other causes than roughness in the mirror shell for the reflectivity reduction have been considered, e.g., the mirror deformation by multilayer stresses (see fig. 8.9) that could shadow a part of the incident mirror. A quantitative evaluation of the mirror deformation shows, indeed, that the error angle is only 0'.5 , too small in comparison to the incidence angle (14'.65) to produce shadowing effects. Alternatively, the deformation could have spread the incidence angles, depending on the impact mirror point: the result could be a smoothing of the Bragg peak, but the integrated reflectivity of the shell Bragg peak is much less than in the witness case, excluding a relevant mechanical deformation effect in the reflectivity peak smoothing.

The flat sample and the mirror *shell* were also measured at the INAF-OAB with an AFM scan, returning a *local* surface roughness value 12 $\AA$ in the wavelength range 10 $\div$ 0.05 μm and 3.3 $\AA$ in the wavelength range 1 $\div$ 0.005 μm: the first value, in particular, can be considered as an upper limit to the multilayer interfacial roughness, as its wavelength range is superposed well to the typical spectral range where the multilayer growth takes place (see sect. 3.5.2, page 68). An example of the taken scans is shown in fig. 8.10.

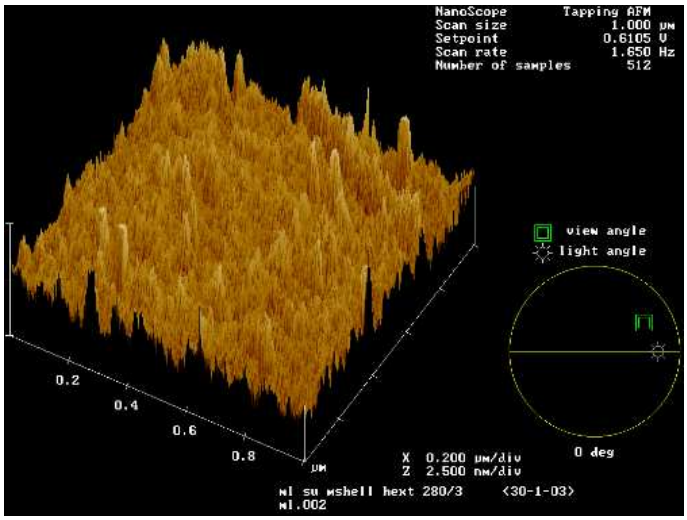

Figure 8.10: An AFM (1 μm wide) scan of the mirror shell sector, measured at the PANTER facility.

Parameters (Å)	Shell 8 keV	(BEDE) 17 keV	Shell (PANTER) 10-50 keV	Witness 8 keV	(BEDE) 17 keV	Witness (PANTER) 10-50 keV
Period	77.0	76.7	78.4	75.0	75.0	71.0
Γ factor	0.29	0.31	0.29	0.31	0.30	0.31
σ(Si on W)	7.5	6.7	8.8	4.3	4.3	4.3
σ(W on Si)	8.3	7.3	10.2	5.5	5.4	5.5
σ(Si on Au)	3.5	3.5	4.0	none	none	none
σNi substrate	2.0	2.0	2.3	1.5	1.5	1.5

Table 8.1: Main parameters for the PANTER / BEDE periodic multilayer coated shell mirror X-ray measurements.

The measurement was also done with a pencil beam at the photon energies of 8.05 and 17.4 keV at the BEDE X-ray facility and the measured profiles (see figure 8.11) were fitted by IMD as well. In particular, we can observe, from the large number of observed peaks, that the multilayer structure is very regular as the peaks are narrow and clearly defined: moreover, the shell multilayer period and the Γ are in good agreement with the corresponding nominal values. Also secondary peaks are visible between the Bragg peaks (even if the angular resolution of the measurement, that can be estimated as 25", does not show them in detail). Also in this case the shell reflectivity is considerably less than that of the witness, confirming the role of the substrate roughness in roughness growth.

The results of the parameters derived by the models applied to the PANTER and pencil beam measurements at INAF-OAB are reported in table 8.1. The pencil beam measurement is representative of a larger surface (some cm^2) than an AFM scan (less, however, than the PANTER characterization), and it is not very much affected by the surface deformation. As can be seen, the derived parameters are in substantial good agreement for the two different testing methods, confirming the role played by the roughness in the shell reflectivity reduction.

Note that the fitting roughness fits the AFM limit for the outer surface roughness and that the roughness of the W and Si surfaces are *different*, a fact that suggests a different microcrystallization state of the two materials. Note also that the substrate roughness cannot be considered the only responsible for the mirror shell degradation: the deposition process itself is still to be optimized, since also the witness mirror interfacial roughness has grown to 5.5 $\mathring{A}$ from a substrate initial value $\sim 1\mathring{A}$.

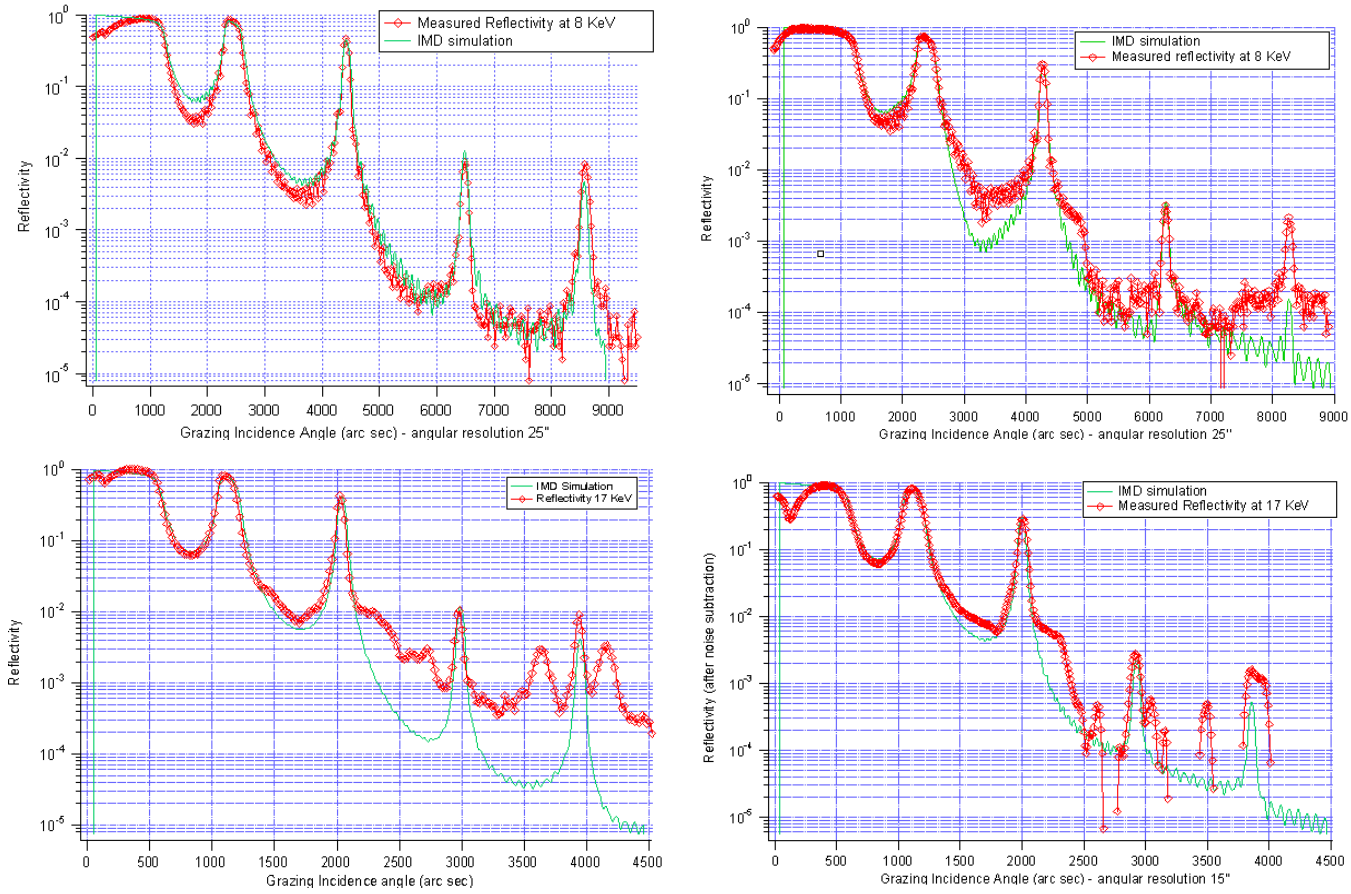

Figure 8.11: BEDE reflectivity measurements of the witness mirror (left) and a shell mirror sector, named 264 (right) / logarithmic plots.
The angular scans are taken at 8.05 keV (top) and at 17.4 keV (bottom). The angular scan have the advantage of a simpler interpretation as a large number of Bragg peaks can be easily obtained (four, in our case): the measurement at a more than an energy may, indeed, help to resolve the degeneration of the reflection scans on the large number of multilayer parameters. In the IMD fits the natural densities of Tungsten and amorphous Silicon are assumed.

8.2.2 W/Si graded multilayer coated shell measurement at the PANTER facility

A measurement has been performed also on a mirror shell with a *graded* W/Si multilayer coating, deposited at the CfA with the same Magnetron sputtering device. The shell Ni substrate was produced by Nickel electroforming of an Au coated mandrel by INAF-OAB. The reflectivity was measured at the PANTER facility (see fig. 8.12): a witness mirror (1 inch diameter) was coated during th same run and successively tested at the INAF-OAB with the AFM, WYKO and the BEDE X-ray diffractometer.

The graded multilayer is structured as a *double power law* (see sect. 3.4.1, page 58):

1. the uppermost 20 bilayers follow a power law with an index $c = 0.25$; the bilayer spacing goes from 107 $\mathring{A}$ to 40 Å, decreasing towards the inner layers. The Γ factor is more or less constant (0.47);

2. the innermost 75 bilayers follow a second power law, with the same index $c = 0.25$, but with a bilayer spacing going from 40 $\mathring{A}$ to 26 Å: the Γ is in this case about 0.38.

The reflectivity measurement performed at the PANTER is shown in fig. 8.12, and confirmed that the d-spacings are near to the desired ones, and as a result the multilayer reflects a wide band of the incident spectrum. The surface roughness is, indeed, quite high (6 $\mathring{A}$ for the inner power-law, $7 \div 8\mathring{A}$ for the outer power law.). A similar problem occurred with the periodic multilayer described in the previous section. Moreover, the low cut-off angle can be fitted only supposing that a low-density layer is present on the multilayer surface, probably a Carbon layer (3 nm) deposited by methane contamination and absorption of the last deposited layer (Silicon).

Also the AFM scan showed the formation of columnar structures on the shell, contributing to the increase in roughness.

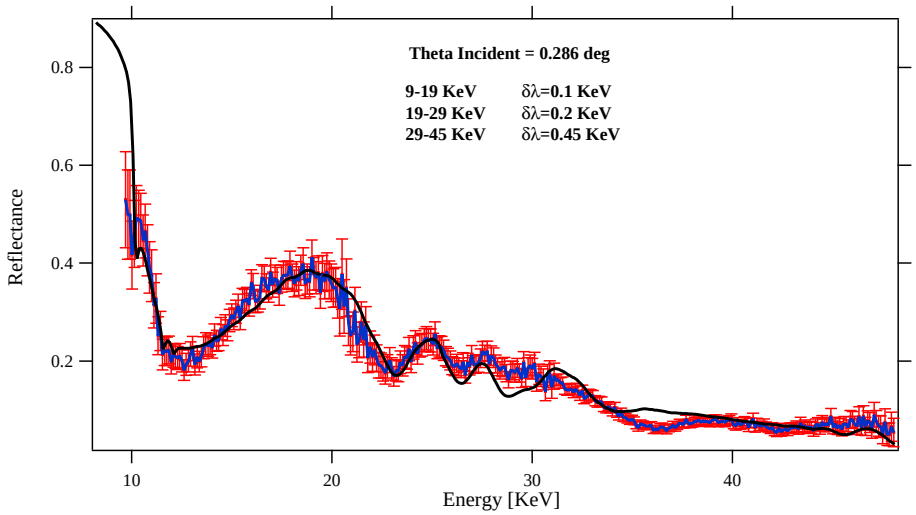

Figure 8.12: PANTER reflectivity measurements of the W/Si graded multilayer coated shell. The double power law used to structure the multilayer (black solid line) fits quite well the experimental data (red dots) with a roughness $\sigma = 6 - 7\mathring{A}$. The measurement was taken with three distinct scans, whose resolutions are indicated in the figure.

In order to understand whether the roughness origin was due to the initial substrate lack of smoothness or in the deposition process, the measurements of the witness sample have been performed at the INAF-OAB: the X-ray reflectivity scan are presented in fig. 8.13.

The reflectivity curves can be easily fitted with the double power law model: the resulting power law properties are slightly different from the PANTER tested shell, but this is not surprising as the position of the witness and of the shell were different:

1. the uppermost 20 bilayers follow a power law with an index $c = 0.25$; the bilayer spacing goes from 111 $\mathring{A}$ to 47 Å, decreasing towards the inner layers. The Γ factor is more or less constant (0.47);

2. the innermost 75 bilayers follow a second power law, with the same index $c = 0.25$, but with a bilayer spacing going from 44 $\mathring{A}$ to 19 Å: the Γ is in this case about 0.38.

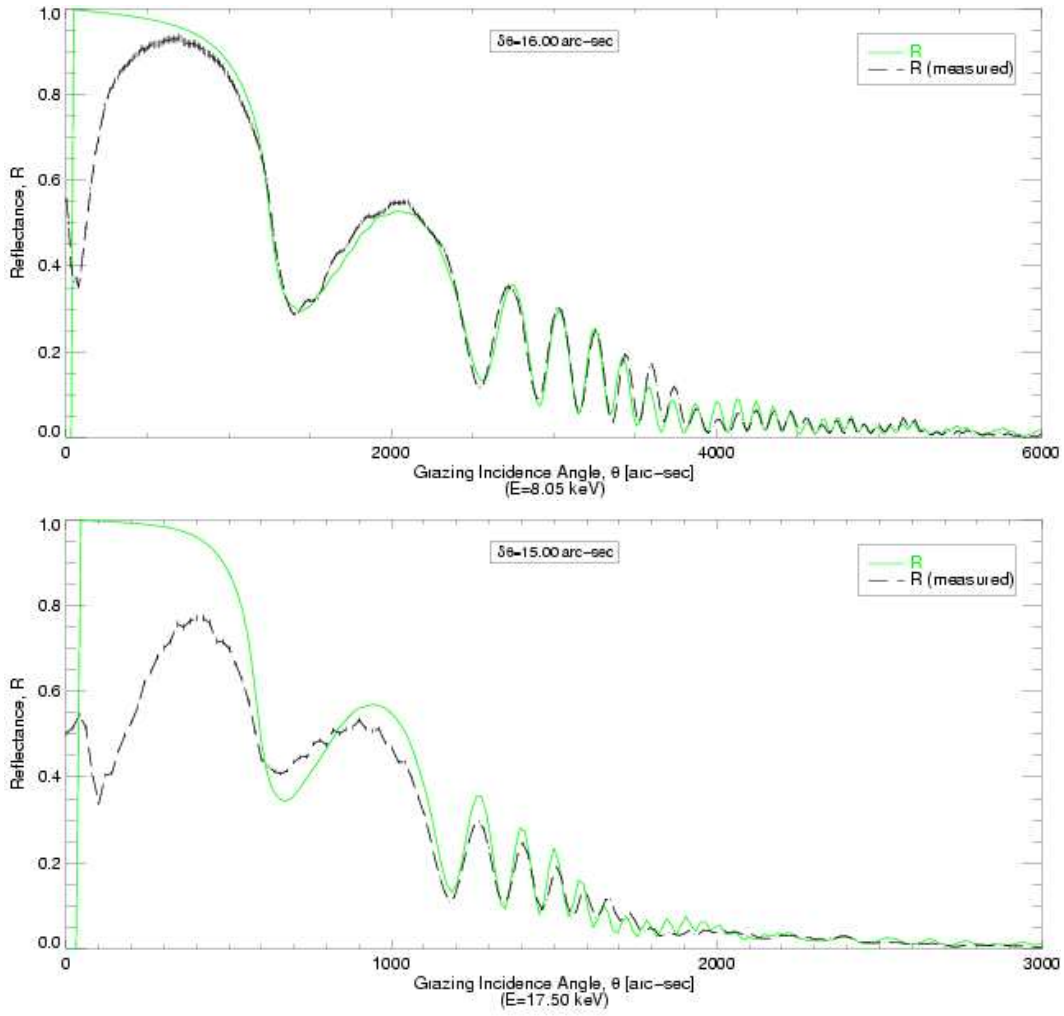

Figure 8.13: Witness reflectivity measurements (linear plots) taken with the BEDE-D1 diffractometer. *(courtesy of D. Vernani).* XRR scan at (top) 8.05 keV and (bottom) at 17.4 keV. The experimental data are fitted with good agreement by the assumed model.

The model could be fitted with a roughness value of 4 $\mathring{A}$ for the uppermost 20 bilayers, and with a roughness of 8 $\mathring{A}$ for the Tungsten and 4 $\mathring{A}$ for the Silicon in the innermost 75 bilayers. The assumed density of Tungsten is 18 g/cm^3 and for Silicon we have assumed the bulk value (2.3 g/cm^3). Also here a thin layer (2 nm) of Carbon is probably present. The roughness is sensitively less than in the shell case, but it is a worth noting that it has increased considerably as the starting substrate smoothness was excellent (1-2 Å). The deposition process is still to be optimized.

The spectral analysis of the substrate roughness was also performed, deriving a Power Spectral Density (see app. B) of the outer multilayer surface in the witness mirror. This was done by means of WYKO and AFM scans (100, 10, 1 μ wide) and with the X-ray scattering (XRS) at 8.05 keV (see sect. 5.3.1, page 120) in the total reflection regime: in such conditions, the single surface formalism may be used as the X-rays are reflected by the first layer (neglecting so the interference of the scattered waves, see sect. 5.3.2, page 124), and the X-ray scattering is determined only by the uppermost layer PSD. This result is thus comparable to the topographic measurements.

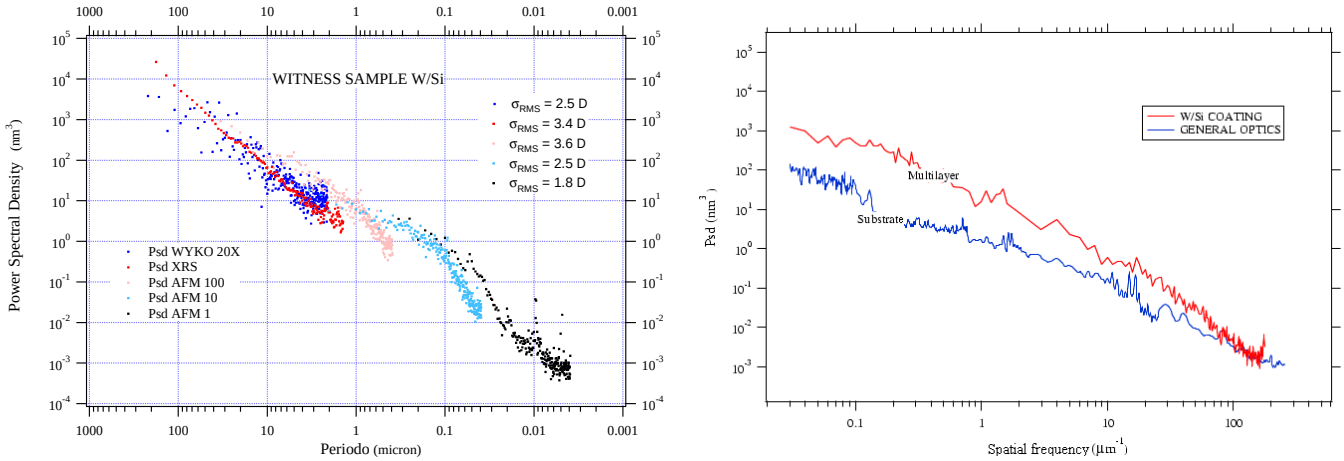

Figure 8.14: (left) PSD resulting from the characterization of the surface of the W/Si coated witness sample. The PSD are well superposed and describe roughly a power-law.
(right) The coating averaged PSD (red line) from 10 to 0.01 μm wavelength. The PSD is compared to the PSD of a fused silica superpolished sample, of the same type as the multilayer substrate. The PSD increase is apparent. *(courtesy of D. Vernani).*

Used instrument	σ(Å)	m_{rms} (mRad)	l_c (μm)
WYKO 20X	2.5	0.28	5.5
XRS	3.4	0.16	13.1
AFM 100	3.6	0.72	3.2
AFM 10	2.5	4.5	3.5
AFM 1	1.8	21.0	5.6

Table 8.2: Surface parameters for the graded shell, as resulting from the complete topographic characterization in fig. 8.14. The m parameter is the slope error (defined in app. B).

The PSD results are shown in fig. 8.14 (left) and the resulting surface characteristic parameters (see app. B) are listed in the tab. 8.2. We can observe that the roughness in the range $10 \div 1$ μm is in good agreement with the value inferred from the X-ray reflectivity. Moreover, the XRS results are in agreement with the topographic data.

Finally, the comparison in fig. 8.14 (right) showed the PSD evident increase from the substrate to the multilayer, especially in the typical spectral range from 10 to 0.1 μm (see sect. 3.5.2, page 68). The deposition process itself tends to grow the interfacial roughness, as already observed.

8.3 *Full-illumination* PANTER characterization of a Pt/C-coated shell

In this section we will expose the measurements performed at the PANTER facility on the Pt/C multilayer-coated mirror shell developed for the first phase of the ASI preliminary project for High-Energy payload. The mirror shell is the final point of a Pt/C multilayer development exposed in the chapt. 7 and it is the first X-ray mirror shell for hard X-rays obtained by direct replication of a mandrel by Nickel electroforming. The mirror shell (whose essential characteristics are reported in the tab. 8.3), was entirely produced at INAF-OAB and Media-Lario and, after integration, was tested in a full-illumination setup, a situation that

reproduces approximately the mirror operative conditions and that allows to derive mirror parameters like the HEW, the effective area, in addition to the simple reflectivity that can be also measured by a pencil-beam.

Profile	Wolter I
Diameter	27 cm
Length	40 cm
Incidence angle	0.193^o
Nickel walls thickness	0.2 mm
Reflective coating	Pt/C periodic multilayer
Number of bilayers	20
Period	6.8 nm
On-axis peak energy	$\sim$ 30 keV

Table 8.3: Some characteristics of the Pt/C coated mirror shell tested at the PANTER facility.

From the description of the production process we can expect that the performances of a multilayer-coated mirror shell after replication will show additional problems with respect to the direct deposition on Silicon Wafers performed in the chapt. 7, like the substrate deformation induced by stresses during the electroforming or release process. Some problems during the deposition of the first two bilayers have been reported, i.e. an e-gun instability while evaporating Carbon, thus we can expect that we will observe some period irregularities in the superficial layers. The replica phase also has shown some problems, i.e. the separation of the multilayer stack has been incomplete, since the first bilayer has not been transferred on the mirror shell (as proved by the X-ray reflectance scan of the residuals on the mandrel): we can, thus, expect that the surface roughness will be much larger than the achievable one with a direct deposition.

After the optic mounting *in the X-ray tube* (see fig. 8.4 on right), on the manipulator (that allows an angular accuracy of 1" in the optic positioning with respect to the beam), the measurement has been dealt in two distinct phases:

- in the first phase the integrated optic has been characterized at *low energies using monochromatic X-ray lines from 0.27 keV to 8.4 keV*: the focal spot has been observed using the PSPC detector. The very limited energy resolution of the PSPC is not a problem since we are operating with monochromatic X-rays. This measurements allowed us to characterize the mirror shell in the total reflection regime, where the interferential behaviour of the multilayer is not involved, and the X-ray scattering is limited: the achieved image quality is thus an index of the mirror profile accuracy, i.e. of the mirror deformation produced by the release:

- the second set of measurements have used the energy-dispersive setup with X-rays from a Tungsten source and the pn-CCD detector: the mirror characterization has so been done up to 42 keV, highlighting the multilayer reflection in the hard X-rays.

The results of the two measurements are mutually consistent.

8.3.1 Source at finite distance

Before the exposition of the results, it is worth noting that even if the PANTER facility is now the best available approximation of an X-ray celestial source, the finite source distance has to be taken into account: some effects on the optical properties of X-ray Wolter I mirror shells are:

- *Focal point deplacement*: given a point-like source on the optical axis at distance X_s from the optic principal plane, the image point will be located at distance X_i, determinated by the classical thin lenses formula:
$$\frac{1}{X_s} + \frac{1}{X_i} = \frac{1}{f} \tag{8.3}$$
where f is the optic focal length (see also bibl. [28]). For a celestial source, $X_s = \infty$ and $X_i = f = 10m$, but since at the PANTER $X_s = 123$ m, $X_i = 10.88$ m. A verification of the focusing properties must hence take into account this preliminary correction (see fig. 8.15).

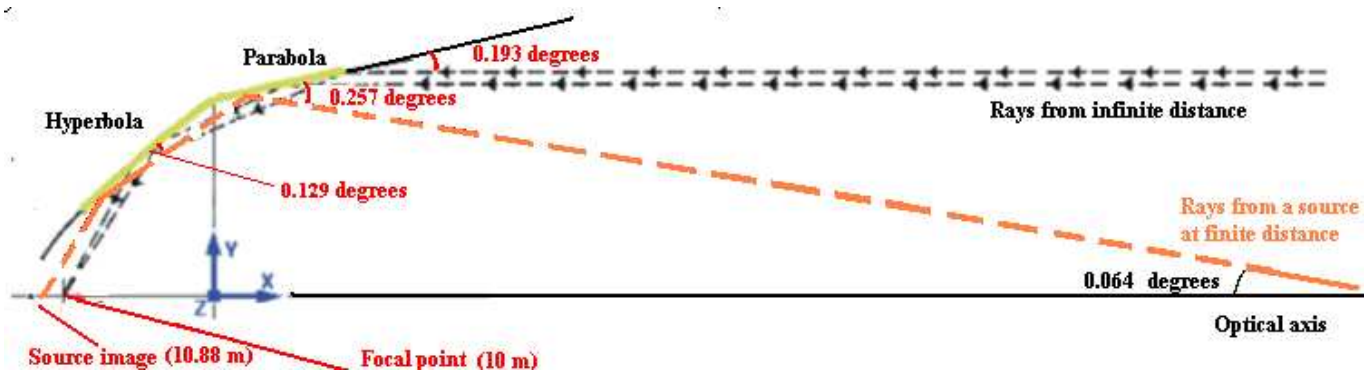

Figure 8.15: An effect of the finite source distance. The mirror shell is designed to collect photons from a celestial source at infinite distance, with a grazing angle of 0.193^o. At the PANTER facility the X-rays form an angle of 0.064^o with the optical axis, i.e. the first reflection on the paraboloid occurs at a grazing angle of 0.257^o and on the hyperboloid at 0.129^o.

- *Effective area reduction*: Wolter I optics are usually designed to reflect at the same grazing incidence angle on both paraboloid and hyperboloid, and the two segments have the same length, so that all the on-axis incident rays on the paraboloid are reflected also by the hyperboloid. If the source has a finite divergence, the reflected rays at the paraboloid front, that should strike the hyperboloid back, miss the reflection on the hyperboloid (see fig. 8.16), thus they are not collected in the optics focus (they would be concentrated in a point at a distance $2f$, but in a complete optic, the dense shell nesting would stop these single-reflected rays), thus a fraction of the optics effective area would be lost. It is possible to calculate (credits: G. Pareschi) that the non-occulted area of the mirror shell is given by the formula:
$$\alpha = \frac{X_s - 4f}{X_s + 4f} = \frac{\theta - \beta}{\theta + \beta} \tag{8.4}$$
in our case $\alpha = 0.51$, hence, the 49% of the shell area is lost. From simple calculations[1] it is easy to derive that the Wolter I geometric area seen by the single parabola from the actual source distance would be 7.46 cm^2, thus the actual geometric area for the PANTER X-ray source is $3.8cm^2$. This value must be reduced by 12 % if we account for the spider arms vignetting.

[1] if r is the average radius and L_p the parabola mirror length, $A_g = 2\pi r L_p \sin(\theta + \beta)$. Once reduced by the α factor, we recover exactly the *hyperboloid* cross-section, seen by the parabola-reflected rays.

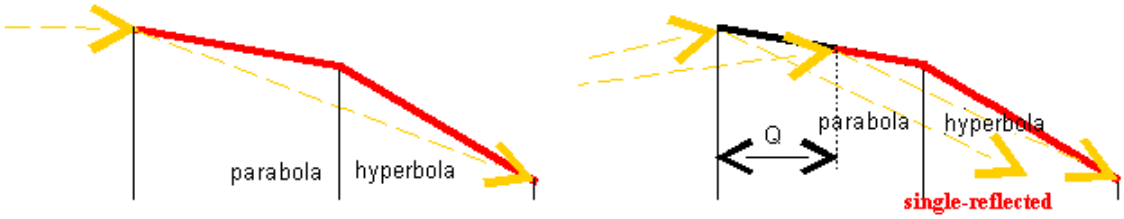

Figure 8.16: Lost illuminated area (Q) by effect of the finite source distance.

- *Incidence on the paraboloid and hyperboloid at two different grazing angles*: X-rays that undergo a double reflection incide on the paraboloid and on the hyperboloid at two different grazing angles: in particular (see fig. 8.15), if θ is the incidence angle for a source at infinite distance and β is the beam divergence ($\beta = R/X_s = 0.064^o$, being R the shell radius), the incidence angle on the paraboloid will be $\theta + \beta = 0.257^o$ and on the hyperboloid $\theta - \beta = 0.129^o$. Note that in this case, the 2.13 becomes $r = X_i \tan(4\theta - \beta)$. For single-layer coated optics, this is not a serious problem, provided that both angles are less then the layer critical angle: since the grazing angles at the two surfaces vary in opposite directions, the product of the two reflectivities remains more or less constant.

  For broad-band multilayer coated optics, the situation can be not so critical also, since the incidence angle variation shifts the energy band of the reflectivity curves, but the product of the two single reflectivities will be non-zero if the band shift is small with respect to the overall multilayer bandwidth, thus the zero-divergence effective area can be recovered from data. The situation is different, instead, for narrow-band multilayer coatings (like that used to coat the characterized shell), and since the two Bragg peaks will be located at two different energies (45 keV on the hyperboloid, 22 keV on the paraboloid), the product of the two reflectivities is expected to vanish: thus, it would be impossible to derive a mirror characterization in hard X-rays. We will see, nevertheless, that we could obtain a definite multilayer coating characterization in hard X-rays from reflectivity data.

- *Focal point blurring*: the finite source distance causes also an intrinsic image blurring. The rms σ_D of the point image (i.e. the angular radius including 68 % of the collected energy) may be expressed by the approximate, semi-empirical formula (see bibl. [28]):

$$\sigma_D = 4\frac{L_p}{f}\tan\left[\alpha\left(\frac{f}{X_s}\right)^2\right] \tag{8.5}$$

  where α is the grazing incidence angle and L_p the length of the single reflection surface (either paraboloid or hyperboloid). The measured rms σ_m is thus $\sigma_m^2 \approx \sigma_D^2 + \sigma_\infty^2$. Here σ_∞ is the true rms that would degrade the image of a celestial X-ray source, thus the true optical performances can be better than the observed ones in the calibration with full-illumination setup: this effect can be important in the calibration of high-resolution optics, like those of Chandra (HPD $\sim$ 0.5") or the future XEUS optics (HEW $\sim$ 2"). In the present case $\sigma_D \sim 0.4$", thus the finite distance has a negligible effect since the measured HPD is 40", almost completely dictated by the mirror profile.

8.3.2 Data reduction

The incident beam is preliminarily characterized by a flat field opening a circular hole in the X-ray screen and measuring the photon count rate incident on the detector, either in monochromatic mode or in energy-

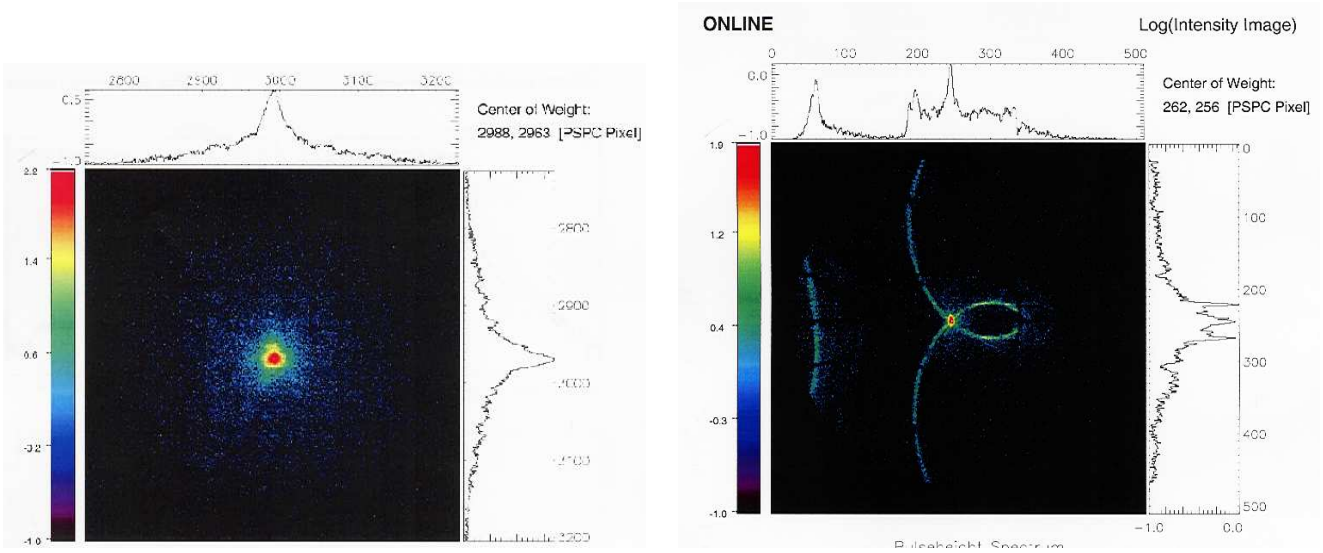

Figure 8.17: (left) The focal spot at the photon energy of 0.27 keV (C-K line). The HEW of the focal spot is 40", in the range of replicated optics. Since at this energy only the uppermost layer is effective in reflection and the scattering is low (scaling as λ^{-2}), the HEW value is dictated by the mirror profile accuracy: the multilayer coating has not degraded the Nickel electroformed shell optical performances.
(right) A typical coma aberration for off-axis incidence. The rays single-reflected by the paraboloid (the outer arc) are also visible (*Credits: W. Burkert, G. Hartner (MPE)).*

dispersive mode: once known the incident flux per unit area ($B_{inc}(E)$), the mirror shell is exposed to the X-ray beam and the collected photons form a focal spot on the detector.

The integration of the the focal spot allows to recover the collected photon rate C_c, and the shell effective area

$$A_{eff}(E) = \frac{C_c(E)}{B_{inc}(E)} \tag{8.6}$$

The reflectivity data are derived from the shell effective area

$$R_p(E)R_h(E) = \frac{A_{eff}(E)}{A_g} \tag{8.7}$$

where A_g is the geometric collection area of the shell (including the vignetting effect due to the finite source distance and the spider shadowing), and R_p, R_h are the reflectivity of the paraboloid and that of the hyperboloid, respectively. For a source at infinite distance $R_p = R_h$, since the grazing incidence angle would be identical: for a source at finite distance, instead, $R_p \neq R_h$. Thus, to interpret the reflectivity data the same multilayer model has been evaluated at the two different grazing angles.

8.3.3 Soft X-rays measurements

The soft X-rays measurements using fluorescence lines ($0.27 \div 8.4$ keV) and the PSPC camera are shown in fig. 8.17. Since at these energies the grazing incidence angle is under the critical angle, the reflectivity is a function of the outermost layer (Platinum) properties. Moreover, at these energies the scattering is very limited (see eq. 2.21), thus, the mirror PSF is dominated by the mirror shape accuracy.

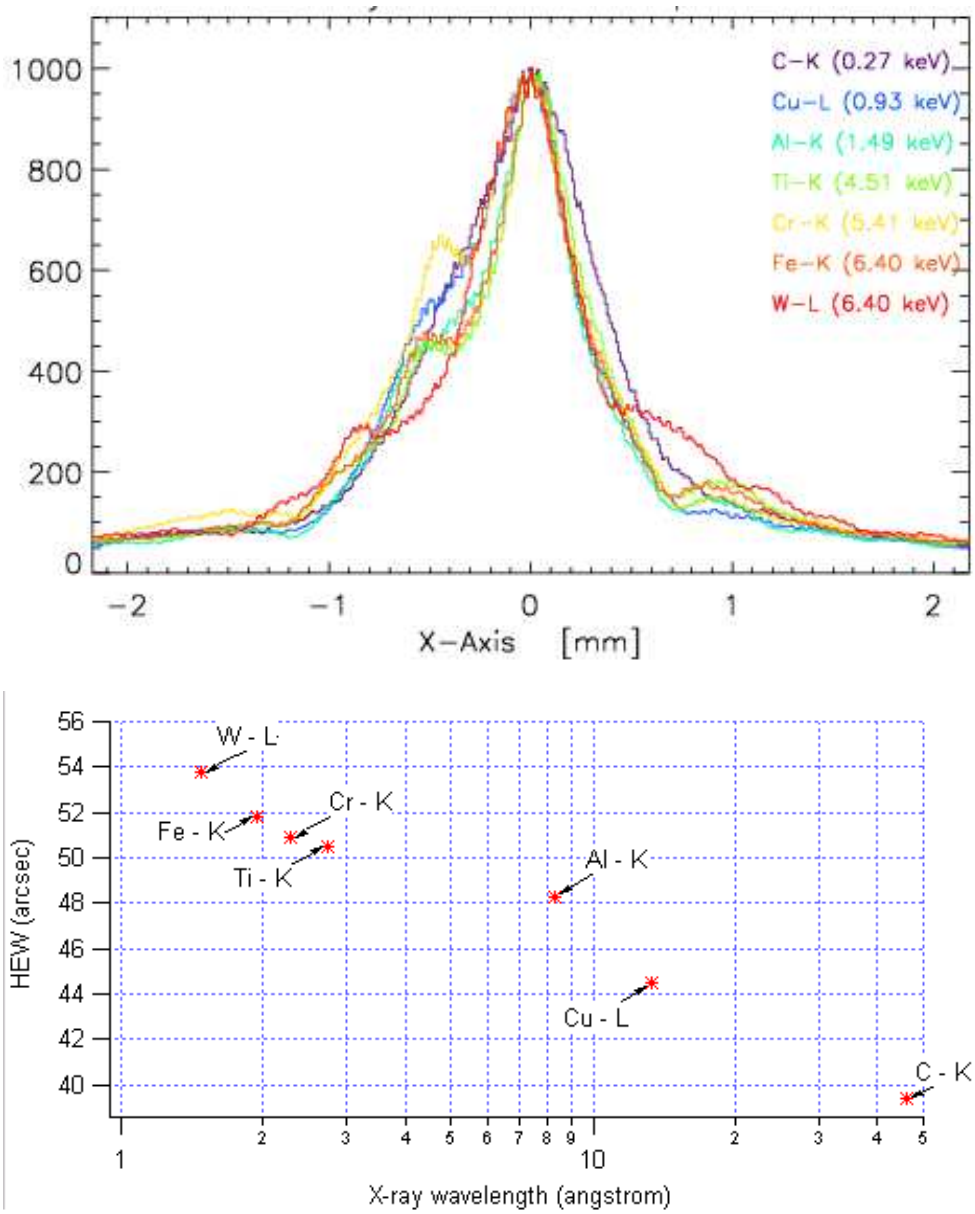

Figure 8.18: (top) Profiles of the focal spot in soft X-rays, measured in the x direction of the PSPC detector. (bottom) The focal spot HEW as a function of the X-ray line wavelength (*Credits: G. Hartner (MPE)*).

1. At the C-K line (0.27 keV), the focal spot has a HEW of 40", in the typical range of replicated optics, i.e., the application of a multilayer coating has not degraded the mirror PSF with respect to a single layer case, used for soft X-rays optics.

2. For increasing energies (see fig. 8.18), there is a PSF broadening (always remaining in the replicated optics order of magnitude), caused by the increasing scattering. The broadening is mainly located in the "wings" of the PSF, that is a feature of X-ray optics.

3. The obtained reflectivity $R_p R_h$ of the Wolter I shell is plotted in fig. 8.19. The obtained fit assumes that the X-rays are reflected in total reflection by the outermost Platinum layer, with a roughness

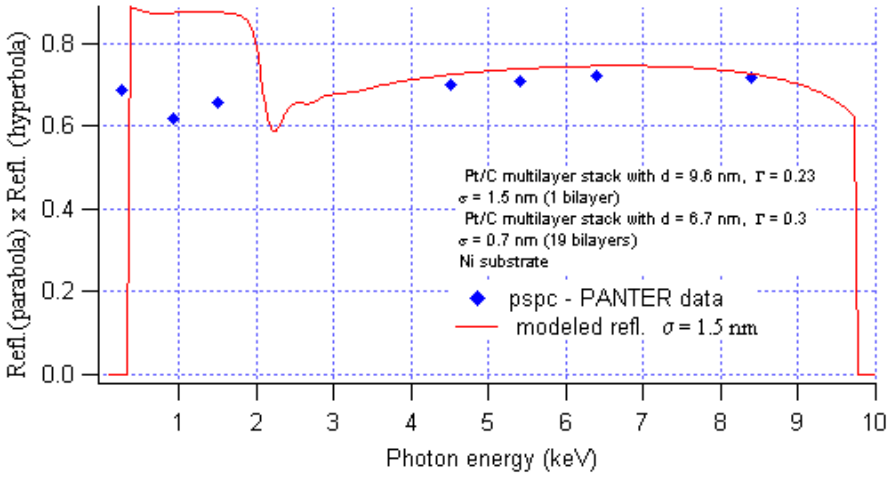

Figure 8.19: The mirror shell effective area derived from the PSPC data, measured in correspondence to fluorescence lines at low energy. The data are compared to a multilayer model with a surface roughness of 15 Å.

rms σ =15 Å: this value is in good agreement with the AFM measurements recently performed at INAF-OAB. Such large roughness value (much larger than the roughness value $-5\mathring{A}-$ achieved in the preliminary deposition on flat samples, see fig. 7.18) may have been caused by the reported problems in the shell release phase. The first three data cannot be fitted in the model: a possible explanation is the presence of a low-frequency roughness component with a "shadowing" effect in grazing incidence.

Emission line	HEW
C-K (0.27 keV)	39.4"
Cu-L (0.93 keV)	44.5"
Al-K (1.49 keV)	48.3"
Ti-K (4.51 keV)	50.5"
Cr-K (5.41 keV)	50.9"
Fe-K (6.40 keV)	51.8"
W-L (8.4 keV)	53.8"

Table 8.4: The HEW of the mirror shell focal spot at the X-ray energies used in the soft X-rays characterization.

8.3.4 Hard X-rays measurements

The illumination with a continuum, hard spectrum measured by the pn-EPIC camera in energy-dispersive mode has reported a significant reflectivity in hard X-rays: the focal spot obtained with the exposure to the bremsstrahlung spectrum of the W target (30 kV) is shown in figure 8.20. The measurement has also been taken with a setup at 45 kV in order to cover a wider hard X-ray energy range (up to 40 keV).

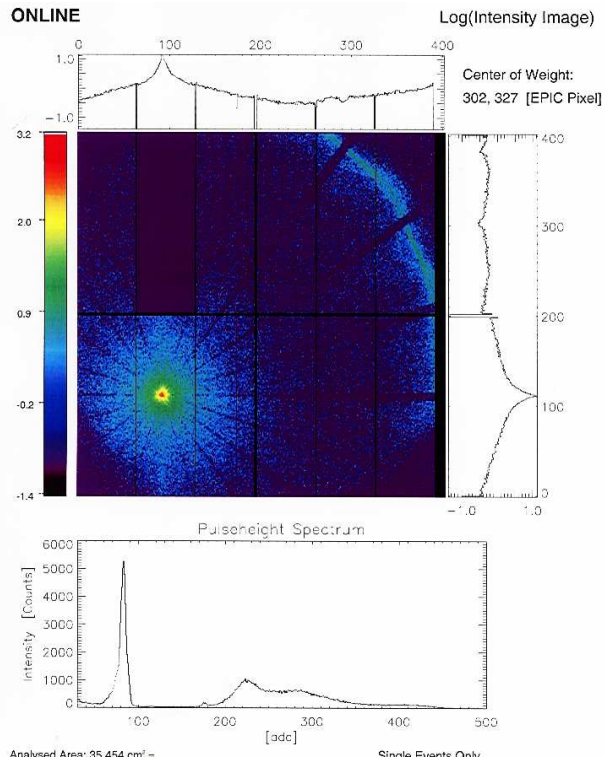

Figure 8.20: The focal spot seen by the pn-EPIC CCD camera. A much larger scattering fraction (visible from the spot broadening, see fig. 8.17) is present at high energies. The arc visible in the upper part of the image is the beam fraction that is single-reflected by the paraboloid, as effect of the finite source distance (*Credits: W. Burkert, G. Hartner (MPE)).*

The main results of this measurement are:

1. The focal spot is strongly broadened, and since the mirror profile accuracy was already observed in soft X-rays, the cause of the broadening is the X-ray scattering .

2. The effective area / *product of the two reflectivities* is measurable also in hard X-rays (see fig. 8.21) and it has a peak around 22.4 keV. The presence of this reflectance peak can be explained evaluating the adopted multilayer reflectivity model at the two different grazing incidence angles. We assume that the reflective coating is a regular multilayer structure composed by 18 Pt/C bilayers with a constant d-spacing 6.7 nm and $\Gamma = 0.3$, i.e. very near to the foreseen structure in the deposition phase. The last bilayer is assumed to have a much larger thickness due to a reported instability of the e-beam during the two first Carbon layer depositions on the mandrel. With this model, the first Bragg peak is located at 22.4 keV for the paraboloid ($\theta_i = 0.257^o$) and at 45 keV for the hyperboloid ($\theta_i = 0.129^o$). At a so small grazing incidence angle, however, the cut-off energy of the hyperbola will be near to 22 keV: thus, the product of the two reflectivities will be non-zero around 22.4 keV, and the observed peak will appear: the thicker, capping bilayer is instead responsible for the formation of the broad reflectivity peak observed at lower energies ($12 \div 20$ keV), strongly enhanced by the finite source distance effect since it falls in the total reflection regime for the hyperbola reflection.

   Assuming this model (18 periodic bilayers with d = 6.7 nm, $\Gamma = 0.3$) and with the constraint of a superficial roughness $\sigma = 15\mathring{A}$ to take into account the low energy data, we can infer for the capping bilayer a d-spacing 96 $\mathring{A}$ and $\Gamma = 0.23$ (i.e. the thickness excess is mainly caused by the Carbon), and

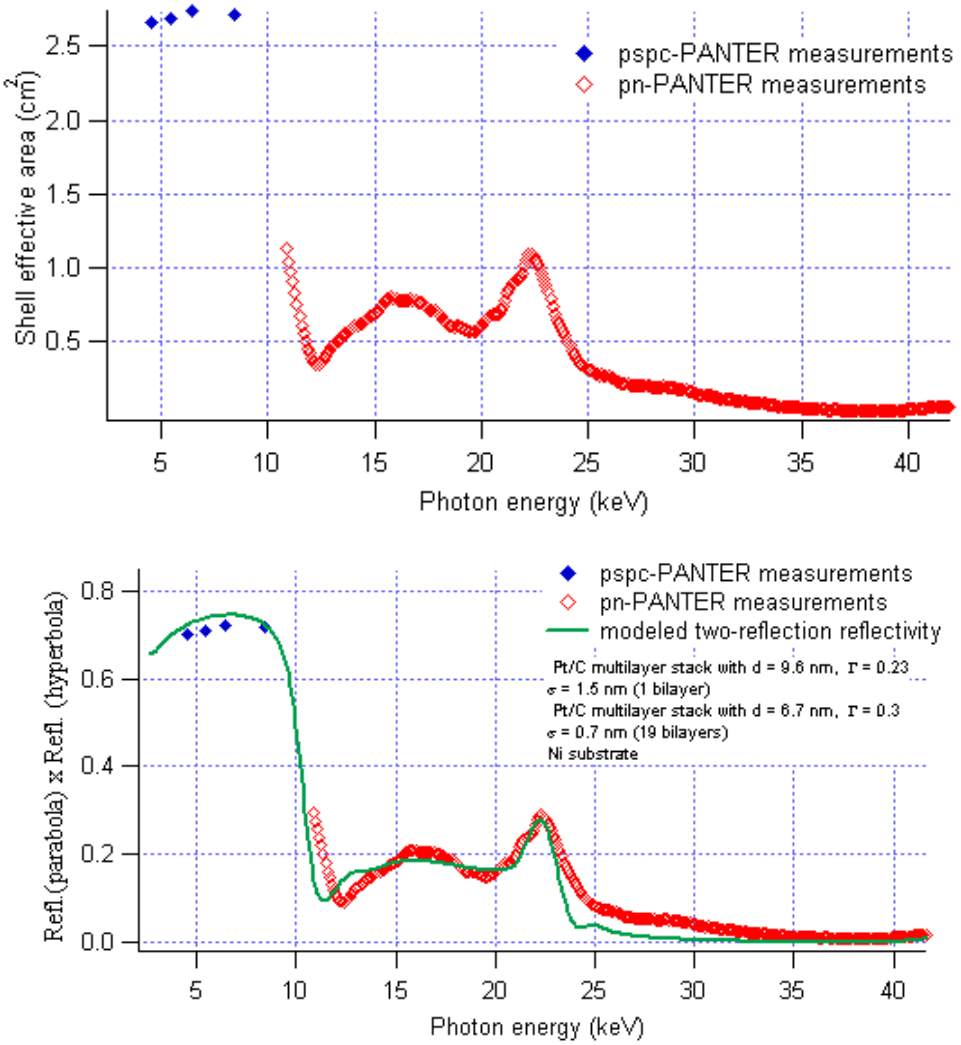

Figure 8.21: (left) X-ray shell effective area and (right) reflectivity in full-illumination setup.

an interfacial roughness of 7 Å, much lower than the surface roughness: this disagreement suggests that a large roughness increase occurred in the shell release from mandrel, as a consequence of the incomplete multilayer transfer of the mirror shell. The stress generated in this phase has also affected the interlayer roughness, but in a lesser extent.

The assumed Carbon density is 1.6 g/cm^3 (as resulted from the sect. 7.3.1 on page 148) and 21 g/cm^3 for Platinum. The reflectivity scans for the paraboloid and the hyperboloid are plotted in figure 8.22.

The product of the two reflectivities in fig. 8.22 derived from the assumed model is well superposed to the experimental reflectivity, as it can be seen in figure 8.21. The result is consistent with the PSPC data, that are reported in the same figure.

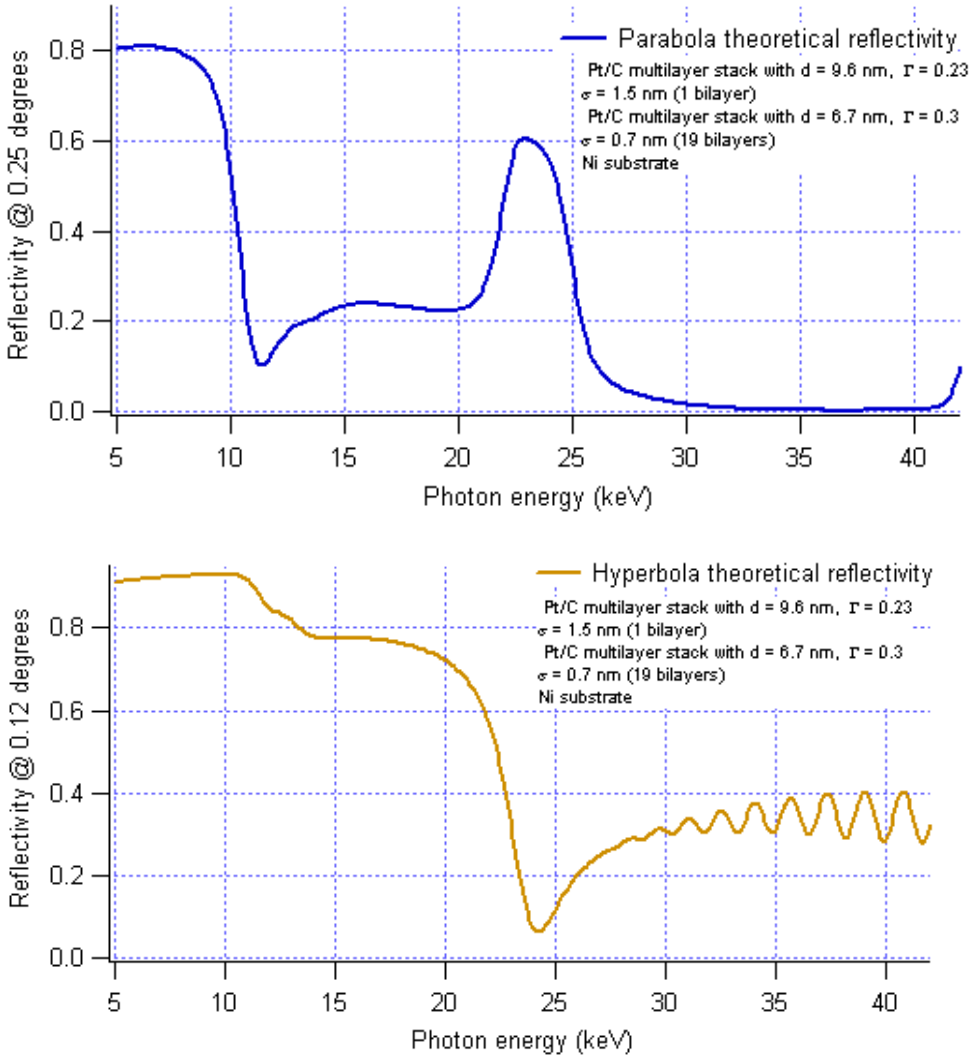

Figure 8.22: The multilayer reflectivity model used to fit the reflectivity data.(top) Modelled reflectivity on the paraboloid at an incidence angle of 0.257^o. Note the sharp Bragg peak at 23 keV produced by the interference in the 18 innermost bilayers and the broad peak at lower energy caused by the larger thickness of the outermost bilayer. (bottom) Modeled reflectivity on the hyperboloid at a grazing incidence angle of 0.129^o. The cut-off energy is located near to the first Bragg peak for the reflection on the paraboloid.

8.4 Conclusions

The provided mirror characterization and multilayer modelization suggested that:

- The Pt/C deposition on flat substrates proved that a good multilayer quality is achievable, provided that we improve the control on the deposition process, especially on the layer thickness and on the roughness increase (from this viewpoint the future use of the ion assistance device will help considerably). These improvements will be necessary in view of the deposition of graded multilayer-coated mirror shells.

- The replication of multilayer coatings from Nickel superpolished mandrels using the Nickel electroforming is possible without degrading the optical performances, also when using very thin Nickel mirror walls. The future activity developments, indeed, will be oriented also to stress measurements and mitigation in order to guarantee good imaging capabilities for graded multilayer coatings, with a much larger bilayer number.
- In order to avoid the degradation of the multilayer performance due to the electroforming and release process, the future developments will be aimed to an improvement of the release, that will be eased by the use of a suitable release agent.

Chapter 9

The PPM code in X-ray multilayer reflectivity fitting

The deposition of flat, multilayer Pt/C and Ni/C coated samples has given since now very interesting and encouraging results. However, a typical e-beam problem is the non-steady evaporation rate, especially with Carbon: this can in turn cause an instability of the layer thickness, and a consequent deviation of the thickness trend from the designed one. This problem is being resolved with the achievement of steady evaporation conditions, as well as the interfacial roughness growth (which will be lowered by using an ion-assistance device), but a diagnostic technique to analyse in detail the layered structure is a fundamental need.

The TEM sections are a viable solution and they can be used for selected samples: as a direct performance test, we always measure X-ray reflectivity (XRR) scans at the two standard energies 8.05 keV and 17.4 keV with the BEDE-D1 diffractometer installed at INAF-OAB. This kind of measurement takes the advantage of being sensitive to some physical layer properties (density, high-frequency microroughness) in addition to the properties (thickness, interdiffusion, crystallization state) that can be studied with a TEM.

The interpretation of the XRR is nevertheless difficult as it depends on a large number of parameters, namely all the thickness, density, roughness, ... values in the stack. To interpret the multilayer structure, a code like IMD is very useful as it is able to provide the average properties of the layers; an alternative code is *PPM* (Pythonic Program for Multilayers) developed by A. Mirone (ESRF), aimed to perform a multiparametric optimization of the reflectivity scan at one or more energies at the same time. The reflectivity fitting can work with an arbitrary number of free parameters searching the combination of values that represents the best possible fit of the scan. Once found a set of values returning a modeled reflectivity well superposed to the experimental one, we can be confident that the found solution represents a good approximation of the multilayer structure. PPM has recently become a subject of interest in the COST (European COoperation in the field of Scientific and Technical research) cooperation promoted by the European Science Foundation.

PPM is a program of large interest for the activity we are developing with multilayers: we have tested PPM on reflectivity scans taken at the INAF-OAB on some multilayer samples (with almost constant d-spacing), whose reflectivity curves we have shown in the previous sections. In the next sections we will show some early results coming from the use of this tool (see also bibl. [141]).

9.1 PPM: Pythonic Program for Multilayers

A layer-by-layer analysis of the stack may be performed with PPM. This code is open-source, downloadable from the URL ftp://www.esrf.fr/pub/scisoft/ESRF_sw/linux_i386_00 it is specifically conceived for a fast determination of the stack parameters by fitting the reflectivity scans even in the details: this allows us to take into account the reflectance features caused by the deepest layers. A scheme of the PPM working principle is shown in fig. 9.1.

The program takes as input the reflectivity curves and a file in XML format that defines the structure scheme. The number of necessary parameters may vary according to the supposed complexity of the stack. For example we can take all the layer thicknesses as free variables, or assume a gradual drift of the layers. Other variables define the layer density and their roughness. The user must also enter the lower and the upper limits and the initial guessed value for every defined variable.

Starting from the initial values, PPM computes the reflectivity curve R_c for every available experimental scan R_m and computes the Figure Of Merit (FOM),

$$FOM = \sum_i \frac{(\ln R_i - \ln R_m)^2}{\ln R_m} \tag{9.1}$$

where i is the index of the angular sampled point. The minimizing algorithm consists in the variation of the stack parameters since the FOM reaches its minimum, a situation corresponding to the best possible fit, that is, the best approximation of the defined structure to the real multilayer structure.

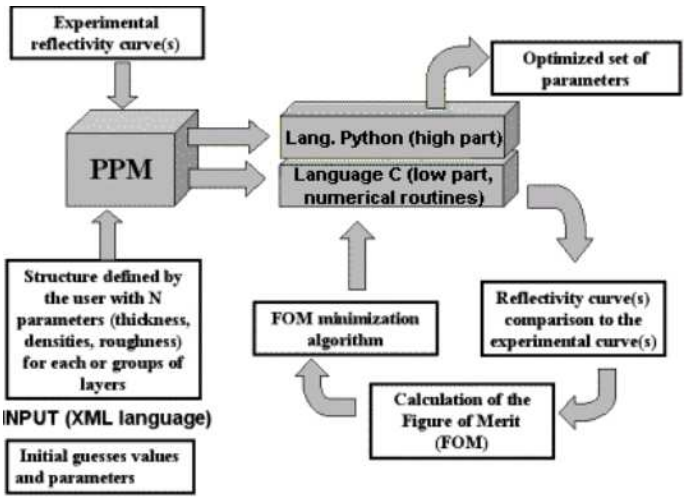

Figure 9.1: A scheme of the working principle of PPM: the reflectivity curves are initially calculated from the parameters values defined by the user for the chosen scheme which approximates the stack structure. The computed reflectivity (at one or more photon energies) is then compared to the experimental one(s). The Figure Of Merit (FOM) to be minimized is the χ^2 of the logarithmic plots: the minimization algorithm (downhill / simulated annealing) varies the stack parameters within the fixed limits by the user. At every cycle the FOM is computed and the parameter set with the minimum FOM value is selected.

The choice of minimizing the χ^2 of the logarithmic reflectivity permits to give more weight in the fit to the reflectance details (which in a linear plot would be likely neglected) that carry important information about the reflection in the deepest layers.

The adopted algorithm that varies the parameters to search the global minimum in the parameter space is a derivation of the well-known *downhill simplex* (see bibl. [104], bibl. [105]) (or amoeba) algorithm. A set

of N+1 points in the N-dimensional parameter space follows a series of moves that converge to the nearest minimum: however, the downhill simplex alone would lead very likely to a local minimum, that could be very far from the global one. For this reason an annealing function (see bibl. [138], bibl. [139], bibl. [140]), which is able to take us out from the local minima, is also implemented.

The simulated annealing function associates to every point of the parameter space a microscopic state of N particles: in this comparison, the convergence to a local minimum is compared to a thermalization process, leading to a state of definite temperature T. The system of particles is assumed to obey the *Boltzmann distribution*, where the FOM (depending on the actual particle state) plays the role of the energy. Using the downhill simplex alone we would exclude completely the moves that increase the FOM, trapping so the system in a local minimum: if the system stabilizes itself according the Boltzmann distribution at a temperature large enough, there is instead a finite likelihood that the system goes out from the local minimum. Usually the initial temperature is set at a high value in order to allow a large number of transitions increasing the FOM, and when the system reaches the equilibrium T is slowly decreased.

When the temperature is decreased, the probability of increasing the FOM during a transition is lower and lower. At this point the system tends to converge towards a more global minimum till a minimum temperature value is reached, where the calculation stops. The probability of finding the global minimum is so increased as a much more large fraction of the parameter space is explored, at a cost of an increase of the computing time (with respect to the *downhill simplex* case).

The annealing procedure has also some critical points, like the choice of the initial temperature and the cooling rate (usually an exponential decrease is adopted). A very slow cooling rate gives a more degree of confidence that the global minimum has been found, but it is more expensive in term of the computing time. These parameters, as well as the multilayer structure and the initial values for the parameters, have also to be carefully chosen in every single case.

The capability of searching the minimum FOM within the allowed values of the stack parameters makes PPM a very powerful tool to fit X-ray reflectivity curves.

9.2 Some early results

A Ni/C multilayer The fitting capabilities of PPM were tested on the multilayers shown in fig. 9.2 The Ni/C multilayer presented in fig. 7.8 was schematized as a succession of 6 blocks formed by 3 bilayers each: in each block the bilayers have a linearly drifting thickness to allow short-term thickness fluctuations. The Ni and the C density, also parameters to be fitted, are assumed to be constant along the stack, whereas the Ni and C roughness are independent in every block. The modeled structure has been fitted simultaneously to both reflectance scans at the photon energies of 8.05 and 17.4 keV.

The excellent agreement of the fitting model with the experimental curve is apparent in fig. 9.2 (at 8.05 and 17.4 keV). The reflectance features are fitted in the all the details, either in the linear scale or in the logarithmic scale. The main deviations are oscillations of the modeled reflectivity around the experimental curve in correspondence to the near-zero reflectance angular regions: they can be eliminated by taking into account the finite angular resolution of the measurement: in fact, if we set the convolution parameter in the source file to the actual measurement angular resolution, the agreement is complete also in those points.

The main result of this two-energy fit may be summarized as follows: the obtained density of Ni is 8.7 g/cm^3 and that of C is 1.7 g/cm^3, in agreement with the found values with IMD. The average roughness is 3.5 $\mathring{A}$ for both Pt and C. The layer thickness trend shows (see fig. 9.3) a slow decrease of the Ni layers

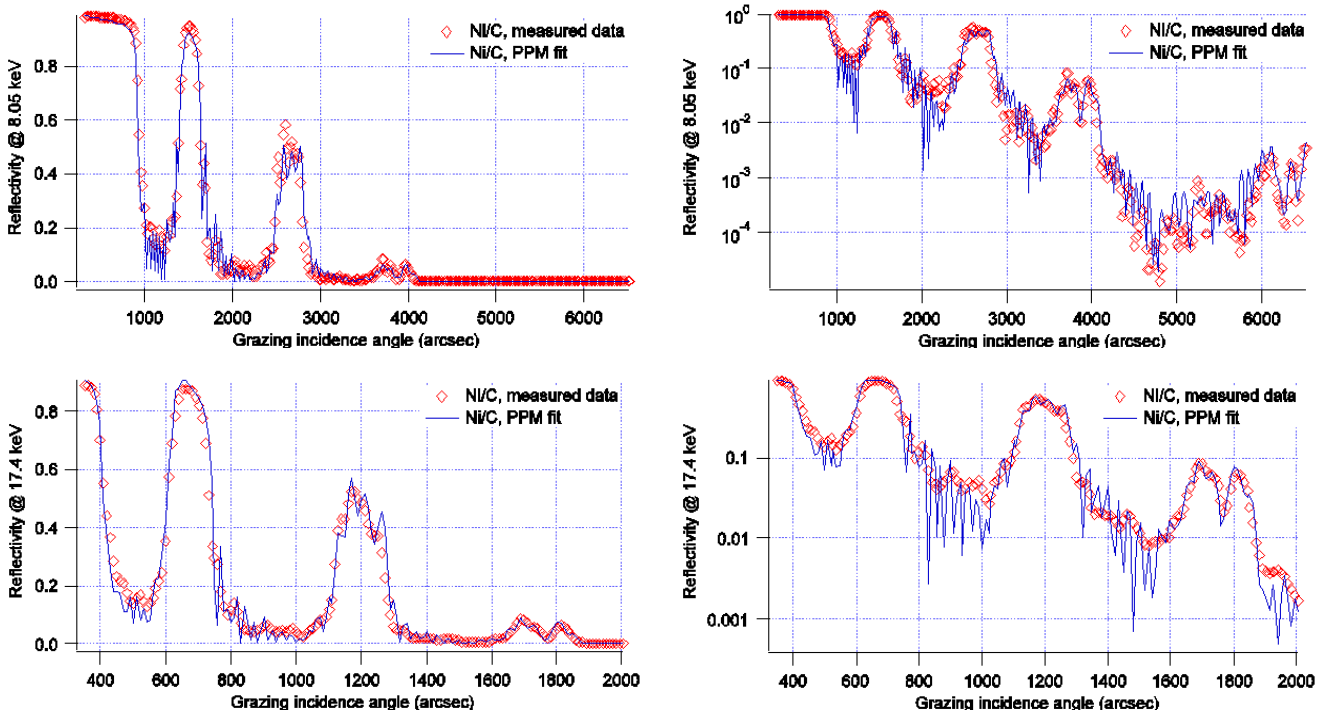

Figure 9.2: The experimental reflectance scans of the Ni/C multilayer compared to the fitting model found by PPM. The fit was run simultaneously on both scans at 8.05 (top) and 17.4 keV (bottom). Linear plot (left) and logarithmic plot (right).

and a very strong increase of the C layers: the main responsible for the thickness drift is C, as previously supposed. The overall period variation over all the stack is 2 nm.

The thickness trend (see fig. 9.3) has been compared to the data derived from the TEM section of the same multilayer (see fig. 7.9). The structure obtained by PPM is in disagreement with the TEM section analysis: this is probably due to the choice of the modeled structure of the stack as a succession of blocks. A better structure should be defined letting all the layers independent in their variations (within quite stringent limits in order to avoid the calculation divergence). This has been done with the next example, a Pt/C multilayer.

A Pt/C multilayer The Pt/C in fig. 7.14 has been fitted assuming a structure with all the layers thicknesses (both Pt and C) as independent parameters. Also the density and the roughness of both Pt and C, assumed to be constant along the stack, are considered as fitting parameters. The multilayer is so fitted with an overall set of 44 free parameters: in figure 9.4 we show a comparison of the achieved fit and the experimental scan. The agreement between model and experiment (only at 8.05 keV) is apparent in both the linear and logarithmic plot.

The result of this fit procedure has returned values in qualitative agreement with the IMD fit. In particular, the Pt density turns out to be 20.6 g/cm^3 and the C density 1.55 g/cm^3. Moreover, the model can be fitted assuming an interfacial density for both C and Pt of 3.5 Å, very near to the substrate value. In fig. 9.5 the thickness trend of all the layers is shown: the Pt layers are almost constant and have the desired value, whereas the Carbon is apparently responsible for most of the period variation in the stack. Moreover, except for three very exceeding values, the layer drift range is quite close to the obtained value with IMD. Unfortunately, for this sample a TEM section is not yet available and we cannot verify the results.

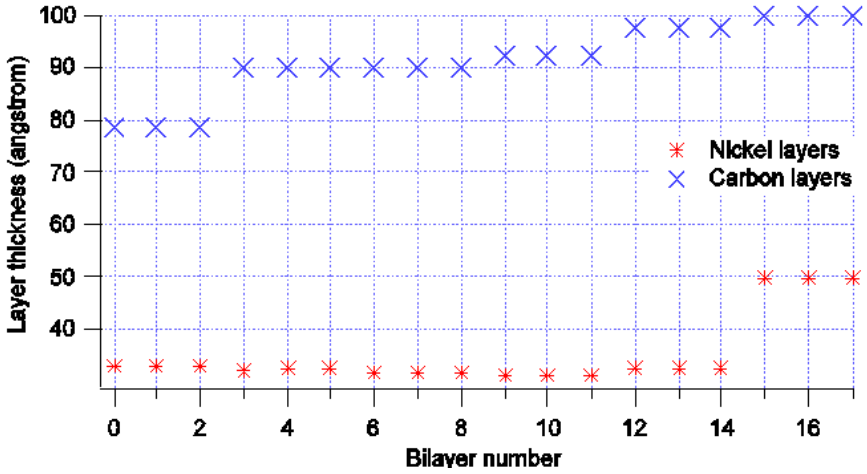

Figure 9.3: (left) The trend of the Nickel and Carbon layer thickness as resulting from the PPM fit. The multilayer was modeled with 6 blocks formed by 3 bilayers each, with in addition a linear drift in every block (as a consequence, the C layers appear grouped). The drift is mainly due to the Carbon layers as in the Pt/C case, but also the Ni contribution is not negligible. The period drift (2 nm) is in agreement with the IMD results.

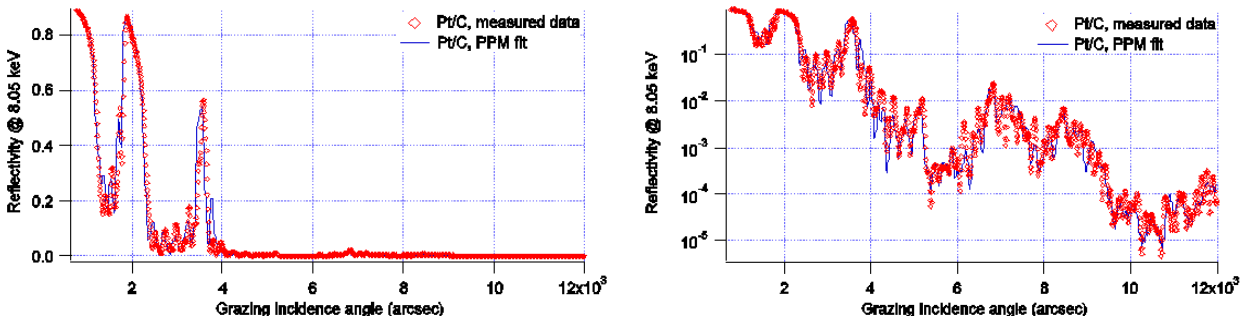

Figure 9.4: the experimental reflectance scan @ 8.05 keV of the Pt/C multilayer compared to the fitting model found by PPM. Linear plot (left) and logarithmic plot (right). The layer-by-layer analysis has found a model in very good agreement with the experiment. Despite the large number of parameters, the calculation has converged to a very good solution.

Mo/Si multilayer fitting Like all numerical codes, PPM has also some limitations: for instance it seems to manage with difficulty the Mo/Si multilayers fit (see fig. 9.6), probably because of the well-known interdiffusion layer Mo_xSi_y with very uncertain composition. Even a 4-layer model produces a not-so performing fitting: it is probable that the composition of this layer is so uncertain that the number of freedom degrees becomes too large. More stringent limits about the interlayer composition are necessary in order to return a performing fit.

9.3 Conclusions

PPM has turned out to be a very powerful fitting tool. Like in all the fitting code, the risk of the local minimisation is always present, especially when the number of free parameters is large: PPM seems to have optimal capabilities to reduce this risk: this occurrence may be reduced by slowing the cooling rate of the annealing algorithm. This would in turn increase even more the computing time, but PPM (which has been developed in a Linux ambient) can be also easily run in a parallel-computing network: this configuration

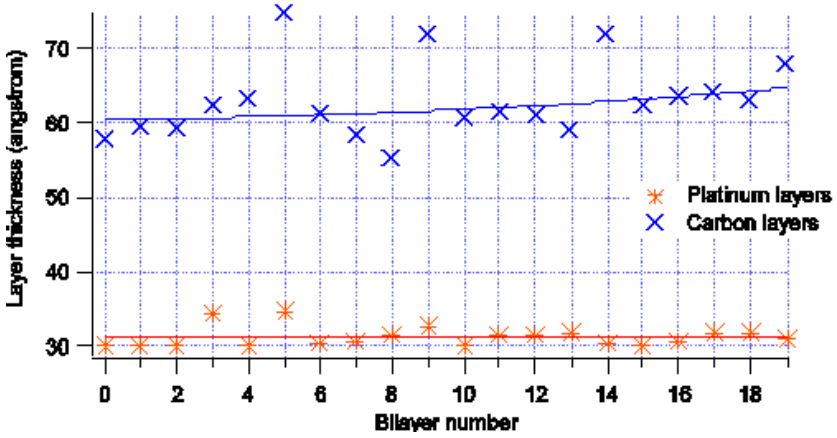

Figure 9.5: The thickness trend of the Pt and C layers, as inferred by PPM. The Pt layers have a more constant thickness (3 nm, as programmed), whereas almost all the period instability was caused by the C layers. Three values are very exceeding, probably due to the too large limits allowed for the C layers.

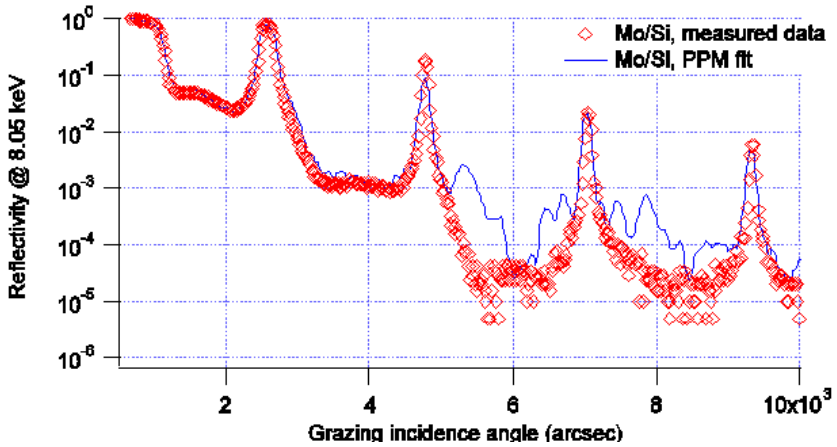

Figure 9.6: A Mo/Si multilayer XRR at 8.05 keV, as fitted by PPM. In this case the fit is not so performing because of the uncertainty in the composition of the interdiffusion layer, that has doubled the number of parameters to be fitted. Some additional constraints about the interdiffusion layer would be necessary.

permits to reduce the time necessary to the elaboration.

In the next developments, a number of multilayers will be produced and the thickness data returned by PPM will be compared to the TEM measurements: in order to take PPM in agreement with the TEM results, it will be necessary to give more stringent limits to the input parameters and to vary the assumed model of the stack, deriving it from the TEM results. We still need a number of cases to be studied, but, by means of the TEM sections, a calibration of PPM in order to provide a complete realistic analysis of the stack structure can be done.

Once calibrated, PPM will be an important tool in the development and use of a multilayer diagnostic. The systematic use of PPM will be very useful in the development of e-beam evaporated multilayers and the production of hard X-rays mirrors for the next hard X-ray telescopes.

Chapter 10

Conclusions and final remarks

The implementation of hard X-ray multilayer coatings is an important development sector, as it will allow a breakthrough in the X-ray astronomy since it will permit the construction of X-ray telescopes with imaging capabilities in hard X-rays (see sections 3.7.1, 3.7.3, 3.7.2, 3.7.4): moreover, the hard X-ray multilayer development activity has a large interest also in other fields of the current research (see sect. 3.8.1 on page 92, 3.8.2 on page 94). The multilayer technology, indeed, is in development progress in order to make them suitable for the specific application (space, nanoelectronics,...) and each case requires a separate study.

From this viewpoint, the developed activity in the framework of this Ph.D. thesis has been very fruitful:

- the feasibility study of the extension of the Ni electroforming technique to multilayer coatings has been started;
- I have explored some deposition methods and manufacturing techniques, improving the tools (X-ray Reflectivity, X-ray Scattering) and the interpretation of the results for the characterization and leading to the understanding of the points to be improved (see sect. 8.2, page 167);
- I have implemented the multilayer e-beam deposition in a deposition chamber previously used only to deposit single layer coatings (see sect. 7), page 139;
- I have investigated and improved the e-beam multilayer deposition (see sect. 7, page 139);
- in the interpretation of the X-ray multilayer reflectivities I have acquired and tested a powerful numerical tool (PPM) (see sect. 9, page 187)
- I have started a multilayer "diagnostic" development from the overall results of the topographic instruments, XRR, XRS, TEM.

From my Ph.D. activity the following papers have been published (also cited in the bibliography) :

1. G. Pareschi, O. Citterio, M. Ghigo, F. Mazzoleni, D. Spiga, *New X-ray missions*, **2003**, Mem. SAIt Suppl., 3, 323
2. D. Spiga, *Characterization of a flat superpolished mandrel prototype with hard (TiN/SiC) overcoating to enhance the surface durability* : **2003**, SPIE Proc. 5168, 518
3. G. Pareschi, G.Di Cocco, E.Caroli, O. Citterio, V. Cotroneo, S.Del Sordo, F.Frontera, L.Gizzi, G.Malaguti, S. Silvestri, D. Spiga, *The HEXIT (High Energy X-ray Imaging Telescope) balloon-borne mission*,

2003, Proc. of the 16th Symposium on European Rockets and Balloon Programmes and Related Research, St. Gallen (CH), 179P

4. H. Brauninger, W. Burkert, G.D. Hartner, O. Citterio, M.Ghigo, F. Mazzoleni, G. Pareschi, D. Spiga *Calibration of hard X-ray (15 ÷ 50 keV) optics at the MPE test facility PANTER*, **2003**, SPIE Proc. 5168, 283

5. D. Spiga, G. Pareschi, O. Citterio, S. Basso, M. Cassanelli, V. Cotroneo, G. Grisoni, B. Negri, G. Valsecchi, D. Vernani, *Developement of multilayer coatings (Ni/C ÷ Pt/C) for hard X-ray telescopes by e-beam evaporation with ion assistance*, **2004**, SPIE Proc. 5488, 813

6. Pareschi G., Cotroneo V., Spiga D., Barbera M., Artale M. A., Collura A., Varisco S., Grisoni G., Valsecchi G.,*Astronomical soft x-ray mirrors reflectivity enhancement by multilayer coatings with carbon overcoating*, SPIE Proc. 5488, 481

7. D. Spiga, G.Pareschi, A. Mirone, C. Ferrero, M. Sanchez del Rio, *Fitting X-ray multilayer reflectivities by means of the PPM code*, SPIE Proc. 5536-26, in press

8. D. Spiga, G.Pareschi, G. Valsecchi, G. Grisoni, *Hard X-ray multilayer coated astronomical mirrors by e-beam deposition*, SPIE Proc. 5533-9, in press

other papers are in preparation and will report the activity in development in the next future:

- extension to other multilayers for X-ray telescopes, like W/Si multilayers;
- development of a practical interpretation method for the XRS from multilayer (see sect.5.3.2) in order to provide a complete characterization of the spectral evolution of the PSD in a multilayer coating;
- calibration of the installed Linear Ion Source parameters (angle, energy, current) in order to smooth multilayer interfaces during the e-beam deposition and improve their optical and mechanical performances;
- calibration of the PPM code to real cases by studying the results derived from the TEM section analysis;
- further improvement of the thickness control and deposition of graded multilayers for wide-band, hard X-ray telescopes.

Appendix A

Single surface X-rays reflection

A.1 Optical constants: free electron gas model

The problem of developing an optics for X-rays is centered on the their peculiar interaction with the matter. As visible light, the propagation of X-rays is ruled by Maxwell's Laws and a plane wave travelling in the x-direction may be represented by the function:

$$\mathbf{E}(x,y,z,t) = \mathbf{E_0} exp\left[\frac{2\pi i}{\lambda_0}(nx - ct)\right] \tag{A.1}$$

where n, the refractive index of the medium, can be written in a complex form:

$$n = 1 - \delta + i\beta \tag{A.2}$$

where β accounts for the absorption losses. Typical values are $\delta \approx 10^{-5} \div 10^{-6}$ and $\beta \approx 10^{-6} \div 10^{-7}$. In visible light, except for propagation in conductors, the imaginary term is usually negligible, and n is significantly bigger than 1. X-rays instead, because of their higher energy, show a different behaviour.

At some keV energies, the main interaction of X-rays with the atoms is photoelectric, peaking at the energies of the bond of the K-shell. The more we go under over this range, the more interaction drops, and the less the structure of the atom becomes important, because the cross-section of photoelectric effect for different shells than K decays with increasing energy. The material thus looks to X-rays like a free-electron gas (Drude model). In this approximation (Thomson scattering), the equation of motion of the free electron:

$$m_e \dot{\mathbf{v}} = -e\mathbf{E} \tag{A.3}$$

has a solution for simple-harmonic oscillation:

$$\mathbf{v} = \frac{ie}{\omega m_e}\mathbf{E} \tag{A.4}$$

this, if N_e is the density of free electrons, in turn implies for $\mathbf{J}$, the current density, and for ρ, the charge density:

$$\mathbf{J} = -\frac{iN_e e^2}{\omega m_e}\mathbf{E} \qquad\qquad \rho = \frac{N_e e^2}{\omega^2 m_e}(i\mathbf{k}\cdot\mathbf{E}) \tag{A.5}$$

the last one may be obtained from the continuity equation, in the form $i\mathbf{k}\cdot\mathbf{J} + (-i\omega\rho) = 0$.

In the plane-wave approximation, the source Maxwell's equations become:

$$\begin{aligned} i\mathbf{k}\cdot\mathbf{E} &= 4\pi\rho \\ i\mathbf{k}\times\mathbf{H} &= \frac{4\pi}{c}\mathbf{J} - \frac{i\omega}{c}\mathbf{E} \end{aligned} \tag{A.6}$$

but, substituting the obtained expressions for the field sources, they become:

$$\begin{aligned} i\mathbf{k}\cdot\mathbf{E}\left(1-\frac{\omega_0^2}{\omega^2}\right) &= 0 \\ i\mathbf{k}\times\mathbf{H} &= -\frac{i\omega}{c}\mathbf{E}\left(1-\frac{\omega_0^2}{\omega^2}\right) \end{aligned} \tag{A.7}$$

where ω_0 is the *plasma frequency*,

$$\omega_0^2 = \frac{4\pi N_e e^2}{m_e} \tag{A.8}$$

the eqs. A.7 are completely analogous to source-free equations in a dielectric material of dielectric constant $1-\frac{\omega_0^2}{\omega^2}$. The refractive index is thus:

$$n = \sqrt{1-\frac{\omega_0^2}{\omega}} \approx 1 - \frac{\omega_0^2}{2\omega^2} \tag{A.9}$$

in the last equation we have approximated ($\omega \gg \omega_0$) since often ω_0 is in the EUV range. As $N_e = \frac{\rho}{A}N_a f$, being ρ the mass density, A the atomic weight, N_a the Avogadro number, f the number of free electrons per atom, we may write:

$$n = 1 - \frac{N_a r_e}{2\pi A}\lambda^2\rho f \tag{A.10}$$

having set $r_e = \frac{e^2}{m_e c^2}$, the classical electron radius.

If we are well above the fluorescence K-edge, we may assume $f \approx Z$: in this case, a better approximation for f_1 is obtained with a small relativistic correction (see bibl. [31]):

$$f_1 \simeq Z^* = Z - \left(\frac{Z}{82.5}\right)^{2.37} \tag{A.11}$$

In the assumed, simplified model, X-rays are not absorbed by the electron gas. This occurs because the conductivity σ is purely *imaginary*: therefore, the current J is delayed by $\pi/2$ with respect to the electric field. The impedance is purely inductive and there is no net energy transfer to the electrons. Physically, this is a consequence of the impossibility for the photons to vanish in a two-body interaction: it would be impossible to conserve the overall 4-momentum. The photon absorption is possible only considering also the presence of the atomic nuclei, and the consequent photoelectric absorption.

To take into account the photoelectric absorption by the bound electrons we introduce a complex factor of scattering (proportional to the atomic photoelectric cross-section σ_{ph}, see fig. 2.4):

$$n = 1 - \frac{N_a r_e}{2\pi A}\lambda^2 \rho (f_1 + i f_2) \tag{A.12}$$

the factors f_1, f_2 are to be determined empirically (see bibl. [32]). The complex term is the previously mentioned $\delta + i\beta$. We note that the real part of the refractive index is *less than 1*[1].

By equating the absorption coefficient $\frac{\rho}{A}\sigma_{ph}$ to the extinction coefficient $\frac{4\pi}{\lambda}\beta$ it easy to derive the expression for f_2:

$$f_2 = \frac{\sigma_{ph}}{2 r_e \lambda} \tag{A.13}$$

the photoelectric cross-section allows also to recover the generic, following expression for f_1:

$$f_1(E) = Z^* + \frac{1}{\pi r_e hc}\int_0^\infty \frac{\varepsilon^2 \sigma_{ph}(\varepsilon)}{E^2 - \varepsilon^2} d\varepsilon \tag{A.14}$$

known as *Kramers-Kronig dispersion relation* (see bibl. [31]). The integral is a generalization of the (discrete) dispersion Lorentz model to a continuous probability of photoionization. It is easy, from a quick investigation of the eq. A.14, to observe that the f_1 coefficient has a minimum followed by a maximum in correspondence to the atomic absorption edges.

A.2 Grazing incidence reflection

Let us now consider an interface between two materials with the real part of the refractive index n_1 and n_2, being θ_1 and θ_2 their relative grazing incidence angles, we could repeat the bound conditions for the electromagnetic fields ($E_1^t = E_2^t$, $H_1^t = H_2^t$), leading to the *Fresnel equations* for the amplitude of the reflected (r) and the transmitted (t) wave (see e.g. bibl. [24]):

$$r_s = \frac{n_1 \sin\theta_1 - n_2 \sin\theta_2}{n_1 \sin\theta_1 + n_2 \sin\theta_2} \tag{A.15}$$

$$t_s = \frac{2 n_1 \sin\theta_1}{n_1 \sin\theta_1 + n_2 \sin\theta_2} \tag{A.16}$$

$$r_p = \frac{n_1 \sin\theta_1 - n_2 \sin\theta_2}{n_1 \sin\theta_2 + n_2 \sin\theta_1} \tag{A.17}$$

$$t_p = \frac{2 n_1 \sin\theta_1}{n_1 \sin\theta_2 + n_2 \sin\theta_1} \tag{A.18}$$

Here the p and s subscripts denote polarization in the incidence plane or in the normal plane respectively. The incidence and the refraction angles are related by the usual *Snell law*:

$$n_1 \cos\theta_1 = n_2 \cos\theta_2 \tag{A.19}$$

[1] This occurs because we are over all the characteristic frequencies ω_i of the atom: in fact, if we had taken into account the electron bonds, we should discover instead of the eq.A.9 the expression $n \approx 1 + \sum_i \frac{\omega_0^2}{2(\omega_i^2 - \omega^2)}$ and, for $\omega \gg \omega_i$, $n < 1$.

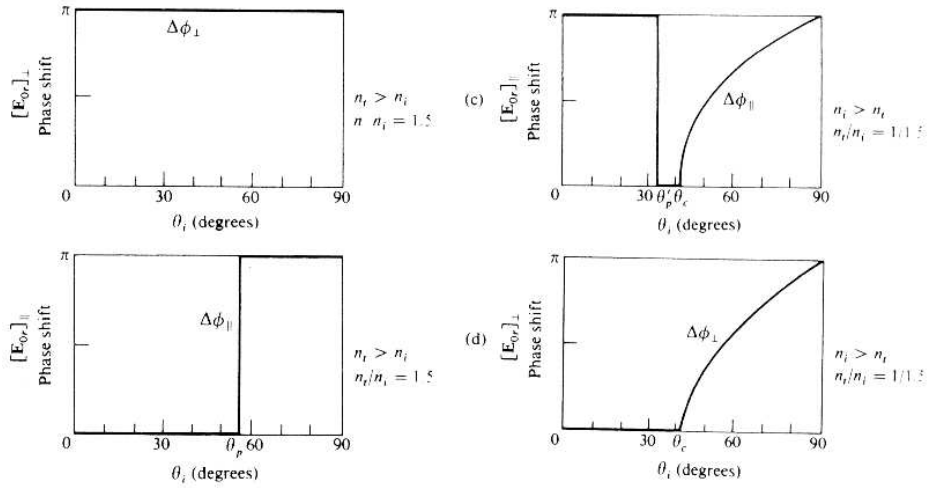

Figure A.1: Phase change of reflected wave as a function of the incidence angle in the visible range, when $n_1 < n_2$ or $n_2 < n_1$ (credits: *Optics*, by Hecht and Zajac). The phase shift at the interface for the reflected wave is very near to 0 or π. In the first case (left) the phase shift of π occurs in the reflected wave in the p-component if the incidence angle is less grazing than the Brewster angle θ_p, whereas the reflected s-component is always π phase shifted. In the second case (right) the phase shift is different from 0 or π in total reflection regime. Otherwise, only the p-component is phase-inverted at grazing angles less than θ_p. The refracted wave has never a phase inversion.

both δ and β contribute to the reflectivity. Let us have an X-ray incident from vacuum on a material with refractive index n, with a grazing incidence angle θ_0. Snell law reduces to $\cos\theta_0 = n\cos\theta$. In X-rays the reflection and the refraction obey the same laws as in the optical range, but because of values of refractive index in eq. A.2 they have different features:

- As the real part of n is less than 1, the refracted X-ray *approaches* the surface, what is uncommon in the visible light.
- Being the n values so close to 1, the deflection of the refracted wave is about $\delta\cot\theta$: that is, very small; e.g. a $1\mathring{A}$ X-ray incident at 45^o on Gold will have a deflection ≈ 10".
- For the same reason, the Fresnel equations give a reflectivity very close to 0 for both polarization at almost all incidence angles.
- After the refraction the X-ray is exponential absorbed according to the law $e^{-(\beta/\lambda)x}$; that is, a $1\mathring{A}$ X-ray in Gold decays of 1/e in a typical length $\lambda/\beta \approx 10^6\lambda = 0.1$ mm.

However, for very small values of θ_1, it is easy to show that the Fresnel equations for the reflected ray may be approximated by:

$$r_s = -r_p = +\frac{\delta_2 - \delta_1}{2\sin^2\theta_1} \tag{A.20}$$

and the reflectivity approaches 1 for decreasing angles down to (in the considered case $\delta_1 = 0$ and $n = 1-\delta_2$) $\theta \simeq \sqrt{2\delta_2}$. In fact, as $n < 1$, for $\theta_0 < \theta_c = \arccos(n)$ it is impossible to satisfy the eq. A.19 and the eqs. A.15 $\div$ A.18 (and in particular the eq. A.20) cease to be valid. The incident ray undergoes to a *total reflection*. Really a reflection of exactly 100% is never reached, because of the X-ray scattering caused by the surface

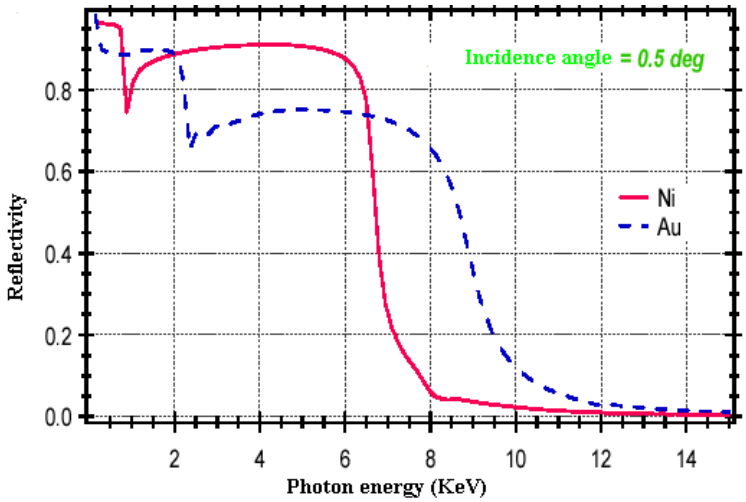

Figure A.2: Reflectivity of Gold and Nickel as a function of X-ray energy at a fixed grazing incidence angle. Gold reflects up to higher energies because it is denser, but it is more photoelectric absorbing due to its high Z value.

microroughness and because of the non-zero photoelectric absorption in the first layers of the material, in which the total reflection occurs (see below).

The relationship defining the *critical angle* for the total reflection $n = \cos(\theta_c)$ may be approximately written as:

$$1 - \delta = \cos(\theta_c) \approx 1 - \theta_c^2/2 \tag{A.21}$$

that is, and using the eq. A.10 with $f \approx Z$,

$$\theta_c \approx \sqrt{2\delta} = \sqrt{\frac{N_a r_e}{\pi A}\lambda^2 \rho Z} \tag{A.22}$$

as $\lambda = hc/E$, being h the Planck constant and E the photon energy,

$$\theta_c \approx \sqrt{\frac{N_a r_e h^2 c^2}{\pi}}\frac{\rho^{1/2}}{E}\sqrt{Z/A} \tag{A.23}$$

from the eq. A.23 it is quite evident how the critical angle increases with the reflecting material density and falls with increasing energy. This fact explains why it is easier to reflect X-rays with denser materials (typically Au, Ir, Pt), and why it is impossible to reflect hard X-rays at enough large angles even using dense coatings.

If we express ρ in g/cm^3, E in keV and θ_c in mrad and we substitute the values(supposing $Z/A \approx 1/2$, light-element approximation), we obtain the practical formula $\theta_c \approx 19.83\rho^{1/2}E^{-1}$.

A complete analysis of the "total reflection" (see e.g. bibl. [24]) show that in such conditions *there is* a refracted wave which penetrates the material, but with exponentially damped amplitude. The total reflection grazing incidence occurs provided that the reflecting material have a larger thickness than the penetration depth of X-rays in it. The $1/e$ penetration depth in total reflection $\theta_0 < \theta_c$ conditions is

$$d_p = \frac{\lambda}{2\pi}\frac{1}{\sqrt{\frac{\cos^2\theta_0}{n^2} - 1}} \approx \frac{\lambda}{2\pi}\frac{1}{\sqrt{\theta_c^2 - \theta_0^2}} \tag{A.24}$$

it is thus an essential requirement that the layer thickness is larger than 5-6 times d_p.

An example of the layer thickness importance is shown in fig. A.3. In the first case (left) the incident X-ray is completely reflected because the refracted wave has completely decayed in the nickel thickness. In the second case (right) the refracted wave had still an appreciable intensity at the end of the layer and developed a transmitted wave: the reflectivity of the layer is thus less than 1, although the reflection is under the critical angle.

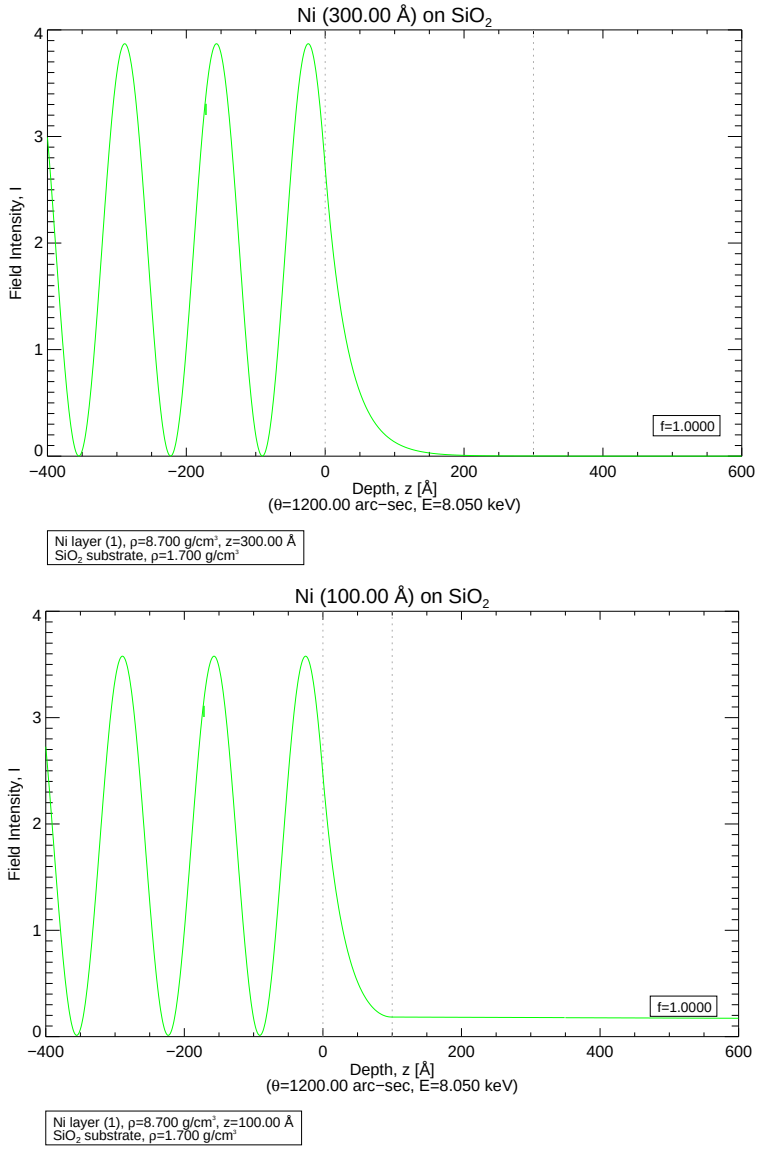

Figure A.3: IMD simulation of a 1.541$\mathring{A}$ s-polarized X-ray at $\theta_0 = 1200$" grazing incidence angle on a 30 nm thick (top) Nickel layer and a 10 nm thick (bottom). The ray incides from the left side and forms a standing wave with the reflected one. The refracted wave emerges on the right with constant amplitude.

Appendix B

Surface Analysis

In this appendix the basics of the surface characterization and analysis will be provided. For a more complete description, see e.g. bibl. [79].

B.1 Parameters of surface finishing characterization

The surface profile may be completely described by a function $z(x, y)$, which gives the height profile at every plane point (x, y). Even the best polished surface shows a "noisy" features when observed with a microscope, we can so assume the properties: $\langle z \rangle = 0$ and $\langle z^2 \rangle > 0$. If the surface is rectangular and L_1, L_2 sized (all definitions are to be intended with $L_1, L_2 \to \infty$ as the surface features are much smaller than the surface sides), this means

$$\langle z \rangle = \frac{1}{L_1 L_2} \int_0^{L_1} \int_0^{L_2} z(x, y)\, dxdy = 0 \qquad \langle z^2 \rangle = \frac{1}{L_1 L_2} \int_0^{L_1} \int_0^{L_2} z^2(x, y)\, dxdy \tag{B.1}$$

the second parameter is the surface variance and its root is called *surface rms* or σ. It is the most important parameter to describe the surface deviation from ideality. These formulas may be restricted to monodimensional profiles $z(x)$: in this case,

$$\langle z \rangle = \frac{1}{L_1} \int_{-\frac{L_1}{2}}^{+\frac{L_1}{2}} z(x)\, dx = 0 \qquad \sigma^2 = \frac{1}{L_1} \int_{-\frac{L_1}{2}}^{+\frac{L_1}{2}} z^2(x)\, dx \tag{B.2}$$

If we neglect the horizontal surface structure we can give also a statistic distribution of heights $p(z)dz$, expressing the likelihood of finding an height between z and $z + dz$: in this case the above formulas become:

$$\langle z \rangle = \int_{-\infty}^{+\infty} zp(z)\, dz = 0 \qquad \sigma^2 = \int_{-\infty}^{+\infty} z^2 p(z)\, dz \tag{B.3}$$

either in 1D or 2D case. The 3rd moment of the distribution is called *skewness* and it is an index of the asymmetry of the distribution (that is, an excess of peaks if positive, an excess of bumps if negative).

However, the σ parameter does not characterize completely a surface, as two surfaces with the same σ may differ very much in smoothness. The horizontal description is thus also very important: let us assume the surface is isotropic, so that all properties are the same in every direction. All the informations we need are so included in a 1D profile z(x). We define the *slope rms* m^2

$$m^2 = \frac{1}{L_1} \int_{-\frac{L_1}{2}}^{+\frac{L_1}{2}} \left(\frac{dz}{dx} \right)^2 dx \tag{B.4}$$

which returns the rms of the surface slope distribution. It easy to show that the parameter

$$c^2 = \frac{1}{L_1} \int_{-\frac{L_1}{2}}^{+\frac{L_1}{2}} \left(\frac{d^2 z}{dx^2} \right)^2 dx \tag{B.5}$$

is the square of *curvature rms*, that is, the squared rms of $\frac{1}{R_c}$ being R_c the local curvature radius[1].

The randomness of a surface is described by the *self-correlation function*: in the 1D case, given a surface section $z(x)$, its definition is

$$K(x) = \frac{1}{L_1} \int_{-\frac{L_1}{2}}^{+\frac{L_1}{2}} z(y) z(x-y)\, dy \tag{B.6}$$

where L_1 goes to infinity as usual. We see at once that K is an even function: $K(x) = K(-x)$. Unless the surface have periodic features (it occurs with polished surfaces by *diamond turning*), $K(x)$ peaks in $x = 0$ ($K(0) = \sigma^2$) and falls down to zero as the surface points at x are compared to more distant points at $x - y$. A *totally* random surface would return $K(x) = 0 \; \forall x \neq 0$: with real surfaces $K(x)$ does not fall abruptly to zero. The *width* of the $K(x)$ function (*correlation length* l_c) is thus an index of the surface randomness: its definition is not unique (see e.g. bibl. [111]) but in practical cases (i.e. when the PSD is a Lorentzian, see below) it approximates quite well an exponential function and we can use the 1/e criterion $K(l_c) = \frac{\sigma^2}{e}$. In practical cases, the measurement of the correlation length is difficult since it depends on the spectral range of sensitivity of the measurement (see sect. B.1.1, page 202).

By making the derivatives of K, after some integration by parts we recover the following expressions for the surface parameters in eq. B.2, eq. B.4, eq. B.5:

$$\sigma^2 = K(0) \qquad m^2 = -\left. \frac{d^2 K}{dx^2} \right|_{x=0} \qquad c^2 = \left. \frac{d^4 K}{dx^4} \right|_{x=0} \tag{B.7}$$

B.1.1 The Power Spectral Density

An equivalent way of describing the surface $z(x, y)$ is of course its *Fourier Transform*:

$$\hat{z}(f_x, f_y) = \frac{1}{L_1 L_2} \int_{-\frac{L_1}{2}}^{+\frac{L_1}{2}} \int_{-\frac{L_2}{2}}^{+\frac{L_2}{2}} e^{-2\pi i (f_x x + f_y y)} z(x, y)\, dx dy \tag{B.8}$$

where f_x, f_y are the *spatial frequencies* along x and y respectively: they go from $-\infty$ to $+\infty$ in ideal case[2]. The Fourier anti-transform is:

$$z(x, y) = L_1 L_2 \int_{-\infty}^{+\infty} \int_{-\infty}^{+\infty} e^{2\pi i (f_x x + f_y y)} \hat{z}(f_x, f_y)\, df_x df_y \tag{B.9}$$

substituting the last definition in the 2D definition of σ^2 and exchanging the integral order,

[1] The definition of curvature radius of a plane curve $z(x)$ is

$$R_c(x) = [1 + z'(x)^2]^{-3/2} |z''(x)|^{-1}$$

if the surface is smooth the first derivative can be neglected with respect to 1.

[2] The classical factor $(2\pi)^{-1}$ here does not appear since the trasnform is performed in frequencies domain f instead of pulsations $2\pi f$. The factor $(L_1 L_2)^{-1}$ is used to make z and $\hat{z}$ homogeneous. A factor $(L_1 L_2)$ will thus appear in the reverse trasform.

$$\begin{aligned}\sigma^2 &= L_1L_2\int_{-\infty}^{+\infty} d^2\underline{f}\int_{-\infty}^{+\infty} d^2\underline{f}'\,\hat{z}(\underline{f})\hat{z}^*(\underline{f}')\int_{-\frac{L_1}{2}}^{+\frac{L_1}{2}} dx\,e^{2\pi i(f_x-f'_x)x}\int_{-\frac{L_2}{2}}^{+\frac{L_2}{2}} dy\,e^{2\pi i(f_y-f'_y)y} = \\ &= L_1L_2\int_{-\infty}^{+\infty} d^2\underline{f}\int_{-\infty}^{+\infty} d^2\underline{f}'\,\hat{z}(\underline{f})\hat{z}^*(\underline{f}')\delta(f_x-f'_x)\delta(f_y-f'_y) = \\ &= \int_{-\infty}^{+\infty} df_x\int_{-\infty}^{+\infty} df_y\,L_1L_2|\hat{z}(f_x,f_y)|^2 \end{aligned} \tag{B.10}$$

as expected from the Parseval's identity. The integrand in the last equation

$$P(f_x,f_y) = L_1L_2|\hat{z}(f_x,f_y)|^2 \tag{B.11}$$

is called the *Power Spectral Density* or PSD. It represents the intensity of the spectral components between (f_x,f_y) and (f_x+df_x,f_y+df_y) and it is of course real and even function of the spatial frequencies.

The PSD is not reversible, in the sense that its knowledge does not allow the *exact* surface reconstruction because the squared module operation has suppressed the informations on the relative phases of the spectral components. Nevertheless, the PSD provides a wide surface description (see bibl. [32], bibl. [82]) and it is a basic tool in studying the physical behaviour of the surface (e.g. the X-ray scattering: sect 5.3.1).

By integrating P on f_x or f_y, recalling the definition of $\hat{z}$, after some algebra

$$\int_{-\infty}^{+\infty} df_x P(f_x,f_y) = \frac{1}{L_1}\int_{-\infty}^{+\infty} dx\frac{1}{L_2}\left|\int_{-\infty}^{+\infty} z(x,y)e^{-2\pi i f_y y}\,dy\right|^2 = P(f_y) \tag{B.12}$$

$$\int_{-\infty}^{+\infty} df_y P(f_x,f_y) = \frac{1}{L_2}\int_{-\infty}^{+\infty} dy\frac{1}{L_1}\left|\int_{-\infty}^{+\infty} z(x,y)e^{-2\pi i f_x x}\,dx\right|^2 = P(f_x) \tag{B.13}$$

$P(f_x)$ is a *monodimensional PSD*, and it is calculated by extracting a profile at a fixed y, computing the $PSD(f_x,y)$ and averaging all the PSD on y. The same for $P(f_y)$: generally $P(f_x)\neq P(f_y)$, and this difference is an index of the surface anisotropy. We can state, collecting the results:

$$\sigma^2 = \int_{-\infty}^{+\infty} df_x\int_{-\infty}^{+\infty} df_y\,P(f_x,f_y) = \int_{-\infty}^{+\infty} P(f_x)\,df_x = \int_{-\infty}^{+\infty} P(f_y)\,df_y \tag{B.14}$$

it easy to see that $P(f_x,f_y)$ has the dimensions of the fourth power of a length (usually nm^4) whereas $P(f_x)$ and $P(f_y)$ is a length at the third power (usually nm^3).

In most cases the X-rays reflecting surfaces are *isotropic*, unless they are specially grinded (e.g. diffraction gratings), thus P does not depend on f_x or f_y separately, but only on the frequency squared module $f^2 = f_x^2+f_y^2$. The isotropy can be checked by substituting $P(f_x,f_y) = P(f\cos\theta_f, f\sin\theta_f)$: in case of isotrophy, the dependence on θ_f should vanish, and the PSD becomes rotation-invariant.

In case of surface isotrophy, we can compute the monodimensional PSD by integrating either on f_x or f_y suppressing the subscript x or y as $P(f_x) = P(f_y)$, and the surface may thus be characterized simply by a monodimensional PSD $P(f)$, computed from any monodimensional profile, e.g. $z(x) = z(x,y_0)$. Note that, in this case, the 2D PSD can also be recovered from the 1D PSD (see bibl. [79]). In the following, we restrict ourselves to isotropic surfaces.

It is easy to show that (*Wiener-Khintchine theorem*) the PSD is the Fourier transform of the self-correlation function $K(x)$ (and vice-versa, as both are real and even):

$$K(x) = \int_{-\infty}^{+\infty} P(f)e^{2\pi i f x}\,df \tag{B.15}$$

for instance, a random surface has $K(x) = \delta(x)$ and P(f) is constant (white spectrum); taking the derivatives of $K(x)$ at $x = 0$ in the eq. B.7 we obtain the practical formulas:

$$\sigma^2 = \int_{-\infty}^{+\infty} P(f)\, df \qquad m^2 = \int_{-\infty}^{+\infty} (2\pi f)^2 P(f)\, df \qquad c^2 = \int_{-\infty}^{+\infty} (2\pi f)^4 P(f) df \tag{B.16}$$

that is, they are the *three first even moments of the PSD* (the odd moments are obviously zero). In particular,

$$m = 2\pi \left(\int_{-\infty}^{+\infty} f^2 P(f)\, df \right)^{1/2} = 2\pi\sigma \frac{\left(\int_{-\infty}^{+\infty} \frac{1}{l^4} P(l)\, dl \right)^{1/2}}{\left(\int_{-\infty}^{+\infty} \frac{1}{l^2} P(l)\, dl \right)^{1/2}} \tag{B.17}$$

in the last equality we have used the identity

$$\sigma^2 = \int_{-\infty}^{+\infty} P(f)\, df = \int_{-\infty}^{+\infty} P(l)\, \frac{dl}{l^2} \tag{B.18}$$

the last root in the eq. B.17 is the root mean square of $\frac{1}{l}$, and its inverse l_c is the mean distance between two adjacent profile peaks: it is a good approximation of the correlation length, thus we may write the eq. B.17 as

$$l_c = \frac{2\pi\sigma}{m} \tag{B.19}$$

often used to measure the correlation length from profile data. This measurement can be, however, considered realistic *only provided that it is independent on the spatial frequency window* of the instrument used to perform the measurement. Extensions of these formulas to the 2D case are straightforward.

B.1.2 Discrete surface sampling

The exposed results suppose always to have a continuous profile z(x): real data are, on the contrary, never continuous and infinite but finite and sampled at discrete intervals. This gives severe limits on the knowledge of the surface power spectrum. Suppose a profile $z(x)$ (but the extension to the 2D case is straightforward) to be sampled at intervals d ant its length to be $L = Nd$, N being the number of sampled points. We can know the profile in the points $x_n = nd$, $n = 0, \cdots, N-1$, corresponding to $z_n = z(x_n)$: the minimum frequency we can compute is the one we can observe one period, that is $f_m = L^{-1}$. The maximum frequency has instead to be $(2d)^{-1}$, corresponding to the maximum distance to a neighbouring maximum and minimum. Both limits are in agreement with the uncertainty principle: we can so write that the allowed frequencies for a set of N sampled points at rate d is

$$\frac{1}{Nd} < |f| < \frac{1}{2d} \tag{B.20}$$

called *Nyquist criterion.*

The sampled points are the true profile z(x) times the *sampling function* $S(x)$

$$S(x) = S_1(x) S_2(x) \tag{B.21}$$

where

$$S_1(x) = \lim_{N\to\infty} \sum_{-N/2}^{+N/2} \delta\left(\frac{x}{d} - n \right) \tag{B.22}$$

$$S_2(x) = \begin{cases} 1 & -\frac{L}{2} < x < \frac{L}{2} \\ 0 & \text{elsewhere} \end{cases} \tag{B.23}$$

the Fourier Transform of $z(x_n) = z(x)S(x)$ must then be *the convolution of the spectrum of the factors*

$$\hat{z_n} = \hat{z}(f) \otimes \hat{S}(f) = \hat{z}(f) \otimes \hat{S}_1(f) \otimes \hat{S}_2(f) \tag{B.24}$$

the $\hat{z}(f)$ is the theoretical profile spectrum, so we have to compute $\hat{S}(f)$. We can compute the two transforms (and neglecting phase factors which can be ruled out by an appropriate choice of the origin),

$$\begin{aligned} \hat{S}_1 &= \lim_{N\to\infty} \int_{-Nd/2}^{+Nd/2} dx\, e^{-2\pi i f x} S_1(x) = \lim_{N\to\infty} \sum_{n=-N/2}^{+N/2} e^{-2\pi i f n d} d = \lim_{N\to\infty} \frac{\sin(\pi N f d)}{\sin(\pi f d)} d \\ \hat{S}_2 &= \int_{-\infty}^{+\infty} dx\, e^{-2\pi i f x} S_2(x) = \int_{-L/2}^{+L/2} dx\, e^{-2\pi i f x} = L \frac{\sin(\pi f L)}{\pi f L} \end{aligned} \tag{B.25}$$

in particular, for N very large

$$\hat{S}_1 = d \sum_{k=-\infty}^{+\infty} \delta(fd - k) = \sum_{k=-\infty}^{+\infty} \delta\left(f - \frac{k}{d}\right) \tag{B.26}$$

This in turn implies[3]

$$\hat{S}(f) = \hat{S}_1 \otimes \hat{S}_2 = L \sum_{-\infty}^{+\infty} sinc\left[\pi L \left(f - \frac{k}{d}\right)\right] \tag{B.27}$$

We can now evaluate the effect of sampling:

- the spectrum of a *limited* sampled profile is *discrete*, as we can know the frequencies only with an uncertainty equal to the width of the function $\hat{S}_2(f)$ which is convoluted with the true spectrum $\hat{z}(f)$: this width is $L^{-1} = (Nd)^{-1}$, thus for the exposed limits in the eq. B.20 we can evaluate the spectrum in the set of frequencies:
$$f_k = \pm\frac{1}{L}, \pm\frac{2}{L}, \ldots, \pm\frac{N}{2L} \tag{B.28}$$
As the spectrum computed at negative frequencies simply mimics the positive part but the spectrum is complex, we will have N real numbers for sampling which return, without information losses, N/2 complex numbers: that is, N real numbers again for the spectrum; from the mathematical viewpoint, we can observe that since the profile is limited, a Fourier series is to be used instead of a Fourier integral;

- the spectrum of a *discrete* sampled profile is also *periodic*: conversely, periodic signals have a discrete spectrum. This means that every true spectral features will be *repeated* at intervals of d^{-1}: this phenomenon is called *aliasing* and the repeated features are called *ghosts*: there is so a more profound reason to stop the spectrum at the Nyquist frequency $(2d)^{-1}$: the range $[-(2d)^{-1}; +(2d)^{-1}]$ is the largest one which is included between two adjacent peaks of $\hat{S}(f)$.

However, the choice of stopping the spectrum at the Nyquist frequency does not guarantee the absence of ghosts in our spectrum $\hat{z_n}(f)$, because the peaks of $\hat{S}(f)$ have a finite width and could always reflect some features in our bandwidth. The reduction of the aliasing is performed by *binning* instead of sampling: we substitute the every punctual sampling $z(x_n)$ with M points uniformly distributed between x_{n-1} and x_n,

$$z(x_{n,m}) = \frac{z(x_n)}{M} \tag{B.29}$$

[3]The result is a formalization of the diffraction pattern from an ideal diffraction grating.

this "histogram" keeps the same information amount (supposing the signal to be regular) but increases the sampling rate by a M-fold factor, thus the aliases now are far apart of the same factor. Taking M large enough we can be sure that there is no reflection in the measured spectrum: this method is called *anti-aliasing filter* and it is included in all the surface analysis routines.

There is not very much to do, instead, to increase the spectral resolution $\Delta f = L^{-1}$, except of course increasing the sample size. The spectral features smaller than Δf will be hidden and the spectral slopes will be always smoother than the real ones. The shape of $\hat{S}_2(f)$ may be modeled by changing the top-hat window function, by weighting the measured profile e.g. with a gaussian (which guarantees the minimum uncertainty): this method, however, reduces the information input available from the profile.

Supposing $L \gg d$ (like in practical cases), the eq. B.27 becomes for almost all frequencies a sum of deltas and the PSD definition given in the previous section may be easily extended to the case of a discrete sampling, remembering that $P(f) = L|\hat{z}(f) \otimes \hat{S}(f)|^2$:

$$P(f_k) = \frac{1}{L}\left|\int_0^L z(x)[e^{-2\pi i f x} \otimes \hat{S}(f)]dx\right|^2 = \frac{1}{L}\left|\int_0^L z_n e^{-2\pi i f_k x}dx\right|^2 = \frac{1}{\Delta f}\left|\frac{1}{N}\sum_{n=0}^{N} z_n e^{-2\pi i f_k x_n}\right|^2 \tag{B.30}$$

where the f_k are provided by the eq. B.28. Hence, as $x_n = nL/N$,

$$P(f_k) = \frac{L}{N^2}\left|\sum_{n=0}^{N} z_n e^{-2\pi i k \frac{n}{N}}\right|^2 \tag{B.31}$$

the dimensions are of course the same as before (nm^3): the obtained result is nothing else than the squared module of the k_{th} Fourier coefficient divided by the spatial frequency bin $1/L$. Using the discrete PSD definition as above, we can express the surface parameters as functions of the sampled profile (provided that $\langle z_n \rangle = 0$):

- The σ^2 roughness:

$$\sigma^2 = \frac{1}{N}\sum_{n=0}^{N} z_n^2 = \sum_{k=-N/2}^{+N/2} P(f_k)\Delta f \tag{B.32}$$

- The m^2 slope rms:

$$m^2 = \frac{1}{N}\sum_{n=1}^{N}\left(\frac{z_n - z_{n-1}}{x_n - x_{n-1}}\right)^2 = \sum_{k=-N/2}^{+N/2} (2\pi f_k)^2 P(f_k)\Delta f \tag{B.33}$$

- The self-correlation function K:

$$K(x_n) = \frac{1}{N}\sum_{k} z_{n-k}\, z_k = \sum_{k=-N/2}^{+N/2} e^{2\pi i f_k} P(f_k)\Delta f \tag{B.34}$$

it is very important to observe that these parameters depend very strongly on the sensitivity frequency window $[f_m, f_M]$: that is, *their value is not unique but the frequency band is always to be specified.* A measurement on the same sample with an instrument with different sensitivity bands could return completely different parameters: PSD data from different instruments are always, instead, comparable. On the other side, the surface parameters of specific interest must very seldom cover a very wide band: e.g. the scattering roughness parameter in X-rays grazing reflection has a significance only in the band $100 \div 0.01\ \mu m$, and we can often neglect the PSD out of these limits.

B.2 PSD models

Many surface power spectra have shapes that may be easily fitted with a simple function. The most used model is (see bibl. [79])the ABC or *K-correlation* model and can be written:

$$P(f) = \frac{A}{[1 + (Bf)^2]^{C/2}} \tag{B.35}$$

its shape is typical of low-pass filters. For $f \ll 1/B$ the spectrum is quite constant, whereas for higher frequencies the spectrum falls steeply. The "knee" is determined by the B value, and in the special case $C = 2$, B is exactly equal to $2\pi l_c$, where l_c is the e^{-1} correlation length: in this case the power spectrum is said to be *Lorentzian*. The parameter A determines the normalization of the whole spectrum and the parameter C the rate of falloff of the power spectrum at high frequencies.

In a log-log plot, the curve may be approximated by two straight lines which are the asymptotes at low and high frequency: they have respectively a constant value and a constant slope, so their intersection (see fig. B.1) determines the knee frequency $f' = B^{-1}$. In practice, f' is very low, often very near to the sensitivity limit of the instrument used for the measurement, so that it cannot be located with sufficient precision. Usually most PSD measurement are performed in the power-law region, so that the use of the eq. B.19 would return a non-realistic value, often located near to the maximum spatial wavelength of the instrument sensitivity window, but

$$\frac{2\pi\sigma}{m} \leq l_c \tag{B.36}$$

the equality holds *only if the knee frequency is included in the instrument spatial frequency window.*

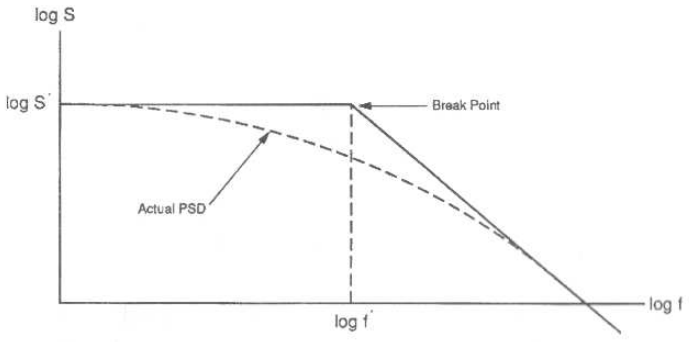

Figure B.1: A typical Lorentzian spectrum. The knee frequency may be located at the intersection of the asymptotes (from bibl. [79]).

The case of a Lorentzian spectrum corresponds exactly to an exponential self-correlation function:

$$K(x) = \sigma^2 e^{-\frac{|x|}{l_c}} \tag{B.37}$$

to prove it, we compute its Fourier transform: by symmetry we can sum the integrals on negative and positive x,

$$P(f) = \int_{-\infty}^{+\infty} e^{2\pi i f x} K(x)\, dx = 2\sigma^2 Re \int_0^{+\infty} e^{2\pi i f x - \frac{x}{l_c}} dx = 2\sigma^2 Re \frac{l_c}{2\pi l_c i f - 1} = \frac{2\sigma^2 l_c}{1 + (2\pi l_c f)^2} \tag{B.38}$$

then, $B = 2\pi l_c = 1/f'$ that is

$$l_c = \frac{1}{2\pi f'} \qquad \sigma = \sqrt{\pi f' P(0)} \tag{B.39}$$

this result is consistent with

$$\int_{-\infty}^{+\infty} P(f)\, df = 2\sigma^2 l_c \int_{-\infty}^{+\infty} \frac{1}{1+(2\pi f l_c)^2} df = \frac{\sigma^2}{\pi} \arctan(2\pi l_c f)|_{-\infty}^{+\infty} = \sigma^2 \tag{B.40}$$

In practice the low-frequency limit is difficult to be explored: in most measurements, in fact, the finished surfaces show a inverse power-law PSD (see bibl. [82]) which is the high-frequency limit of a K-correlation model:

$$P(f) = \frac{K_n}{f^n} \tag{B.41}$$

with $n = C$, $1 < n < 3$ and K_n constant. The apparent divergence at $f = 0$ is avoided substituting the correct form for low frequencies, while $n > 1$ guarantees the finiteness of the integral at high frequencies. This kind of surface is called *fractal*: the cases n=1,2,3 are called *extreme*, *Brownian*, *marginal*, respectively. The fractals are typical structures of nature and are met in almost all the field of physics: in particular, the power spectrum in eq. B.41 with $n = 2$ shows the main fractal feature, the *scale invariance*; in fact, it becomes

$$P(f) = K_2 l^2 \tag{B.42}$$

meaning that the amplitude of perturbations of length l scales exactly with l^1, i.e. it is scale-invariant.

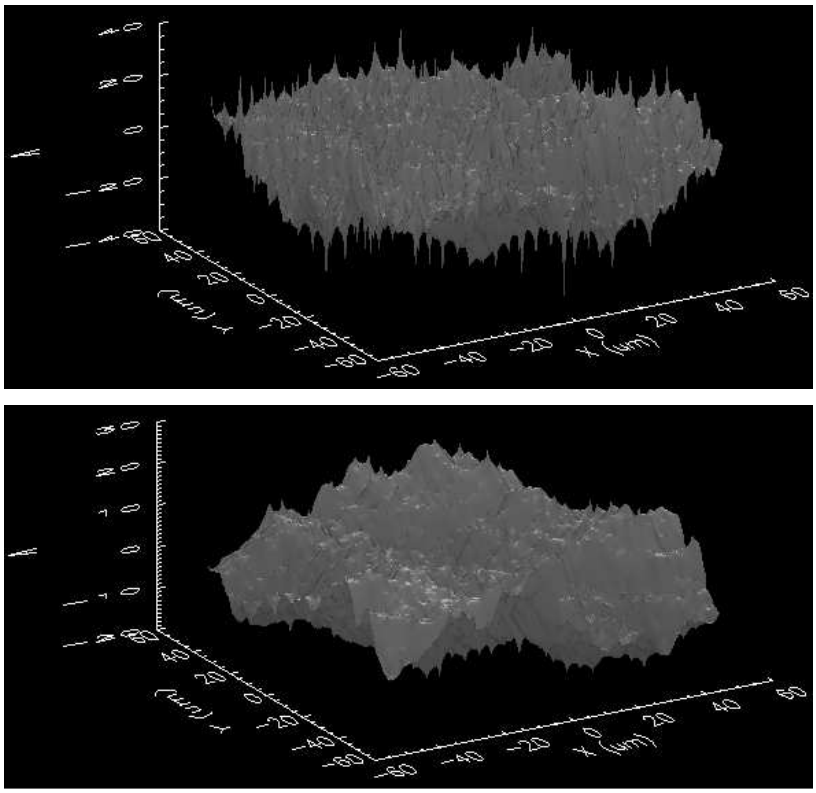

Figure B.2: Two simulations (IDL routine) of $100\mu m \times 100\mu m$ wide surfaces with the same $\sigma = 1$ nm, but having 1D PSD with spectral indexes n = 2.2 (top) and n = 3.0 (bottom). Note in the first case the larger content in high frequencies. The m parameter equals 108" and 27" respectively.

Appendix C

X-ray Scattering from rough surfaces: an interpretation

C.1 Scattering from a single boundary

In the following pages we will derive a formula that recovers a known result, the surface PSD-X-ray scattering link, assuming that it results from the superposition of the elementary dipole elastic scattering from the atomic electrons. This interpretation leads to the grazing-incidence limit of the Fresnel equations.

Let us assume to have a sample with volume V and a rectangular, reflecting surface A (L_1, L_2 sized). Let us have a reference frame with the x axis oriented as L_1 and the y axis as L_2. Radiation with wavelength λ incides in the xz plane forming with the negative x semiaxis an angle θ_i, and is scattered at the angles (θ_s, ϕ_s) as in fig. 5.13.

We suppose the radiation to be uniform and extended more than the surface, so that all the surface is covered by the incident radiation flux S. If the incident field amplitude is E_i,

$$S = \frac{c}{8\pi} E_i^2 \tag{C.1}$$

and the collected intensity by the surface is thus:

$$I_0 = \frac{c}{8\pi} E_i^2 L_1 L_2 \sin\theta_i \tag{C.2}$$

the cause of microscopic scattering of photons are the electrons. Each electron at coordinates $\underline{r} = (x, y, z)$ scatters the electric field $\underline{E}(\underline{r})$ in the direction (θ_s, ϕ_s) through an area da (at distance R from the surface) with intensity $S_s da = S_s R^2 d\Omega$, that is, per solid angle unity

$$d(E_s^2) = \frac{d\sigma_s}{d\Omega}(\theta_s, \theta_i, \phi_s) E(\underline{r})^2 d\Omega \tag{C.3}$$

the $\frac{d\sigma_s}{d\Omega}$ represents the differential electronic cross-section *evaluated at the scattering angles* (θ_s, ϕ_s) *for an incident ray at* θ_i. Of course it depends on the polarization: for sake of simplicity, we suppose the wave to be p-polarized (i.e. in the incidence plane). Each scattered wave at $\underline{r}$ takes its phase shift $\xi(\underline{r})$. As there are $\mathcal{N}$ free electrons per volume unit, the scattered electric field amplitude E_t is the integral of the contribution from all the volume elements of the volume V:

$$E_t = \int_V \mathcal{N} E_s(\underline{r}) e^{i\xi(\underline{r})}\, d^3\underline{r} \tag{C.4}$$

The scattered intensity I by the surface into the solid angle $d\Omega$ is thus

$$dI = \frac{c}{8\pi}|E_t|^2 R^2 d\Omega \tag{C.5}$$

by substituting the above relationships in the eq. C.5

$$\frac{dI}{d\Omega} = \frac{c}{8\pi}\frac{d\sigma_s}{d\Omega}\mathcal{N}^2 \left| \int_V E(\underline{r}) e^{i\xi(\underline{r})}\, d^3\underline{r} \right|^2 \tag{C.6}$$

the same equation may be obtained using a s-polarized ray: as the above formula depends only on the squared amplitude of the electric field, we can sum the p and s contribution and we obtain the eq. C.6 again, *for an unpolarized wave*. There $\frac{dI}{d\Omega}$ represents the total scattered power distribution and $\frac{d\sigma_s}{d\Omega}$ is the total electron scattering cross section for an incident unpolarized wave. The polarization of the scattered wave is completely embedded in the dependence of σ_s on the scattering angles (see below, eq. C.20).

The equation C.6 shows how the scattering pattern (left-hand side) depends on the measurable quantities, and it is exactly valid only for incidence angles larger than the critical angle. The differential electron scattering cross-section depends on the adopted theory and approximations (Rayleigh, Thomson, Compton,...).

The integral in the $||$ brackets depends instead on topographical properties of the surface A. To prove it, observe that the direction vectors of the incident and scattered waves $\underline{u_i}$, $\underline{u_s}$ are

$$\underline{u_i} = (\cos\theta_i, 0, -\sin\theta_i) \quad \underline{u_s} = (\cos\theta_s\cos\phi_s, \cos\theta_s\sin\phi_s, \sin\theta_s) \tag{C.7}$$

Now, let the surface profile be $z(x, y)$. The phase delay of the scattered wave at the coordinates $\underline{r} = (x, y, z)$ is thus:

$$\xi(\underline{r}) = \frac{2\pi}{\lambda}(\underline{u_s} - \underline{u_i}) \cdot \underline{r} \tag{C.8}$$

and if we define:

$$l_x = \frac{\lambda}{\cos\theta_s\cos\phi_s - \cos\theta_i} \quad l_y = \frac{\lambda}{\cos\theta_s\sin\phi_s} \quad \alpha = 2\pi\frac{\sin\theta_s + \sin\theta_i}{\lambda} \tag{C.9}$$

the integral may be written as:

$$\int_V E(\underline{r}) e^{-i\xi(\underline{r})}\, d^3\underline{r} = \int_A dxdy\, e^{-i\frac{2\pi}{l_x}x}\, e^{-i\frac{2\pi}{l_y}y} \int_{-\infty}^{z(x,y)} dz\, E(x, y, z) e^{-i\alpha z} \tag{C.10}$$

because the scattering material is extended up to the upper surface, described by $z(x, y)$. Now, $E(z(x, y))$ is the refracted ray amplitude at the surface. If we are observing much above the critical angle the reflection is low and we can approximate it with E_i (eq. C.2). On the other side, because of absorption, the ray does not propagate to infinity and we can set $E(x, y-\infty) = 0$. However, the E amplitude very slowly varies with z and we can consider it constant in comparison to the exponential factor[1]. The z integral is thus easily solved: an area integral remains,

$$\int_V E(\underline{r}) e^{-i\xi(\underline{r})}\, d^3\underline{r} = -\frac{E_i}{i\alpha}\int_A e^{-i\frac{2\pi}{l_x}x}\, e^{-i\frac{2\pi}{l_y}y} e^{-i\alpha z(x,y)}\, dxdy \tag{C.11}$$

this is the 2D Fourier transform of $e^{-i\alpha z}$ in l_x and l_y, the surface *spatial wavelengths*; they are related to the scattering angles as in the eq. C.9. Their reciprocal are the *spatial frequencies*, $f_x = l_x^{-1}$, $f_y = l_y^{-1}$. The zero frequency is in correspondence of the reflected and transmitted ray ($\theta_s = \pm\theta_i$, $\phi_s = 0$) and the maximum

[1] We have, in practice, constructed the *vibration curve* at every (x,y)

frequency is $2/\lambda$ in back-scattering ($\theta_s = \pi - \theta_i$, $\phi_s = 0$) this corresponds to the impossibility of measuring surface details less than the wavelength in use.

To simplify the notation, let us say $\underline{x} = (x, y)$ and $\underline{f} = (f_x, f_y)$:

$$\int_V E(\underline{r}) e^{-i\xi(\underline{r})}\, d^3\underline{r} = -\frac{E_i}{i\alpha}\int_A e^{-i\xi(\underline{x})}\, d^2\underline{x} = -\frac{E_i}{i\alpha}\int_A e^{-2\pi i \underline{f}\cdot\underline{x}}\, e^{-i\alpha z(\underline{x})}\, d^2\underline{x} \tag{C.12}$$

substituting the eq. C.12 in the eq. C.6 and considering the eq. C.2, we arrive to the result

$$\frac{1}{I_0}\frac{dI}{d\Omega} = \frac{d\sigma_s}{d\Omega}\frac{\mathcal{N}^2}{\alpha^2 L_1 L_2 \sin\theta_i}\left|\int_A e^{-2\pi i \underline{f}\cdot\underline{x}} e^{-i\alpha z(\underline{x})}\, d^2\underline{x}\right|^2 \tag{C.13}$$

Let now suppose that, as usually, the smooth-surface limit is met: $2\pi z \sin\theta_{i,s} \ll \lambda$, meaning $\alpha z \ll 1$: the exponential in the eq. C.10 may be developed in series: $e^{-i\alpha z} \simeq 1 - i\alpha z + \cdots$.

Zero-order approximation At first, we approximate $e^{i\alpha z} \simeq 1$ (corresponding to an ideally smooth surface), and the squared module of the area Fourier integral in eq. C.13 is reduced to:

$$\begin{aligned}\left|\int_A e^{-i\xi(\underline{r})}\, d^3\underline{r}\right|^2 &\simeq \left|\int_{-\frac{L_1}{2}}^{+\frac{L_1}{2}} dx\, e^{-2\pi i f_x x}\int_{-\frac{L_2}{2}}^{+\frac{L_2}{2}} dy\, e^{-2\pi i f_y y}\right|^2 = \\ &= L_1^2\frac{\sin^2(\pi f_x L_1)}{(\pi f_x L_1)^2} L_2^2\frac{\sin^2(\pi f_y L_2)}{(\pi f_y L_2)^2}\end{aligned} \tag{C.14}$$

this is the usual diffraction pattern from a rectangular aperture. As $L_1 \gg l_x$ and $L_2 \gg l_y$, we can neglect the diffraction effect by passing to limit $L_1 \to \infty$, $L_2 \to \infty$, the normalized $sinc^2$ functions become *Dirac delta functions*:

$$L_1\frac{\sin^2(\pi f_x L_1)}{(\pi f_x L_1)^2} \overset{L_1\to\infty}{\longrightarrow} \delta(f_x) \tag{C.15}$$

and similarly for y: substituting in the eq. C.13,

$$\frac{1}{I_0}\frac{dI_r^{(0)}}{d\Omega} = \frac{d\sigma_s}{d\Omega}\frac{\mathcal{N}^2}{\alpha^2\sin\theta_i}\delta(f_x)\delta(f_y) \tag{C.16}$$

the eq. C.16 shows that (as expected) at the zero-order (no roughness) the scattered brightness collapses in the reflected ray in the specular direction. The subscript r stands for "reflected" to stress that it is a reflection term. The integrated intensity distribution reduces to:

$$I_r^{(0)} = I_0\int_{4\pi}\frac{d\sigma_s}{d\Omega}\frac{\mathcal{N}^2}{\alpha^2\sin\theta_i}\delta(f_x)\delta(f_y)\cos\theta_s d\phi_s d\theta_s \tag{C.17}$$

the delta integral may be calculated by replacing the angular variables on the whole sphere with (f_x, f_y), returning (using the Jacobian $|J| = \lambda^{-2}\sin\theta_s\cos\theta_s$)

$$I_r^{(0)} = I_0\frac{\mathcal{N}^2\lambda^2}{\sin\theta_i}\int_{-\frac{2}{\lambda}}^{+\frac{2}{\lambda}}\frac{d\sigma_s}{d\Omega}\frac{\delta(f_x)\delta(f_y)}{\alpha^2\sin\theta_s}df_x df_y \tag{C.18}$$

as we use X-rays ($\lambda \approx 1\mathring{A}$) and only the lowest frequencies give a contribution to the integral, the integration limits can be approximated as $\pm\infty$.

Recalling the definition of α, the integral is solved simply evaluating the integrand at zero frequencies and we obtain the reflected ray $I_r^{(0)}$: dividing it by the incident intensity we can provide for the reflectivity $R_F = I_r^{(0)}/I_0$ the expression:

$$R_F = \left(\frac{\lambda^2 \mathcal{N}}{4\pi \sin^2 \theta_i} \right)^2 \left. \frac{d\sigma_s}{d\Omega} \right|_{(\theta_i, 0)} \tag{C.19}$$

This is exactly the *Fresnel reflectivity* as in appendix A.1 in grazing-incidence approximation (eq. A.20 and A.10) with $\theta_i > \theta_c$, provided that the scattering cross-section is identified as the *Thomson cross-section* σ_T for unpolarized radiation:

$$\frac{d\sigma_T}{d\Omega} = \frac{1}{2} r_e^2 (\underbrace{1}_{s-pol.} + \underbrace{\cos^2(2\theta_i)}_{p-pol.}) \overset{\theta_i \to 0}{\simeq} r_e^2 \tag{C.20}$$

being $r_e = \frac{e^2}{m_e c^2}$ the classical electron radius and $2\theta_i$ the scattering angle in the specular direction. This interpretation of the reflection process led us to the same results of the electromagnetic theory in the considered approximations. In particular, we have obtained the approximate form of the Fresnel equation only because we have neglected the effect of the reflected field on the vibrations of the electrons: this effect is very important because in the assumed model the reflected ray would go to infinity for $\theta_i \to 0$; however, as the field of the reflected ray becomes stronger, it changes the electron oscillation and it tends to cancel the refracted ray, so that we can no longer assume a slow decrease of the field in the material: the divergence of the eq. C.19 is thus avoided.

We can so physically understand why a critical angle *exists*: the scattered waves superpose to form the reflected ray but their contribution is cancelled if the refracted ray has a significant intensity at a depth of some $d_i = \frac{\lambda}{2 \sin \theta_i}$. When θ_i becomes very small, a large number of scatterers is found at depth less than d_i; they will so have almost the same phase in superficial regions and almost all the incident energy will be reflected. This condition is favoured by a high concentration of electrons on the surface, as it is the case of with dense materials.

First and second order approximation We include now the term $-i\alpha z$. The squared module of the Fourier area integral in eq. C.12 becomes:

$$\begin{aligned} \left| \int_A d^2\underline{x}\, e^{-i\xi(\underline{x})} \right|^2 &\simeq \left| \int_A d^2\underline{x}\, e^{-2\pi i(f_x x + f_y y)} (1 - i\alpha z) \right|^2 = \\ = \int_{A'} d^2\underline{x}'\, e^{2\pi i \underline{f}\cdot\underline{x}'} \int_A d^2\underline{x}\, e^{-2\pi i \underline{f}\cdot\underline{x}} &- i\alpha \int_{A'} d^2\underline{x}'\, e^{2\pi i \underline{f}\cdot\underline{x}'} \int_A d^2\underline{x}\, e^{-2\pi i \underline{f}\cdot\underline{x}} z(\underline{x}) + \\ + i\alpha \int_A d^2\underline{x}\, e^{-2\pi i \underline{f}\cdot\underline{x}} \int_{A'} d^2\underline{x}'\, e^{2\pi i \underline{f}\cdot\underline{x}'} z(\underline{x}') &+ \alpha^2 \int_A d^2\underline{x}\, e^{-2\pi i \underline{f}\cdot\underline{x}} z(\underline{x}) \int_{A'} d^2\underline{x}'\, e^{2\pi i \underline{f}\cdot\underline{x}'} z(\underline{x}') \end{aligned} \tag{C.21}$$

now L_1 and L_2 go to infinity, and the second and the third integral reduce to $\hat{z}(f_x, f_y)\delta(f_x)\delta(f_y)$. The integration on the solid angle reduces these terms to $i\alpha\hat{z}(0,0) \propto \langle z \rangle = 0$ and so they vanish[2]: the fourth integral is non-zero as it tends to the power spectrum of $z(x,y)$, $|\hat{z}(f_x, f_y)|^2$, multiplied by the factor$\alpha^2 L_1 L_2$.

[2] A different choice of the average surface value would result in an unessential phase factor.

As the terms in α have vanished, the first perturbative non-zero term is quadratic: in the assumed approximation we must so take into account the further term of the exponential development $-\alpha^2 z^2/2$, and by collecting the products we see that the first non-zero terms are those in α^0 and α^2:

$$\left|\int_A d^2\underline{x}\, e^{-i\xi(\underline{x})}\right|^2 \simeq \left|\int_A d^2\underline{x}\, e^{-2\pi i \underline{f}\cdot\underline{x}}\right|^2 + \alpha^2\left|\int_A d^2\underline{x}\, e^{-2\pi i \underline{f}\cdot\underline{x}} z(\underline{x})\right|^2 + \\ -\alpha^2 Re\left(\int_{A'} d^2\underline{x}'\, e^{-2\pi i \underline{f}\cdot\underline{x}'}\int_A d^2\underline{x}\, e^{2\pi i \underline{f}\cdot\underline{x}} z^2(\underline{x})\right) \tag{C.22}$$

the first integral returns the already calculated specular reflected ray. The second integral corresponds to a scattering term, and will be calculated below. As L_1 and L_2 go to infinity, the third integral reduces to

$$-\alpha^2\delta(f_x)\delta(f_y)\, Re\left(\int_A d^2\underline{x}\, e^{2\pi i \underline{f}\cdot\underline{x}} z^2(\underline{x})\right) \tag{C.23}$$

this is another delta-like term. We may then add it to the delta in the eq. C.16,

$$\frac{1}{I_0}\frac{dI_r}{d\Omega} = \frac{d\sigma_T}{d\Omega}\frac{\mathcal{N}^2}{\alpha^2\sin\theta_i}\delta(f_x)\delta(f_y)\left[1 - \frac{\alpha^2}{L_1L_2}Re\left(\int_A d^2\underline{x}\, e^{2\pi i \underline{f}\cdot\underline{x}} z^2(\underline{x})\right)\right] \tag{C.24}$$

the first effect of roughness is a reduction of reflectivity in the specular direction. If we integrate on angles and change the variables as above, we can exchange the frequency and the surface integrals: the Fourier kernel is hence evaluated by the delta functions at zero frequencies, and

$$I_r = I_0\frac{\lambda^4\mathcal{N}^2}{16\pi^2\sin^4\theta_i}\left.\frac{d\sigma_T}{d\Omega}\right|_{(\theta_i,0)}\left[1 - \frac{(2k\sin\theta_i)^2}{L_1L_2}\int_A d^2\underline{x}\, z^2(\underline{x})\right] = I_0 R_F(\theta_i)[1 - (2k\sin\theta_i\sigma)^2] \tag{C.25}$$

as expected, the reflectivity is the Fresnel reflectivity reduced by the factor included in the [] brackets (called *Strehl factor*), that is, the first-order approximation of the Debye-Waller factor (see eq. 2.21).

Let us now compute the scattering term I_s. By substituting in the eq. C.13 the second integral in the eq. C.23,

$$\frac{1}{I_0}\frac{dI_s}{d\Omega} = \frac{d\sigma_T}{d\Omega}\frac{\mathcal{N}^2}{\sin\theta_i}\left[L_1L_2|\hat{z}_{L_1L_2}(f_x,f_y)|^2\right] \tag{C.26}$$

passing to the limits $L_1 \to +\infty$, $L_2 \to +\infty$ as above, we obtain in the [ ] brackets of the eq. C.26 the surface PSD (*Power Spectral Density*) $P(f_x, f_y)$ (see appendix B),

$$\frac{1}{I_0}\frac{dI_s}{d\Omega} = \frac{\mathcal{N}^2}{\sin\theta_i}\frac{d\sigma_T}{d\Omega}P(f_x,f_y) \tag{C.27}$$

The equation above is a very important result: *the scattered intensity per solid angle is proportional to the surface PSD*, evaluated at spatial frequencies related to the scattering angles by the eq. C.9. Conversely, a scattering measurement may be used to provide a complete spectral analysis of the surface.

Isotropic surface scattering Let us restrict to the case of X-rays scattering in grazing incidence on a smooth, isotropic surface. The scattered power per solid angle depends mainly on f, and its relationship to the scattering angles determines the intensity distribution. As the surface is smooth, the scattering angles will be near to $(\theta_i, 0)$: we can so develop $\cos\theta_s$ and $\cos\phi_s$ as

$$\cos\theta_s \approx \cos\theta_i - \sin\theta_i(\theta_s - \theta_i) \qquad\qquad \cos\phi_s \approx 1 - \frac{\phi_s^2}{2} \tag{C.28}$$

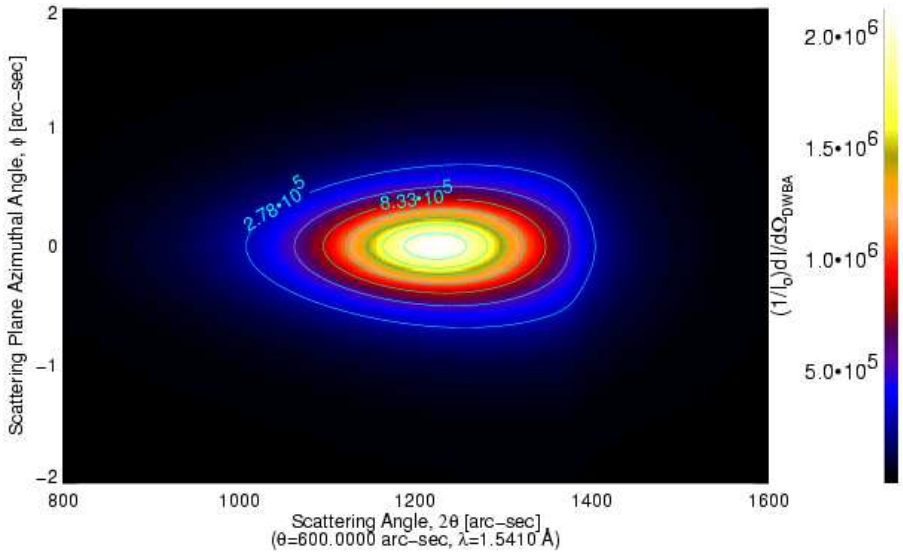

Figure C.1: Contour plot of the 2D scattering of 8.05 keV X-rays incident on a Silicon surface (IMD simulation with $\sigma = 5\mathring{A}$, the PSD is a Lorentzian with $l_c = 0.01mm$, C=2). The incidence angle is 600", thus below the Si critical angle (700" $\div$ 800"). The y axis (very stretched) coincides with the ϕ_s direction, the x axis is in the θ_s direction. The isophotes are roughly ellipses centered on the specular direction with an ellipticity slowly decreasing with θ_s.

and substituting in f^2,

$$f^2\lambda^2 \approx 2\cos\theta_i \sin\theta_i(\theta_s - \theta_i)^2 + \cos\theta_i^2(\phi_s)^2 \tag{C.29}$$

the scattering isophotes in (θ_s, ϕ_s) (see fig. C.1) are hence ellipses centered on $(\theta_i, 0)$ with the axis θ_s / axis ϕ_s ratio of about $(\tan\theta_i)^{-1/2}$. In grazing incidence, the scattering in θ_s direction is thus 100-1000 times more effective than in the ϕ_s direction. This is the reason why in the following we shall consider only the monodimensional scattering along θ_s.

Assuming all the scattered power around $\phi_s \approx 0$, we integrate on the azimuthal angle ϕ_s,

$$\frac{1}{I_0}\frac{dI_s}{d\theta_s} = \frac{\mathcal{N}^2}{\sin\theta_i}\int_0^{2\pi}\frac{d\sigma_T}{d\Omega}P(f_x, f_y)\cos\theta_s d\phi_s \tag{C.30}$$

due to the smallness of the scattering angles, only for $\phi_s \approx 0$ the integrand carries a significant contribution, and so we can consider the differential cross-section constant with ϕ_s. Moreover, at $\phi_s \approx 0$, eq. C.9 yields $\cos\theta_s d\phi_s \approx \lambda df_y$: we integrate $P(f_x, f_y)$ on f_y returning $P(f_x)$, and recalling the expression for R_F:

$$\frac{1}{I_0}\frac{dI_s}{d\theta_s} = 4k^3 R_F(\theta_i)Q(\theta_s, \theta_i)\sin^3\theta_i \frac{P(f_x)}{2\pi} \tag{C.31}$$

where we used $k = \frac{2\pi}{\lambda}$ and defined (following bibl. [82]) the *Q polarization factor*

$$Q(\theta_s, \theta_i) = \frac{\left.\frac{d\sigma_T}{d\Omega}\right|_{(\theta_s,0)}}{\left.\frac{d\sigma_T}{d\Omega}\right|_{(\theta_i,0)}} \tag{C.32}$$

the factor $Q(\theta_s, \theta_i)$ depends on the assumed dependence of the scattering cross-section on the scattering and incidence angles: as $\theta_s \to \theta_i$ Q must tend to 1. As we identified σ_s with σ_T, we can write (the incidence angle is θ_i, the electron scattering angles are $\theta_s + \theta_i$ and $2\theta_i$):

$$Q(\theta_s, \theta_i) = \frac{1 + \cos^2(\theta_s + \theta_i)}{1 + \cos^2(2\theta_i)} \tag{C.33}$$

the cosines are the contribution of the p-polarized radiation. For $\theta_s \sim \theta_i$ it easy to show that we can approximate

$$Q(\theta_s, \theta_i) \approx \sqrt{\frac{1+\cos^2(2\theta_s)}{1+\cos^2(2\theta_i)}} \tag{C.34}$$

by recalling the obtained expression for R_F (eq. C.19) and $\frac{d\sigma_T}{d\Omega}$ (eq. C.20), this expression becomes

$$Q(\theta_s, \theta_i) \approx \frac{\sin^2\theta_s}{\sin^2\theta_i}\sqrt{\frac{R_F(\theta_s)}{R_F(\theta_i)}} \tag{C.35}$$

this result (the same as the obtained one in the vector *Rayleigh-Rice theory*) is interesting because it involves the surface reflectivity evaluated at the scattering angle. Although the developed theory is rigorously valid above the critical angle, these results are valid also in the total reflection regime (see bibl. [79]), since the result depends only on outer surface topography and it is independent on details of propagation of X-rays in the reflecting material. Substituting the expression of $Q(\theta_s, \theta_i)$ we obtain, finally,

$$\frac{1}{I_0}\frac{dI_s}{d\theta_s} = \frac{16\pi^2}{\lambda^3} Q_{is} \sin^2\theta_s \sin\theta_i P(f) \tag{C.36}$$

where $Q_{is} = [R_F(\theta_s)R_F(\theta_i)]^{1/2}$ and we have suppressed the subscript x in the $P(f)$ due to surface isotropy. The eq. C.36 is the equation we will use in all of our, single-boundary, scattering measurements. The same formula is reported in many classical papers[3] (bibl. [82], bibl. [111]).

It is evident from the form of the Q factor that the scattering effect is larger at scattering angles below the critical angle, and falls above this limit. Moreover, at incidence angles on rough surfaces much larger than the surface critical angle, the scattering at $\theta_s \approx \theta_c$ is so enhanced by the Q factor increase that it may take over the PSD fall at high frequencies (see appendix B). In this case a broad scattering peak appears around $\theta_s \simeq \theta_c$, below the incidence angle (*Yoneda effect*, see fig. C.2). Similarly, at $\theta_i < \theta_c$, the rise of the factor $\sin^2\theta_s Q(\theta_s)$ up to θ_c and its fall over this limit should cause a second broad peak around θ_c, called *anti-Yoneda peak*.

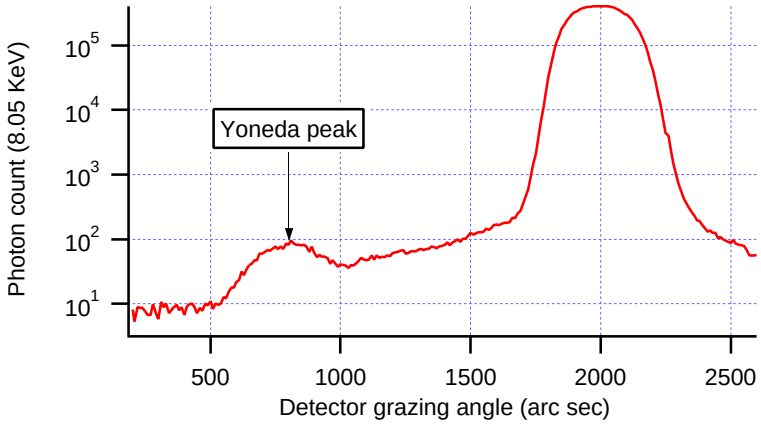

Figure C.2: The Yoneda effect observed in the scattering of the Si surface capping on a Mo-Si multilayer, in correspondence of the Silicon critical angle. The 8.05 keV beam incides at the first Bragg peak at 2000" and the surface roughness is 2.8 Å.

[3] An additional $(2\pi)^{-1}$ factor might appear in the PSD definition, so that the eq. C.36 could appear multiplied by 2π.

The exposed analysis suggests interesting considerations about the scattering-reflectivity link. In the described model (free electron gas, absorption free) the surface roughness scatters the radiation at different angles than the specular direction, but the overall energy must be conserved: assuming the constance of the refracted ray (see eq. 2.22), we must conclude that the integral of scattered power in all directions should return the Fresnel reflectivity. In fact, in the second-order approximation,

$$\frac{1}{I_0}\int \frac{dI(\theta_s)}{d\theta_s}\,d\theta_s \approx R_F(\theta_i)[1-(2k\sin\theta_i)^2] + \frac{16\pi^2}{\lambda^3}R_F(\theta_i)\sin\theta_i \int [R_F(\theta_s)R_F(\theta_i)]^{1/2}\sin^2\theta_s P(f)d\theta_s \quad \text{(C.37)}$$

as $\sin\theta_s d\theta_s = \lambda df$ and $\langle Q\rangle \approx 1$,

$$\frac{1}{I_0}\int \frac{dI(\theta_s)}{d\theta_s}\,d\theta_s \approx R_F(\theta_i)[1-(2k\sin\theta_i)^2] + 4k^2 R_F(\theta_i)\sin^2\theta_i \int P(f)df = R_F(\theta_i) \quad \text{(C.38)}$$

We can so conclude that the separation between reflection and scattering *depends only on the angular resolution of the source and detector*. As scattering is always present, we never measure the pure reflectivity (delta-like) in the specular direction because of the non-zero beam divergence and detector aperture width; we always include *also the scattered rays up to the half angular acceptance of the detector* $\frac{\Delta\theta}{2}$, corresponding to a wavelength range between 0 and $l_M \approx f_m^{-1}$ as above. The other wavelengths do not contribute to reflect and so they appear as scattered rays: the maximum wavelength which scatters the beam out of the detector is thus

$$l_M = \frac{\lambda}{\cos\theta_i - \cos(\theta_i + \Delta\theta/2)} \simeq \frac{2\lambda}{\sin\theta_i \Delta\theta} \quad \text{(C.39)}$$

whereas the minimum observable (ideally) wavelength is $\frac{\lambda}{2\cos\theta_i} \approx \frac{\lambda}{2}$. In practice, the scattering quickly decays for increasing θ_i and becomes surely negligible when θ_s is larger than some tenth degrees. The range $[l_m, l_M]$ is the wavelength interval where the PSD has to be reduced in order to improve the reflectivity. In X-rays (e.g. $\lambda = 1\mathring{A}$) and in grazing incidence (e.g. $\theta_i = 1000$"), and in order to obtain an image "blurring" not larger than 20", the spatial wavelength interval of interest turns out to be

$$0.01\mu m < l < 100\mu m \quad \text{(C.40)}$$

which covers the full AFM range[4]. As a consequence, the σ rms of the surface which is used in the eq. 2.21 is to be computed by integration of the PSD in this wavelength range. This might explain why the reflectivity and the scattering measurements are not always so easily comparable.

C.2 Scattering from a multilayer-coated surface

The equation eq. C.6 may be extended easily to a multilayer structure with imperfect boundaries. Let us have a two-material multilayer with N/2 bilayers, a period d and Γ as ratio metal/period. The absorber (h) and the spacer (l) have free electron-density $\mathcal{N}_h$ and $\mathcal{N}_l$ respectively. The substrate electron density is $\mathcal{N}_0$, as above, and $\mathcal{N}_{N+1} = 0$ is the vacuum density. Under the approximation that the multiple scattering may be neglected (justified by the smooth-surface condition and the poor scattering in transmission), the scattering pattern has to be

$$\frac{dI}{d\Omega} = \frac{c}{8\pi}\frac{d\sigma_s}{d\Omega}\left|\int_V \mathcal{N}(\underline{r})E(\underline{r})e^{-i\xi(\underline{r})}\,d^3\underline{r}\right|^2 \quad \text{(C.41)}$$

[4]In EUV reflection ($\lambda = 13.4nm$, $\theta_i \simeq 90^o$) the scattering wavelengths are more or less the same.

in this case the vertical structure is important and we cannot easily integrate on the z variable as above: moreover, the knowledge of the radiation field inside the multilayer stack is necessary. We define $z_0, z_1, \ldots, z_N$ the upper layer boundary profiles (functions of x and y), with the increasing index from the bottom to the top of the stack: the odd boundaries are the absorber/spacer transitions, the spacer/absorber transitions are the even ones. Of course, z_0 is the substrate/spacer boundary and the z_N is the absorber-vacuum boundary. The electric field intensity is a function of the bilayer number (see sect. 3.3.3, page 55), slowly decreasing because of the progressive reflection and absorption in the stack. We denote with E_n its value in the n^{th} layer ($E_{N+1} = E_r$, the refracted ray in the stack at the first layer). We can so write:

$$\int_{-\infty}^{Nd/2} \mathcal{N}(z)E(z)e^{-i\alpha z}\,dz = \sum_{n=0}^{N+1} \mathcal{N}_n \int_{z_{n-1}}^{z_n} E(z)_n e^{-i\alpha_n z}\,dz \tag{C.42}$$

where $\alpha_{n=l,h}$ is defined like in the equation C.9, with the incidence and the scattering angles evaluated in the l or h material, respectively, and multiplied by the refractive index of the material. The lower substrate boundary is $z_{-1} = -\infty$ and $E(z_{-1}) = 0$. The integral may now be solved:

$$\int_{-\infty}^{Nd/2} \mathcal{N}(z)E(z)e^{-i\alpha z}\,dz = \sum_{n=0}^{N+1} \left[\frac{\mathcal{N}_n}{-i\alpha_n}(E_n e^{-i\alpha_n z_n} - E_{n-1}e^{-i\alpha_{n-1}z_{n-1}}) \right] \tag{C.43}$$

as before we approximate as before the exponentials at the first order:

$$e^{-i\alpha z_n} = e^{-i\alpha\langle z_n\rangle}[1 - i\alpha\langle z_n\rangle] \tag{C.44}$$

the $\langle z_n\rangle$ indicate the average value of the profiles. If the boundaries were ideal ($\Delta z_n = z_n - \langle z_n\rangle = 0$), there would be no scattering: only the phase factors $e^{i\alpha\langle z_n\rangle}$ would survive and the interference would simply return the reflected ray. We are instead interested in the first perturbative terms Δz_n and so we may write, rearranging the terms:

$$\int_{0}^{Nd/2} \mathcal{N}(z)E(z)e^{-i\alpha z}\,dz \approx \sum_{n=0}^{N} E_n e^{-i\alpha\langle z_n\rangle}\frac{\mathcal{N}_n - \mathcal{N}_{n+1}}{-i\alpha} + \sum_{n=0}^{N} E_n(\mathcal{N}_n - \mathcal{N}_{n+1})e^{-i\alpha\langle z_n\rangle}\Delta z_n \tag{C.45}$$

here α is an average value of α_l and α_h. We guess that the scattering term is the second sum, with $\mathcal{N}_{odd} = \mathcal{N}_1$, $\mathcal{N}_{even} = \mathcal{N}_h$ except $\mathcal{N}_0$.

We can now insert this result in the eq. C.41: we obtain from the first term the reflected ray[5], while for the second the integration on x and y will return the surface Fourier transform of the Δz_n. By computing the squared module, all the scatering terms average to zero (being the average value of the transforms) except

$$\frac{dI_s}{d\Omega} = \frac{c}{8\pi}\frac{d\sigma_s}{d\Omega}\left|\sum_{n=0}^{N}(-1)^n E_n e^{-i\alpha\langle z_n\rangle}(\mathcal{N}_2 - \mathcal{N}_1)\int_A \Delta z_n e^{2\pi i(f_x x + f_y y)}\,dxdy\right|^2 \tag{C.46}$$

except for $n = 0$, where $\Delta\mathcal{N} = \mathcal{N}_0 - \mathcal{N}_l$, and for $n = N$, where $\Delta\mathcal{N} = \mathcal{N}_h$. The spatial frequencies are defined exactly like in the eqs. C.9, without refractive correction because they involve only the horizontal component of the photon momentum, which is conserved (see the Snell law). The angles θ_s, θ_i, ϕ_s may be

[5] assuming a trend $T_n = e^{-(N-n)\xi/2}$, with $\xi = 2r_F \sin(\pi k\Gamma)$, the sum in the reflected ray is easily calculated and returns approximately a typical saturation behaviour $R(N) = (1 - e^{-N\xi})^2$ at the Bragg peak.

so evaluated in the vacuum. Introducing the amplitude transmittance in the n^{th} layer $T_n = E_n/E_r$, and the definition of I_0 as before,

$$\frac{1}{I_0}\frac{dI_s}{d\Omega} = \frac{(\Delta\mathcal{N})^2}{L_1 L_2 \sin\theta_i}\frac{d\sigma_s}{d\Omega}\left|\sum_{n=0}^{N}(-1)^n T_n e^{-i\alpha\langle z_n\rangle}\int_A \Delta z_n e^{-2\pi i(f_x x + f_y y)}\,dxdy\right|^2 \tag{C.47}$$

and again we can introduce the reflectivity r_F of each boundary absorber/spacer and spacer/absorber (eqs. A.20 and A.10)

$$r_F(\theta_i) = \left(\frac{\lambda^2\,\Delta\mathcal{N}}{4\pi\sin^2\theta_i}\right)^2 \left.\frac{d\sigma_T}{d\Omega}\right|_{\theta_i,0} \tag{C.48}$$

and defining the average factor $Q_{is} = [r_F(\theta_i) r_F(\theta_s)]^{1/2}$ and the Fourier transforms $\widehat{\Delta z_n} = \hat{z}_n$

$$\frac{1}{I_0}\frac{dI_s}{d\Omega} = \frac{16\pi^2}{\lambda^4} r_F(\theta_i)\sin^3\theta_i Q(\theta_i,\theta_s) L_1 L_2 \left|\sum_{n=0}^{N}(-1)^n T_n e^{-i\alpha\langle z_n\rangle}\hat{z}_n(f_x,f_y)\right|^2 \tag{C.49}$$

the $|\,|$ brackets include the sum of all the boundaries, weighted upon the relative amplitude of the electric field in the layer. If we execute all the products, this time, they may be distinguished into two classes:

$$P_n = L_1 L_2 |\hat{z}_n|^2 \qquad C_{nm} = L_1 L_2 Re(\hat{z}_n^* \hat{z}_m) \tag{C.50}$$

the P_n are the Power Spectral Density of the interfaces, whereas the C_{nm} are the crossed spectral densities of the m^{th} boundary with the n^{th} boundary. Under the hypothesis that there is no lateral phase shift of the spectral components in different layers ($Im(\hat{z}_n^* \hat{z}_m) = 0$), executing the products and summing the conjugates, the scattering pattern is now described by:

$$\frac{1}{I_0}\frac{dI_s}{d\Omega} = \frac{16\pi^2}{\lambda^4} r_F(\theta_i)\sin^3\theta_i Q_{is}\left[\sum_n T_n^2 P_n(\underline{f}) + \sum_{n>m} 2(-1)^{n+m} C_{nm}(\underline{f})\, T_n T_m \cos(\alpha\Delta_{nm})\right] \tag{C.51}$$

where we defined $\Delta_{nm} = \langle z_n\rangle - \langle z_m\rangle$. If the surfaces are isotropic, we can integrate as above on the ϕ_s angle to obtain a linear description of the scattering diagram, that can be used to compute the interfacial PSDs:

$$\begin{aligned}
\frac{1}{I_0}\frac{dI_s}{d\theta_s} &= \frac{16\pi^2}{\lambda^3} Q_{is}\sin\theta_i \sin^2\theta_s [P_{unc}(f) + P_{corr}(f)] \\
P_{unc} &= \sum_n T_n^2 P_n(f) \\
P_{corr} &= 2\sum_{n>m}(-1)^{n+m} C_{nm}(f)\, T_n T_m \cos(\alpha\Delta_{nm})
\end{aligned} \tag{C.52}$$

these equations are reported and commented in detail in sect. 5.3.2.

Bibliography

[1] P.A. Charles, F.S. Seward, *Exploring the X-ray Universe* : **1995**, Cambridge Univ. Press

[2] Tanaka et al., *Unusual Properties of X-ray Emission near the Galactic Center*: **2000**PASJ 52, L25

[3] Baganoff et al., *Rapid X-ray flaring from the direction of the supermassive black hole at the Galactic Centre*: **2001**, Nature 413,45

[4] Orlandini, Dal Fiume, *Hard X-ray tails and cyclotron features in X-ray pulsars*: **2001**, AIP Conference Series Vol. 599, P 283

[5] Santangelo et al., *A BeppoSAX Study of the Pulsating Transient X0115+63: The First X-ray Spectrum with Four Cyclotron Harmonic Features*: **1999**, Astrophys. J. Lett. 523, P L085-L088

[6] A. Malizia et al., **2004**, Proc. INTEGRAL workshop, Munich 2004

[7] F. Frontera et al. *Broadband spectrum of Cygnus X-1 in two spectral states with BeppoSAX*: **2000**, The Astrophysical Journal 546, 1027-1037

[8] Belloni et al., *On the nature of XTE J0421+560/CI Cam*: **1999**, The Astrophysical Journal, July 1999

[9] M. Van der Klis, *Millisecond Oscillations in X-ray Binaries*: **2000**, Annual Review of Astronomy and Astrophysics

[10] T. Montmerle, *X-rays and regions of star formation: a combined ROSAT-HRI/near-to-mid IR study of the rho Oph dark cloud*: **2000**, Astronomy and Astrophysics

[11] Perola et al., *Compton reflection and iron fluorescence in BeppoSAX observations of Seyfert type 1 galaxies*, **2002**: Astronomy and Astrophysics

[12] L. Ferrarese, *Supermassive Black Holes*: **2002**,Phys.World 15N6 (2002) 41-46

[13] Primini et al., *The CfA Einstein Observatory extended deep X-ray survey*: **1991**, Astrophysical Journal, vol. 374, June 20, p. 440-455

[14] Setti and Woltjer, *Active galactic nuclei and the spectrum of the X-ray background*: **1989**, Astronomy and Astrophysics, 224, L21

[15] A. Soltan, *Masses of Quasars*: **1982**, Royal Astronomical Society Monthly Notices, vol. 200, July 1982, p. 115-122

[16] G. Hasinger et al., *The ROSAT Deep Survey. I. X-ray sources in the Lockman Field*: **1998**, Astronomy and Astrophysics, v.329, p.482-494

[17] Della Ceca et al., *A Medium Survey of the Hard X-ray Sky with ASCA. II. The Source's Broadband X-ray Spectral Properties*, **1999**: The Astrophysical Journal, Volume 524, Issue 2, pp. 674-683

[18] Giommi et al., *The BeppoSAX 2-10 keV Survey*: **2000**, Astronomy and Astrophysics 362..799G

[19] A. Comastri et al, *The BeppoSAX View of the Hard X-ray Background*: **2000**

[20] De Luca A., Molendi S., *The 2-8 keV cosmic X-ray background spectrum as observed with XMM-Newton*: **2004**, Astronomy and Astrophysics, v.419, p.837-848

[21] Makishima et al., *The Nature of Ultraluminous Compact X-Ray Sources in Nearby Spiral Galaxies*: **2000**, The Astrophysical Journal, Volume 535, Issue 2, pp. 632-643

[22] Fusco-Femiano et al., *Hard X-Ray Emission from the Galaxy Cluster A2256*: **2000**, The Astrophysical Journal, Volume 534, Issue 1, pp. L7-L10

[23] Trincheri et al., *Broad Band X-ray Spectra of M31 Sources with BeppoSAX*: **1999**, Astronomy and Astrophysics

[24] B.Rossi, *Optics* : Masson

[25] D. Attwood, *Soft X-rays and Extreme Ultraviolet Radiation: Principles and Application* : **2000**, Cambridge University Press

[26] R. Giacconi, B.Rossi, **1960**, J. Geophys. Res. 65, 773

[27] H. Wolter, **1952**, Annalen der Physik 10,94

[28] L. P. Van Speybroeck, R. C. Chase, *Design parameters of Paraboloid-Hyperboloid Telescopes for X-ray Astronomy*: **1972**Applied Optics 11,2

[29] R.Petre, P.J. Selermitos, **1985**, Applied Optics 12,24

[30] H. W. Schnopper et al., *Thin shell plastic optics for laboratory applications*, **2004**, SPIE Proc. 5537-15

[31] Thompson et al., *X-ray data Booklet*, Center for X-ray Optics, University of California

[32] E. Spiller, *Soft X-rays Optics*, **1994**, SPIE Optical Engineering Press

[33] F. Frontera et al., *The high energy instrument PDS on-board the Beppo-SAX X-ray astronomy satellite*, **1997**, Astron. Astroph. Suppl. 122, 357

[34] O. Citterio et al., *Optics for the X-ray imaging concentrators aboard the X-ray astronomy satellite SAX* : **1988**, Applied Optics, 27-140

[35] F. A. Jansen, *XMM: advancing science with the high-throughput X-ray spectroscopic mission* : **1999**, ESA Bulletin 100, 15

[36] D. N. Burrows et al., *SWIFT X-ray telescope*: **2000**, SPIE Proc., 4140-64

[37] http://SWIFT.gsfc.nasa.gov/docs/SWIFT/

[38] Barthelmy, S. D. on behalf of the SWIFT Instrument Team: *The Burst Alert Telescope (BAT) on the SWIFT MIDEX Mission*: **2000** SPIE Proc. 4140

[39] O. Citterio et al., *Characteristics of the flight model optics for the JET-X telescope on-board the Spectrum-X-Gamma Satellite*: **1996**, SPIE Proc., 2805-56

[40] A. Moretti, S. Campana, G. Tagliaferri, *SWIFT XRT point spread function measured at the PANTER end-to-end test*: **2003**, SPIE Proc., 3766

[41] http://sci.esa.int/science-e/www/area/index.cfm?fareaid=21

[42] P. Ubertini et al., *IBIS: the gamma-ray imager onboard INTEGRAL*, **1999**,Astroph. Lett. and Comm., 39, 331

[43] N. Kaiser, *Some Fundamentals of Optical Thin Film Growth*in *Optical Interference Coatings*, **2003**, Springer

[44] S. Yulin, *Multilayer Coatings for EUV/Soft X-ray Mirrors*, ibidem

[45] G. N. Strauss, *Mechanical Stresses in Optical Coatings*, ibidem

[46] H. K. Pulker, *Film Deposition Methods*, ibidem

[47] P. Vukusic, *Natural coatings*, ibidem

[48] INAF-OAB Authors et al., *HEXIT-SAT a mission concept for grazing incidence telescopes in X-ray astronomy from 0.1 to 70 keV:*, **2003**

[49] B. D. Ramsey et al., *HERO: High-Energy Replicated Optics for hard X-ray balloon payload*: **2000**, SPIE Proc., 4138-147

[50] F. A. Harrison et al., *Development of the High-Energy Focusing Telescope (HEFT) balloon experiment*: **2000**, SPIE Proc. 4012-693

[51] Y. Tawara et al., *InFocus baloon-borne hard X-ray experiment with multilayer supermirror telescope*: **2001**, SPIE Proc. 4496-109

[52] P. Ferrando et al., *SYMBOL-X: a new generation X-ray telescope*: **2003**, SPIE Proc. 5168

[53] http://constellation.gsfc.nasa.gov/

[54] F. Harrison et al., *Technology development for the Constellation-X Hard X-ray telescope*: **1999**, SPIE Proc. 3765-104

[55] *The XEUS Telescope*: **2001**, ESA SP-1253

[56] A. Parmar et al., *Science with XEUS / the X-ray Evolution Universe Spectroscopy Mission*, **2004**, SPIE Proc. 5488

[57] M. Bavdaz et al., *XEUS mission reference design*, **2004**, SPIE Proc. 5488

[58] M. Bavdaz et al., *Status of X-ray Optics Development for the XEUS mission*, **2004**, SPIE Proc. 5488

[59] M. Bavdaz, A. Peacock, *Progress at ESA on High Energy Optics Technology*: **2003**SPIE Proc. 5168

[60] K.D. Joensen, F.E. Christensen et al., *Design of grazing-incidence multilayer supermirror for hard X-rays reflectors*: **1995**, Applied Optics, Vol. 34, 7935

[61] K. D. Joensen et al., *Grazing incidence Fe-line using W/B_4C multilayers* : **1994**, SPIE Proc. 2011, 373

[62] R.C. Catura et al., *Calculated performance of a Wolter I X-ray telescope coated by multilayers*:**1983**, Opt. Eng. 22,140

[63] J.H. Underwood, T.W. Barbee, *Layered synthetic microstructures as Bragg diffractors for X-rays and extreme ultraviolet: theory and predicted performance*: **1981**, Applied Optics, Vol. 20, No. 17

[64] M.C. Weisskopf, S.T. O'Dell, **1997**, SPIE Proc. 3313, 2-17

[65] P.Conconi et al., *Numerical optimization of wide-field grazing incidence X-ray optics with polynomial profile for astronomy*, **2004**, SPIE Proc. 5536-7, in press

[66] D.L. Windt, W.K. Waskiewicz, J.E. Griffith, *Surface finish requirements for soft X-ray mirrors*, **1994**, Applied Optics, Vol. 33

[67] A. Baranov et alii, *High resolution Carbon/Carbon multilayers*: **2002**, SPIE Proc. 4782 160-168

[68] I.V. Kozhevnikov, *Analysis of X-ray scattering from a rough multilayer mirror in the first-order perturbation theory*: **2003**, Nuclear Instruments and Methods in Physics Research A498, 482-495

[69] I. V. Kozhevnikov, *Physical analysis of the inverse problem of X-ray reflectometry*: **2003**, Nuclear Instruments and Methods in Physics Research A508, 519-541

[70] N. Locksley, B.K. Tanner, D.K. Bowen, *A novel beam conditioning monochromator for high-resolution X-ray diffraction*: **2005**, J. Appl. Cryst. 28, 314

[71] I. Kozevnikov et al., *Design of X-ray supermirrors*: **2001**, Nuclear Instruments and Methods in Physics Research A460, 424-443

[72] P. Mikulik, *X-ray reflectivity from planar and structured multilayers*: **1997**, Ph.D. Thesis at CNRS, Grenoble, France

[73] L. Peverini, *Master Degree thesis*, Milano University

[74] V. Cotroneo, *Master Degree thesis*, Milano University

[75] S. Abdali, Ph.D. thesis

[76] F.E. Christensen, S. Abdali et alii, *High resolution X-ray scatter and reflectivity study of sputtered Ir surfaces*: SPIE Proc. Vol. 2011

[77] D.G. Stearns, *X-ray scattering from interfacial roughness in multilayer structures*: **1992**, Journal of Applied Physics, 71(9)

[78] D.G. Stearns, D.P. Gaines, D.W. Sweeney, *Non-specular X-ray scattering in a multilayer-coated imaging system*: **1998**, Journal of Applied Physics, 84(2)

[79] J.C. Stover, *Optical Scattering: measurement and analysis*, **1995**, SPIE Optical Engineering Press

[80] J.M. Bennett and L. Mattsson, *Introduction to Surface Roughness and Scattering*, **1999**, Optical Society of America press

[81] T. Karabacak et al., *Large-angle in-plane light scattering from rough surfaces*: **2000**, Applied Optics Vol. 39 n.25

[82] E.L. Church, *Role of surface topography in X-ray scattering*: **1979**, SPIE Proc. Vol. 184 Space Optics / Imaging X-ray Optics Workshop

[83] E.L. Church, H. A. Jenkinson and J. M. Zavada, *Relationship between Surface Scattering and Microtopographic Features*: **1979**Optical Engineering 18(2) 125

[84] E. I. Church and P. Z. Takacs, *The interpretation of glancing incidence scattering measurements*, **1986**, SPIE Proc. 640, 126-133

[85] K. K. Madsen, F. E. Christensen et al., *X-ray study of W/Si multilayers for the HEFT hard X-ray telescope*: **2004**, SPIE Proc. 5168, 41-52

[86] D. D. Ryutov, *Thermal stresses in the reflective X-ray optics for the Linac Coherent Light Source*: **2003**, Review of Scientific Instruments 74-8

[87] E.L. Church, H. A. Jenkinson and J. M. Zavada, *Measurement of the finish of diamond-turned metal surfaces by differential light scattering*: **1977**, Optical Engineering 16(4) 360-374

[88] E. Spiller, D. , M. Krumrey, *Multilayer X-ray mirrors: interfacial roughness, scattering, and image quality*, **1993**, Journal of Applied Physics 74(1)

[89] S. Romaine et al., *Characterization and Multilayer coating od cylindrical X-ray optics for X-ray astronomy*, **1998**, SPIE Proc. 344, 552-555

[90] G. Pareschi et al., *Replication by Ni electroforming approach to produce the Con-X/HXT hard X-ray mirrors*, **2002**, SPIE Proc. 4851-528

[91] G. Pareschi, O. Citterio, M. Ghigo, F. Mazzoleni, D. Spiga, *New X-ray missions*, **2003**, SAIT Conference 2003

[92] D. Spiga, *Characterization of a flat superpolished mandrel prototype with hard (TiN/SiC) overcoating to enhance the surface durability* : **2003**, SPIE Proc. 5168-55

[93] G. Pareschi, G.Di Cocco, E.Caroli, O. Citterio, V. Cotroneo, S.Del Sordo, F.Frontera, L.Gizzi, G.Malaguti, S. Silvestri, D. Spiga, *The HEXIT (High Energy X-ray Imaging Telescope) balloon-borne mission*, **2003**, Proc. of the 16th Symposium on European Rockets and Balloon Programmes and Related Research, St. Gallen (CH), 179P

[94] Spiga D., Pareschi G., Citterio O., Banham R., Cassanelli M., Cotroneo V., Grisoni G., Negri B., Valsecchi G., Vernani D., *Developement of multilayer coatings (Ni/C- Pt/C) for hard X-ray telescopes by e-beam evaporation with ion assistance*: **2004**, SPIE Proc. 5488, 813

[95] Pareschi G., Cotroneo V., Spiga D., Barbera M., Artale M. A., Collura A., Varisco S., Grisoni G., Valsecchi G., *Astronomical soft x-ray mirrors reflectivity enhancement by multilayer coatings with carbon overcoating*: **2004**,SPIE Proc. 5488, 481

[96] D.Spiga, G.Pareschi, G.Valsecchi, G.Grisoni, *Hard X-ray multilayer coated astronomical mirrors by e-beam deposition*, SPIE Proc. 5533-9, in press

[97] P. Zhao et al., *Chandra X-ray Observatory mirror effective area*: **2003**, Proceedings of the 2003 Chandra Calibration Workshop

[98] D.E Graessle et al. *Molecular contamination of iridium coated mirrors*: **1994**, SPIE Proc. 2279-12

[99] P. Conconi et al., *Wide-field X-ray imaging for future missions including XEUS*: **2004**, SPIE Proc.5168-334

[100] S.Romaine, G.Pareschi et al., *Development of a prototype Nickel optic for the Con-X hard X-ray telescope*: **2003**, SPIE Proc. 5168-32

[101] O. Citterio et al., *Multilayer optics for hard X-ray astronomy by means of replication techniques*: **1999**, SPIE Proc. 3766-310

[102] O. Citterio et al., *Development of soft and hard X-ray optics for astronomy: progress report II and considerations on material properties for large-diameter segmented optics of future missions* : **2001**, SPIE Proc. 4496-23

[103] D. W. Windt, *IMD: code for modeling the optical properties of multilayer films*: **1998**, Computer in Physics, 12, 360

[104] G. Pareschi, V.Cotroneo, *Soft (0.1 -10 keV) and hard (>10 keV) X-ray multilayer mirrors for the XEUS astronomical mission*, **2004**SPIE Proc. 5168, 53

[105] V.Cotroneo, G.Pareschi, *Global optimization of X-ray astronomical multilayer mirrors by an iterated simplex procedure*, SPIE Proc. 5533-5, in press

[106] J.M. Revillard, *Determination of X-ray multilayer structures using a simulated annealing algorithm*, **1994**, ESRF, non published

[107] S. Lunt et al. *Design of bifunctional XUV multilayer mirrors using a genetic algorithm*, **2001**, Journal of X-ray Science and Technology 9, 1-11, IOS Press

[108] M. Sanchez del Rio, G. Pareschi, *Global optimization and reflectivity data fitting for X-ray multilayer mirrors by means of genetic algorithms*, **2000**, SPIE Proc. 4145-88

[109] F. Zocchi, P. Binda, *Genetic algorithm optimization of X-ray multilayer coatings*: SPIE Proc. 5536-23, in press

[110] A.J. Fennelly and E.L. Fry, *Bremsstrahlung Optical Monitoring System (BOMS) for In Situ spectral characterization and optical film thickness monitoring of electron beam evaporated X-ray coatings and multilayers / design concept*: **1994**, SPIE Proc. 2279

[111] E.L. Church, *Comments on the correlation length*: **1986**, SPIE Proc. Vol. 680 Surface characterization and testing

[112] D.K. Bowen, B.K. Tannen, *High Resolution X-ray Diffractometry and Topography*, **1998**, Taylor and Francis

[113] P.B. Mirkarimi, D.G. Stearns et al., *Defects from substrate particles depend on sputter deposition process*, **2000**, Solid State Technology 11/2000, www.solid-state.com

[114] N. Ohnishi et al., *HRTEM analysis of Pt/C multilayers*: **2003**, SPIE Proc. 5168

[115] J.D. Rancourt, *Optical Thin Films: user handbook*, **1996**, SPIE Press

[116] D.L Smith, *Thin Film Deposition: Principles and Practice*: **1995**, Mc Graw-Hill

[117] R.E. Hummel, K.H. Guenther, *Handbook of optical properties / volume 1: thin films for optical coatings*, **1995**, CRC Press

[118] R. R. Willey, *Practical design and production of thin films*: **2002**, Marcel Dekker Inc.

[119] P.J. Martin, *J. Mater.*: **1986**, Science

[120] E. Zoethout et alii, *Stress mitigation in Mo/Si Multilayers for EUV lithography*: **2003**, SPIE Proc. 5037

[121] J.M. Slaughter, A. Mirone et al., *Structure and performance of Si/Mo multilayer mirrors for the extreme ultraviolet* **1994**Journal of Applied Physics, Vol 76(4) 2144-2156

[122] G.H. Vineyard, *Grazing-incidence diffraction and the distorted-wave approximation for the study of surfaces*: **1982**Physical Review 26,8

[123] W. Ensinger, *Ion sources for ion-beam assisted thin-film deposition*: **1992**, Review Scientific Instruments 63 (11)

[124] H.-J. Voorma et al., *Angular and energy dependence of ion bombardment of Mo/Si multilayers*, **1997**, Journal of Applied Physics Vol. 82 N.4

[125] E.J. Puik, M.J. Van der Wiel, *Ion Etching of thin W layers: enhanced reflectivity of W-C multilayer coatings*, **1991**, Applied Surface Science 47, 63-76

[126] W. T. Pawlewicz et al., *Low-energy high-flux ion assisted deposition of oxide optical coatings*: **1994**, SPIE Proc. 2262, 1-12

[127] K. Soyama et al., *Enhancement of reflectivity of multilayer neutron mirrors by ion polishing: optimization of the ion beam parameters*: **1999**, Journal of Physics and Chemistry od Solids 60, 1587-1590

[128] H. R. Kaufman and J.M.E. Harper, *Ion-assist applications of broad-beam sources*: **2004**, SPIE proc.

[129] E. Louis et al., *Enhancement of reflectivity of multilayer mirrors for soft X-ray projection lithography by temperature optimization and ion bombardment*, **1994**, Microelectronic Engineering 23, 215-218

[130] E. Spiller, *Enhancement of the reflectivity of multilayer X-ray mirrors by ion polishing*: **1990**Optical Engineering, 29 n.6 p. 609

[131] P. Tuffanelli,*Ph.D. Thesis*, Ferrara University

[132] M. Gambaccini et al., *A Bragg Diffraction Base Quasi-monochromatic Source for Mammography using Mosaic Crystals*

[133] A.K. Freund, *Mosaic crystal monochromators for synchrotron radiation instrumentation*: **1988**, Nuclear Instruments and Methods in Physics Research A266, 461-466

[134] F. Frontera, G. Pareschi, *Hard X-ray imaging via focusing optics with mosaic crystals*: **1995**, Exp. Astr. 6,25

[135] S. Melone et alii, *Gamma-ray focusing concentrators in astrophysical observations by crystal diffraction in Laue geometry*: **1993**, Review Scientific Instruments 64 (12)

[136] T.R. Lindquist and W.R. Webber, *A focusing X-ray telescope for use in the study of extraterriestrial X-ray sources in th energy range 20-140 keV*: **1968**, Canadian Journal of Physics, vol. 46, S1103

[137] A. Pisa, F. Frontera et al., *Feasibility study of a Laue lens for hard X-rays*: SPIE Proc. 5536-04, in press

[138] S. Kirkpatrick, C. D. Gelatt, M. P. Vecchi, *Optimization by simulated annealing*: **1983**, Science 220, 4598

[139] V. Cerny, *A thermodynamical approach to the travelling salesman problem: an efficient simulation algorithm*, **1982**, Report, Comenius University; Bratislava, Slovakia

[140] E. Ziegler, C. Ferrero, F. Lamy, C. Chapron, Ch. Morawe, *Characterisation of nanometer layered structures using multiple wavelength X-ray reflectometry and simulated annealing data analysis*, CPDS **2002**, Advances in X-ray Analysis, 45

[141] D.Spiga, G.Pareschi, A.Mirone, C. Ferrero, M. Sanchez del Rio, *Fitting X-ray multilayer reflectivities by means of the PPM code*: **2004**, SPIE Proc. 5536-26, in press

[142] H. Brauninger, W. Burkert, G.D. Hartner, O. Citterio, M.Ghigo, F. Mazzoleni, G. Pareschi, D. Spiga *Calibration of hard X-ray ($15 \div 50$ keV) optics at the MPE test facility PANTER*, **2003**, SPIE Proc. 5168, 283

Acknowledgements

I thank sincerely *INAF-Brera Astronomical Observatory* for hosting my Ph.D activity in these three years, and in particular: *G. Pareschi* and *O. Citterio* (INAF-OAB) for the supervision and collaboration in my Ph.D. work; *S. Basso, S. Cantú, M. Ghigo, V. Cotroneo, F. Mazzoleni, R. Valtolina, D. Vernani* for technical support and collaboration, and all the working people there.

I am grateful to *Universitá di Milano Bicocca* for this Ph.D. course in Astronomy and Astrophysics and for financial support. I am grateful especially to *G. Chincarini, S. Bonometto, G. Sironi*, for continuous support and useful advices. Many thanks also to all my *Ph.D. colleagues* for the friendly collaboration.

I thank sincerely also all *Media-Lario s.r.l.* for hosting me and for the e-beam deposition facilities availability: in particular *G. Nocerino, A. Valenzuela, G. Valsecchi, G. Grisoni, M. Cassanelli, R. Banham, F. Zocchi, P. Binda, F. Marioni, R. Cappadona* for support and collaboration.

The collaboration *ESF - COST, action P7* is acknowledged to support my STSM at ESRF to acquire the use of PPM, in particular the coordinators *T. Krist* (Hahn-Meitner Institute), *M. Idir* (Synchrotron SOLEIL), *A. Erko* (BESSY). At ESRF I have appreciated the contribution of *C. Ferrero, A. Mirone, M. Sanchez Del Rio* (ESRF, Scientific Software Group) for the assistance in PPM training, and *L. Peverini* (ESRF, Beam Line 5) for useful discussions.

The *Center for Astrophysics*, Boston, is acknowledged for the collaboration in the development of multilayer-coated optics prototypes for Constellation-X/HXT. I thank very much H. Brauninger, W. Burkert and G. Hartner (MPE) for assistance, planning and collaboration in measurements at the PANTER facility, and all the PANTER technical personnel.

ASI (the Italian space agency) is acknowledged to support the missions for my training activities.

I thank also *C. Ferrari* (CNR-IMEM, Parma, Italy) for performing the Ni/C multilayer TEM analysis, *P. Cerutti* for performing the TiN and Ni sample superpolishing, *A. Mengali* (Ce. Te. V.) for the SiC deposition and *ZEISS* for the SiC sample superpolishing.